



The
University
Of
Sheffield.

**Validation of immature ovine bone models using digital image
correlation**

Melanie Jegu

A thesis submitted in partial fulfilment of the requirements for the degree of
Doctor of Philosophy

The University of Sheffield
Faculty of Engineering
Department of Mechanical Engineering

12th of January 2023

ACKNOWLEDGEMENTS

First and foremost, I would like to acknowledge my project supervisors, Xinshan Li, and Hassan Ghadbeigi, for supporting me throughout a PhD and a pandemic. More specifically, I would like to thank Shannon, for her unwavering patience and understanding, and for restoring my academic confidence in numerous occasions. I would also like to give recognition to the technical staff that provided me with both technical and educational support, in particular to Julie Marshall and Richard Kay. Thanks to Zainab Altai, Marco Palanca and Feng Yu who kindly and patiently shared their expertise with me. Thanks to all my fellow graduate teaching assistants, and of course Harry and Matteo – to me the Structures Lab was a much-needed place of rest and recharge. Special thanks to Luke for kindly taking the time to help me with all things DIC. Jess, Stella, Ahmed and Dylan for your friendship. Thank you to Ellie, Mark and Elo for providing me with shelter when I needed it the most; literally but more importantly emotionally. Finally, a massive thank you to my parents for all the work they put in behind the scenes.

ABSTRACT

Data on paediatric bone properties is very limited due to the scarcity of specimen in this particular age range, and due to ethical complexities regarding experimental testing on paediatric cadavers. A recently validated technique for adults using CT-based finite element analysis (FEA), has the potential to provide a deeper understanding of immature bone fracture mechanism without the need of extensive paediatric cadaveric testing. This thesis aimed to investigate the validity of a CT-based FEA approach for immature bones, using lamb bones as surrogate to children's bones, by comparing strain results against 3D digital image correlation (3D-DIC) data during four-point bending tests.

In this thesis, two experimental set-ups were designed to run four-point bending tests on lamb femur specimens using 3D-DIC to capture full-field surface strain. The first set of experiments applied bending load directly onto the femurs, whereas the second set of experiments embedded the bones with the load applied to the embedding materials instead. The four-point bending tests were replicated using an image-based FEA approach. The FE geometries were segmented from either QCT or μ CT images. The material properties were derived from the CT image's attenuations using existing empirical findings relating elastic modulus to bone mineral density. Various model set-ups and boundary conditions have been investigated in order to determine the best ones that matched the experimental results.

Through assessing and comparing results obtained in the experimental tests and the FEA, the improved FE approach was successfully validated using lamb bones. Furthermore, it was concluded that the cortical region of the diaphysis (mineralised bone) of infants and toddlers can be modelled with adequate accuracy using just a homogeneous mesh of isotropic elastic modulus. For children of three years and above, anisotropy of the bone may need to be considered to appropriately replicate the properties of lamellar bone. Further studies are required in order to better characterize the empirical relationship between elastic modulus and mineral density in immature bone, as well as the cortical and trabecular bone material properties at various developmental ages. The periosteum plays an important role in the fracture behavior of immature bone; thus, it is important to separately characterize the material properties of the periosteum. For a complete representation of bone *in vivo*, both the periosteum and the mineralizing bone should be integrated into the FE model.

ABBREVIATIONS

BMD	Bone mineral density
BV	Bone volume
CT	Computed tomography
QCT	Quantitative computed tomography
μ CT	Micro computed tomography
CAD	Computer aided design
DIC	Digital image correlation
DoF	Depth-of-field
FBP	Filtered backprojection
FE	Finite element
FEA	Finite element analysis
FEM	Finite element modelling
HA	Hydroxyapatite
HU	Hounsfield unit
K_2HPO_4	Dipotassium phosphate
kVp	Kilovoltage peak
mAs	Milliamperage second
NA	Neutral axis
PCA	Physical child abuse
ROI	Region of interest
AOI	Area of interest
VOI	Volume of interest
STL	Faceted body file format
SG	Strain gauges
TV	Total volume

NOMENCLATURE

a	X-ray attenuation
\mathbf{a}	Acceleration
B	Strain-displacement matrix
\mathbf{b}	Body forces
C	Correlation function; contour surface; Right Cauchy Green deformation tensor
D	Stiffness matrix
E	Elastic modulus
F	Deformation gradient tensor
\mathbf{F}	Load
G	Shear modulus
I	Reference image
I^*	Deformed image
K	Global stiffness matrix
k_e	Element (local) stiffness matrix
m	Mass
N	X-ray intensity, shape function
\mathbf{n}	Normal vector
p	Porosity
S	Surface
t	Time
\mathbf{t}_n	Traction vector (stress vector)
\mathbf{u}	Displacement
V	Volume
\mathbf{v}	Velocity
ρ	Density
ε	Strain
ω	CT voxel dimension
μ	Attenuation
σ	Stress
ν	Poisson's ratio

CONTENTS

Acknowledgements.....	2
Abstract.....	3
Abbreviations	4
Nomenclature	5
Contents.....	6
List of figures.....	10
List of tables	16
1 Introduction.....	18
1.1 Statement of the problem	18
1.1.1 Key facts on the prevalence of child maltreatment.....	18
1.1.2 Statistics relating bone fracture to child maltreatment	18
1.1.3 Clinical guidelines on fracture differentiation	19
1.2 Applying finite element modelling to medico-legal affairs.....	19
1.3 Project aims and objectives	20
1.4 Chapter by chapter overview	21
1.5 List of contributions.....	23
2 Literature review	24
2.1 Bone structure and development.....	24
2.1.1 Composition of the bone	24
2.1.2 Microstructure of bone	24
2.1.3 Macrostructure of long bones	26
2.1.4 Development of long bones	27
2.1.5 Mechanical and material properties of bone tissue.....	31
2.1.6 Fracture patterns in immature long bone	35
2.2 Animal surrogates for immature whole bone testing.....	36
2.2.1 Ovine femur	37
2.2.1 Experimental mechanical testing on ovine femur	39
2.2.1.1 Storage.....	39
2.2.1.2 Bending tests	40
2.2.1.3 Surface strain measurements.....	40
2.2 Finite element analysis for biomechanics.....	42
2.2.1 Computed tomography based subject specific bone modelling	42
2.2.2 Adaptation of the modelling pipeline to paediatric	46
2.2.3 Experimental validation of the in-house femur FE model	46
2.2.4 DIC for the experimental validation of femur models.....	47

3	General methods: Experimental tests	48
3.1	Bending Theory.....	48
3.2	Digital Image Correlation	49
3.2.1	Fundamental principles of DIC.....	50
3.2.2	Basic principles of photography for DIC	58
3.2.3	Stereo-system set-up.....	60
4	General methods: CT-based FEA	64
4.1	CT-based modelling	64
4.1.1	Computed tomography	64
4.1.2	Semi-automated 3D segmentation.....	70
4.2	Continuum mechanics for FEM.....	72
4.2.1	Displacement and strain	72
4.2.2	Stress	74
4.3	The finite element method.....	79
4.3.1	Element type and shape functions	80
4.3.2	Strain and stress vectors in FEA.....	81
4.3.3	Principle of virtual works in FEA	81
5	Four-point bending test on whole lamb bones	83
5.1	Introduction	83
5.2	Methods	83
5.2.1	Materials (bones).....	83
5.2.2	Sample preparation	85
5.2.3	Experimental set-up	86
5.2.4	Force-displacement data processing.....	91
5.2.5	Digital image processing.....	92
5.3	Results	97
5.3.1	Part one: critical experimental events.....	97
5.3.2	Part two: force-displacement plots and DIC surface strain contours ..	102
5.4	Discussion	108
5.4.1	Force-displacement curves.....	108
5.4.2	Surface strain contours.....	109
5.4.3	Data for finite element model validation	110
5.4.4	Limitations of the experimental method.....	110
5.4.5	Suggested improvements to the experimental method.....	115
5.5	Conclusions.....	117
6	Four-point bending FEA on whole lamb bones	118
6.1	Method	119
6.1.1	QCT scanning	122

6.1.2	Segmentation	122
6.1.3	Reconstruction.....	123
6.1.4	Alignment	124
6.1.5	Outlining the cortical bone	126
6.1.6	Material properties.....	127
6.1.7	Boundary conditions.....	134
6.1.8	Comparison against experimental results	141
6.2	Results	142
6.2.1	Part one	142
6.2.2	Part two	144
6.3	Discussion	147
6.3.1	Boundary conditions.....	147
6.3.2	Model types.....	149
6.3.3	Material properties.....	151
6.4	Conclusions.....	154
7	Four-point bending test on embedded lamb bones.....	156
7.1	Introduction.....	156
7.2	Methods	157
7.2.1	Materials (bones).....	157
7.2.2	Sample preparation	158
7.2.3	Cleaning and cutting	158
7.2.4	Embedding.....	159
7.2.5	Rehydration and painting	164
7.3	Experimental set-up.....	166
7.3.1	Four point bending set-up	166
7.3.2	Stereo system set up and calibration	167
7.3.3	Lighting, aperture and shutter speed	170
7.3.4	Force-displacement data processing.....	171
7.3.5	Digital image processing.....	172
7.4	Results	176
7.4.1	Part one: Force-displacement and fracture type.....	176
7.4.2	Part two: Linear correction of force-displacement plots.....	179
7.4.3	Part three: DIC	181
7.5	Discussion	190
7.5.1	Force-displacement curves.....	191
7.5.2	Slopes.....	191
7.5.3	Surface strain contours.....	194
7.6	Experimental set-up and techniques	195

7.6.1	DIC image quality.....	195
7.6.2	Embedding material	196
7.6.3	Embedding method	196
7.6.4	Incident of the stereo system and ROI	197
7.7	Conclusions.....	197
8	Four-point bending FEA on embedded lamb bones.....	199
8.1	Introduction.....	199
8.2	Method.....	200
8.2.1	μCT scanning.....	201
8.2.2	Segmentation	203
8.2.3	Reconstruction.....	204
8.2.4	Cortical bone and marrow	206
8.2.5	Boundary conditions.....	208
8.2.6	Material properties.....	209
8.2.7	Mesh.....	212
8.3	Results	213
8.3.1	Strain contours (with cortical bone elastic modulus of 20GPa)	214
8.3.2	Sensitivity analysis of the cortical bone elastic modulus.....	222
8.4	Discussion	223
8.4.1	Reaction forces	224
8.4.2	Strain contours	224
8.4.3	Assumptions and limitations	225
8.5	Conclusions.....	226
9	Conclusions, limitations and future work.....	228
9.1	Conclusions.....	228
9.1.1	Experimental recommendations	228
9.1.2	Computational recommendations.....	230
9.2	Limitations	232
9.2.1	Experimental limitations.....	232
9.2.2	Computational limitations	233
9.3	Future work	233
	REFERENCES	236
	Appendix	243
	Chapter 5 appendix.....	243
	Chapter 7 appendix.....	244

LIST OF FIGURES

Figure 2-1: Structure of human cortical and trabecular bone.	25
Figure 2-2: Transverse image of a mixed microstructure in bovine cortical bone.	26
Figure 2-3: Inner structure of a typical long bone.	27
Figure 2-4: Development of long bone from embryo to foetus and during childhood.	28
Figure 2-5: Structure of the human femur shown in the posterior and anterior views.	29
Figure 2-6: CT image of the anterior view of the growing human femur.	30
Figure 2-7: Load-deformation curves of femoral cortical bone tissue loaded in bending.	31
Figure 2-8: Immature long bone diaphyseal fractures.	36
Figure 2-9: Diagram of lamb anatomical planes.	37
Figure 2-10: Cranial, medial, caudal and lateral view of the left ovine femur.	38
Figure 3-1: Free body diagram of four-point bending loading conditions.	48
Figure 3-2: Bending moment and shear force diagrams of a beam under bending.	49
Figure 3-3: Diagram of a beam under positive bending.	49
Figure 3-4: Steps for DIC technique.	50
Figure 3-5: Schema of the interrogation points over an ROI.	51
Figure 3-6: Illustration of a subset over a speckle pattern for DIC.	51
Figure 3-7: Schema of the effect of subset size on correlatable area in DIC.	52
Figure 3-8: Schema of the relationship between step size and subset size in DIC.	52
Figure 3-9: Reference image of a speckled pattern converted into grey level matrix.	53
Figure 3-10: Displaced image of speckle pattern I^* and its grey level matrix.	53
Figure 3-11: Reference image with initial position of the interrogation point.	54
Figure 3-12: Image of a displaced, deformed and darkened speckle pattern.	55
Figure 3-13: Example set up for 3D-DIC with two cameras placed at an angle.	56
Figure 3-14: Front view and isometric view of a circular beam under bending.	58
Figure 3-15: Diagram of the basic components of a camera.	59
Figure 3-16: Diagram showing the effect of camera aperture on the depth of field.	59
Figure 3-17: Diagram showing how to obtain a sharp image over a curved surface.	61
Figure 3-18: Top view diagram of a DIC stereo-system showing the focal point and DoF.	62
Figure 4-1: CT scan slices of lamb femur.	64

Figure 4-2: Diagram of a single slice CT scanner.....	65
Figure 4-3: Diagram of a CT reconstruction matrix.	66
Figure 4-4: Algorithm representation for a four-voxel CT image.	67
Figure 4-5: Backprojection reconstruction for a slice with three objects.....	68
Figure 4-6: Blurring effect of backprojection around a single object.	68
Figure 4-7: CT filtering functions using convolution kernels (Goldman 2007).	68
Figure 4-8: Active contour evolution using the Geodesic method.	71
Figure 4-9: Active contour evolution using the Region Competition method.....	71
Figure 4-10: Volume of lamb bone segmented from CT-images.....	72
Figure 4-11: Illustration of an object in a 3D space.	72
Figure 4-12: Illustration of the paths used to calculate strain.....	74
Figure 4-13: Illustration of the traction vector acting on a surface of a body under load.....	75
Figure 4-14: Illustration of the stress components on a differential volume.	76
Figure 4-15: Illustration of a 10-node tetrahedral (a) and 20-node hexahedral (b).....	81
Figure 5-1: CT-based reverse engineered model of lamb femur bone O1001.	85
Figure 5-2: Cranial view of a fresh immature ovine femur bone from the left hind leg.....	86
Figure 5-3: Front view of the four-point bending setup.....	87
Figure 5-4: Left hand side DIC camera frame of four bones focused on the ROI.	87
Figure 5-5: Top view of the DIC stereo system.....	88
Figure 5-6: Image of the 3D printed bone taken through.	89
Figure 5-7: Picture of the DIC set-up used in this chapter	90
Figure 5-8: Captures of the 3D printed bone through cameras 1 (a) and 2 (b).	90
Figure 5-9: Image optimisation for correlation using VIC-Snap on the 3D printed bone	91
Figure 5-10: Raw image of the speckled AOI obtained through camera 2.....	93
Figure 5-11: Change in correlatable area on DIC images of bone O1001.....	94
Figure 5-12: Plot of the increase in correlatable area over the AOI vs. the subset size.	95
Figure 5-13: Image correlated with a subset size of 61pxls and the strain.	96
Figure 5-14: Fracture frame of bone O1001 showing a complete transverse fracture.....	97
Figure 5-15: Raw force displacement graph of bone O1001 under four-point bending.	98
Figure 5-16: Complete failure frame of bone O1002 under four-point bending.....	99

Figure 5-17: Raw force-displacement graph of bone O1002 under four-point bending.....	99
Figure 5-18: Frames showing top rods in contact with bone A1003.....	100
Figure 5-19: Frames showing fracture initiation of bone A1003 under the left rod..	101
Figure 5-20: Complete failure frame of bone A1003 under four-point bending.....	101
Figure 5-21: Raw force-displacement graph of bone A1003 under four-point bending.	102
Figure 5-22: Floor noise captured on static frames of bone O1001.....	103
Figure 5-23: Force displacement plots corrected for pre-loading of bones under bending.	104
Figure 5-24: Surface strains of bone O1001 under bending obtained through DIC.....	105
Figure 5-25: Surface strains of bone O1002 under bending obtained through DIC.....	106
Figure 5-26: Surface strains of bone A1003 under bending obtained through DIC.....	107
Figure 5-27: Diagram of the cross-section of a hollow cylinder under a point load.....	109
Figure 5-28: Frame of bone O1002 showing localised crushing of the bone.	111
Figure 5-29: DIC image of the top surface of bone O1002 in the testing set up.	111
Figure 5-30: Ridges on the surface of bone A1003, caused by spray painting.....	112
Figure 5-31: Bumps on the surface of bone O1002 cause by underlying tissue.....	112
Figure 5-32: Second principal plane strain of bone O1002 under bending.	113
Figure 5-33: Post failure image of bone O1002.....	113
Figure 5-34: Image of poor speckle pattern.	114
Figure 5-35: Image processed to differentiate speckles.....	115
Figure 5-36: Diagram of alternative loading for four-point bending.	116
Figure 6-1: Front view of the four-point bending setup used in Chapter 5.....	119
Figure 6-2: Force-displacement plot of bone O1001 under bending.	120
Figure 6-3: List of different FE models.....	121
Figure 6-4: The adapted CT2S pipeline.....	122
Figure 6-5: Cross-sectional CT scan of bone O1001 with 'Standard and 'Bone' kernel.....	122
Figure 6-6: Segmentation of the whole bone over the original CT image.....	123
Figure 6-7: Segmentation of the bone marrow over the CT image.....	123
Figure 6-8: Cranial view and medial view of a 3D model.....	124
Figure 6-9: The three landmarks used for creating a local coordinate system..	125
Figure 6-10: Faceted body of bone with landmarks which defined the sagittal plane.....	125

Figure 6-11: The cranial and caudal curvature used to define the transverse plane.	126
Figure 6-12: Faceted body of bone O1001 showing the distal and proximal planes.....	126
Figure 6-13: Solid body of bone O1001	127
Figure 6-14: CT image of a Mindways phantom scanned with bone O1001.....	129
Figure 6-15: Plot of the given equivalent K_2HPO_4 density against the pixel value.	130
Figure 6-16: CT scan image of bone O1001 with midshaft section of the cortical bone.....	131
Figure 6-17: CT scan image of bone O1001 with segmented VOIs of trabecular bone	131
Figure 6-18: Elastic modulus convergence plots for element-specific CT-based material ...	133
Figure 6-19: Cross-section of bone O1001 along the sagittal plane.....	134
Figure 6-20: Lateral and isometric views of the shaft solid body of bone O1001	135
Figure 6-21: Cranial and caudal views of the bone shaft solid model.	135
Figure 6-22: Force-displacement curve of bone O1001 under bending with a linear fit.....	136
Figure 6-23: Diagram of the boundary conditions applied to bone O1001.....	136
Figure 6-24: Principal strain convergence plots on direct boundary conditions model	137
Figure 6-25: Assembly of the femoral shaft and the rods for contact simulation.....	138
Figure 6-26: Diagram of the boundary conditions applied to the bone O1001 assembly....	139
Figure 6-27: Principal strain convergence plots on bonded model.	140
Figure 6-28: Surface strains of bone O1001 under bending obtained through DIC	141
Figure 6-29: FE surface strains of bone O1001 using direct boundary conditions.	143
Figure 6-30: FE surface strains of bone O1001 using direct boundary conditions.	143
Figure 6-31: Linear corrections of force-displacement curves of bone O1001.	144
Figure 6-32: DIC and FE surface strains of bone O1001 using direct boundary conditions..	145
Figure 6-33: DIC and FE surface strains of bone O1001 using direct boundary conditions..	146
Figure 6-34: FE surface strains of bone O1001 using contact boundary conditions.	148
Figure 6-35: FE surface strains of bone O1001 using direct boundary conditions.	150
Figure 6-36: Cross-section of bone O1001 corresponding to the left border of the ROI	150
Figure 6-37: Transverse segmentation over CT image of bone O1001 at the midshaft.....	153
Figure 7-1: Diagram of improved experimental set-up for four-point bending	156
Figure 7-2: Femur with an elastic showing the shortest path along the bone.	159
Figure 7-3: Illustration of lamb femur clamped in vice, sawed off at the proximal end.	159

Figure 7-4: Dimensions for embedding of the proximal and distal ends of the femur.	160
Figure 7-5: Images of the preliminary four point bending tests.....	161
Figure 7-6: Set-up for aligning and embedding bone shafts into blocks of PMMA.	162
Figure 7-7: CT-based reverse engineered model of lamb femur bone O2001	163
Figure 7-8: Embedded uPVC dummy, PVC1, used to test the set-up of the stereo system.	164
Figure 7-9: Rehydration process of bone A2004 and A2005 prior to speckle painting	164
Figure 7-10: Fine and dense black speckle pattern sprayed over white	165
Figure 7-11: Non-uniform fine to medium black speckle pattern sprayed over white	165
Figure 7-12: Dense pattern with medium size black speckles sprayed over white	166
Figure 7-13: Simply supported embedded bone for four point bending	167
Figure 7-14: Front view image of a uPVC dummy placed in the bending set-up.....	167
Figure 7-15: Dummy uPVC sample, PVC1, painted with a fine speckle pattern	168
Figure 7-16: Diagram of the DIC system set-up in relation to the sample and testing rig. ..	168
Figure 7-17: Lighting set-up used to capture DIC images of embedded bones.....	170
Figure 7-18: Image optimisation for correlation using VIC-Snap on PVC1..	171
Figure 7-19: Raw image of the speckled AOIs.	174
Figure 7-20: Plots of the increase in correlatable area over the AOI vs. the subset size.....	175
Figure 7-21: Raw force-displacement plots of specimens under four-point bending	177
Figure 7-22: Embedded bone A2001: raw force-displacement plot.....	178
Figure 7-23: Embedded bone A2003: raw force-displacement plot.....	178
Figure 7-24: Embedded bone A2005: raw force-displacement plot.....	179
Figure 7-25: Four-point bending force-displacement plots linearly corrected.	181
Figure 7-26: Frame of PVC1 placed on the testing rig	182
Figure 7-27: DIC projection error with minimum and maximum values for strains	182
Figure 7-28: Floor noise captured on static frames of bone O2002.....	183
Figure 7-29: Surface strains of bone O2001 under bending obtained through DIC.	184
Figure 7-30: Surface strains of bone O2002 under bending obtained through DIC	185
Figure 7-31: Surface strains of bone A2001 under bending obtained through DIC.....	186
Figure 7-32: Surface strains of bone A2002 under bending obtained through DIC	187
Figure 7-33: Surface strains of bone A2003 under bending obtained through DIC.	188

Figure 7-34: Surface strains of bone A2004 under bending obtained through DIC	189
Figure 7-35: Surface strains of bone A2005 under bending obtained through DIC.	190
Figure 7-36: Diagram of equivalent radius 1 and 2, r_1 and r_2	192
Figure 7-37: Plot of the slope of region D attributed to bending	192
Figure 7-38: Embedding methods for whole lamb femur without removing both ends.....	196
Figure 8-1: The front view shows the x-y plane of the four-point bending setup.	201
Figure 8-2: Jig for μ CT-scanning of embedded bone.	202
Figure 8-3: μ CT images of the transverse and sagittal sections of bone O2001.	203
Figure 8-4: Segmentation of the cortical bone and marrow of embedded bone O2001.	203
Figure 8-5: Segmentation of bone O2001 within the global coordinate system.....	204
Figure 8-6: Proximal and distal views of the segmentation of embedded bone O2001	205
Figure 8-7: Solid bodies of the embedding cubes extruded from bone O2001.....	206
Figure 8-8: Extraction of surface points over the faceted body of bone O2001.	207
Figure 8-9: FE model assembly of specimen O2001.	208
Figure 8-10: Medial and lateral views of the bone O2001 assembly.	209
Figure 8-11: Diagram of the boundary conditions applied to bone O2001.....	209
Figure 8-12: Diagram of the five cross-sections used for image analysis on porosity.....	211
Figure 8-13: Transverse μ CT images of bone O2001 and A2005.....	212
Figure 8-14: Meshed FE assembly of specimen O2001 with 1mm elements.	212
Figure 8-15: Principal strain convergence plots.	213
Figure 8-16: Diagram showing the positions of the cranial and lateral lines in the model. .	214
Figure 8-17: DIC measured and FE predicted surface strains of bone O2001	215
Figure 8-18: DIC measured and FE predicted surface strains of bone O2002	216
Figure 8-19: DIC measured and FE predicted surface strains of bone A2001.	217
Figure 8-20: DIC measured and FE predicted surface strains of bone A2002.	218
Figure 8-21: DIC measured and FE predicted surface strains of bone A2003.	219
Figure 8-22: DIC measured and FE predicted surface strains of bone A2004.	220
Figure 8-23: DIC measured and FE predicted surface strains of bone A2005.	221
Figure 8-24: FE predicted reaction force and principal strains for bone O2001.	222
Figure 8-25: FE predicted surface strains of bone O2001 with decreasing elastic modulus.	223

LIST OF TABLES

Table 2-1: Findings on trabecular bone samples of the proximal tibia reported	38
Table 5-1: List of lamb femur samples used for experimental testing..	84
Table 5-2: Dimensions of lamb femurs O1001, O1002, A1003 and A1004	85
Table 5-3: Displacement rate of the load cell for the four-point bending test.	88
Table 5-4: Calibration data for the stereo system.	89
Table 5-5: DIC image acquisition intervals for each test.	91
Table 5-6: Data from the speckle size analysis.	94
Table 5-7: Optimal subset size for DIC determined from speckle analysis.....	96
Table 5-8: DIC projection error.....	102
Table 5-9: Table of the slope and intercept of the linear fit for each bone.	104
Table 6-1: Typical composition of the solid reference materials in a Mindways phantom..	128
Table 6-2: The mean intensity of the reference materials in the Mindways phantom.	129
Table 6-3: Mean intensity and derived densities and elastic moduli of the midshaft	131
Table 6-4: Mean intensity and derived densities and elastic moduli of trabecular bone. ...	132
Table 6-5: Strain contours for bone O1001 captured using DIC at 2.7kN.	142
Table 6-6: FE predicted reaction force for bone O1001.	147
Table 7-1: List of lamb femur samples used for experimental testing.	158
Table 7-2: Dimensions of lamb femurs.....	163
Table 7-3: Calibration data for the stereo system of O2001, O2002, A2001 and A2002.	169
Table 7-4: Calibration data for the stereo systems of A2003, A2004 and A2005.....	169
Table 7-5: Lens aperture and shutter speed of DIC cameras.	171
Table 7-6: Data from the speckle size analysis.	174
Table 7-7: Optimal subset size for DIC determined from the speckle analysis.	176
Table 7-8: Slope, force and displacement data of force-displacement plots.	181
Table 7-9: Cross-sectional mediolateral dimensions of the lamb femurs.	192
Table 8-1: Scanco μ CT-scan mean intensity of the cortical bone.....	210
Table 8-2: FE predicted reaction force for bone O2001.	215
Table 8-3: FE predicted reaction force for bone O2002.	216
Table 8-4: FE predicted reaction force for bone A2001.	217

Table 8-5: FE predicted reaction force for bone A2002.	218
Table 8-6: FE predicted reaction force for bone A2003.	219
Table 8-7: FE predicted reaction force for bone A2004.	220
Table 8-8: FE predicted reaction force for bone A2005.	221

1 INTRODUCTION

1.1 Statement of the problem

Child maltreatment is a prevailing global public health issue, often referred to as a silent epidemic. It is an offense primarily committed behind closed doors. Consequently, due to its criminal nature, child abuse is difficult to detect and assess. This hinders the implementation of strategies available to resolve it (Butchart 2006).

If undetected, child abuse can lead to significant health complications such as physical impairments, neurodevelopmental disorders, mental health problems and even death (Kaffman 2009, Norman et al. 2012). Therefore, improving the accuracy of child abuse detection is of the utmost importance as it allows for the immediate implementation of judicial measures, enabling the safeguarding of children at risk.

1.1.1 Key facts on the prevalence of child maltreatment

Statistics on child abuse comparing detected cases and adult testimonies suggested that a significant amount of ongoing abuse remains undetected. The former is believed to be particularly true for infants and toddlers as they have limited communication skills, minimal contact with the public (e.g schools) and cannot defend themselves.

Physical child abuse (PCA) is the second most prevailing type of child maltreatment. Criminal records show that at least one child-homicide is reported weekly by the British Police. Children under the age of one year have the highest rate of homicide across the nation, 36 per every million population (Key Non Parliamentary Papers Office For National 2018); which highlights their vulnerability.

1.1.2 Statistics relating bone fracture to child maltreatment

Bone fracture is the 4th most common injury sustained by child victims of violence after hematomas, contusions of the skin and burns. Indeed, over 30% of children suspected of abuse have fresh or healing fractures (Bilo, Robben and VanRijn 2010). These statistics imply that bone fracture and bone fracture sequelae could serve as critical evidence for detecting abuse.

1.1.3 Clinical guidelines on fracture differentiation

There are several routes through which physical child abuse can be detected for further investigation. These include the testimony of a witness, a deposition of a victim and a third party's concern. Healthcare practitioners play an important role in raising concerns. Indeed, many abuse cases are first detected in the hospital's emergency department.

Several clinical guidelines have been put in place by organizations at an international and national level to aid healthcare professionals detect potential PCA cases (Butchart, Organization and Neglect 2006). A well-known and widely used example is The National Institute for Health and Care Excellence (NICE)'s clinical guideline, *Child maltreatment: when to suspect maltreatment in under 18s*. It suggests that abuse should be considered if:

“...a child has one or more fractures in the absence of a medical condition that predisposes to fragile bones... or if the explanation is absent or unsuitable”

Like other similar guidelines, the descriptions given above are imprecise and somewhat subjective. More importantly they are also exclusive of children with bone disease. This comes in contradiction with research suggesting that children with long standing illness or impairment may be at greater risk of abuse (Key Non Parliamentary Papers Office for National 2020).

Unlike other prevailing injuries, bone fracture patterns often show no obvious indication of abuse (Bilo et al. 2010). As of today, the mechanism of immature bone fracture is not clear enough to confidently attribute specific fracture patterns to loading conditions. Studies often conclude that fractures on their own cannot be evidence of abusive cause (Kemp et al. 2008). Hence, it can be difficult for medical staff and Child Protection professionals to determine the validity of a carer's testimony based solely on medical examinations (imaging, skeletal survey, etc). Conclusively, a deeper knowledge of the paediatric fracture mechanism is necessary to allow for the successful implementation of clearer, perhaps both qualitative and quantitative, PCA diagnostic guidelines.

1.2 Applying finite element modelling to medico-legal affairs

Immature bone fracture mechanism has long evaded the understanding of scientists. Data on paediatric bone properties is very limited due to ethical complexities regarding experimental

testing on paediatric cadavers, and of course, the scarcity of normal specimen in the immature age range. Moreover, most experimental data on mechanical properties of immature human cortical bone is dated (Hirsch and Evans 1965, Weaver 1966). These difficulties are pushing paediatric biomechanical bone research towards non-invasive approaches such as finite element modelling (FEM).

Computed tomography (CT) based FEM is an *in-silico* method that has been widely used to predict subject-specific bone strength (Qasim et al. 2016). The success of CT-based finite element analysis (FEA) in adults suggests that there is a potential to expand applications to a younger age range. CT-based FEM could be used to better understand immature bone fracture mechanism and could also in turn generate quantitative estimates of fracture loads, patterns, and locations for any given bone structure and material property.

Once processed, this information could be used to provide a table of bone injury tolerances; which would serve as an assisting tool for the diagnosis and prognosis of paediatric fracture, as well as a quantitative tool to differentiate accidental from non-accidental injuries.

CT-based FEM has been extensively developed to analyse bone fracture mechanisms in adults, particularly for osteoporotic hip fracture. Modelling pipelines have been developed to estimate femoral neck strength and the likelihood of fracture under various loading conditions. Experimental set-ups for validating these FEMs have been optimised to specifically predict adult femoral neck fracture. One such pipeline developed at the University of Sheffield is called CT to Strength, or CT2S (<https://ct2s.insigneo.org/ct2s/>). The pipeline has been experimentally validated on cadaveric specimen showing over 95% accuracy (Schileo et al. 2008b, Juszczak, Cristofolini and Viceconti 2011, Grassi et al. 2012, Schileo et al. 2014, Zani et al. 2015). It has also been retrospectively validated on an elderly cohort of 100 women with 83% accuracy (Altai et al. 2019). However, the CT2S pipeline is yet to be validated for its use in immature bones.

1.3 Project aims and objectives

An investigation of the important parameters in the modelling of immature bone will allow for a more accurate modelling of paediatric bone FEMs from which injury tolerances under specific loading scenario can be estimated. This project therefore, aims to broaden the

knowledge on immature bone fracture mechanism through FEA by modifying the CT2S pipeline and experimentally validate the critical steps and assumptions using immature ovine (or lamb) bone.

The objectives of this study are:

- a. **Carry out mechanical tests on lamb femurs.** Design a repeatable experiment where machine and methods will be adapted to fit immature bone. Perform bending tests on immature ovine femurs using stereo digital image correlation (DIC) to capture surface strain contours.
- b. **Replicate the mechanical tests *in silico* and validate the modelling approach.** Apply the in-house FE model pipeline to generate sample-specific FE models of the tested immature ovine femurs, extracting material properties for ovine bone from the literature and implementing them into the in-house pipeline to replicate the bending tests *in-silico*. Compare the model predictions against experimental results.
- c. **Perform a parameter analysis of the FEA.** Run a sensitivity analysis for various input parameters to better understand the most influential parameters for immature ovine bone FEA; aiming to find the most appropriate modelling approach for immature bone and revise the current modelling pipeline according to the validation protocol.

1.4 Chapter by chapter overview

The thesis is laid out as a four-part study with two sets of experimental mechanical tests and two corresponding sets of finite element analysis. A chapter-by-chapter overview is given below.

Chapter 2: Literature review

Chapter 2 reviews the existing literature on pediatric bone fracture mechanism. This chapter also discusses existing workflows to create bone FE models and their respective validation approach, in particular in combination with 3D-DIC.

Chapters 3 and 4: General methods: Experimental tests and CT-based FEA

Chapter 3 describes the general methods used throughout this thesis to experimentally test long bones under four-point bending, while using 3D-DIC to obtain surface strain

measurements. Chapter 4 describes the general workflow used to create and validate CT-based FEMs of long bones, as well as the basic principles upon which the workflow is built.

Chapter 5: Four-point bending test on whole lamb bones

Chapter 5 describes the first set of experiments using whole lamb bones subjected to four-point bending tests using 3D-DIC to capture surface strains. This chapter explores the feasibility and challenges in performing four-point bending tests on immature ovine femurs, by observing the load-displacement curve, failure mode and strain distributions with DIC. Suggestions are made at the end of the chapter in order to improve the experimental set-up to achieve higher consistency.

Chapter 6: Four-point bending FEA on whole lamb bones

Chapter 6 consists of replicating the four-point bending tests of Chapter 5 *in silico* using multiple QCT-based FE models. In this chapter, a variety of modelling approach has been investigated, including different methods of meshing, material properties and boundary conditions. The validity of each model set-up and its method will be assessed by comparing surface strain contours with the results obtained from the DIC in order to determine the best approach.

Chapter 7: Four-point bending test on embedded lamb bones

This chapter reports on the second set of experiments using embedded lamb bones subjected to four-point bending tests and 3D-DIC, based on recommendations made in Chapter 5. In this chapter, the immature ovine bones are fixed in potting material to improve experimental accuracy and repeatability. This has achieved some success, but also comes with limitations, which are discussed towards the end of the chapter.

Chapter 8: Four-point bending FEA on embedded lamb bones

In Chapter 8, the tests of Chapter 7 are replicated *in silico* using FE models generated from μ CT images. The best FE model set-up determined in Chapter 6 is used and validated by comparing surface strain contours with the results obtain from the DIC.

Chapter 9: Conclusions, limitations and future work

Chapter 9 gives an overall conclusion on the work carried out in this thesis, tying back to the application to children's bones. The chapter summarises main findings from both sets of experiment and model validation work, suggests the most appropriate workflow for the modelling of immature bone, and assesses limitations and the potential approach for future work.

1.5 List of contributions

- Jegu, M, Altai, Z, Cheong, V, Ghadbeigi, H, Li, X. Validation of immature ovine bone models using digital image correlation: a preliminary study. Submitted to the European Society of Biomechanics Congress 2020 (cancelled due to COVID).
- Jegu, M, Altai, Z, Cheong, V, Ghadbeigi, H, Li, X. Validation of immature ovine bone models using digital image correlation: a preliminary study. Accepted for poster presentation at the Insigneo Showcase 2020.
- Jegu, M, Altai, Z, Cheong, V, Ghadbeigi, H, Li, X. Validation of immature ovine bone models using digital image correlation. Accepted for poster presentation at the BioMedEng21 Conference 2021.
- Jegu, M, Altai, Z, Cheong, V, Ghadbeigi, H, Li, X. Use of digital image correlation to validate immature ovine models. Accepted for oral presentation at the International Symposium on Computer Methods in Biomechanics and Biomedical Engineering 2023.

2 LITERATURE REVIEW

This section provides a review of the relevant literature. Figures were generated by the author unless otherwise cited.

2.1 Bone structure and development

Bones are living tissues in our bodies. Bone and other connective tissues such as cartilage, tendons and ligaments collectively form our skeletal system. The former protects our vital organs and structurally supports the body, allowing for mobility.

2.1.1 Composition of the bone

Bone is mainly made of collagen fibres and mineral. *In vivo* bone has between 10% and 20% water. Approximately 60-70% of dehydrated bone is bone mineral. The composition of the mineral component can be approximated as hydroxyapatite (HA), with the chemical formula $\text{Ca}_{10}(\text{PO}_4)_6(\text{OH})_2$ (Lu et al. 1996, Agna, Knowles and Alverson 1958). Two other major functions of bone are to provide an environment for marrow where blood cells are produced and to store minerals.

2.1.2 Microstructure of bone

Bone (osseous tissue) is not uniformly solid. It can be divided into two parts of different densities: trabecular and cortical (Figure 2-1). Trabecular bone, also known as spongy bone or cancellous bone, has a porosity of 40-95%. It is composed of trabeculae that connect to form a sponge-like structure. On the other hand, cortical bone, or compact bone, is a dense tissue with a porosity of 5-15% (Morgan, Unnikrisnan and Hussein 2018). Cortical bone can appear in different types of microstructural organizations defined as woven bone, plexiform bone, and primary and secondary osteonal bone. These are usually associated with either species, bone maturity or both. All four structures are discussed below as these must be taken into consideration to better understand the differences between immature and mature bone and the implications of using animal surrogate bone tissue in experimental research (see section 2.2).

Woven cortical bone, as the name suggest, has the least organised structure. It is the only structure which can be formed *de novo*, i.e. it does not need to form on existing bone or

cartilage tissue. Furthermore, it is capable of forming very rapidly, hence its disorganised structure. Unsurprisingly, it is often found in very young growing skeletons under the age of five years old. In adults, it is only found to form in bone as a response to trauma or pathology (Robyn 2019).

Plexiform cortical bone has a brick-like structure. It also has the ability to form relatively quickly. Due to its structure however, plexiform bone is capable of withstanding heavier loads for longer periods of time than woven bone. Plexiform bone is often found in rapidly growing species such as bovine or ovine, but it is rarely found in active species such as humans and canines.

Primary and secondary osteonal bone have the most elaborate structure. Primary and secondary bone form into haversian systems, which are made up of column-like microstructures called osteons. Osteons are an amalgamation of concentric lamellae. At the central axis of osteons, called the central canal, lies the blood vessels (Figure 2-1).

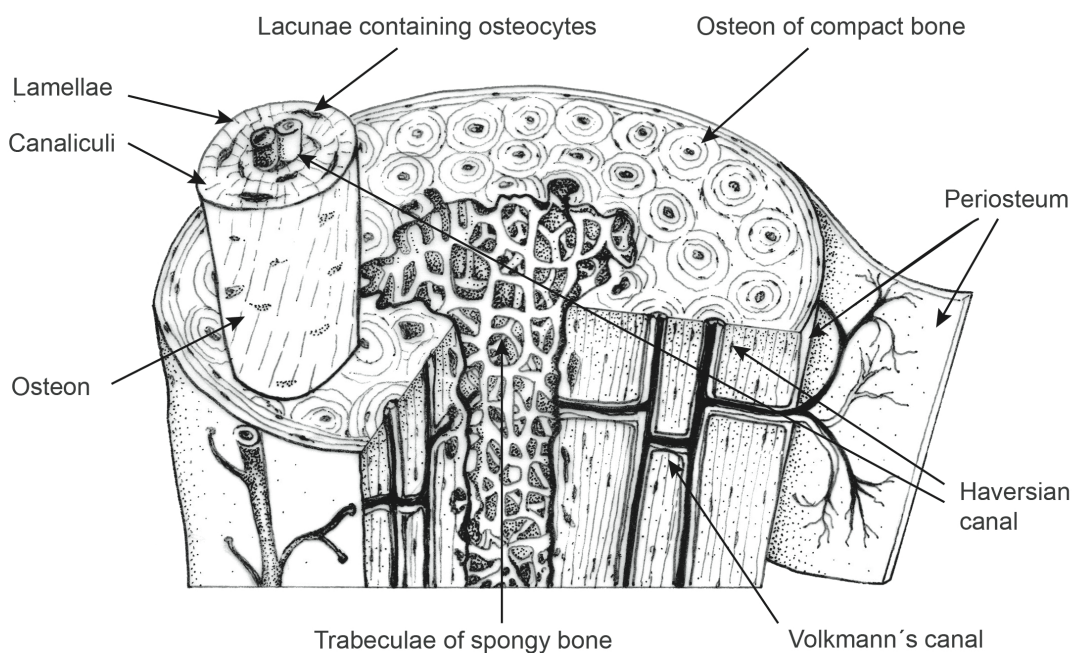


Figure 2-1: Structure of human cortical and trabecular bone.

What differentiates primary from secondary bone is the way in which the osteons are formed. Primary osteons are likely formed by mineralization of cartilage, whereas secondary bone is formed by replacement of existing bone (i.e. remodelling). Primary and secondary osteonal cortical bone can be found in active species such as humans and dogs, as well as along

plexiform bone in high load bearing sites of mature sheep and cows (Carter, Hayes and Schurman 1976) (Figure 2-2). For instance, (Lipson and Katz 1984) found that the anterior-medial quarter of bovine tibia contained plexiform bone and the posterior lateral quarter contained haversian bone.

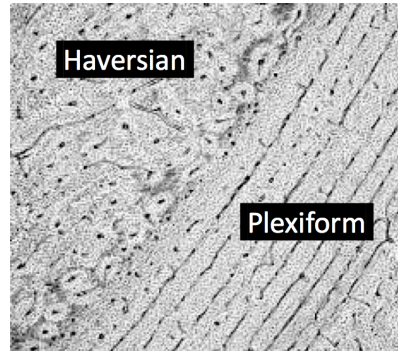


Figure 2-2: Transverse image of a mixed microstructure in bovine cortical bone obtained by optical microscopy. Reproduced from Guillaume Haïat, Magali Sasso, Salah Naili, Mami Matsukawa; Ultrasonic velocity dispersion in bovine cortical bone: An experimental study. *J Acoust Soc Am* 1 September 2008; 124 (3): 1811–1821. <https://doi.org/10.1121/1.2950091>; Figure 8, with the permission of the Acoustical Society of America.

2.1.3 Macrostructure of long bones

Our skeleton can be divided into five categories of bone: flat, short, long, irregular, and sesamoid. In the adult human skeleton these add up to a total of 206 bones and each carries a specific function. The humerus, radius, ulna, metacarpal, phalanges, metatarsals, tibia, fibula, and femur are all long bones. The work in this thesis focuses on immature long bone fractures. Flat short, irregular and sesamoid bones are not further discussed as they are not within the scope of this study.

Long bones have a shaft, the diaphysis, with two bulbous ends, the epiphyses. The transitional regions between the diaphysis and the epiphyses are called metaphyses (Figure 2-3). The cortical bone forms the outer layer of long bones, with a thicker layer all along the diaphyseal region and a thinner layer at the epiphyses. The central axis of the shaft is hollow and is called the medullary cavity. The epiphyses are filled with trabecular bone. Another two crucial parts of the long bone in terms of biomechanics are the articular cartilage and the periosteum. The articular cartilage is a type of cartilage found at the distal and proximal surfaces of the epiphyses. This allows for smooth articulation at the joint and protects the bone from

frictional damage. The periosteum is a layer of fibrous connective tissue that protects the diaphysis.

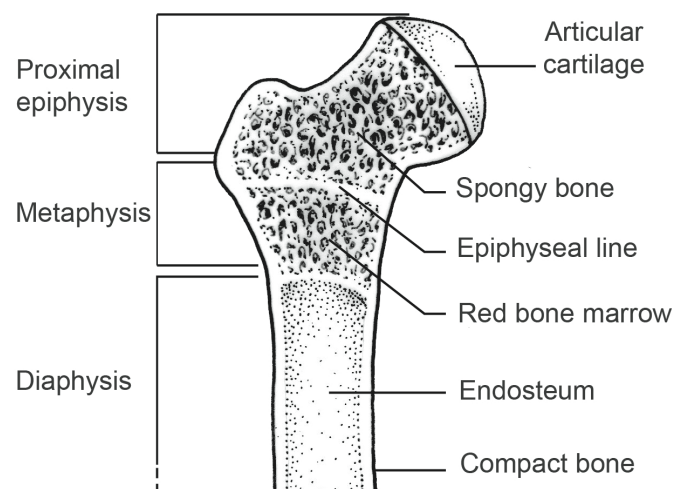


Figure 2-3: Inner structure of a typical long bone.

2.1.4 Development of long bones

Long bones are formed through endochondral ossification, a process during which bone tissue replaces a hyaline cartilage template. In the early stages of embryonic development, the skeleton consists of fibrous membrane and hyaline cartilage. Ossification first begins at the centre of the diaphysis, i.e. the primary ossification centre. At birth, long bones have cartilage (or mineralising bones) at both epiphysis and the joint surfaces (articular cartilage). A few months after birth, secondary ossification centres appear in both epiphyses. As the epiphyses continue to ossify, the epiphyseal plate appears between the epiphysis and the diaphysis. From birth to the end of puberty, bones grow in length at the epiphyseal plates by producing cartilage and replacing it with bone. In contrast, bone growth in width originates from the periosteum (Figure 2-4).

During growth, muscles also attach to the periosteum rather than the bone itself. This allows for the coordinated growth of the bone and soft tissues. Accordingly, as the periosteum is replaced by bone, its thickness, and therefore structural strength, decreases with age until early adulthood (Standring 2005). Overall, skeletal maturity (i.e. complete ossification and fusion of all ossification centres) happens by the age of 25 years old at the latest (Cech 2011).

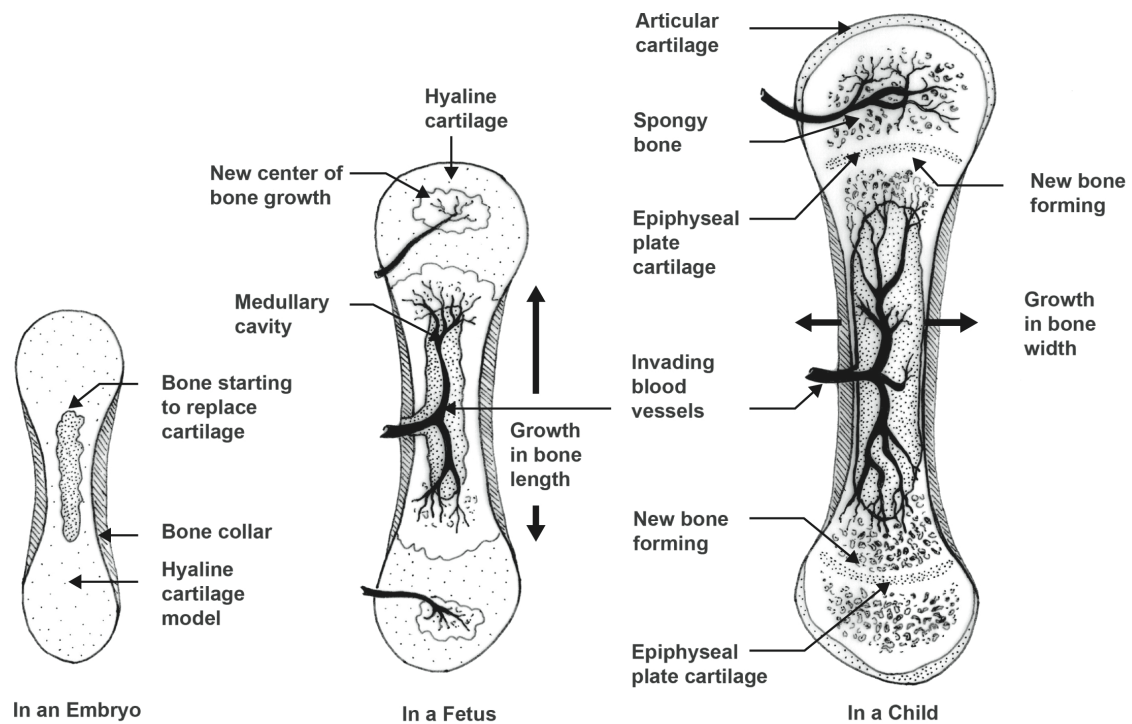


Figure 2-4: Development of long bone from embryo to foetus and during childhood.

2.1.4.1 The femur and its developing stages

The femur (Figure 2-5) is the long bone of the thigh, which articulates with the hip joint and the knee at the proximal and distal end, respectively. Proximally, an adult femur has a head, neck and two trochanters. Distally, it has a medial and lateral condyle Figure 2-5.

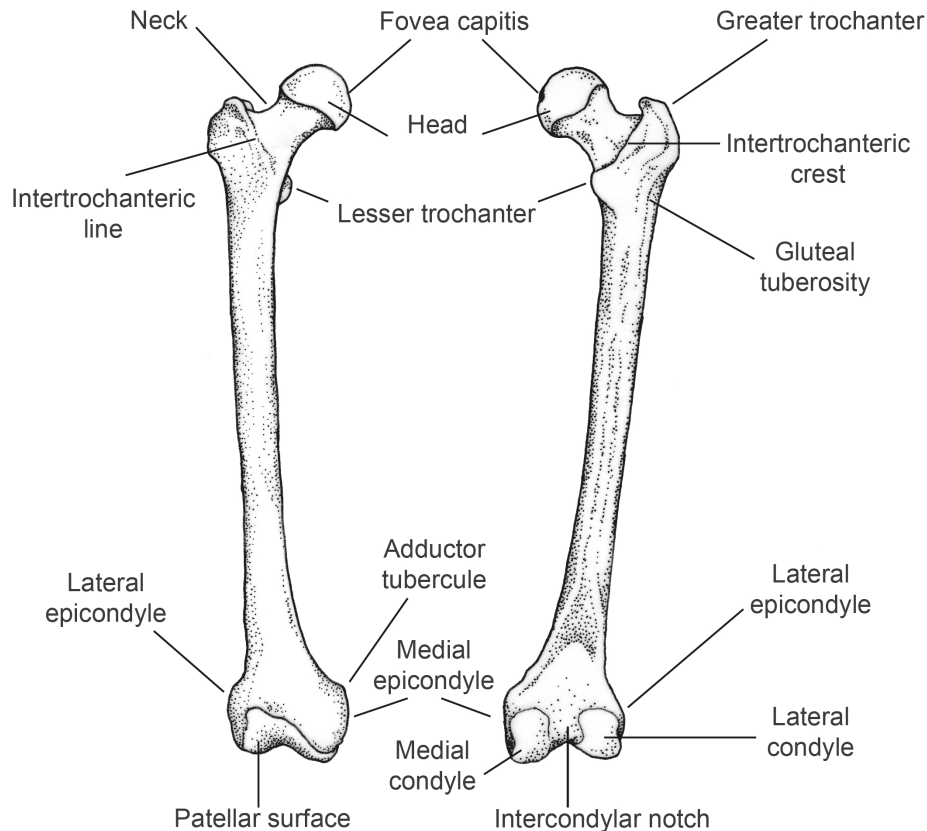


Figure 2-5: Structure of the human femur shown in the posterior (left) and anterior (right) views.

The skeletal development of the femur can be described in the following stages (Scheuer 2000):

1. **Formation of the cartilaginous femur.** The cartilaginous femur begins to form in the 7th week from implantation and is complete by the end of the embryonic period.
2. **Appearance of the primary ossification centre.** Ossification first appears in the midshaft at weeks 7-8. By about 12 weeks, ossification in the shaft has almost reached the neck region proximally and the lower epiphysis distally.
3. **Appearance of the secondary ossification centres.** At the distal end of the femur, the secondary ossification centre responsible for the formation of the condyles starts to appear at 36-40 weeks. It is sometimes absent in premature infants.

At the proximal end of the femur, ossification happens in three individual centres: the femoral head, the greater trochanter, and the lesser trochanter. These appear during infancy and childhood between 0.5-1 year for the femoral head, 2-5 year for the greater trochanter and 7-12 years for the lesser trochanter.

4. **Fusion of the ossification centres to the midshaft.** The secondary ossification centres fuse with midshaft during adolescence (12 to 20 years). The femoral head fuses first followed by the greater trochanter, the condyles, and the lesser trochanter.

During growth, the femur lengthens at the epiphyseal plates and its shaft thickens by cortical ossification of the periosteum. The femur also undergoes morphological changes as a response to the changes in mobility from infancy to childhood. During early childhood, the angle between the neck and the shaft rapidly decreases from an average of 140° to 125° to allow for the mechanical transition between crawling and walking. The cross-section of the shaft changes from an approximate circle to a more elongated shape in the anterior posterior direction. At a tissue level, the trabecular architecture of the neck and shaft also changes during the early years; remodelling occurs in response to weight bearing as the child begins to stand and walk (Townesley 1948).

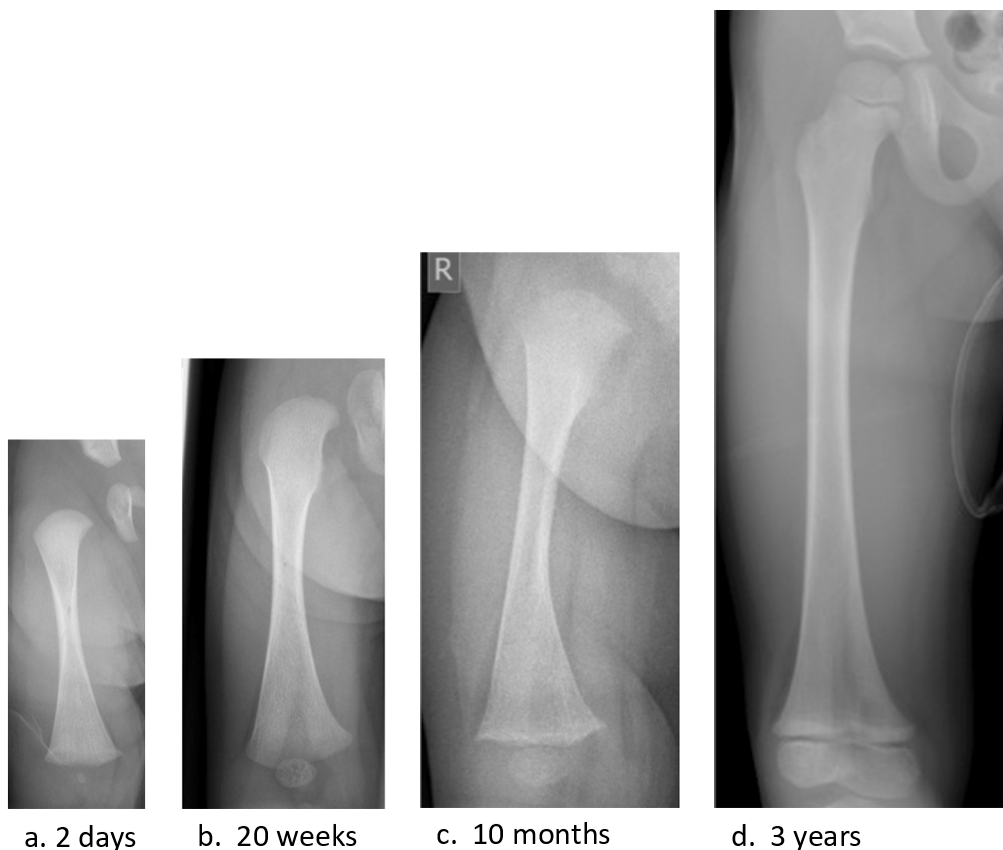


Figure 2-6: CT image of the anterior view of the growing human femur (courtesy of Profesor Amaka Offiah from the Sheffield Children’s Hospital).

2.1.5 Mechanical and material properties of bone tissue

Cortical bone exhibits a clear linear elastic stress-strain behaviour under both tension and compression. It is weaker in tension than in compression. Under tension, it yields at a strain of approximately 0.73% (Bayraktar et al. 2004). Trabecular bone does not exhibit a clear linear elastic stress-strain behaviour nor does it have a distinctive yield point. However, it is still frequently treated as a linear elastic material, and its yield point is defined by the 0.2% offset method. Similarly to cortical bone, trabecular bone is also weaker in tension than in compression. Under tension, it yields at a strain of approximately 0.62% (Bayraktar et al. 2004).

Some mechanical properties of cortical bone have been shown to vary between different age ranges. Similarly to adult bone, foetal to adolescent cortical bone exhibits a linear elastic stress-strain behaviour (Ambrose et al. 2018, Zimmermann et al. 2019, Öhman et al. 2011). During the woven microstructure period (foetal and infant), bone has a much higher yield strain (Ambrose et al. 2018). Unlike older bone, its stress-strain curve largely plateaus before fracture (Zimmermann et al. 2019, Currey and Butler 1975). In children (from 4 years old) and adolescents, cortical bone increases in stiffness and strength and decreases in ductility with age until full maturity. Unlike stiffness, strength and ductility, no significant difference has been found between the yield strain of children and adult (Öhman et al. 2011, Currey and Butler 1975). Figure 2-7 shows the stress-strain curve differences between children and adult cortical bone, particularly children's bone post-elastic behaviour and its ability to deflect and absorb more energy before failure.

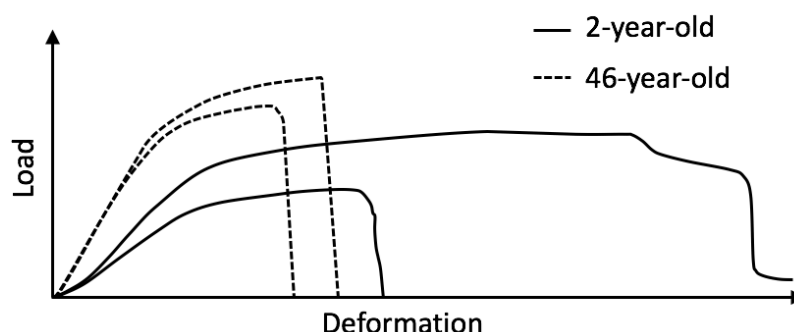


Figure 2-7: Three-point bending load-deformation curves of femoral cortical bone tissue from a 2-year-old and a 46-year-old female. The curves reported are the curves with the greatest and least plastic deformation

out of 4 samples from the 2-year-old and 6 samples from the 46-year-old. Adapted from Currey and Butler (1975).

2.1.5.1 Viscoelasticity

As mentioned in section 2.1.1, bone consists of bone tissue and non-mineralised tissue, i.e. bone marrow (blood vessels, blood, red and yellow marrow, nerve tissue, miscellaneous cells, and interstitial fluid); which sits within the pores of trabecular bone and porous compact bone. At higher strain rates (>10% strain per seconds), the viscous flow of marrow increases the strength, modulus and energy absorption of porous bone. However, under moderate physiological loading conditions (0.1–1.0% strain per seconds), such as walking, porous bone is not hydraulically strengthened by the presence of marrow (Carter and Hayes 1977). Note that dynamic loads and viscoelasticity are not within the scope of this thesis, and that the bone mechanical properties described from this point on apply to quasi-static conditions only.

2.1.5.2 Elastic modulus vs. bone density

The mechanical and material properties of bone tissue vary greatly. These variations are attributed to differences in tissue density and bone mineral density. The relationship between bone stiffness and density has been largely studied in the field of bone mechanics. There are over twenty empirical mathematical expressions formulated in the literature to express the elastic modulus (E) of human bone against its apparent density¹ or ash density² (ρ), reported in a review by (Helgason et al. 2007a). It was found that power equations of the form $E = A\rho^B$ had higher determination coefficient than linear regressions. Furthermore, apparent density and ash density were found to be linearly proportional (Keyak and Falkinstein 2003, Schaffler and Burr 1988, Schileo et al. 2008b), therefore making them interchangeable in the aforementioned power equations. Note that apparent and ash density are measurements

¹ Apparent density is a measure used to quantify the compactness of bone tissue. It is defined as the ratio of the wet weight over the total volume of the sample (bone tissue plus pore spaces).

² Ash density is a measure used to quantify the mineralization of bone tissue. It is defined as the ratio of the ash weight over the total volume of the sample (bone tissue plus pore spaces).

In this thesis, all mentions of apparent and ash densities are as described above. However, note there are some instances outside of this work, in which apparent density is defined as the dry weight over the total volume, and ash density is defined as the ash weight over the bone volume (bone tissue volume only).

taken over a total bone volume; a volume which is taken up by both bone tissue and pore spaces. Therefore, expressing elastic modulus in terms of apparent and ash density indicates that elastic modulus is correlated to both tissue density and porosity.

Porosity alone has been found to have a significant influence on the mechanical properties of bone. Porosity greatly decreases the ultimate stress as well as the elastic modulus of cortical bone. (Schaffler and Burr 1988) and (Currey 1988) found that the effect of porosity (p) on the tensile elastic modulus (E) could be determined as follows:

$$\text{Schaffler and Burr:} \quad E = 33.9 (1 - p)^{10.9} \text{ [GPa]} \quad \text{Eq.2-1}$$

$$\text{Currey:} \quad E = 23.4 (1 - p)^{5.7} \text{ [GPa]} \quad \text{Eq.2-2}$$

Immature cortical bone has a lower ash content and is more porous than mature bone (Ambrose et al. 2018). Throughout the skeletal development, bone tissue increases in mineral content while porosity decreases. Concurrently, the growing bone increases in stiffness and strength, and decreases in toughness and ductility (Currey and Butler 1975). Furthermore, the increase in strength through skeletal development is also attributed to geometric growth (Forman et al. 2012). Therefore, it is unsurprising that material properties change substantially within the first year of infancy. For instance, in infants below the age of 1 year old, tibial cortical bone elastic moduli range from as low as 0.45GPa to 1.98GPa (Ambrose et al. 2018). During childhood, the tibial cortical stiffness increases dramatically, reaching an average elastic modulus of 17GPa in the teens (Hirsch and Evans 1965, Tommasini et al. 2005). Interestingly, (Öhman et al. 2011) found that for children too, the relationship between elastic modulus and ash density could be written as a power equation in the form of $E = A\rho^B$.

2.1.5.3 Heterogeneity and variations of bone

Bone is a heterogeneous material. The tissue architecture of bone, and consequently its density and elastic moduli, changes from site to site to better adapt to its mechanical environment, i.e. loading type and direction. For instance, the shaft of a femur is made of compact cortical bone, the lamellar structure of which aligns with axial stress; whereas the femoral condyles are made of trabecular bone which can better support contact pressure ranging between full knee flexion and extension. Undoubtedly, material properties of bone tissue vary from site to site within the same bone.

Mechanical property variations are also found between anatomic sites. For instance, when looking at the relationship between elastic modulus and density for trabecular bone, (Morgan, Bayraktar and Keaveny 2003) found that at a given density, specimens from the tibia had higher moduli than those from the vertebra and femoral neck, and that those from the trochanter had higher moduli than the vertebra. Again, these variabilities are attributed to architectural adaptation to the mechanical environments of each bone. Indeed, Morgan found that tissue moduli computed using methods that account for inter-site architectural variations did not differ across site; highlighting that the site-specificity in apparent modulus-density relationships may be attributed to differences in architecture. In accordance to Morgan's findings, Öhman et al. (2011) found no significant difference in the elastic modulus-density relationship of the tibial and femoral shaft, which have similar mechanical environments and bone architecture.

Finally, bone properties will inevitably vary from subject to subject. Substantial variations can be correlated to pathology such as osteoporosis, osteogenesis imperfecta, rickets, etc. (Osterhoff et al. 2016, Zioupos and Currey 1998, Aerssens et al. 1998).

2.1.5.4 Anisotropy of bone

Cortical bone has anisotropic material properties. Mechanical properties of plexiform and haversian bone, which are organised structures, can be measured in the three orientations longitudinal, tangential or radial. Plexiform bone, in which all three orthogonal directions are structurally distinguishable, has different elastic moduli along the three axes (i.e. orthotropic). Plexiform bone is stiffer in the longitudinal direction, followed by the tangential direction and finally the radial direction, $E_{long} > E_{tang} > E_{rad}$. The following elastic moduli ratios, $E_{long} : E_{tang} : E_{rad}$, measured through ultrasound were published in the literature 1.0:0.67:0.53 (Van Buskirk, Cowin and Ward 1981) and 1.0:0.72:0.58 (Lipson and Katz 1984). On the other hand, haversian bone which is microstructurally symmetric in the transverse plane (tangential and radial), is said to have transversally isotropic material properties, and to be stiffer longitudinally than transversally, $E_{long} > E_{trans}$. In the longitudinal direction, haversian bone is less stiff than plexiform bone, however, it may have better crack arresting capabilities due to its longitudinal microstructure (Cowin 2001).

2.1.6 Fracture patterns in immature long bone

Due to the process of bone formation and development, immature long bone has different fracture patterns to what is seen in adult bone. Fracture patterns can be divided into two broad groups, meta-epiphyseal fractures and shaft fractures. Meta-epiphyseal fractures, also called Slatter-Harris fractures, occur near the growth plate, which is a point of weakness in the morphology of the growing long bone. Shaft fractures, on the other hand, occur along the diaphysis, and can be further classified using the following types (illustrated in Figure 2-8):

Complete fracture

There are three recognisable patterns of complete fractures: spiral fractures, transverse fractures, oblique fractures or sometimes a combination of multiple patterns. These are rarely presented as comminute fractures in children and are often less severely displaced than in adults. The periosteum can remain intact or be partially torn. Spiral fractures are believed to result from torsion load, transverse fractures from bending and oblique fractures from shear stress (Bilo et al. 2010, Cowin 2001).

Buckle (torus) fracture

Buckle fractures occur under uniaxial compressive stress, at regions of lower density such as the distal metaphysis (Bilo et al. 2010).

Plastic bowing (deformation)

Plastic bowing results from bending load. Immature bone is said to be “ductile” enough for bones to enter the plastic region without failure, i.e. fracture. This often occurs when a compressive load is applied eccentrically to the bone (Bilo et al. 2010).

Greenstick fracture

Greenstick fracture is a partial fracture, which is only observed in children. It occurs when the bone is subjected to bending stress. In this case, the fracture initiates at the point of highest tensile stress but will remain incomplete. The periosteum can also remain intact and act as a retaining sleeve (Bilo et al. 2010).

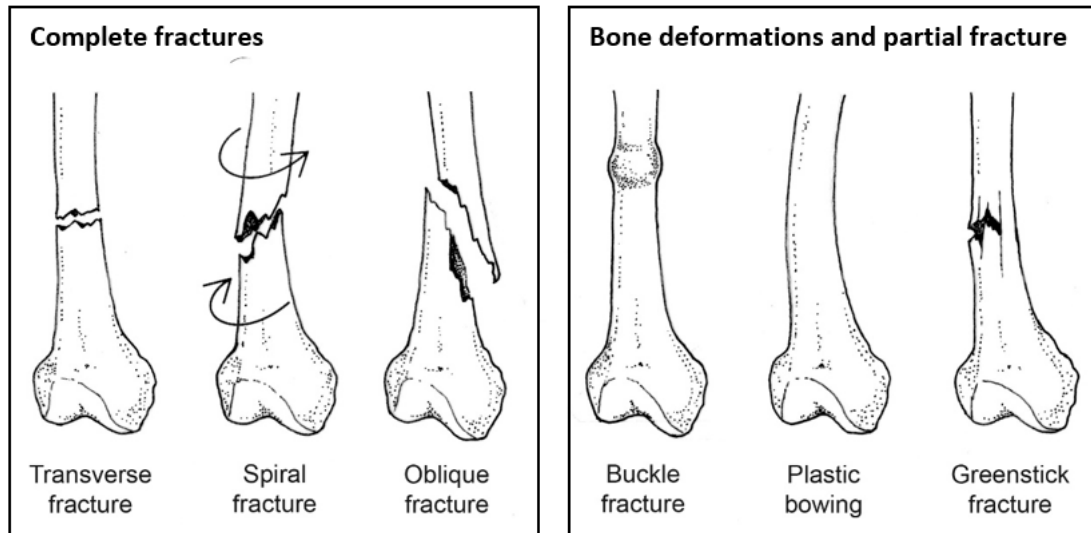


Figure 2-8: Immature long bone diaphyseal fractures.

Although the above description associated each fracture pattern with possible stress states, it is however difficult to directly associate fracture types with pure loading conditions due to the geometrical asymmetry and uncertainty around stress propagation (Cheong and Bull 2015). Previous attempts to correlate fracture type and loading conditions in paediatric bones have been largely unsuccessful.

2.2 Animal surrogates for immature whole bone testing

As stated in Section 1.2, obtaining young human whole bones for experimental research is ethically challenging. Previous studies have used animal surrogates to bypass this issue (Torzilli et al. 1981, Martini et al. 2001, Theobald, Qureshi and Jones 2012). For this thesis, a number of factors needed to be considered when selecting an animal surrogate. These factors were chosen to replicate the FE-modelling challenges associated with immature femurs (see chapter 4), particularly the anatomy, size, length-to-thickness ratio (curvature and hence bending moment), cortical thickness, cortical structure, and bone composition. Other extrinsic aspects to be taken into consideration were again ethics and availability.

There are no existing comparative studies on interspecies immature bone properties; nevertheless, assumptions can be made from the literature on mature animal bone and adult human bone. Dogs are the most appropriate surrogates for adult long bones due to their similar length-to-thickness aspect ratio, cortical structure and bone material composition (Shea 2003, Aerssens et al. 1998). However, experimental testing on dogs can present

difficulties due to ethics (as pets) and availability. Large farm animals are another popular choice in experimental research, particularly porcine and ovine specimens. The accessibility of farm animal bones as a by-product of the food industry makes them ideal for experimental testing as it avoids availability and ethical complications. Porcine bone tissue is physiologically similar to human bones; however, porcine bones have a substantially different length to thickness ratio to that of humans, which is representative of their rapid growth rate and weight gain. Alternatively, sheep have a more adequate size, length-to-thickness aspect ratio and cortical thickness, and are thus more appropriate for experimental validation of immature bone fracture using a combined experimental and FE approach (Pearce et al. 2007, Martini et al. 2001).

2.2.1 Ovine femur

Ovine are quadrupeds with two forelimbs and two hindlimbs. The femurs are located at the top of the hindlimbs (Figure 2-9).

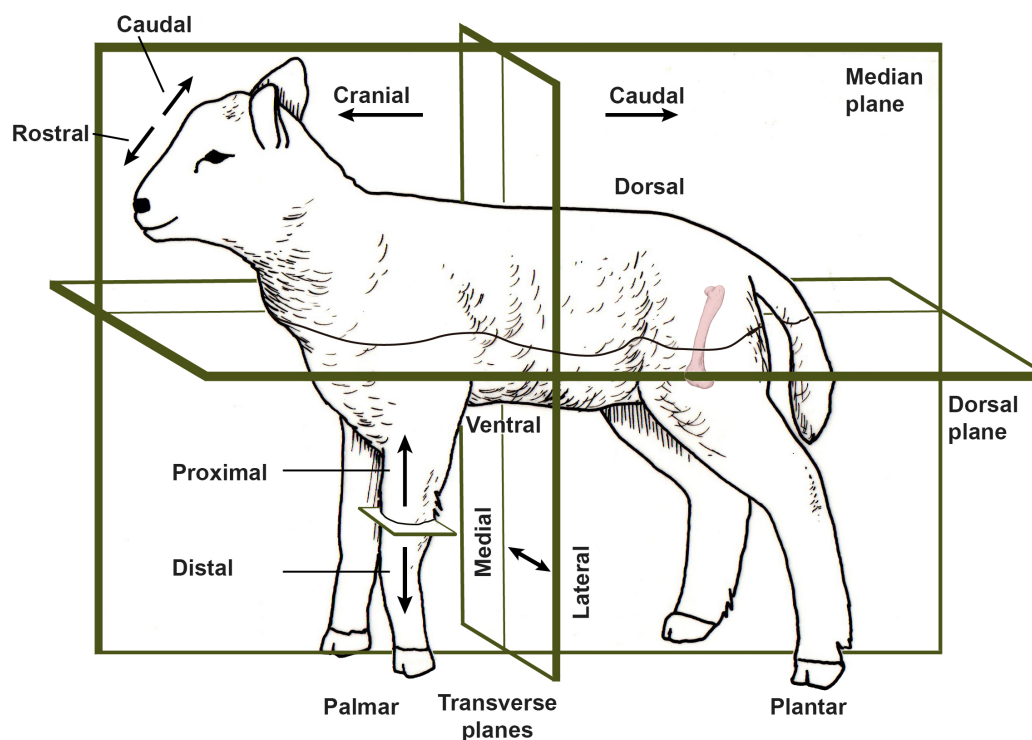


Figure 2-9: Diagram of lamb anatomical planes and position of the femur in the hind limbs.

Although the anatomy of ovine femur greatly resembles that of adult femur, there are indeed some distinctive differences (Figure 2-10). For instance, the femoral neck is much shorter and

less distinguishable in sheep. The trochanters also protrude less. Furthermore, ovine femoral shafts are shorter and relatively thicker, and are noticeably curved in the median plane. Note that some differences arise between breeds as well. As for its microstructure, unlike healthy adult femur, ovine adult femur contains both haversian and plexiform cortical bone.

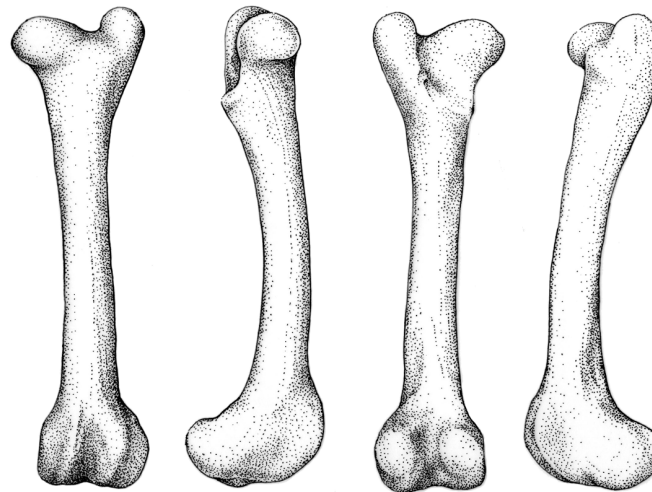


Figure 2-10: Cranial, medial, caudal and lateral view of the left ovine femur.

The literature on ovine femur is limited. However, extensive studies on ovine tibia provide good insight on the material properties. The most comprehensive study on ovine trabecular bone of the proximal tibia contained a large cohort (n = 50) with equal sample sizes across five age groups ranging from 3-80 months (Nafei et al. 2000). Note that in this study the elastic modulus was measured in compression over the three orthogonal directions of the bone tissues, $E_{compression} = (E_{long} + E_{tang} + E_{rad})/3$. The mechanical anisotropy ratio was calculated as the ratio of the longitudinal elastic moduli over the average of the tangential and radial moduli. The dry apparent density was calculated as the dry weight over the total volume (Table 2-1).

Age [months]	Elastic modulus [MPa]	Mechanical anisotropy ratio	Dry apparent density [g/cc]	Ash density [g/cc]	Porosity percentage [%]
3	646 (60)	1.42 (0.08)	0.405 (0.01)	0.25 (0.01)	81.2 (0.6)
6	599 (91)	1.49 (0.09)	0.448 (0.03)	0.29 (0.02)	80 (1.1)
9	764 (116)	1.59 (0.16)	0.429 (0.02)	0.29 (0.01)	81.1 (0.7)
36	869 (224)	1.68 (0.10)	0.563 (0.04)	0.37 (0.03)	75.2 (1.9)
80	1514 (296)	1.92 (0.13)	0.665 (0.04)	0.45 (0.03)	70.7 (1.8)

Table 2-1: Mean values (and standard error of the mean) of findings on trabecular bone samples of the proximal tibia reported (Nafei et al. 2000).

As for ovine cortical tibia, (Grant et al. 2014), who tested on a single mature sheep, found that the ultrasound elastic modulus ranged from 15-25GPa longitudinally, 8-17GPa tangentially and 11-17GPa radially. Grant also measured the apparent density of each sample (measured via CT scan). After plotting the longitudinal elastic modulus against the apparent density, an exponential curve was fitted yielding the following relationship:

$$E \text{ [GPa]} = 12.35 \times \rho_{app}[\text{g/cc}]^{1.32} \quad (R^2 = 0.55) \quad \text{Eq. 2-3}$$

2.1 Experimental mechanical testing on ovine femur

Quasi-static testing has been extensively performed on whole bones. These tests are performed to obtain structural stiffness and strength, derived from measured strain data to validate numerical bone models. There are multiple types of testing methods for measuring mechanical properties and responses of whole bones. These most commonly replicate relevant physiological loadings associated with fractures. As mentioned in section 2.1.6 paediatrics femur fractures are products of multiple loading types, bending being the loading type associated to the most fracture types (complete transverse and oblique fractures, greenstick partial fractures and bowing deformation). Along with bending tests, classical surface strain measurement methods can be used to obtain surface strain in the region of interest. However, these require special adaptation to account for properties intrinsic to bone tissue, such as heterogeneity, asymmetry, surface roughness and moisture, as described in the following sections.

2.1.1 Storage

Mechanical properties of bone are heavily dependent on moisture content. *In vitro* studies showed great variations in stiffness and strength between normal (or artificially hydrated) and dehydrated bone (Zdero, Aziz and Nicayenzi 2017). Therefore, for an accurate representation of *in vivo* properties, bone specimen must be at a hydrated state during experimental testing (Zhang et al. 2018). The less destructive way of storing whole bone is frozen at -20° in sealed (often vacuum sealed) plastic bags (Linde and Sørensen 1993). Some studies chose to maintain the bones hydrated whilst stored. To do so the bone is wrapped in gauze soaked with physiological saline. In this case, additional time must be given for the gauze to defrost and the bones to thaw prior to testing (Cheong et al. 2017). Other studies

prefer to store whole bones in airtight plastic bags and to only rehydrate the bones by plunging the specimen in physiological saline as it thaws (Zani et al. 2015). Either method seem to be used interchangeably. Nevertheless, considerations should be given to minimise the exposure time at room temperature because room temperature saline preservation time has been shown to strongly affect the stiffness and strength of bone (Linde and Sørensen 1993, Zhang et al. 2018).

2.1.2 Bending tests

Bending tests are a staple in the field of biomechanics. There are two types of bending tests commonly used in whole bone testing: three-point bending and four-point bending. Three-point bending tests are extensively used in biomechanics due to the simplicity of the experimental set-up. Three-point bending tests can easily be performed on small thin specimens, e.g. mouse tibia, as only one load needs to be applied at the centre of the specimen span (Deckard, Walker and Hill 2017). However, when using larger and thicker specimens, a three-point bending loading set up will lead to high shear stress relative to the bending stress at the midspan-section of the bone.

On the other hand, four-point bending tests introduce constant bending stress at the centre of the specimen between the two upper loads and minimises local shear. However, when testing a curved and/or asymmetric specimen, it may lead to uneven distribution of loading (Cowin 2001). Unequal force distribution can be minimised by using a rocker mechanism as reported in (Cheong et al. 2017). It can also be minimised by embedding both ends of the specimen and applying the loads on the embedding. The latter also provides better control over the alignment of the specimen, and thus leads to better repeatability (Zdero et al. 2017).

2.1.3 Surface strain measurements

Strain gauges (SG) rosette, a type of triaxial electrical resistance extensometer, are considered the gold standard for strain measurement in bone biomechanics (Grassi and Isaksson 2015). Using strain gauges on bone tissue requires a few additional preparation steps. Before adhering an SG to a specimen, all soft tissues must be removed from the location of adhesion. Thus, this process would potentially disregard the mechanical contribution of the periosteal sheath on immature bones. The bone must also be locally treated to allow for the bonding

material to adhere. Finally, the strain gauges must be waterproofed so that the specimen can be continuously hydrated during experimental testing. Regarding immature FEM validation, the two main disadvantages of the use of SG are that it only allows for the measurement of discrete regions, and that the smallest of immature bones may lack flat surfaces to fit strain gauges.

Digital Image Correlation (DIC) is now a relatively well known image-based non-contact method used to measure full-field displacement and deformation of biological and biomaterials (Palanca, Tozzi and Cristofolini 2016). To perform DIC, digital images of a specimen must be taken during the experiment at different states, i.e. different load/time. The test sample must have random contrasting visual features, e.g. speckles. The images are then processed with correlation-based matching algorithms to extract full-field surface displacement and strain.

Similar to SGs, 3D-DIC requires specific preparation for whole bone applications (Palanca et al. 2016). For 3D-DIC, all soft tissues in the region of interest (ROI) must be removed. The ROI is usually sanded, painted (matt white solvent-based base coat with black speckles) and tested shortly after painting (Grassi et al. 2014). In previous femoral studies, speckles have been created either manually with a black permanent marker (Grassi et al. 2014, Grassi et al. 2016), by splattering paint with a brush (Zdero et al. 2017) or using an airbrush (Dickinson et al. 2011, Grassi et al. 2012, Grassi et al. 2013). The permanent marker method is best for obtaining repeatability in speckle size and controlling speckle distribution. However, this method can be very time consuming, which is problematic when working with fresh specimens. Splattering paint with a brush is economic, quick and simple, but it can result in uneven size and distribution of speckles. Finally using an airbrush is best to obtain evenly distributed fine speckles over the whole ROI but the control over speckle size is limited.

The main benefit of 3D-DIC over the gold standard SG method for whole bone FEM validation is that it can capture full-field strain rather than discrete area strains. This allows for a more extensive comparative analysis between experimental and numerical data (Dickinson et al. 2011, Grassi et al. 2014, Helgason et al. 2014, Grassi et al. 2016). On the other hand, the main disadvantage of the use of DIC is that it has only been applied to bone biomechanics for approximately a decade, thus no consensus exists on its reliability for whole bone FEM

validation. To the author's knowledge, no existing studies compare the effect of surface treatment, local dehydration and reinforcement in SG against the effect of surface preparation and painting in DIC. However, it is argued that the application of paint is likely to have less effect than SG reinforcement and that pat drying the surface for painting has less or equal effects to the harsher drying and degreasing processes for the adhesion of SGs (Dickinson et al. 2011).

2.2 Finite element analysis for biomechanics

2.2.1 Computed tomography based subject specific bone modelling

As stated in section 2.1, there is significant variability in bone geometry and mechanical property across all bone specimens. Subject-specific modelling aims to account for this variability by extracting both geometry and elastic modulus non-intrusively from *in vivo* subjects (Viceconti 2014).

CT-based FEM is a non-invasive method by which the geometry and material properties of a patient's bone are extracted from quantitative CT images. At the University of Sheffield, an in-house pipeline has been developed to assess bone strength and predict the risk of femoral neck fracture in osteoporotic patients (Viceconti et al. 2012, Taddei et al. 2014). The latter is based on the empirical evidence that:

1. the elastic modulus of adult bone is proportional to its mineral density, which can be estimated from CT images,
2. the variation of elastic modulus the femur can be accurately represented with a heterogeneous mesh,
3. the anisotropy of the femur is inconsequential when assessing ultimate strength; thus, it can be simplified with isotropic elements,
4. the human adult proximal femur behaves linearly with only elastic deformation up to failure (Juszczyk et al. 2011),
5. yield strain values are the failure criteria for trabecular and cortical bone (Bayraktar et al. 2004).

The current in-house pipeline and the experimental data on which it stands are described below.

2.2.1.1 Geometry

Due to its high mineral content, bone shows high contrast in CT images against surrounding soft tissues (Zannoni, Cappello and Viceconti 1998). This allows for the bone geometry to be extracted by segmentation of quantitative CT images (Yushkevich et al. 2006).

The Standardization and Terminology Committee (STC) of the International Society of Biomechanics (ISB) defines the principal axis of the femur as a line passing through the centre of the femoral head, which is coplanar to an axis passing through the centre of both condyles (Wu et al. 2002). This reference system has been used by various in-house CT-based FEA studies of the proximal femur (Altai et al. 2019, Qasim et al. 2016).

2.2.1.2 Material properties

The resulting geometry is meshed and material properties are assigned to the model using an open source software called *Bonemat* (Taddei et al. 2007). The software is used to map elastic modulus derived from the CT attenuation onto the meshed geometry.

The steps for derivation of the material properties and the empirical relationships used in the in-house pipeline are as follows:

Densitometric calibration $HU \rightarrow \rho_{QCT}$

Quantitative CT-scanners have a range of adjustable settings to enhance the visualization of specific tissues and organs, e.g. scanning mode, slice spacing, peak voltage, and X-ray tube current. Each setting combination returns a slightly different attenuation. Therefore, for each setting, a densitometric calibration must be performed to quantify CT-density against Hounsfield Unit (i.e. grey intensity):

$$\rho_{QCT} = x HU - y \quad \text{Eq.2-4}$$

where x and y vary according to the settings used during the CT scan.

CT densitometric calibrations are performed by scanning a phantom of known material density. Phantoms are specific to the tissue being observed, e.g. the phantoms used for the calibration of bone images are typically made of minerals which resemble the minerals found in bone tissue. Two popular phantoms found in literature are the

European Spine Phantom (QRM-EFT), containing hydroxyapatite (HA) (Kalender et al. 1995); and the Mindways Phantom, containing dipotassium phosphate (K_2HPO_4).

Correction of the calibration $\rho_{QCT} \rightarrow \rho_{ash}$

Although HA and K_2HPO_4 closely resemble bone mineral, a slight difference could still result in the under or over estimation of bone density (Winsor et al. 2021). The difference between the phantom CT-density and bone density is accounted for by a process called correction of the calibration. The corrections are based on experimental findings on the relationship between a set of phantom materials and ash density.

Equations Eq.2-5 and Eq.2-6 have been found to be the most appropriate for correcting the calibration of the European Spine Phantom and the Mindways Phantom, respectively.

European Spine Phantom (Schileo et al. 2008a):

$$\rho_{ash} = 0.8772 \rho_{HA} + 0.07895 \quad \text{Eq.2-5}$$

Mindways Phantom (Knowles, Reeves and Ferreira 2016):

$$\rho_{ash} = 1.22 \rho_{k_2HPO_4} - 0.0523 \quad \text{Eq.2-6}$$

where ρ_{HA} and $\rho_{k_2HPO_4}$ are the relevant CT densities, sometimes referred to as ρ_{QCT} .

Ash density – apparent density ratio $\rho_{ash} \rightarrow \rho_{app}$

Experimentally, the elastic modulus of the bone is often measured with respect to the apparent density (Helgason et al. 2007a). To bridge this mathematical gap, (Schileo et al. 2008a) found that the ratio between ash density and apparent density is constant through all densities (cortical and trabecular) in healthy adult human and bovine femur:

$$\rho_{app} = \frac{1}{0.6} \rho_{ash} \quad \text{Eq.2-7}$$

Note that Schileo did not specify or differentiate between the cortical microstructure of the bovine sample. Therefore, an assumption has to be made as to whether the equation is solely applicable to lamellar bone or whether it is inclusive of plexiform bone.

From equation 2.7 it can be implied that in healthy mature bone the ratio of mineral to organic matter is constant. To the author's knowledge this constant has not been investigated in immature bone, therefore particular care should be taken when converting apparent density to ash density for elastic modulus derivation in immature bone, particularly when applying it to woven bone.

Elastic modulus – apparent density $\rho_{app} \rightarrow E$

The in-house pipeline is based on (Schileo et al. 2007) study, which demonstrated that proximal femur models are most accurate when the elastic modulus (E) of bone is derived from a site-specific data (Morgan et al. 2003), and that the equation below is suitable for whole bone density range, i.e. trabecular and cortical bone in the proximal femur.

$$E_{proximal\ femur}[GPa] = 6.850 \rho_{app}[g/cc]^{1.49} \quad \text{Eq.2-8}$$

It is important to highlight that the equation Eq.2-8 was obtained from on-axis experimental testing on the trabecular bone of the femoral neck. Contrary to Schileo's conclusion on the trabecular-cortical inclusivity of the equation, Morgan emphasised that modulus-density relationships are site-specific due to inter-site architectural variations (see section 2.1.5.1). This equation was used in Schileo et al. 2007 to model the proximal femur as it mainly consists of trabecular bones. However, as Morgan et al (2003) pointed out in the limitations of their findings, Eq.2-8 does not stand true for the thicker cortical shaft of the femur and caution should be applied when used in that context.

The CT2S pipeline (and its constitutive equations) was originally developed to model the adult proximal femur and validated against cadaver experiments. Since then, there are a multitude of similar pipelines that have been used to model other human and animal bones. As explained above, relevant elastic modulus-density empirical relationships are needed to model other bones or bone sites. For instance, to model the femoral shaft, one would need an empirical relationship between elastic modulus and density.

Öhman found that the elastic modulus-ash density of the femoral and tibial shafts was as follows:

$$E_{femoral\ and\ tibial\ shaft}[GPa] = 12.9\rho_{ash}[g/cc]^2 \text{Eq. 2-9}$$

Öhman's sample pool covered a large age range, with bones extracted from children as young as 4 years old, suggesting that the above equation could be suitable for the FE modelling of paediatric femurs. Note that this equation is limited to cortical lamellar bone and would not necessarily be suitable for younger children with woven bone.

2.2.2 Adaptation of the modelling pipeline to paediatric

In recent studies, the existing modelling pipeline has been used to provide quantitative information on paediatric bone mechanics and fracture mechanisms (Li et al. 2015, Altai et al. 2018). As discussed in section 2.1, immature bone greatly differs in geometry and composition from adult bone. Accordingly, specific adaptations of the CT-based modelling methods were employed to model paediatric bone in order to simulate bending and torsional loads.

(Li et al. 2015) first adapted the pipeline to model and simulate four-point bending on the femurs of a paediatric cohort aged 0-3 years. Due to the absence of epiphysis in very young bone, a new reference system was created using the distal and proximal ossification centres as landmarks. This study was later expanded with a larger cohort of young children in order to simulate both bending and torsional loads (Altai et al. 2018). Both studies were able to apply the pipeline to a large immature age range and generate sensible FE results. However, it is worth noting that both studies used the same empirical relationships to derive Young's modulus of the infant bone based on CT attenuation, which was a big assumption given the knowledge that immature bone has a different structure and composition compared with adult bones. Such assumption was made due to a lack of available data to accurately characterise immature bone mechanical properties at the time of the study.

2.2.3 Experimental validation of the in-house femur FE model

The in-house FE modelling pipeline has been validated retrospectively (Altai et al. 2019, Qasim et al. 2016) and experimentally, but only for femoral neck fracture in adults.

(Taddei et al. 2006) was the first to experimentally validate the model by measuring strain at the femoral neck of cadaveric specimen, a procedure adequate for testing of wet bones (Cristofolini and Viceconti 1999), and reported an error of 40%. The pipeline was then

improved and refined against experimental measurements to reach an accuracy of 95% (Grassi et al. 2012, Schileo et al. 2007, Schileo et al. 2008a, Schileo et al. 2008c, Zani et al. 2015). In the experimental tests, the cadaveric femurs were loaded both under stance and side fall conditions. Strain gauges were mostly bonded to the femoral neck, limiting the validation to the proximal end of the femur.

2.2.4 DIC for the experimental validation of femur models

In the past decade, studies have explored the use of 3D-DIC for the validation of FE models of the proximal femur; first using composite femurs and then cadavers.

In the early 2000s, experiments on proximal composite femur (i.e. of known material properties) established that DIC is a useful tool for the validation of biomechanical models. (Dickinson et al. 2011) and (Grassi et al. 2013) tested composite proximal femurs under static stance loading and measured surface strains using 3D-DIC. They generated FE models of the composite femur and compared FE-predicted strains against the experimental DIC results. The results were analysed both qualitatively by comparing strain distribution over the whole correlated area, and quantitatively by comparing strains in multiple localised areas emulating the equivalent of strain gauges. Dickinson and Grassi found that the DIC and FE showed excellent agreement, therefore supporting DIC's potential for biomechanical model validation.

A further study by (Grassi et al. 2016) demonstrated the use of 3D-DIC for FE validation on three human male cadaver proximal femurs. The alignment between the experimental set-up and the FE model was established using anatomical features. FE-predicted strains were again compared qualitatively and quantitatively against DIC. This study further illustrates that 3D-DIC could be a suitable method for validating FE models of immature long bones.

3 GENERAL METHODS: EXPERIMENTAL TESTS

The overall objective of the work undertaken in this thesis was to experimentally validate the in-house CT-based FEM pipeline for immature ovine bone. To do so, repeatable mechanical experiments were designed and adapted to fit lamb femur bones. Two sets of four-point bending tests were performed; the first set was performed on simply supported whole femurs (including periosteum), and the second set was performed on cropped femoral shafts embedded at both the proximal and distal ends. Images of the specimens were taken during the experimental tests and surface strains were calculated by DIC on the captured images. A brief description of bending theory, the fundamental principles of DIC, and the basic principles of photography are provided in this chapter.

3.1 Bending Theory

Four-point bending tests are flexural tests used to observe the mechanical behaviour of a material under bending stress, i.e. normal stresses. A four-point bending test generally consists of a simply supported beam carrying two equidistant vertical loads between the supports (Figure 3-1).

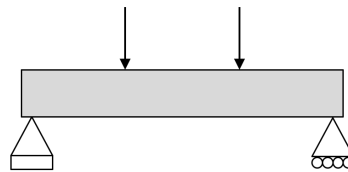


Figure 3-1: Free body diagram of four-point bending loading conditions.

Consider a beam under four-point bending, along its axis, the beam will experience a constant positive bending moment between the two loading points, and a combination of constant shear force and linearly increasing bending moment at both ends (see Figure 3-2).

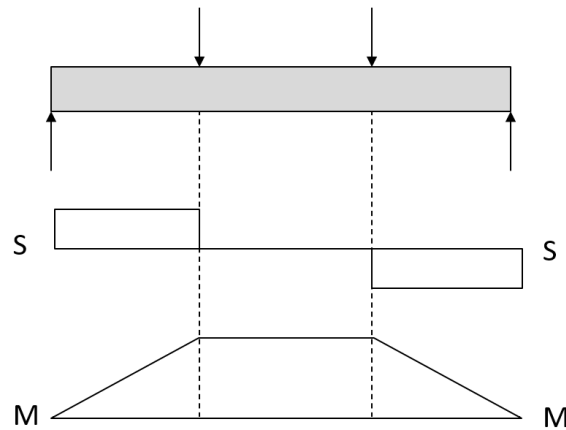


Figure 3-2: Bending moment (M) and shear force (S) diagrams of a beam under four-point bending.

In the mid-section, where bending moment is constant, the beam will experience compression (top) and tension (bottom) in the direction tangential to the curvature of the beam (Figure 3-3. a). The bending stresses will change linearly from compressive to tensile across the height of the beam (Figure 3-3. b). The maximum principal stresses of the beam will be located at the top and bottom surfaces of the beam; corresponding to maximum compression and maximum tension. The position at which the stresses change from compressive to tensile is called the neutral axis (NA) and coincides with the centroid of the cross-section.

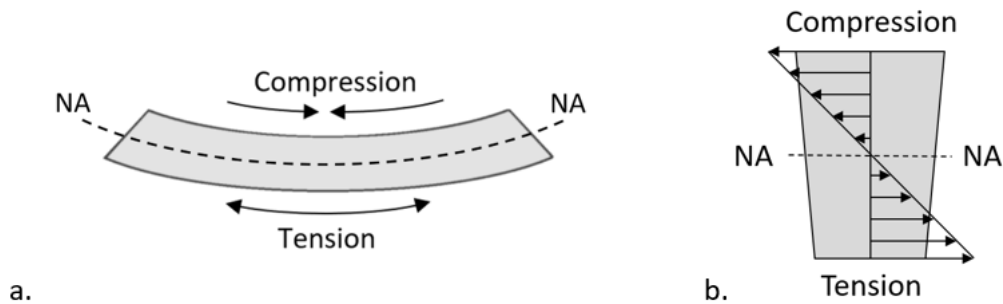


Figure 3-3: Diagram of (a) a beam under positive bending showing the direction of tensile and compressive stresses; and (b) cross-section showing the change in stress across the height of the beam. Note that the cross-section of the beam will widen at the top and become narrower at the bottom due to the Poisson effect.

3.2 Digital Image Correlation

This section gives an overview of the basic principles of 3D-DIC and of the testing method used in this thesis; including specific considerations for DIC testing of whole bone. There are

many open source and commercial packages for DIC. The information given in this sections is applicable to VIC Snap and VIC-3D by Correlated Solution which were used in this PhD work. Additional details relevant to each individual batch of experiments will be given later in Chapter 5 and Chapter 7, respectively. Alternatively, further information can also be found on the iDIC guideline (International Digital Image Correlation Society 2008).

3.2.1 Fundamental principles of DIC

Digital Image Correlation (DIC) is an image-based non-contact method used to measure full-field displacement and deformation. To perform DIC, digital images of a specimen must be taken during the experiment at different states, i.e. different load/time. The test sample must have non-repetitive isotropic high-contrasting visual features, e.g. black on white speckles, white on black speckles, natural patterns. The images are then processed with correlation-based matching algorithms to extract full-field displacement from which other quantities of interest, such as strain, can be derived (Figure 3-4).

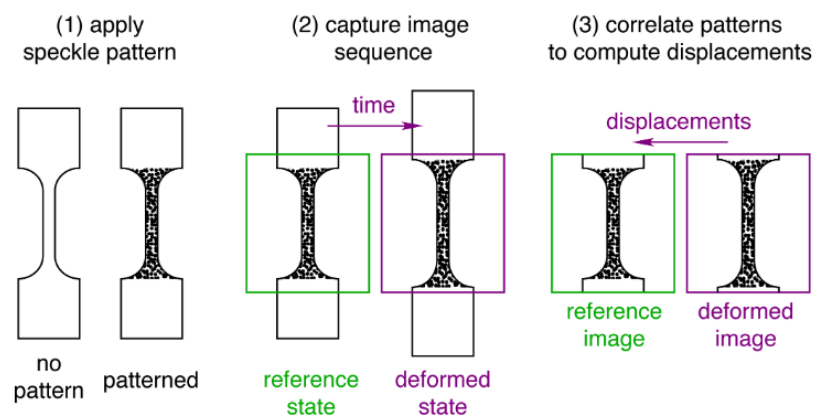


Figure 3-4: Steps for DIC technique, (1) a pattern is applied on the ROI of the specimen, (2) images of the ROI are captured at a reference (undeformed) state and at a deformed state, and (3) the speckle patterns are correlated between the reference and deformed image to compute displacement (Le Page, 2019).

3.2.1.1 Interrogation points, step size and subsets

To obtain full-field displacements, the area within the ROI is discretised into evenly distributed points, referred to as interrogation points. It is at these points that the displacement is individually measured. Interrogation points are commonly distributed in a grid pattern as shown in Figure 3-5. The density of interrogation points within the ROI (i.e. the spatial resolution) is defined by the step size (distance between interrogation points); a smaller step

size results in a larger number of interrogation points but longer computational time (Figure 3-5).

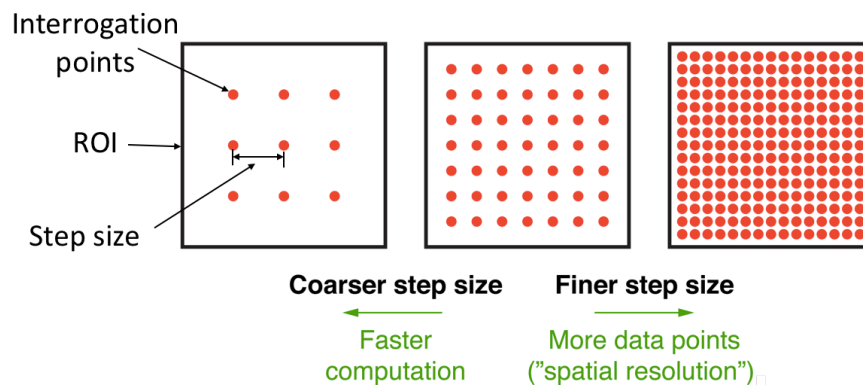


Figure 3-5: Schema of the interrogation points over an ROI and the relationship between step size and spatial resolution in DIC. Decreasing the step size increases the amount of interrogation points within the ROI and in turn increases the spatial resolution.

The relative displacement of the interrogation points between the reference image and the deformed image is measured by correlating small patterned areas surrounding said points. These areas are referred to as subsets. Subsets are typically squared and their height/width is commonly referred to as the subset size. Subsets must be large enough to contain a sufficiently distinctive pattern of speckles so that they can be correlated between images. For example when using a speckle pattern, each subset should contain at least three distinctive speckles (Sutton 2009), as shown in Figure 3-6.

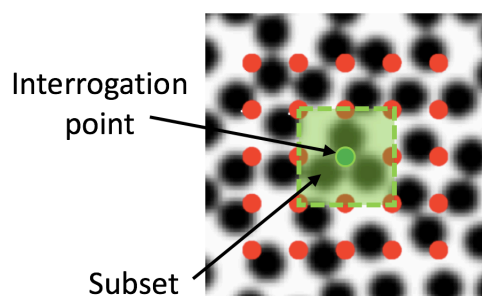


Figure 3-6: Illustration of a subset over a speckle pattern for DIC. To insure correlation, a subset should encompass at least three distinctive speckles.

Conversely, the subset size should be kept to minimum in order to ensure that the interrogation points are sufficiently close to the ROI boundaries to evaluate displacements; which in turn maximises the correlation area over the ROI (Figure 3-7).

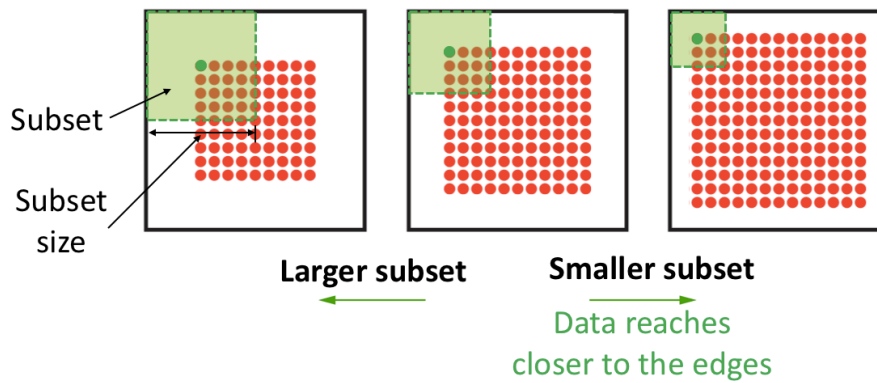


Figure 3-7: Schema of the effect of subset size on correlatable area in DIC. Smaller subsets allow for data to reach closer to the edges of the ROI, increasing the area of correlation.

It is important to consider the relationship between the subset and step size. For most applications, using a step size of $1/3$ to $1/2$ the subset size is recommended. Having a step to subset size ratio smaller than $1/3$ can lead to increased self-correlation errors. This is because the speckle pattern within the subsets of neighbouring interrogation points will become increasingly similar and are no longer distinguishable (Figure 3-8).

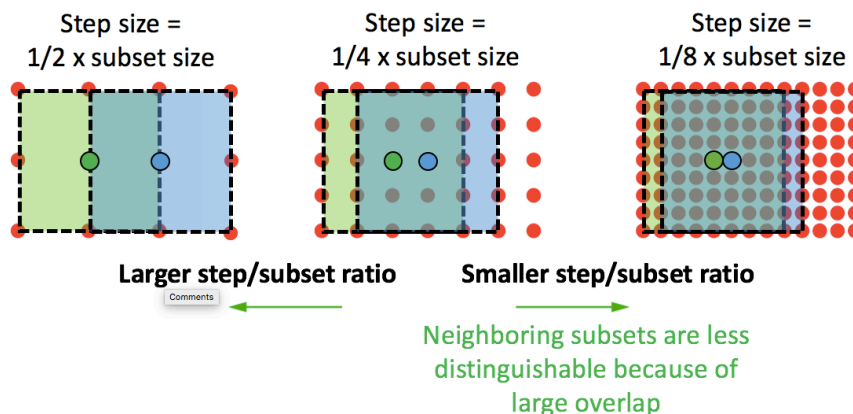


Figure 3-8: Schema of the relationship between step size and subset size in DIC. As the ratio of step size to subset size increases, the overlapping area between subsets of neighbouring interrogation points increases.

With large overlaps the subsets are no longer distinguishable from one another, meaning that intercorrelation between neighbouring interrogation points is more likely to occur.

3.2.1.2 Correlating subsets

The searching and matching of subsets between images is done through grey level correlation. Consider the speckled reference image I shown in Figure 3-9.a. First, the pixels in the image are assigned a grey level ranging from 0 (black) to 255 (white), creating a 7x7 pixel

matrix (Figure 3-9.b). Now take an interrogation point within the reference image, e.g. green point at $x = 4$ and $y = 4$, and set around it a subset of a given size n , e.g. $n = 2$.

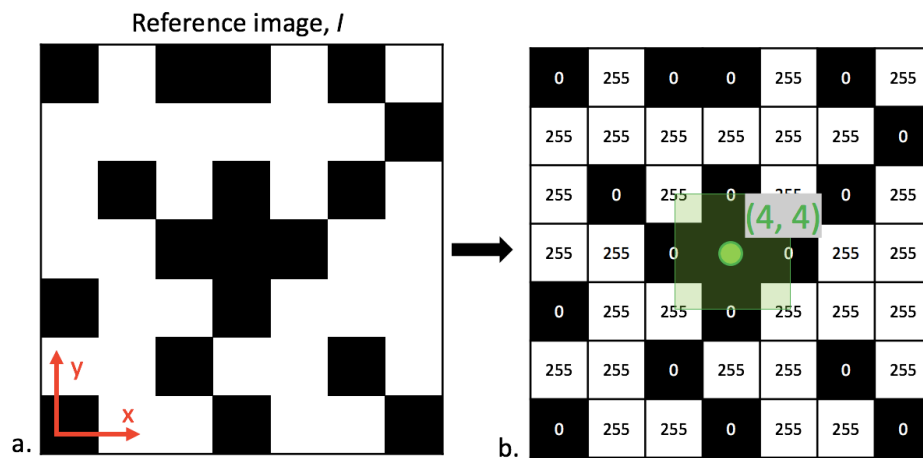


Figure 3-9: Reference image I of a speckled pattern (a) converted into grey level matrix with an arbitrary interrogation point and its squared subset located at $(x, y) = (4, 4)$ highlighted in green (b). Note that the speckle pattern does not have to be binary and that the pixels can take any value between 0 (black) and 255 (white).

Now, imagine the speckle has been displaced by an unknown vector $[u \ v]$, creating image I^* as shown in Figure 3-10.a. To find the displaced subset, correlation (similarity) is calculated at different surrounding points on the grey level matrix of the new displaced image, for example the blue dot moved by $[u \ v] = [0 \ 2]$ and the red dot moved by $[u \ v] = [-1 \ -2]$ (Figure 3-10.b).

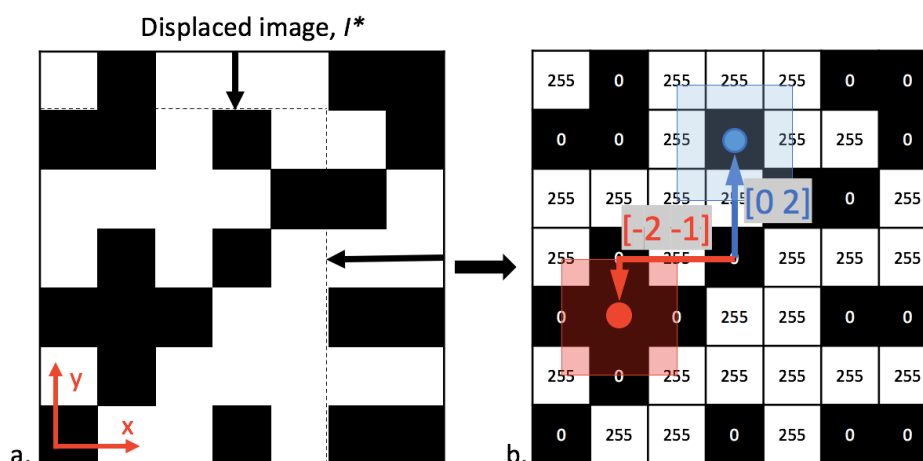


Figure 3-10: Image of the displaced pattern I^* (a) and its grey level matrix (b) showing the original placement of the interrogation point in green and example points at which the correlation can be calculated in the displaced image.

A classic correlation function used is the sum of squared differences (SSD) of the pixel values; smaller values equate to a better similarity (Eq. 3-1).

$$C(x, y, u, v) = \sum_{i, j = -n/2}^{n/2} (I(x + i, y + j) - I^*(x + u + i, y + v + j))^2 \quad \text{Eq. 3-1}$$

Labels in the diagram:
 - Reference image pixel coord. points to (x, y)
 - Displacement points to (u, v)
 - Correlation function points to $C(x, y, u, v)$
 - subset size points to $n/2$
 - Reference image points to $I(x + i, y + j)$
 - Displaced image points to $I^*(x + u + i, y + v + j)$
 - Pixel value at $(x+i; y+j)$ points to $I(x + i, y + j)$
 - Pixel value at $(x+u+i; y+v+j)$ points to $I^*(x + u + i, y + v + j)$

Applying the correlation function to displacements $[0 \ 2]$ and $[-2 \ -1]$ results in a C value of 1625625 and 0 respectively (Figure 3-11). This indicates that the red subset perfectly matches the reference image's green subset. Thus, we can conclude that the green interrogation point was displaced by $[-2 \ -1]$.

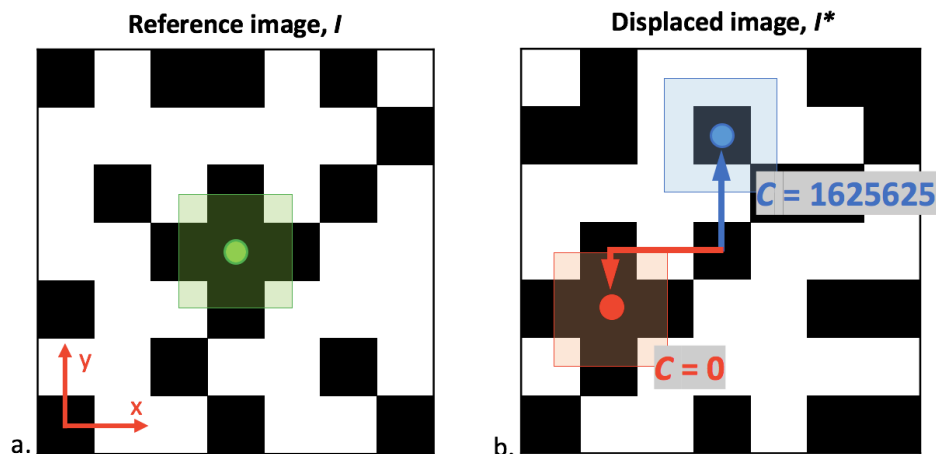


Figure 3-11: Reference image with initial position of the interrogation point in green (a). Displaced image showing correlation value at the blue point and at the red point.

Now consider a speckle pattern that has been displaced and also deformed. The squared subset of the reference image will now be matched to a non-squared equivalent in the deformed image. To account for the deformation of the subset, a subset shape function is included in the correlation function.

Lastly, during image acquisition, it is common for lighting conditions to change, and for the patterns on the test piece to become lighter or darker when tensed or compressed (Figure 3-12). To account for these changes, correlation functions also include a photometric transformation, which allows for the entire subset to get lighter or darker.

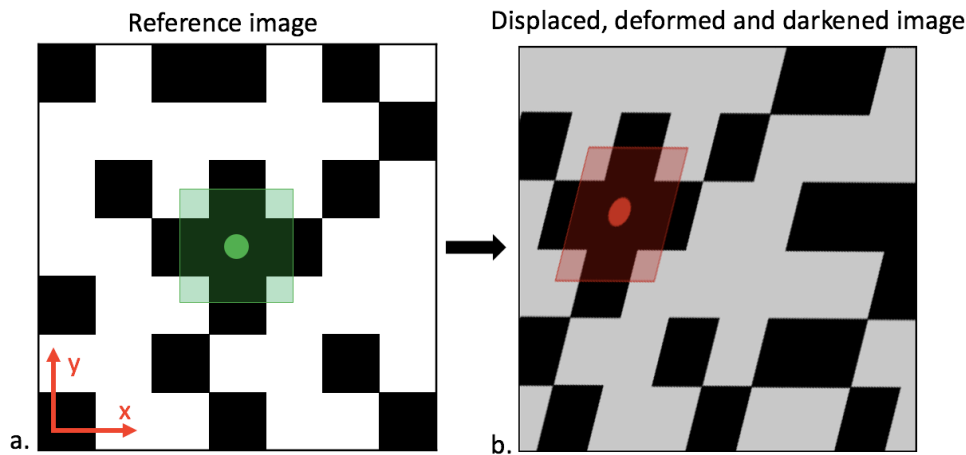


Figure 3-12: Reference image of a speckle pattern (a) and image of the displaced, deformed and darkened speckle pattern (b) showing the effect on a subset.

Note that in reality the test specimen does not move in pixel increments therefore the image needs to be detected at non-integer locations. To do so correlation algorithms use grey level interpolation which convert pixelated (discrete) fields into a continuous spline.

The subset correlation process is performed for every interrogation point within the ROI. Therefore, displacement data is retrieved at every point across the ROI. Other quantities of interest, such as strain, can then be derived from the displacement data at each point.

In this thesis, a convergence analysis was performed to obtain the most appropriate subset and step size for each experimental test.

3.2.1.3 2D-DIC vs 3D-DIC

There are two imaging techniques used for DIC, 2D-DIC and 3D-DIC. 2D-DIC is performed with a single camera. The use of this technique is limited to flat specimen undergoing motion parallel to the camera plane (it must not move towards or away from the camera) as the system cannot distinguish between out-of-plane motion and in-plane dilatation. On the other hand, 3D-DIC (aka. stereo digital image correlation) is a technique that uses synchronised images of the specimen taken from two different planes to obtain 3D information of the tested specimen through stereo-triangulation (Figure 3-13). This technique is much less limited as it allows for the measurement of 3D displacement and surface strains on curved specimens (Pan 2018).

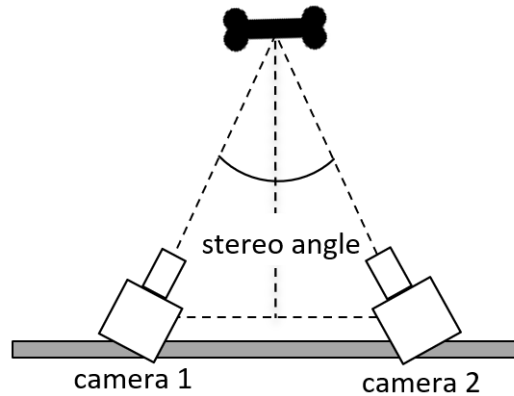


Figure 3-13: Example set up for 3D-DIC with two cameras placed at an angle.

In 3D-DIC an extra step is required to obtain 3D temporal displacements. Before calculating displacements, 3D reconstructions of the reference and deformed specimen are obtained using inter-camera correlation and stereo-triangulation.

Inter-camera correlation follows the same principle as described in section 3.2.1.2.; interrogation points are placed and located between the plane images of camera 1 and camera 2 via subset correlation. Stereo-triangulation is a mathematical approach used to determine the location of the interrogation points within a common 3D coordinate system, creating a virtual 3D surface. Stereo-triangulation uses the intersection of optical rays (epipolar projection lines) and the relative distance between the two cameras to place points in a 3D space. Note that the relative distance between the two cameras is measured via stereo-calibration, see section 3.2.3.2.

Once the virtual 3D reference and deformed state surfaces are obtained, the displacements of the interrogation points can be calculated within the 3D space.

3.2.1.4 Coordinate systems

Different coordinate systems can be used in 3D-DIC. Coordinate systems can be auto-generated or user-defined. The most simplistic auto-generated coordinate system is the camera coordinate system. In a camera coordinate system, the origin is placed at the centre point between the two camera sensors along the baseline, the x-axis is co-linear to the baseline, the z-axis is normal to the average plane between the two sensor planes, and the y-axis is normal to the x and z axes. All studies in this thesis use a camera coordinate system.

3.2.1.5 Strain calculations

VIC-3D calculates surface strains in an FEA-like manner (see section 4.2). First, a triangular surface mesh is generated using the interrogation points as nodes. Then, tensor strains are calculated for each triangle using the displacement data of each point. Lastly, strains are interpolated from the surrounding triangles to each point. Note that the strains are measured in-plane for 2D-DIC, and are measured tangential to the surface of the test piece for 3D-DIC.

VIC-3D outputs major and minor principal surface strains (ε_1 and ε_2 respectively). It also outputs plane strains along the x and y axes (ε_{xx} and ε_{yy} respectively), however these are calculated from the individual camera's 2D correlation (similarly to 2D-DIC). For many 3D-DIC setups, the x axis or y axis will naturally align with the axial or transverse strain axis of the test piece, however this does not apply for curved specimen. In the case of a cylindrical object under four-point bending, the axial surface strain, ε_a , will remain closely aligned to the x-axis, and can therefore be approximated to the x-strain, ε_{xx} . However, the transverse surface strains, ε_t , will only align with the y-axis along the neutral plane of the specimen. As one moves away from the neutral plane, the transverse strain will rotate within the yz plane, and thus, can no longer be approximated to the y-axis strain, ε_{yy} (Figure 3-14). However, for simplicity, please note that in this thesis all DIC strains are labelled ε_{xx} and ε_{yy} .

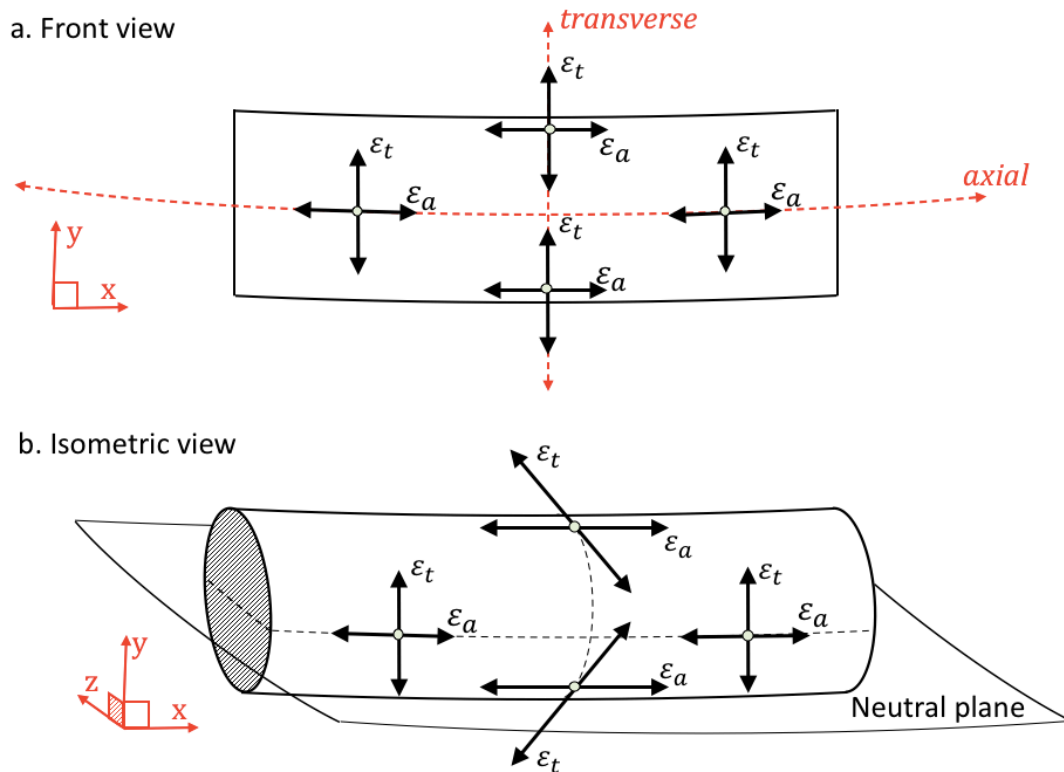


Figure 3-14: (a) Front view and (b) isometric view of a circular beam under bending showing the orientation of transverse and axial strains along and across the beam.

3.2.2 Basic principles of photography for DIC

Precision and accuracy in DIC are highly dependent on image quality, i.e. sharpness and contrast. A good quality image can be achieved with good camera equipment; but it is also subject to camera settings including focal length, aperture and shutter speed. The basic structure of a camera is shown in Figure 3-15. The lens is the part of the camera that focuses light by refraction. Moving the lens allows the user to change the focal length of the camera, i.e. the distance between the camera and the plane of focus. The aperture is the opening which allows light to enter the camera. Aperture controls the depth of field (DoF), or the distance between which objects appear sharp in an image.

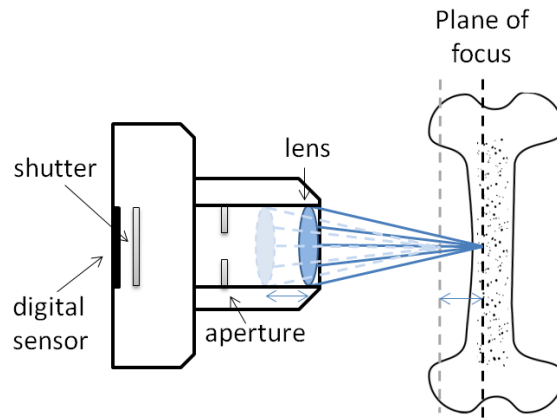


Figure 3-15: Diagram of the basic components of a camera showing how the lens position determines the plane of focus.

Closing an aperture will increase both the front and rear DoF, although the rear DoF will be substantially larger (Figure 3-16). Changing the aperture size will also affect the amount of light passing through to the camera, i.e. the exposure. A wide aperture will pass a lot of light, resulting in a bright picture, whereas a small aperture will result in a dark image. Too much exposure or too little exposure decreases the range of dark-to-bright tones in an image and can result in poor contrast and loss of detail. It is worth noting that aperture is usually referred to in terms of focal ratio or *f-number*. An aperture of small diameter will have a large *f-number* and vice-versa.

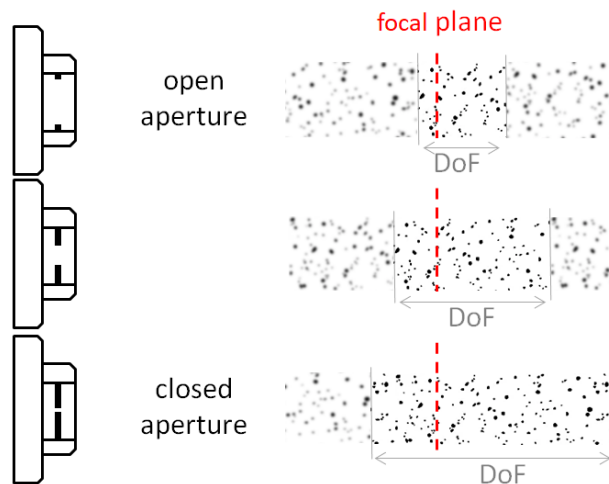


Figure 3-16: Diagram showing the effect of camera aperture on the depth of field.

Exposure is also dependent on shutter speed. A shutter is a device which opens and closes at a constant frequency. It controls the exposure time, i.e. the amount of light reaching the receptor. Accordingly, a slow shutter speed renders brighter images, and a fast shutter speed

renders darker images. Additionally, the shutter speed also affects the sharpness of an image when capturing objects in motion. Indeed, decreasing the shutter speed will not only allow more light into the receptor, but it will also make objects in motion appear blurry. Conversely, increasing the shutter speed will decrease the amount of light reaching the camera, but it will make objects in motion appear sharper. It is important to consider shutter speed when taking images during a continuous (moving) experiment.

External environment/lighting can also be used to improve the image of an object. Darkening the background behind the target object can help minimise noise and unnecessary light exposure. External lighting can also be used to increase the brightness of the object. To increase the brightness of an object without increasing noise/background lighting, light sources should be placed behind the camera lens and should be directed onto the target object. The light sources should be cold to avoid heat damage to the tested specimen and to avoid generating heat waves between the test piece and the cameras which would deform the image.

The best balance between camera settings and external lighting varies from specimen to specimen. The surface geometry of a specimen (degree of curvature), the speckle size, the location of the ROI, and even the type of mechanical test being captured need to be taken into consideration when adjusting the camera set-up and settings.

3.2.3 Stereo-system set-up

It is important to consider the relative positioning of the cameras and test piece when performing 3D-DIC. Ideally, the cameras should be secured on a beam mounted on a tripod. This ensures that the relative distance between the cameras is secure and constant throughout testing. The cameras should be set parallel and in-plane with the ROI of the test piece. The cameras should be placed so that the ROI fills up most of the field of view so that potential deformation and displacements of the test piece can be fully captured. The distance between the two cameras should be set to create the desired stereo angle. The optimal stereo angle is dependent on the hardware's focal length capacity and the required DoF for the specific set-up. Typically, the stereo angle should be approximately 15°-35°. Based on internal recommendations I chose to use a 30° stereo angle.

3.2.3.1 Camera settings

The position and settings of the cameras can be fine-tuned in live capture using VIC Snap as it allows one to map contrast and over-exposure during live capture. VIC SNAP also has a photo histogram tool that allows you to plot a histogram of the tonal range over a selected region of interest. The cameras should be set so that most of the region of interest appears sharp and has sufficient contrast for DIC analysis. For a highly curved surface, this means focusing on the outer most point and increasing the depth of field to include the top and bottom lines (Figure 3-17).

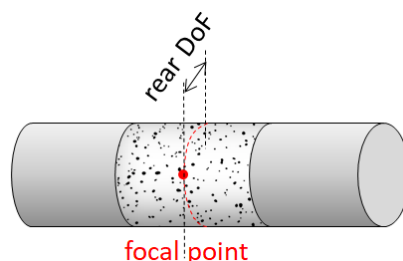


Figure 3-17: Diagram showing how to obtain a sharp image over a curved surface by focusing on the closest point (red) and increasing the depth of field (DoF) to encompass the whole of the ROI.

First, the cameras should be focused roughly around the closest point of the ROI. To do so the aperture of the cameras must be fully opened making the plane of focus clear on the image. The lenses can then be adjusted accordingly. Using the cross-hair tool in VIC SNAP, the position of the cameras can be re-adjusted so that the midpoint of both images matched. The lenses can then be re-focused. Finally, the aperture and shutter speed can be set to achieve a balance between DoF and resolution.

Note that for a stereo set up the ROI should be in focus for both cameras, see Figure 3-18.

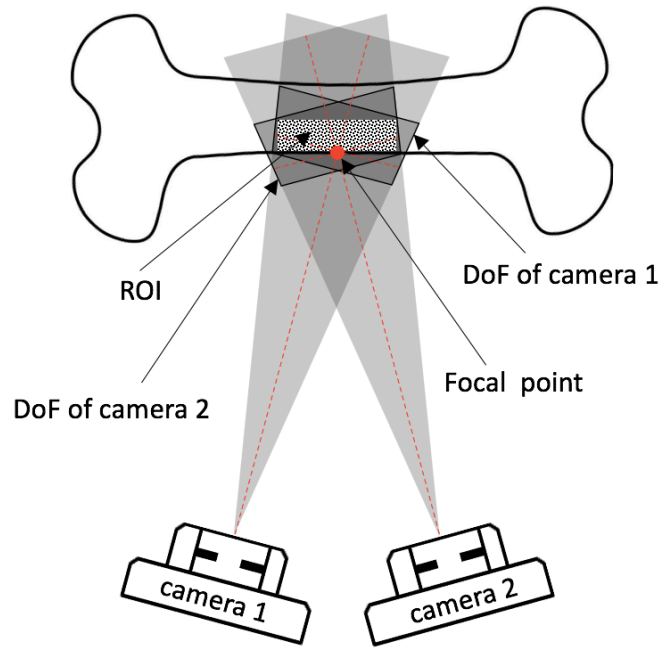


Figure 3-18: Top view diagram of a DIC stereo-system showing the joint focal point and the overlapping DoF of both cameras over the ROI.

In this thesis, the shutter speed was primarily used as a mean to increase the exposure. Little regard was given to motion as the test was set at a slow pace and rapid motion was not expected until failure.

3.2.3.2 Stereo system calibration

Stereo system calibration is a process used to measure the position of the two cameras with respect to one-another. Calibration is performed by capturing images of a plate with a dotted pattern of known dimension, commonly a system-specific calibration plate. Calibration is performed once the positioning of the cameras and the focal length has been seen. For calibration, multiple images must be taken within the ROI of the calibration plate with translations and rotations. The system then calculates the positioning of the cameras using stereo-triangulation.

3.2.3.3 Error and noise

Noise in DIC can arise from floor vibration, lighting and set-up. The noise can be assessed by taking a few static images of each specimen before loading and correlating the images for the variables of interest (e.g. displacement and strain). The resulting contours can help indicate regions of high noise and uncertainty. Errors should fall well beneath the values associated

with the test piece. For instance, the noise in the strain contour map for bone should be well below the yield strains mentioned in section 2.1.5.

VIC 3D outputs a projection error value for each image. Based on the stereo set-up obtained through calibration, for a given point in an image of camera 1 (reference image), a line on which the point should fall (epipolar line) is predicted in an image of camera 2. The projection error is the distance of a point from the epipolar line on which it is supposed to sit. Projection errors are typically caused by a disturbance of the set-up such as a change in the focus or camera position. Projection errors above 0.1pxls may indicate issues that will offset the image scale. Projection errors are more of a concern when measuring positions and displacements. The effect of projection errors on strains is less evident as strain is a unitless measure, i.e. if the scaling error is the same in the undeformed and deformed image, then the strain will not be affected. However, projection errors are systematic errors which increase with out-of-plane displacement, thus it should be considered carefully when measuring strains on a test piece that has undergone out-of-plane displacement. Note that high projection errors will not affect the output contours of static noise images discussed above.

3.2.3.4 Speckle painting on fresh bones

For DIC analysis in this thesis, the bones had to be covered in a contrasting pattern of speckles. Painting speckles on fresh (i.e. hydrated) bones required some surface preparation. Prior to painting, the bones were allowed to defrost and reach room temperature in order to avoid surface condensation, which would cause the paint to bubble. They were then pat dried and swiftly painted with a matt white background and black speckles. Testing freshly painted hydrated bones also created time constraints. Leaving the painted bones out for too long would have allowed the outer cortical layer to dry, potentially changing its material properties. Additionally, biological fluids would have seeped from the marrow through the bone and damaged the painted speckle pattern. To minimise the aforementioned, all bones tested were prepared individually and immediately before the test.

4 GENERAL METHODS: CT-BASED FEA

In this thesis, two sets of FE models were generated from either standard medical CT scans or μ CT scans of the tested bones. Individual scan-based FE models were created from geometry segmentation, and bending was simulated *in silico* to predict surface strain contours, which were then compared against the DIC strain contours. This chapter describes the general methods used in these studies, as well as the basic principles upon which they are built.

4.1 CT-based modelling

4.1.1 Computed tomography

During CT-based subject-specific modelling, each specimen is individually scanned to generate a stack of images, which are in turn segmented to generate a 3D digitised geometry (faceted body). The resulting faceted body can then be converted into a solid body with Computed Aid Design (CAD) software or directly meshed for FE analysis.

CT is a medical imaging technique which enables the internal visualization of the body based on the x-ray attenuation coefficient of the scanned tissues (material). It can be used for a variety of tissue densities and organ sizes; but is particularly efficient for the visualization of the skeleton as bones have much higher attenuation compared to surrounding soft tissues. CT scans combine a series of x-ray slices taken from different angles around the patient and use computer processing to create cross-sectional images from the measured x-ray attenuations (reconstruction matrices), which are then stacked for 3D visualization (Figure 4-1). These principles are the same for clinical CT scanners and μ CT scanners. For

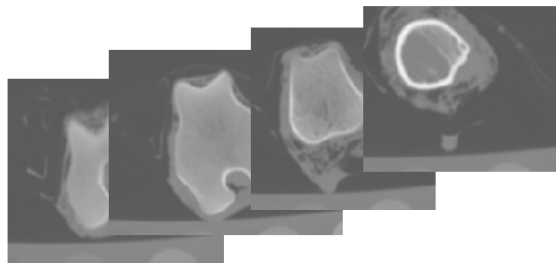


Figure 4-1: CT scan slices of lamb femur.

4.1.1.1 Fundamental principles of CT

This section will discuss the fundamental principles of CT looking at first generation CT scanners. First generation CT scanners used a simple system consisting of an x-ray beam and an x-ray tube moving synchronously across a patient. Take a single slice of thickness T across the patient with an x-ray tube on one side and an x-ray detector on the opposite side (Figure 4-2). Now discretize the slice into a matrix of voxels (also known as reconstruction matrix), where each voxel, of XY -dimension w_i , has material of unknown attenuation coefficient μ_i .

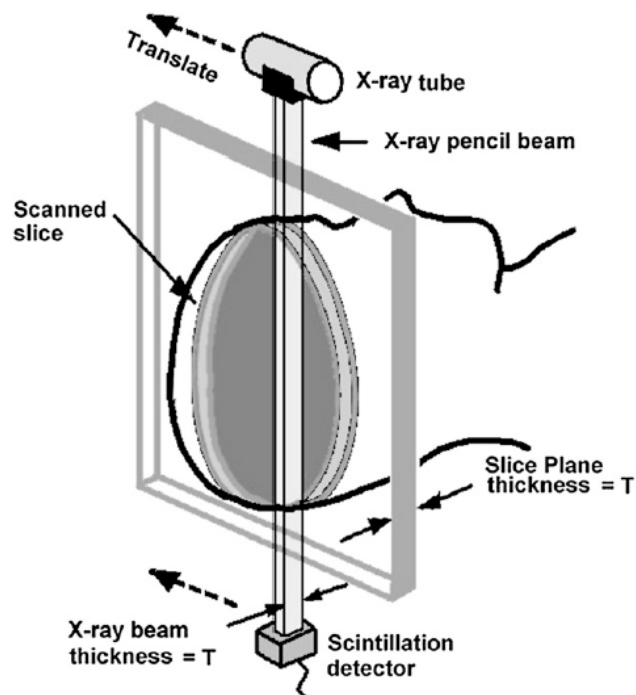


Figure 4-2: Diagram of a single slice CT scanner. X-ray beam is emitted out of the x-ray tube and detected by the scintillation detector. The process is repeated across the slice plane (Goldman 2007).

Consider a beam of initial intensity N_o passing through a row of voxels with attenuation coefficients $\mu_1 \dots \mu_n$ and resulting in a beam of intensity N_i (Figure 4-3).

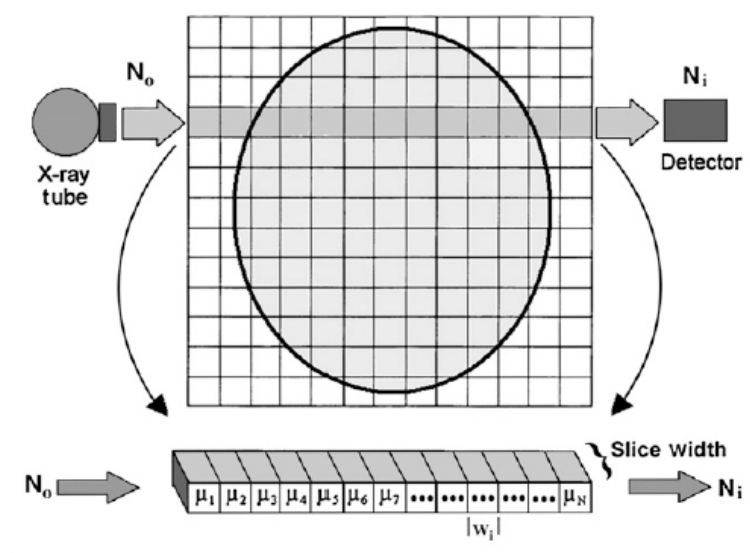


Figure 4-3: Diagram of a CT reconstruction matrix (Goldman 2007).

Now take the intensity N_1 exiting the first voxel of attenuation coefficient μ_1 . Using the expression for exponential attenuation,

$$N_1 = N_o e^{-(w_1 \mu_1)} \quad \text{Eq. 4-1.}$$

Similarly for each adjacent voxel the intensity is expressed as:

$$N_2 = N_1 e^{-(w_2 \mu_2)} = N_o e^{-(w_1 \mu_1)} e^{-(w_2 \mu_2)} \quad \text{Eq. 4-2}$$

$$N_3 = N_2 e^{-(w_3 \mu_3)} = N_o e^{-(w_1 \mu_1)} e^{-(w_2 \mu_2)} e^{-(w_3 \mu_3)} \quad \text{Eq. 4-3}$$

.....

Therefore, N_i can be written as:

$$N_i = N_o e^{-(w_1 \mu_1)} e^{-(w_2 \mu_2)} e^{-(w_3 \mu_3)} \dots e^{-(w_n \mu_n)} \quad \text{Eq. 4-4}$$

and re-written as:

$$-\ln\left(\frac{N_i}{N_o}\right) = \sum_{i=1}^n w_i \mu_i \quad \text{Eq. 4-5}$$

or as:

$$Y_i = \sum_{i=1}^n a_i \quad \text{Eq. 4-6,}$$

where $Y_i = -\ln\left(\frac{N_i}{N_0}\right)$ is the derived measurement of the sum of the attenuation values in the voxels along the path of the ray, and $a_i = w_i\mu_i$ is the attenuation value of each voxel along the path of the ray.

This process is repeated across and around the matrix allowing for the construction of a system of equation which can be solved for $a_{11} \dots a_{nn}$.

For example, consider a simple 2x2 reconstruction matrix, through which an x-ray beam is projected in the following six paths (Figure 4-4),

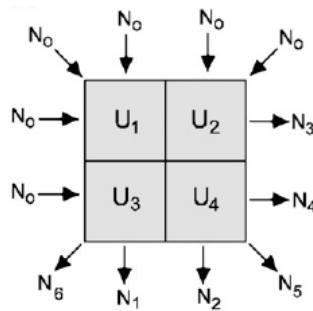


Figure 4-4: Algorithm representation for a four-voxel image where N_0 is the original x-ray intensity entering the image, U_{1-4} are the attenuation values and N_{1-6} are the exiting x-ray intensity (Goldman 2007).

The system of equations would be:

$$\begin{cases} Y_1 = a_1 + a_3 \\ Y_2 = a_2 + a_4 \\ Y_3 = a_1 + a_2 \\ Y_4 = a_3 + a_4 \\ Y_5 = a_1 + a_4 \\ Y_6 = a_2 + a_3 \end{cases} \quad \text{Eq. 4-7}$$

4.1.1.2 Filtered backprojection (FBP)

Modern CT scans generate much larger reconstruction matrices. To bypass the computational expense of solving large system of equations, modern CT images are reconstructed using backprojection. Backprojection is a method where the attenuation measurement of each path is simply distributed equally to the voxels on the path. This is repeated for each path at each angle and the attenuation values measured for each voxel are added. Consider a slice with three objects of different attenuation coefficients shown in Figure 4-5. If the slice is scanned at three different angles, and three sets of data are collected for each orientation, these are then superimposed to generate the final image.

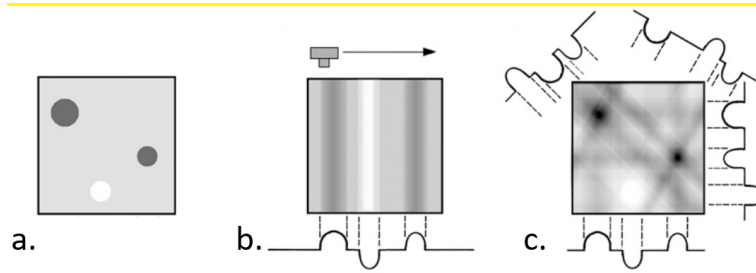


Figure 4-5: Backprojection reconstruction for a slice with three objects of different attenuation coefficients (adapted from (Goldman 2007)). (a) Real image of the three objects. (b) Image generated from a single projection. (c) Image generated from four superimposed projections at different angles.

The process of backprojection requires a lot less computational power; but results in blurry images. Consider the top left object in the figure above with backprojection, the attenuation of the object appears highest at its center, where it is thickest, and decreases toward its edges; i.e. it is blurred (Figure 4-6).

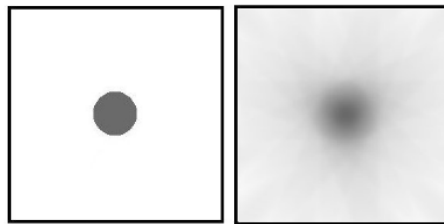


Figure 4-6: Blurring effect of backprojection around a single object adapted from Goldman (2007).

The blurring effect of backprojection can be reversed by a mathematical process called filtering (using convolution kernels). To de-blur an image, a filter function is applied to each view before backprojection (Figure 4-7).

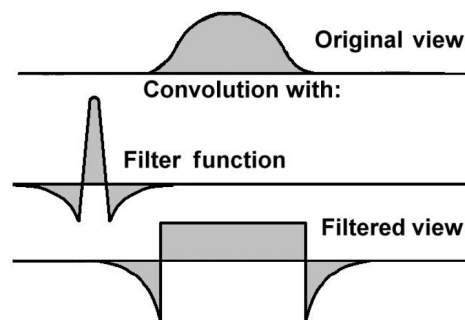


Figure 4-7: CT filtering functions using convolution kernels (Goldman 2007).

It is important to note that filtering not only sharpens the blur created by backprojection, but it also aggravates the effect of noise on an image (graininess). The choice of filter is dependent on operator and the type of tissue being observed. For example, images of soft tissues (low-contrast boundaries with surrounding tissues) benefit more from reduced noise. On the other hand, an image of bone (high-contrast boundaries against surrounding soft tissues) would benefit more from harsher filtering for a resulting image with better resolution. Clinical CTs often have pre-set reconstruction filters. Common filters are: “Standard”, which is normally used to deliver the best compromise between resolution and image noise when scanning soft tissue, “Smooth”, “Detail” and “Bone”.

4.1.1.3 X-ray technical factors

Projections can be affected by x-ray production factors, namely the exposure time, the amperage and the peak voltage.

Amperage is the amount of x-ray photons produced. An increase in the rate of amperage per second (mAs, milliamperage second) improves the resolution, or density, of the projection. Noticeably, increasing the exposure time will also increase the total amount of x-ray photon and thus improve the projection density. However, a long exposure time could result in a blurry projection if the patient is moving.

The peak voltage, referred to as kVp (kilovoltage peak) is the maximum strength of the x-ray beam reached during exposure, i.e. its ability to penetrate through tissue. For example, scanning thicker body parts such as the lumbar region would require higher kVp for the x-ray photons to reach the detector. Inversely, scanning a finger would require lower kVp.

These factors dictate the x-ray beam energy, which in turn returns different attenuation coefficients for the scanned tissues.

4.1.1.4 Hounsfield units

CT numbers are a conventional way to quantify tissue attenuation regardless of the CT scanner and technical settings. CT scanners are routinely calibrated so that scanning water returns a CT number of 0 HU. A CT number, measured in Hounsfield units (HU), is defined as:

$$CT\ number\ [HU] = \frac{K \times (\mu_{voxel} - \mu_{water})}{\mu_{water}} \quad \text{Eq. 4-8,}$$

where μ_{voxel} is the attenuation coefficient calculated for each voxel of the reconstruction matrix, μ_{water} is the attenuation coefficient of water, and K is an integer constant standardized at either 1000 or 1024. For a correctly calibrated scanner, the CT number of a voxel containing water should be 0 [HU]. Similarly, the CT number of a voxel containing air (for which $\mu_{air} \approx 0$) should be approximately -1000 [HU]. In clinical settings, the CT number of a voxel containing cortical bone should be approximately 1000 [HU].

4.1.2 Semi-automated 3D segmentation

Image segmentation is a process used to split digital images into multiple segments in order to contour organs. Semi-automated segmentation was used in this thesis to extract the femoral geometries from the scans. All the segmentations in this thesis were processed with the open-source software ITK-SNAP version 3.8.0.

4.1.2.1 Segmentation Method

ITK-SNAP uses a combination of thresholding and active contour evolution (i.e. moving contour by iteration) (Yushkevich et al. 2006). First the user picks a threshold limit to temporarily convert the image into a binary image, making the target organ more discernable to the user (note that the threshold limit is only a tool to help the user find their target organ; does not affect the final contour). The user then initiates an active contour by placing “bubbles” within the target organ/structure. The outline/outlines of the bubbles become the initial contour/contours; whose surface is defined as $C(u, v; t)$, parametrized by variables u , v , and the time variable t . Then the initial contour evolves as per the following partial differential equation:

$$\frac{\partial}{\partial t} C(t, \mathbf{u}, \mathbf{v}) = \mathbf{F}\mathbf{n} \quad \text{Eq. 4-9,}$$

where \mathbf{n} is the unit normal to the contour and \mathbf{F} is the sum of the forces that act on the contour. In ITK-SNAP, \mathbf{F} is derived using two well know active segmentation methods: Geodesic Active Contours and Region Competition.

With the Geodesic Active Contour method, \mathbf{F} is defined by a speed function and an advection force. The speed function is derived from the gradient magnitude of the image’s CT-number. It acts in the outward direction, causing the contour to expand. The speed function takes a value close to 1 in regions where the intensity (e.g. CT-number) is nearly constant and takes

a value close to 0 where intensity values drastically change. On the other hand, the advection force acts inwards when the contour directly approaches an edge of intensity (Figure 4-8).

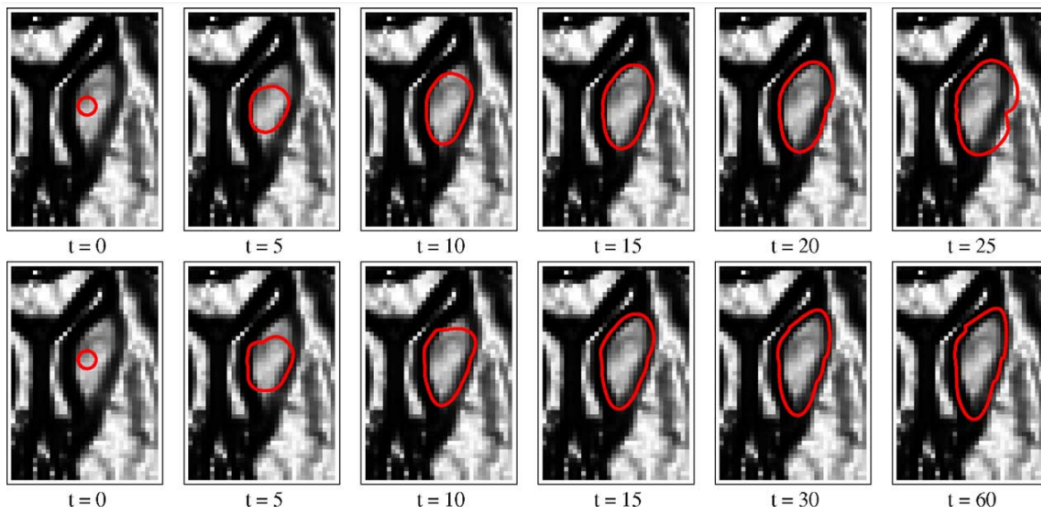


Figure 4-8: Active contour evolution using the Geodesic method without (top) and with (bottom) the advection term (Yushkevich 2006).

With the Region Competition method, F is computed by estimating the probability that a voxel belongs to the organ of interest and the probability that it belongs to the background (Figure 4-9). In ITK-SNAP, these probabilities are estimated using fuzzy thresholds.

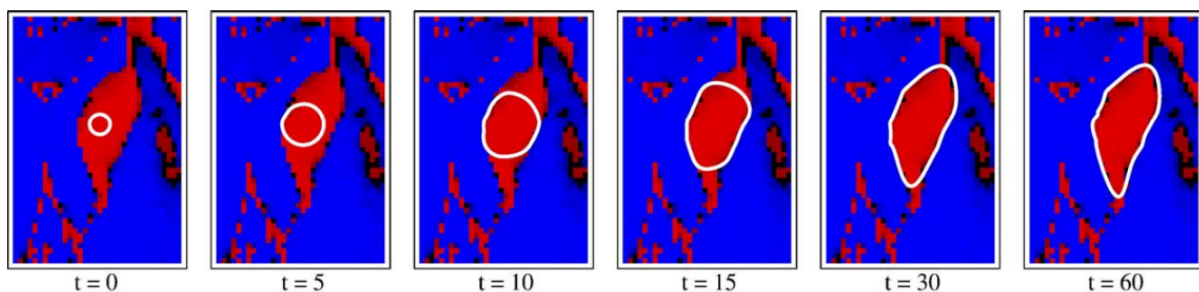


Figure 4-9: Active contour evolution using the Region Competition method (Yushkevich 2006).

The number of iterations, or time t , is determined by the user. Once the iteration is finished, the contour can be altered manually by the user if needed following a process similar to paint tools. The final contour can then be exported as a faceted body for CAD (Figure 4-10).



Figure 4-10: Volume of lamb bone segmented from CT-images.

4.2 Continuum mechanics for FEM

The fundamentals of continuum mechanics used for FEA formulations are explained in this section.

4.2.1 Displacement and strain

Take an object in a 3D space with orthogonal coordinate system e_i , represented by a collection of material points (Figure 4-11). Each material point can be represented by a unique vector \mathbf{X} . If the configuration is deformed by a function f , the vector between the reference and deformed configuration is defined as the displacement function $u(\mathbf{X})$ such that,

$$\mathbf{u} = \mathbf{x} - \mathbf{X} \quad \text{Eq. 4-10}$$

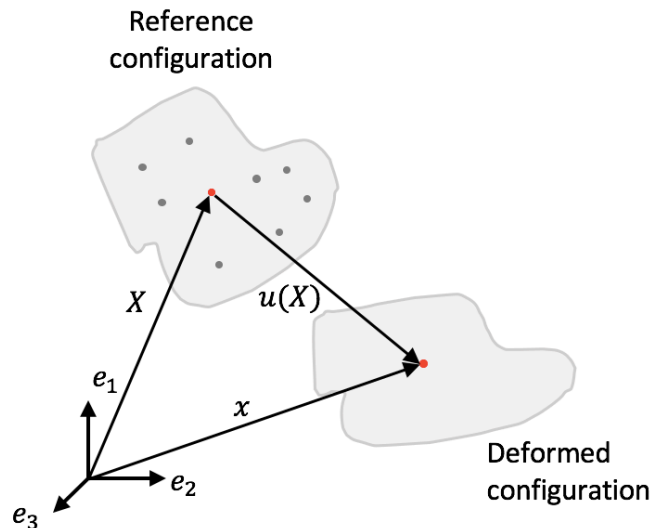


Figure 4-11: Illustration of an object in a 3D space with a material point at \mathbf{X} from the origin, which has been deformed so that the material point has been displaced by $u(\mathbf{X})$ and is now located at \mathbf{x} from the origin.

Now take an adjacent point at a distance $d\mathbf{X}$ and $d\mathbf{x}$ in the reference and deformed configuration respectively (Figure 4-12). By equating the vector paths highlighted in pink and blue from the origin to point P we obtain:

$$\mathbf{x} + d\mathbf{x} = \mathbf{X} + d\mathbf{X} + \mathbf{u}(\mathbf{X} + d\mathbf{X}) \quad \text{Eq. 4-11}$$

$$\therefore d\mathbf{x} = d\mathbf{X} + \mathbf{u}(\mathbf{X} + d\mathbf{X}) - (\mathbf{x} - \mathbf{X}) \quad \text{Eq. 4-12}$$

Substituting the displacement (Eq. 4-10) into the right hand side of Eq.4-12,

$$d\mathbf{x} = d\mathbf{X} + \mathbf{u}(\mathbf{X} + d\mathbf{X}) - \mathbf{u}(\mathbf{X}) \quad \text{Eq. 4-13}$$

$$\therefore d\mathbf{x} = (\mathbf{I} + \nabla\mathbf{u}) d\mathbf{X} \quad \text{Eq. 4-14}$$

or

$$d\mathbf{x} = \mathbf{F}d\mathbf{X} \quad \text{Eq. 4-15}$$

where \mathbf{F} is the deformation gradient tensor. To obtain the change of the length (norms) between the points we can dot both sides of Eq.4-15,

$$\|d\mathbf{x}\|^2 = d\mathbf{X} \cdot (\mathbf{F}^T \mathbf{F}) d\mathbf{x} \quad \text{Eq. 4-16}$$

with $\mathbf{C} = \mathbf{F}^T \mathbf{F}$ is defined as the Right Cauchy Green deformation tensor. Expanding \mathbf{C} we obtain;

$$\mathbf{C} = \mathbf{I} + \nabla\mathbf{u} + \nabla\mathbf{u}^T + \nabla\mathbf{u}^T \nabla\mathbf{u} \quad \text{Eq. 4-17}$$

The change in lengths (strains) of the continuum is characterised by the terms $\nabla\mathbf{u} + \nabla\mathbf{u}^T + \nabla\mathbf{u}^T \nabla\mathbf{u}$. The Right Cauchy Green deformation tensor can be written as:

$$\mathbf{C} = \mathbf{I} + 2\boldsymbol{\varepsilon}_{Green} \quad \text{Eq. 4-18}$$

where $\boldsymbol{\varepsilon}_{Green} = \frac{1}{2} (\nabla\mathbf{u} + \nabla\mathbf{u}^T + \nabla\mathbf{u}^T \nabla\mathbf{u})$ is defined as the Lagrangian Green strain tensor.

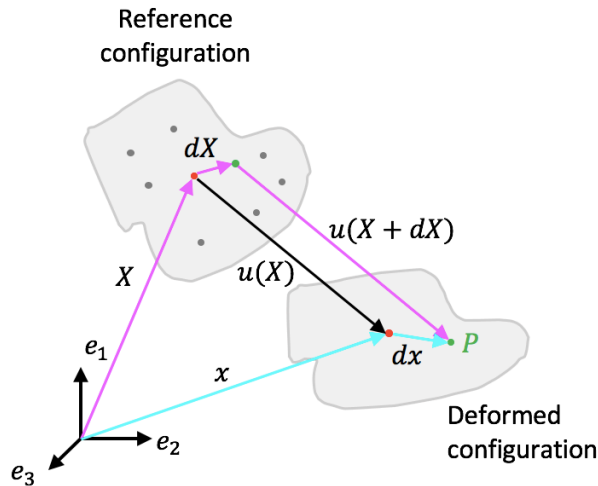


Figure 4-12: Illustration of the paths used to calculate strain between two material points after deformation of the object.

Notice that for small displacements (e.g. stiff material such as cortical bone),

$$\nabla \mathbf{u}^T \nabla \mathbf{u} \ll \nabla \mathbf{u} \therefore \nabla \mathbf{u}^T \nabla \mathbf{u} \cong \mathbf{0} \quad \text{Eq. 4-19}$$

Thus, for small displacements the Green strain tensor can be approximated to:

$$\boldsymbol{\varepsilon}_{Green} \cong \frac{1}{2} (\nabla \mathbf{u} + \nabla \mathbf{u}^T) \quad \text{Eq. 4-20}$$

which is known as the small strain tensor,

$$\boldsymbol{\varepsilon}_{small} = \frac{1}{2} (\nabla \mathbf{u} + \nabla \mathbf{u}^T) \quad \text{Eq. 4-21}$$

or in component form ($i, j = 1..3$),

$$\varepsilon_{ij} = \frac{1}{2} \left(\frac{\partial u_i}{\partial x_j} + \frac{\partial u_j}{\partial x_i} \right) \quad \text{Eq. 4-22}$$

Note that the small strain tensor is symmetric such that its 3x3 matrix is:

$$\boldsymbol{\varepsilon} = \begin{bmatrix} \varepsilon_{11} & \varepsilon_{21} & \varepsilon_{31} \\ \varepsilon_{21} & \varepsilon_{22} & \varepsilon_{32} \\ \varepsilon_{31} & \varepsilon_{32} & \varepsilon_{33} \end{bmatrix} \quad \text{Eq. 4-23}$$

4.2.2 Stress

4.2.2.1 Traction vector

The traction vector (stress vector) \mathbf{t}_n on a surface represents the force acting on the surface with normal vector \mathbf{n} (Figure 4-13). Stress is the internal resistance of a body to an external

force. Stress is commonly denoted by sigma, σ . The stresses acting normal to the surfaces are called normal stresses σ_n . The stresses acting parallel to the surfaces are called shear stresses τ_n . The normal stress scalar is the projection of t_n onto n , thus it can be expressed as:

$$\sigma_n = t_n \cdot n \quad \text{Eq. 4-24}$$

Similarly, the shear stress scalar can be expressed as:

$$\tau_n = \|t_n - \sigma_n n\| \quad \text{Eq. 4-25}$$

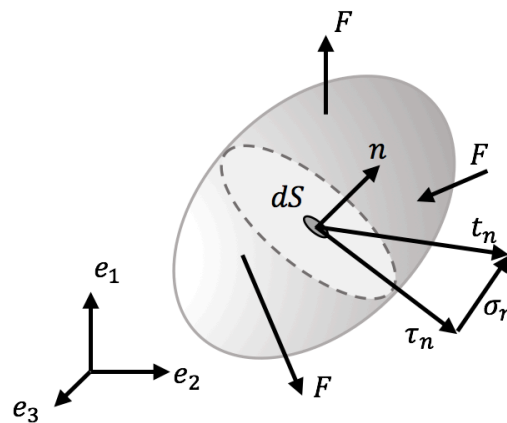


Figure 4-13: Illustration of the traction vector t_n acting on a surface S with normal vector n , of a 3D body under load F .

4.2.2.2 Cauchy Stress tensor

For a three dimensional orthogonal coordinate system e_i , the stress tensors σ_{ij} of a differential volume dV is illustrated in Figure 4-14 below:

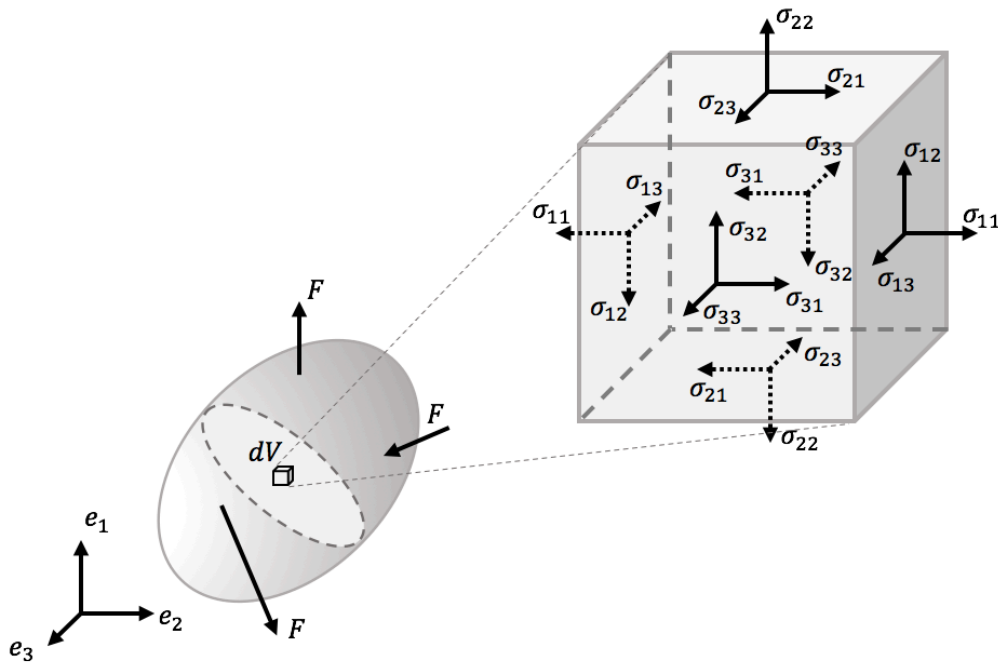


Figure 4-14: Illustration of the stress components on a differential volume.

By applying Newton's equations of motion, the following equation can be derived:

$$t_n = \sigma^T n \quad \text{Eq. 4-26}$$

where σ is a 3x3 matrix called the Cauchy stress tensor,

$$\sigma = \begin{bmatrix} \sigma_{11} & \sigma_{21} & \sigma_{31} \\ \sigma_{12} & \sigma_{22} & \sigma_{32} \\ \sigma_{13} & \sigma_{23} & \sigma_{33} \end{bmatrix} \quad \text{Eq. 4-27}$$

Note that to maintain rotational equilibrium stresses must be equal in magnitude, i.e. $\sigma_{ij} = \sigma_{ji}$. Therefore the stress tensor is symmetric and can be expressed as:

$$\sigma = \begin{bmatrix} \sigma_{11} & \sigma_{21} & \sigma_{31} \\ \sigma_{21} & \sigma_{22} & \sigma_{32} \\ \sigma_{31} & \sigma_{32} & \sigma_{33} \end{bmatrix} \quad \text{Eq. 4-28}$$

4.2.2.3 Equations of equilibrium

Newton's 2nd Law of Motion states that the rate of change of the linear momentum of any object with respect to time is equal to the net force acting on the object:

$$\sum F = \frac{d}{dt}(mv) = m \frac{dv}{dt} = ma \quad \text{Eq. 4-29}$$

where t is time, m is the mass, v is the velocity and a is the acceleration.

Applying it to a differential volume $\Delta x_1 \times \Delta x_2 \times \Delta x_3$, with a density ρ we can obtain the following stress equation of equilibrium:

$$\begin{aligned}\frac{\partial \sigma_{11}}{\partial x_1} + \frac{\partial \sigma_{21}}{\partial x_2} + \frac{\partial \sigma_{31}}{\partial x_3} + \rho b_1 &= \rho a_1 \\ \frac{\partial \sigma_{12}}{\partial x_1} + \frac{\partial \sigma_{22}}{\partial x_2} + \frac{\partial \sigma_{32}}{\partial x_3} + \rho b_2 &= \rho a_2 \\ \frac{\partial \sigma_{13}}{\partial x_1} + \frac{\partial \sigma_{23}}{\partial x_2} + \frac{\partial \sigma_{33}}{\partial x_3} + \rho b_3 &= \rho a_3\end{aligned}\quad \text{Eq. 4-30}$$

or

$$\sum_{j=1}^3 \frac{\partial \sigma_{ji}}{\partial x_j} + \rho b_i = \rho a_i \quad \text{Eq. 4-31}$$

where b_i are the body forces in the i direction and a_i is the acceleration in the i direction.

4.2.2.4 Principle of virtual work

The Principle of Virtual Work is an approximation method which states that a deformable body is in equilibrium when internal virtual strains equate external virtual work:

$$\int \text{real stressess} \times \text{virtual strains} = \text{real forces} \times \text{virtual displacements}$$

Recall the stress equations of equilibrium, for a static body $\mathbf{a} = 0$, the following governing equation can be obtained from Eq.4-31:

$$\sum_{i,j=1}^3 \frac{\partial \sigma_{ji}}{\partial x_j} + \sum_{i=1}^3 \rho b_i = \mathbf{0} \quad \text{Eq. 4-32}$$

Multiplying by virtual displacement \mathbf{u}^* to get:

$$\sum_{i,j=1}^3 \frac{\partial \sigma_{ji}}{\partial x_j} \mathbf{u}_i^* + \sum_{i=1}^3 \rho b_i \mathbf{u}_i^* = \mathbf{0} \quad \text{Eq. 4-33}$$

Using the product rule, the partial derivative $\frac{\partial(\sigma_{ji}u_i^*)}{\partial x_j} = \frac{\partial \sigma_{ji}}{\partial x_j} u_i^* + \sigma_{ji} \left(\frac{\partial u_i^*}{\partial x_j} \right)$, therefore Eq.34-

3 can be written as:

$$\sum_{i,j=1}^3 \left(\frac{\partial(\sigma_{ji}u_i^*)}{\partial x_j} - \sigma_{ji} \left(\frac{\partial u_i^*}{\partial x_j} \right) \right) + \sum_{i=1}^3 \rho b_i \mathbf{u}_i^* = \mathbf{0} \quad \text{Eq. 4-34}$$

Moving $\sigma_{ji} \left(\frac{\partial u_i^*}{\partial x_j} \right)$ to the right hand side,

$$\sum_{i,j=1}^3 \frac{\partial(\sigma_{ji}u_i^*)}{\partial x_j} + \sum_{i=1}^3 \rho b_i \mathbf{u}_i^* = \sum_{i,j=1}^3 \sigma_{ji} \left(\frac{\partial u_i^*}{\partial x_j} \right) \quad \text{Eq. 4-35}$$

Note that the stress is a symmetric tensor, therefore the right hand side term can be expanded to:

$$\sum_{i,j=1}^3 \frac{\partial(\sigma_{ji}u_i^*)}{\partial x_j} + \sum_{i=1}^3 \rho b_i u_i^* = \sum_{i,j=1}^3 \frac{1}{2}(\sigma_{ji} + \sigma_{ij}) \frac{\partial u_i^*}{\partial x_j} \quad \text{Eq. 4-36}$$

and rearranged to:

$$\sum_{i,j=1}^3 \frac{\partial(\sigma_{ji}u_i^*)}{\partial x_j} + \sum_{i=1}^3 \rho b_i u_i^* = \sum_{i,j=1}^3 \sigma_{ji} \frac{1}{2} \left(\frac{\partial u_i^*}{\partial x_j} + \frac{\partial u_j^*}{\partial x_i} \right) \quad \text{Eq. 4-37}$$

Substituting the small strain tensor (Eq.4-22) into the right hand side gives:

$$\sum_{i,j=1}^3 \frac{\partial(\sigma_{ji}u_i^*)}{\partial x_j} + \sum_{i=1}^3 \rho b_i u_i^* = \sum_{i,j=1}^3 \sigma_{ji} \epsilon_{ij}^* \quad \text{Eq. 4-38}$$

Integrating over the domain,

$$\int_V \sum_{i,j=1}^3 \frac{\partial(\sigma_{ji}u_i^*)}{\partial x_j} dV + \int_V \sum_{i=1}^3 \rho b_i u_i^* dV = \int_V \sum_{i,j=1}^3 \sigma_{ji} \epsilon_{ij}^* dV \quad \text{Eq. 4-39}$$

$$\therefore \int_S \sum_{i,j=1}^3 \sigma_{ji} u_i^* \cdot \mathbf{n} dS + \int_V \sum_{i=1}^3 \rho b_i u_i^* dV = \int_V \sum_{i,j=1}^3 \sigma_{ji} \epsilon_{ij}^* dV \quad \text{Eq. 4-40}$$

Rearranging the first term so that it can be written as:

$$\int_S \sum_{i,j=1}^3 \sigma_{ji} \cdot \mathbf{n} u_i^* dS + \int_V \sum_{i=1}^3 \rho b_i u_i^* dV = \int_V \sum_{i,j=1}^3 \sigma_{ji} \epsilon_{ij}^* dV \quad \text{Eq. 4-41}$$

Finally, the traction vector (Eq.4-24) can be substituted into the right hand side and the summation symbols can be dropped for the vectorial multiplications, resulting in:

$$\int_S \mathbf{t}_n \cdot \mathbf{u}^* dS + \int_V \rho \mathbf{b} u^* dV = \int_V \sum_{i,j=1}^3 \sigma_{ji} \epsilon_{ij}^* dV \quad \text{Eq. 4-42}$$

Note that the left hand side of the equation is the external virtual work, composed of the traction vector and body forces. The right hand side of the equation is the internal virtual work.

4.2.2.5 Material Constitutive equations

First, redefine the stress and strain tensors as column vector with six components,

$$\boldsymbol{\sigma} = [\sigma_{11} \ \sigma_{22} \ \sigma_{33} \ \sigma_{21} \ \sigma_{32} \ \sigma_{31}]^T \quad \text{Eq. 4-43}$$

and

$$\boldsymbol{\epsilon} = [\epsilon_{11} \ \epsilon_{22} \ \epsilon_{33} \ 2\epsilon_{21} \ 2\epsilon_{32} \ 2\epsilon_{31}]^T \quad \text{Eq. 4-44}$$

Linear elastic materials obey Hooke's Law; therefore, stress is related to strain by:

$$\sigma = D \varepsilon \quad \text{Eq. 4-45}$$

where D is the elastic stiffness matrix and its inverse D^{-1} is the flexibility, or compliance, matrix.

In this PhD work, bone will be regarded as an isotropic material. For an isotropic material, the flexibility or compliance matrix, D^{-1} is:

$$D^{-1} = \begin{bmatrix} 1/E & -\nu/E & -\nu/E & 0 & 0 & 0 \\ -\nu/E & 1/E & -\nu/E & 0 & 0 & 0 \\ -\nu/E & -\nu/E & 1/E & 0 & 0 & 0 \\ 0 & 0 & 0 & 1/G & 0 & 0 \\ 0 & 0 & 0 & 0 & 1/G & 0 \\ 0 & 0 & 0 & 0 & 0 & 1/G \end{bmatrix} \quad \text{Eq. 4-46}$$

where:

E = Young's modulus

ν = major Poisson's ratio

$G = \frac{1}{2} \frac{E}{1+\nu}$ = shear modulus

By rearranging Eq.4-46 the following equations, referred to as material constitutive equations, can be derived:

$$\varepsilon = D^{-1} \sigma \quad \text{Eq. 4-47}$$

$$\left\{ \begin{array}{l} \varepsilon_{11} = \frac{1}{E} [\sigma_{11} - \nu(\sigma_{22} + \sigma_{33})] \\ \varepsilon_{22} = \frac{1}{E} [\sigma_{22} - \nu(\sigma_{11} + \sigma_{33})] \\ \varepsilon_{33} = \frac{1}{E} [\sigma_{33} - \nu(\sigma_{22} + \sigma_{11})] \end{array} \right\} \quad \text{Eq. 4-48}$$

$$\left\{ \begin{array}{l} \varepsilon_{12} = \frac{\sigma_{21}}{G_{21}} \\ \varepsilon_{32} = \frac{\sigma_{32}}{G_{32}} \\ \varepsilon_{31} = \frac{\sigma_{31}}{G_{31}} \end{array} \right\} \quad \text{Eq. 4-49}$$

4.3 The finite element method

FEM is a numerical technique that uses computation power to calculate approximate solutions to problems that cannot be solved numerically. These problems typically have one or more of the following features: complex geometries, complex material properties, and

complex external conditions. FEM approaches these complex problems by splitting geometries into a number of small elements that are connected together at nodes, forming a mesh. Once discretized, equilibrium requirements are satisfied over a finite number of discrete elements rather than over a continuous body. FE analysis software, such as Ansys, is widely used in all major engineering industries, including biomechanics.

Formulations in FE start with an independent variable (variable assumed to be unknown to start with), which is computed by solving a system of simultaneous algebraic equations. The independent variable, typically displacement for a quasi-static structural analysis, is then used to derive all other variables (i.e. strains and stresses).

4.3.1 Element type and shape functions

Several different element shapes can be used for FEM. The element shape should be suitable to the problem at hand, as well as to the level of approximation and accuracy needed. The commonly used solid elements in 3D problems include tetrahedral and hexahedral shapes. Tetrahedral elements are good for meshing objects with high curvature, such as bones. On the other hand, hexahedral elements perform better numerically due to their shape.

In the FEA we express the approximation of the general displacement at any point inside the element in terms of nodal displacements u_e , which are constants, and shape functions N , which are location dependent:

$$\mathbf{u} = \mathbf{N} \mathbf{u}_e \quad \text{Eq. 4-50}$$

Linear elements are elements with linear shape functions, based on which the displacement between the nodes is approximated. Quadratic elements have an extra node in the middle of each line segment. In quadratic elements the displacement is estimated using quadratic shape functions. Note that higher order elements return a better approximation but at a higher computational cost. Taking into account shape complexities and existing literature on femur modelling, both 10-node tetrahedral and 20-node hexahedral were used in this thesis (Figure 4-15).

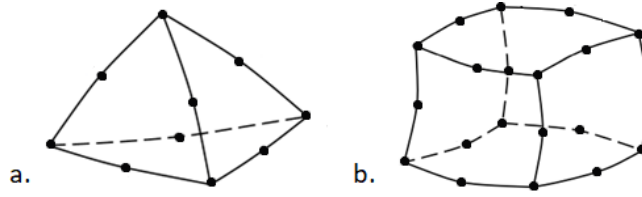


Figure 4-15: Illustration of a 10-node tetrahedral (a) and 20-node hexahedral (b).

4.3.2 Strain and stress vectors in FEA

Recall that from the displacement function we can determine strain (Eq.4-21),

$$\varepsilon = B u_e \quad \text{Eq. 4-51}$$

where $[B]$ is the strain-displacement matrix, based on the element shape functions.

Consequently, we can determine stress from strain using Eq.4-45,

$$\sigma = D B u_e \quad \text{Eq. 4-52}$$

4.3.3 Principle of virtual works in FEA

Knowing the general displacements, strains and stresses in terms of nodal displacement, the Principle of Virtual Work can be applied to FE. Substituting in Eq4-52 Eq.4-51 and Eq.4-50 into Eq.4-42 gives:

$$\int_V (B u_e^* D) (B u_e) dV = \int_S t_n \cdot (u_e^* N^T) dS + \int_V \rho b (u_e^* N^T) dV \quad \text{Eq. 4-53}$$

Factoring out u_e^* gives,

$$\int_V B^T D B dV u_e = \int_S t_n \cdot N^T dS + \int_V \rho b N^T dV \quad \text{Eq. 4-54}$$

This gives an equation of the following form,

$$k_e u_e = f_e \quad \text{Eq. 4-55}$$

Where $[k_e]$ is the element (local) stiffness matrix.

These local stiffness matrices can be used to construct the global stiffness matrix $[K]$ for the entire structure, where n is the total number of elements,

$$K = \sum_{i=1}^n k_{e_i} \quad \text{Eq. 4-56}$$

Once the global stiffness matrix is defined, the global equation is solved to find displacement \mathbf{u} in order to achieve the new equilibrium.

5 FOUR-POINT BENDING TEST ON WHOLE LAMB BONES

5.1 Introduction

Emerging finite element modelling approaches require experimental validation to assess their accuracy. The design of a mechanical test method is dependent on the particularities of the case at hand. In the case of CT-based subject specific lamb femur FE models, the anatomy and material complexities of bone tissue must be given great consideration. The experiments should be well-thought so that orientation, constraints, loads and strains can be accurately identified with a good level of repeatability.

DIC allows the measurement of continuous strain contours over a wide area (typically flat), making it ideal for comparison against FE-predicted strains. This is particularly convenient for studying immature bone, whose material property and mechanical behaviour is not well-known, hence making it difficult to predict the exact location of fracture initiation. To the author's knowledge, there is yet to be an established method for the experimental validation of immature femur FE models.

Experimental testing and 3D-DIC on immature ovine femur differ from that of adult human femur in several ways, particularly in terms of size and shape of the bone, periosteal thickness and fracture behaviour. The aim of this chapter is to design a repeatable mechanical test in order to collect strain data using DIC on immature ovine femoral shaft; which would then be used for CT-based FEM validation (described in Chapter 6). This chapter explores the feasibility and challenges in performing four-point bending tests and DIC concurrently on immature ovine femurs, by observing the load-displacement curve, failure mode and strain distribution.

5.2 Methods

5.2.1 Materials (bones)

A total of five food graded lamb femurs were collected for testing. Ethical approval was waved on the basis that these bones were by-product of food production.

Two lamb femurs, labelled O1001 and O1002, were purchased from a separate Sheffield supermarket, Ozmen. These were pre-cut and picked from a display refrigerator.

Unfortunately, when collected, the bones showed signs of dryness and oxidation and the periosteum presented obvious damage. The origin of O1001 and O1002 was unknown.

Three further lamb femurs, labelled A1003, A1004, D1005 and D1006, were collected from a local butcher in Sheffield called the Beeches of Walkley. All four bones were butchered from the same frozen slaughter leg batch (label attached in Appendix 1). The legs were defrosted and the femurs were removed by the butcher on demand and immediately stored frozen. All four femurs came from a certified UK origin.

In UK, the common practice is to select lambs for slaughter by size rather than by age. Consequently, the exact age of each lamb was unknown. However, the maximum age difference between the three femurs could be estimated, as the lambing season takes place from November to May, with births peaking in the spring. This means these lambs could have a maximum age difference of six months. The sex of each lamb was also not recorded as it is not a standard procedure for food production.

Two of the bones, D1005 and D1006, were used as dummies to practice sample preparation and to test the experimental procedure and set up. Therefore, no DIC result was presented here for these two bones. In addition to D1005 and D1006, a 3D-printed bone was used as a third dummy to adjust the experimental set-up.

Once collected, all bones were separated and wrapped with tissue soaked in a phosphate buffered solution. Each bone was double bagged individually, labelled and stored frozen at -20° degrees, following a standard protocol (Zdero et al. 2017). Table 5-1 provides a summary of the six ovine femurs used in this chapter.

Specimen	Source	Origin	Batch	Limb
O1001	Ozmen	Unknown	n/a	Left
O1002	Ozmen	Unknown	n/a	Left
A1003	Beeches of Walkley	UK	17905219	Left
D1005	Beeches of Walkley	UK	17905219	Right
D1006	Beeches of Walkley	UK	17905219	Left

Table 5-1: List of lamb femur samples used for experimental testing. Samples D1005 and D1006 are underlined as they were used as dummies and no results were presented for either.

The thickness and diameter of each bone (Table 5-2) was measured via CT and computer aided design (CAD) (Figure 5-1).

Specimen	Craniocaudal Diameter [mm]	Thickness [mm]			Radius of curvature [mm]		
		Cranial	Caudal	Average	Cranial	Caudal	Average
O1001	19.4	2.94	2.41	2.68	304	160	232
O1002	19.4	3.00	2.50	2.75	297	208	252
A1003	21.8	2.60	2.23	2.42	223	107	165

Table 5-2: Dimensions of lamb femurs O1001, O1002 and A1003 based on an alignment system described in Chapter 6. The measurements were taken via CAD on CT-based reverse engineered models as shown in Figure 5-1.

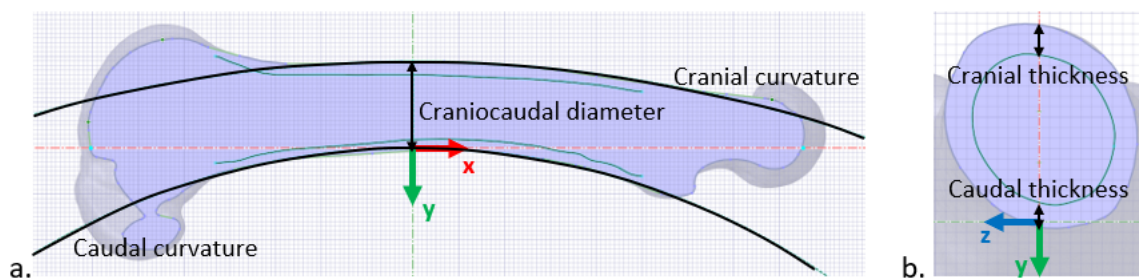


Figure 5-1: CT-based reverse engineered model of lamb femur bone O1001; a. medial view of the sagittal plane showing the craniocaudal diameter; b. transverse cross-section of the mid-section, showing the cranial and caudal cortical thickness.

5.2.2 Sample preparation

The bones were cleaned and painted with speckles in order to perform DIC. The sample preparation procedure; which was practiced on dummies D1005 and D1006, is detailed below.

5.2.2.1 Cleaning and cutting

Each bone was fully defrosted before all soft tissue was carefully removed. The soft tissue was dissected and scraped off from the bone using surgical scalpels, blade no.10 and no.11 (Swan Morton). Particular attention was given in order to remove as much soft tissue as possible from the shaft, without damaging the periosteal sheath (Figure 5-2). Once cleaned, all specimens were wrapped in PBS-soaked cloth and individually double bagged in sealable bags to be stored at -20°C.

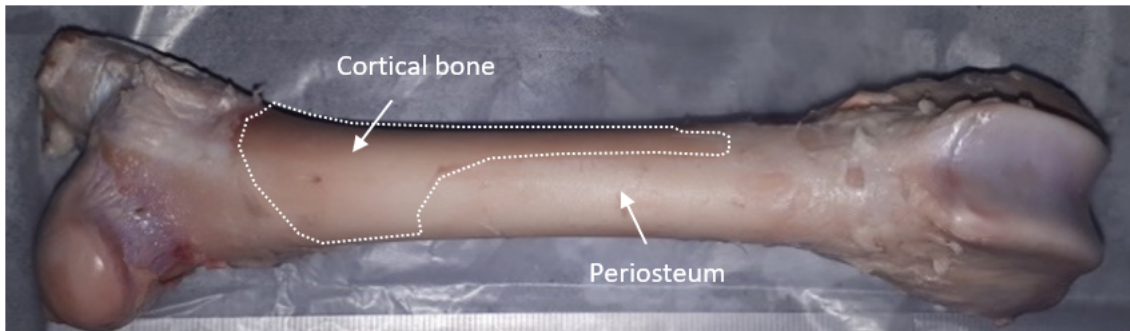


Figure 5-2: Specimen D1005, cranial view of a fresh immature ovine femur bone from the left hind leg. Soft tissue was removed using a scalpel exposing a patch of periosteum on the right-hand side. The periosteum appears as a translucent milky toned membrane and is relatively shimmery. In contrast, the cortical bone surface, which is seen on the left-hand side, appears to be matt.

5.2.2.2 Thawing and painting

The bones were painted just before their individual test. Each bone was left to thaw at room temperature in its sealed bag wrapped in PBS-soaked cloth for at least 3 hours. They were then pat-dried and left to air dry for 5 mins. The shafts were spray painted with thin layers of matt white multi-purpose solvent-based paint (Rust-Oleum: Painter's Touch) until the midshaft surface was uniformly covered. Spray painting was done at room temperature in a spraying booth. The bones were then left to dry again for another 3-5 minutes. Using black acrylic paint (Crafter's Acrylic) and a paint brush with synthetic stiff bristles (Wilko), a speckle pattern was manually created on the white surface by flicking the brush.

5.2.3 Experimental set-up

5.2.3.1 Four-point bending set-up

A 25kN load cell tensile testing machine (Tinius Olsen) was used to perform the four-point bending tests. The specimens were simply supported on two 10mm diameter rods without any constraint. Both the top and bottom rods were levelled and fixed at the same distance for all specimens. The top rods were fixed at 40mm distance; spanning approximately 25% of the total length of each bone), whereas the bottom rods were fixed at 80mm distance; spanning approximately 50% of the total length (Figure 5-3).

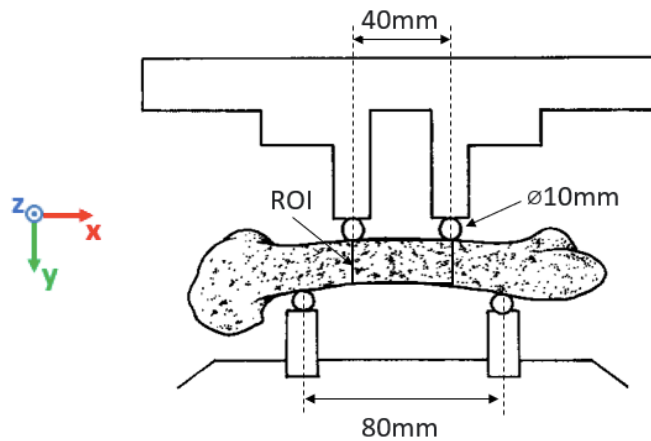


Figure 5-3: Front view of the four-point bending setup: a simply supported bone on 10mm diameter steel rods spanning 80mm, with loaded steel rods on the top, spanning 40mm. The region of interest (ROI) is defined as the surface between the two top rods.

Specimens O1001, O1002 and A1003 were placed as shown in Figure 5-4.

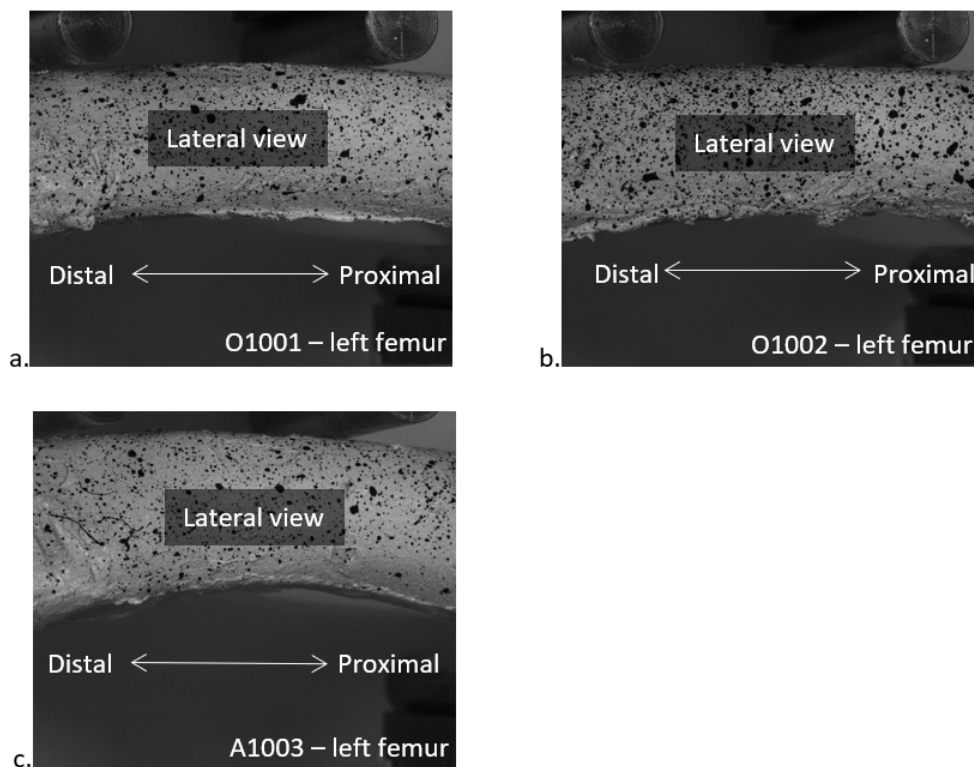


Figure 5-4: Left hand side DIC camera frame of four bones focused on the ROI in the four-point bending set-up; O1001 (a), O1002 (b) and A1003 (c) were placed with the lateral side facing forward, the distal end to the left and the proximal end to the right.

The top rods were lowered until near contact (no pre-load was applied). All specimens were loaded to failure at a constant rate controlled by displacement.

The dummy bones, D1005 and D1006, were tested (without DIC) to gauge the duration of the test until fracture. The displacement rates of the rods were chosen based on the duration of the tests, a suitable acquisition interval (Table 5-3) and the system’s memory capacity for image storage. The displacement rates for each bone are listed in the table below.

Specimen ID	O1001	O1002	A1003
Displacement rate [mm/min]	3	2	3

Table 5-3: Displacement rate of the load cell for the four-point bending test.

5.2.3.2 Stereo system set-up and calibration

The DIC system was set-up using a 3D printed bone (which resembled the actual bone geometry) for spatial reference. Two cameras (Allied Vision: Pike F-505) were secured on a C-beam attached to a tripod. The tripod was positioned 460mm away from the rig and the cameras were placed 240mm apart so that the stereo angle was set at approximately 30°, as shown in Figure 5-5.

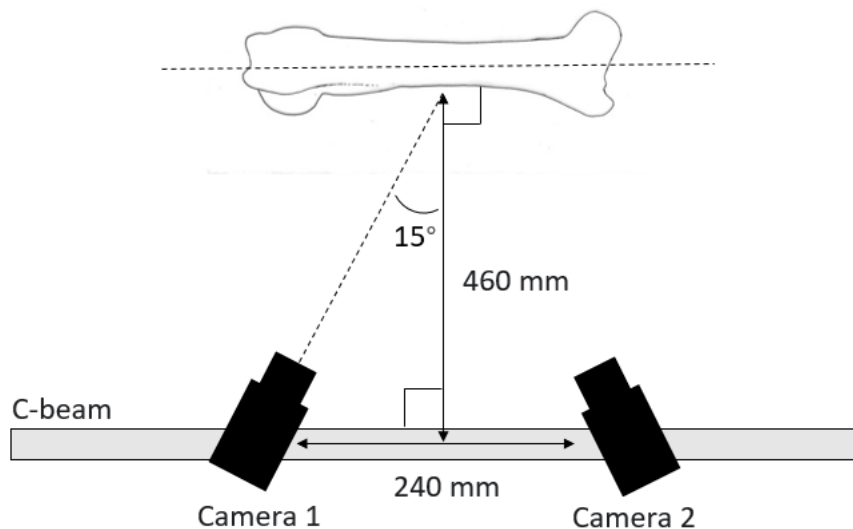


Figure 5-5: Top view of the DIC stereo system showing the cameras placed 460 mm away from the specimen and at a distance of 240 mm from each other, forming a stereo angle of 15°.

The tripod was adjusted so that the cameras were horizontally in-plane with the bone and the C-beam was parallel to the length of the bone. Both cameras were levelled and set to capture the same region of interest (ROI) on the specimen; i.e. the middle region between the two top rods. The cameras were first focused on the general area. Using a crosshead tool (VIC-Snap, Correlated Solutions), they were then finely adjusted onto a single speckle at the

middle of the ROI. Lastly, using a closed aperture (narrow DoF), the cameras were re-focused onto that same middle speckle (Figure 5-6). The final stereo angle and positioning of the cameras was obtained through calibration of the system as described below.

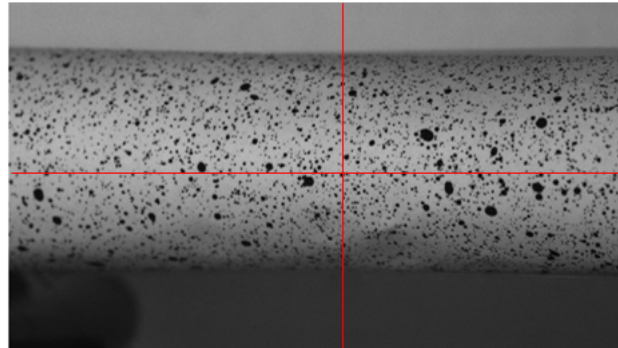


Figure 5-6: Image of the 3D printed bone taken through Camera 2 (right hand side) of the DIC system. The camera is focused onto a single speckle chosen at the middle of the ROI, located using the cross-head tool (red) in VIC-Snap.

In order to calibrate the DIC system, the dummy bone was taken off the testing machine. The system was calibrated using a 12x8x2.5mm calibration plate. Sixty images of the calibration plate were taken by rotating and translating the plate in all directions. The system was calibrated using the calibration tool in VIC 3D with a standard deviation below 0.3 pixels. The calibration data of each camera is listed in the table below:

Camera	Centre [pxls]		Focal length [pxls]		Magnitude [pxls/mm]		
	x	y	x	y	Average	Minimum	Maximum
1	1215	1058	16934	16934	45	44	47
2	1220	1029	16900	16900	45	44	46

Table 5-4: Calibration data for the stereo system (Figure 5-5). This calibration data was used for all the image correlation in this chapter.

5.2.3.3 Lighting, aperture and shutter speed

The cameras and the system set-up were optimised to obtain sharp images with good contrast over the ROI on the 3D printed bone. The images were taken in a dim room in order to minimise surrounding light. Two studio lamps with 28W 5000K-5500K bulbs were placed at an angle above the cameras and pointed towards the bone in order to avoid any light distortion on the ROI. A white background was placed behind the bone during testing (Figure 5-7).



Figure 5-7: Picture of the DIC set-up used in this chapter showing two studio lamps placed above the cameras and pointing towards the testing rig.

In order to ensure that the whole ROI was in focus, i.e. that the DoF was large enough to cover the depth of the ROI, the shutter speed was set to the maximum and the aperture was slowly decreased on each camera until there was no over exposure and that the uncertainty interval calculated by the DIC software was lowest on the largest possible area of the ROI (Zdero et al. 2017).

It is worth noting that for a given aperture and a given shutter speed, the cameras were returning images with significantly different exposure even though the lighting and positioning was approximately symmetrical (Figure 5-8). Hence, the aperture was not the same for cameras 1 and 2.

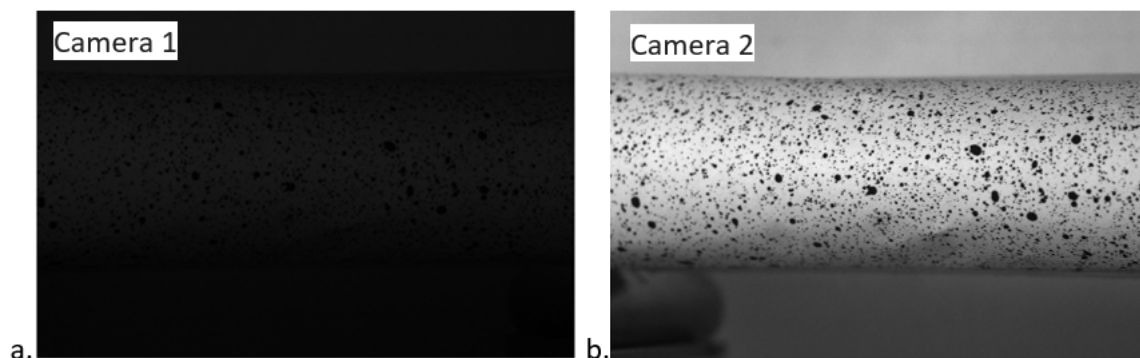


Figure 5-8: Captures of the 3D printed bone through cameras 1 (a) and 2 (b) of the DIC stereo system. Both images were taken with the same shutter speed and aperture (15ms and f/8 respectively), however the exposure in the two images are very different.

Once optimised on the 3D-printed bone, the aperture of each camera (f/6.8 and f/8 for cameras 1 and 2, respectively) was kept fixed for the rest of the bones tested. The shutter

speed on the other hand, was regulated to avoid over exposure for each individual specimen (Figure 5-9).

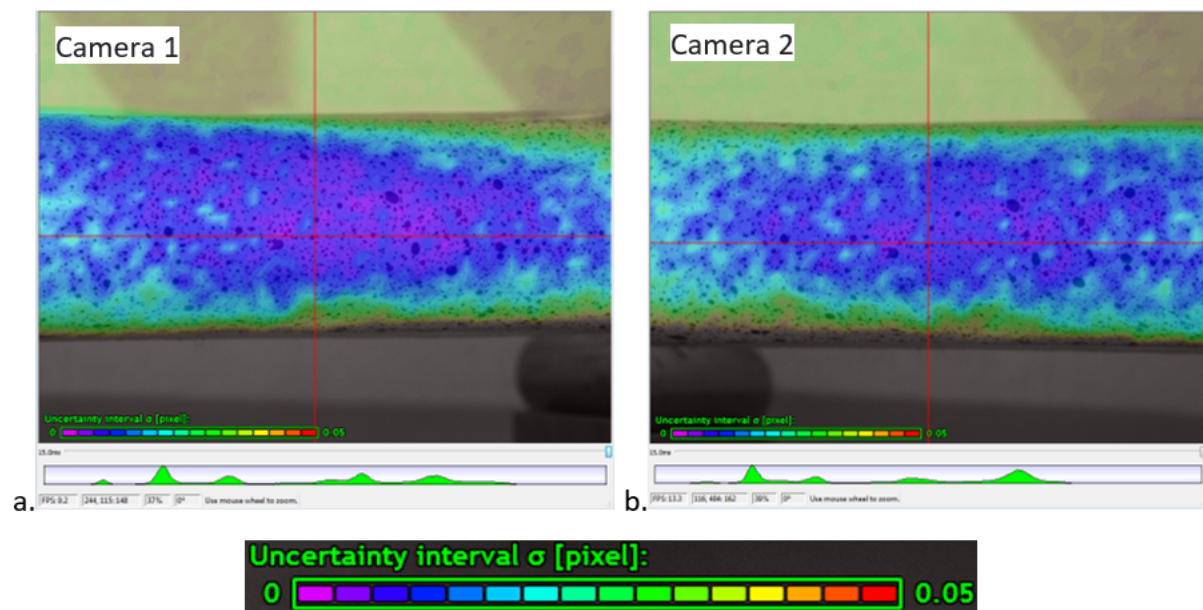


Figure 5-9: Image optimisation for correlation using VIC-Snap on the 3D printed bone. The colour map corresponds to the software calculated uncertainty interval over the captured image; (a) image taken with camera 1 (LHS of the stereo system) with an aperture of f/6.8; (b) image taken with camera 2 (RHS of the stereo system) with an aperture of f/8. The green histogram shows the intensity distribution.

5.2.4 Force-displacement data processing

The testing machine and the cameras were started off manually and separately; i.e. no automatic start. Images were taken at regular intervals during the tests. The DIC images and the force displacement data were correlated during postprocessing by matching the start time of the tensile machine to the first DIC image in which the rods moved. Therefore, the maximum discrepancy between the DIC data and the Tinius data was assumed to be a single acquisition interval as shown in Table 5-5.

Specimen ID	O1001	O1002	A1003
Acquisition interval [ms]	400	400	600

Table 5-5: DIC image acquisition intervals for each test.

The force and displacement data of the load cell were recorded with time. The raw force was plotted against displacement. Once plotted, the pre-contact, compliance and linear phases were visually identified and compared against uncorrelated images of critical events.

Regular intervals across the force-displacement graphs were identified and compared to the captured images. Similarly, critical events (e.g. fracture) visible in the footage were located on the force-displacement plots.

5.2.5 Digital image processing

The raw force-displacement plots were corrected for pre-contact. Linear fits (or straight lines) were plotted over each curve in order to identify the linear regions. A point was selected manually at the end of each linear fit. DIC was performed on the frames corresponding to each point with the software *VIC-3D Release 8* (Correlated Solutions Inc., Columbia, SC). The same points were later on simulated using a CT-based FE modelling approach, and compared against the DIC results in Chapter 6.

Since the deformation analysed was in the linear region, i.e. small deformations, the engineering strain was selected as the output strain. Both longitudinal and transverse surface strains (in the x and y direction, see section 3.2.1.5) and principal surface strain maps were generated.

To perform DIC, two important parameters had to be selected to optimise the spatial resolution, the subset size and the step size. The methodology used to select the subset and step size for the image correlation is detailed below.

5.2.5.1 Speckle analysis for subset size

A smaller subset size returns a better spatial resolution. However, in order to be correlatable, a subset must be large enough to contain a recognisable grey pattern; the rule of thumb being a minimum of three speckles within a subset. An image analysis was carried out with an image processing program, ImageJ, to select the smallest suitable subset size for each bone. A systematic iterative method was used to determine the most appropriate subset size for each bone looking at both speckle pattern and surface irregularity.

Using ImageJ, the image was thresholded for the speckles (Figure 5-10). An area of interest (AOI) between the two top rods was selected and the speckles were measured and outlined using the *Analyse Particles* tool. The dimension of each speckle was defined by its bounding rectangle.

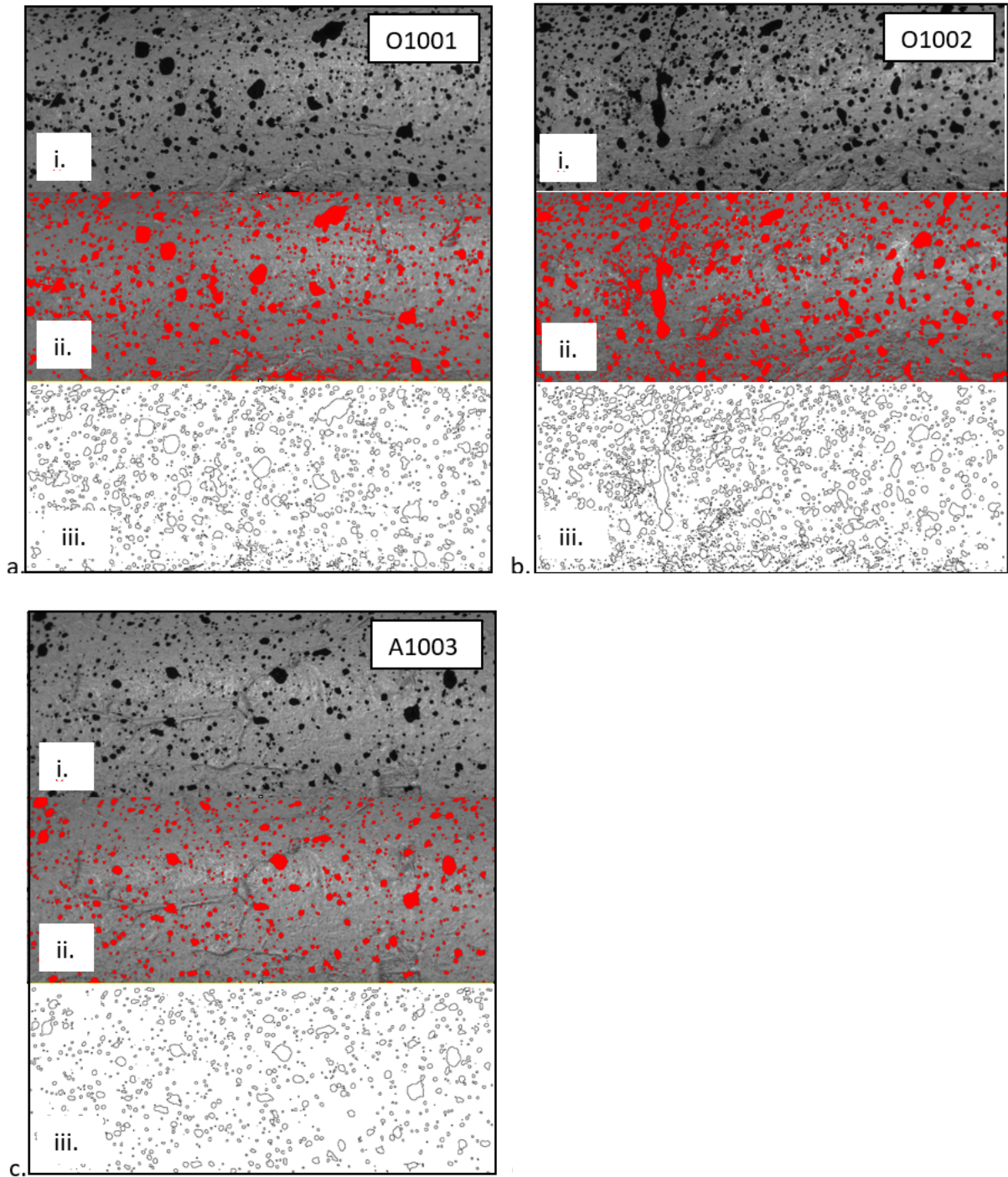


Figure 5-10: Bones O1001 (a), O1002 (b), A1003 (c). (i) Raw image of the speckled AOI obtained through camera 2 (right side) of the stereo system. (ii) Thresholded image differentiating the speckles (red) from the background. (iii) Processed image with outline of the speckles identified through thresholding.

	Mean [pxls]		SD [pxls]		Min [pxls]		Max [pxls]	
	Width	Height	Width	Height	Width	Height	Width	Height
O1001	9.61	9.23	9.58	8.87	2	2	132	99
O1002	7.33	7.22	8.69	10.88	1	1	109	318
A1003	8.79	8.35	7.60	6.97	1	1	62	64

Table 5-6: Data from the speckle size analysis listing the mean, minimum and maximum speckle size of each bone over the AOI.

For each bone, a convergence study was carried out plotting subset size against the change in correlated area. This was performed to maximise the correlatable area at a constant step to subset size ratio. The step size was chosen to be approximately one third of the subset size as per the user manual of VIC-3D for each iteration. The starting subset size for convergence was set as three times the mean speckle size. The image correlation was performed in the software VIC-3D, and the correlated area was measured using MATLAB (Figure 5-11).

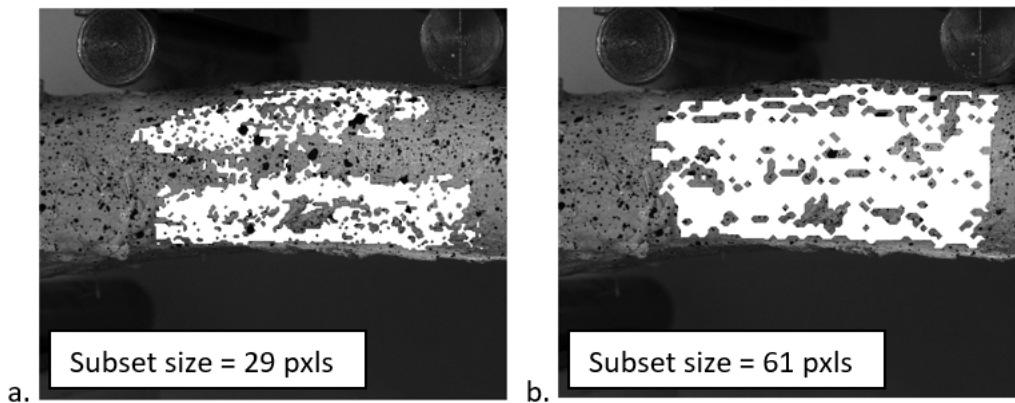


Figure 5-11: Change in correlatable area (white) on DIC images of bone O1001 with a subset size of 29 pixels (a) and 61 pixels (b), both performed with a step size approximately equal to one-third of the subset size.

For bones O1001, O1002, the maximum correlatable area was obtained with a subset size of 61 pixels. For bone A1003 the maximum correlatable area was obtained with subset sizes of 55 pixels.

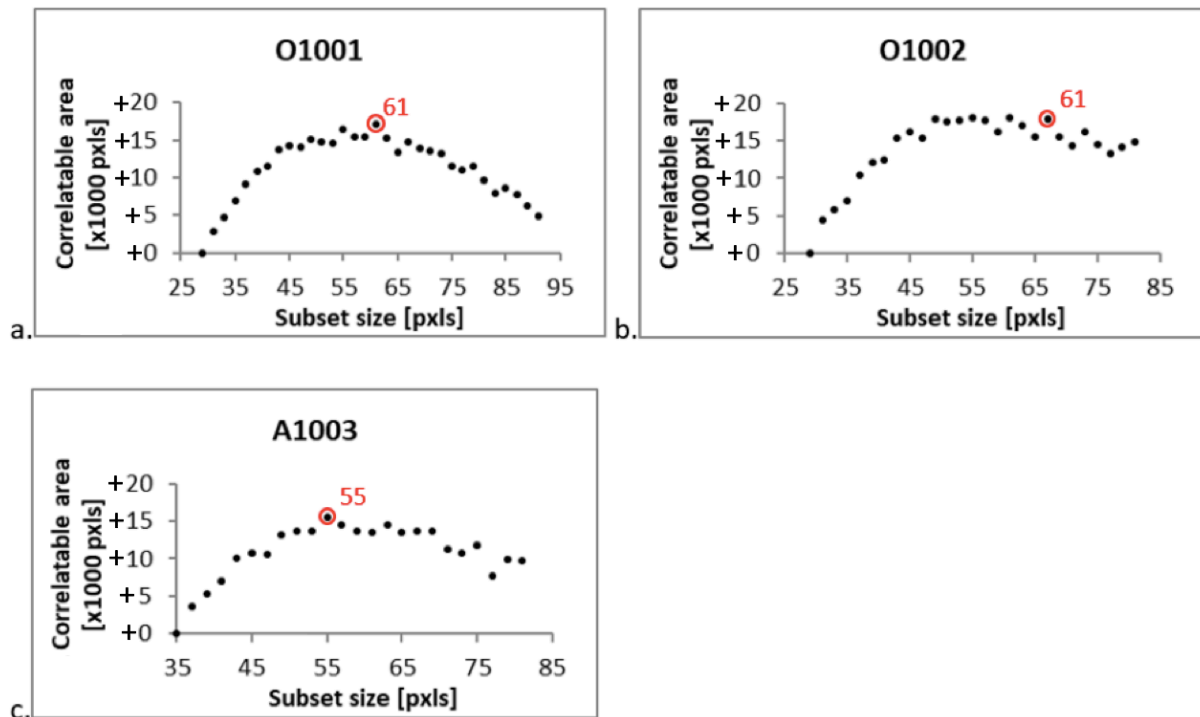


Figure 5-12: Plot of the increase in correlatable area over the AOI against the subset size used for the correlation, in which the step size is approximately one-third of the subset size for each iteration.

5.2.5.2 Step size and filter size

The step size has a greater impact on the spatial resolution compared to the subset size, with a finer step size yielding a better spatial resolution. A smaller step size (i.e. more data points) also enables better correlation at the boundaries; which translates into a larger data area. However, a very small step size would risk an increase in self-correlating errors (Chapter 3). The VIC-3D software manual recommends using a step to subset size ratio of at least 1/3 to avoid significant errors building up.

If needed, errors incurring from self-correlation can be smoothed using either a Gaussian or box filter in VIC 3D. This allows the user to get smooth DIC images and increase the AOI coverage with a smaller step size. Filtering must be applied with care as the process can impact the accuracy of the results.

In this chapter, two sets of strain images were generated for each bone. First, a set of images was generated with a 1/3 step to subset size ratio (as recommended by the software); these images were used as a sanity check (Appendix 2). Second, a set of images was generated with a 1/6 step to subset size ratio to achieve a large AOI coverage, these are later presented in

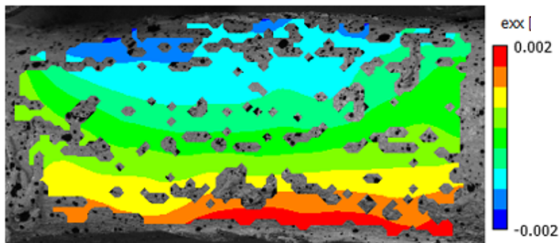
the results section. The subset sizes (established above) and the corresponding step sizes are listed in the table below (Table 5-7).

	O1001	O1002	A1003
Subset size [pxls]	61	61	55
Step size ($\approx 1/6$) [pxls]	10	10	9
Step size ($\approx 1/3$) [pxls]	20	20	18

Table 5-7: Optimal subset size for DIC determined from the previous section. The subset size selected returns the largest correlatable area over the AOI of each bone.

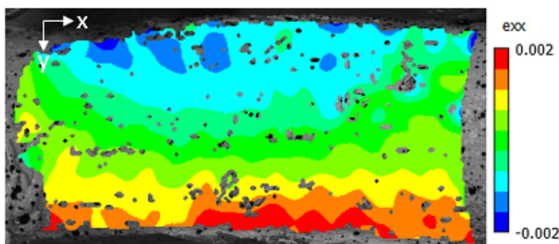
The first set of strain image was obtained with a 1/3 step to subset size ratio and a default Gaussian smoothing filter of 15 pixels (Figure 5-13.a). The second set was obtained with a 1/6 step to subset size ratio and a default Gaussian filter of 15pxls (Figure 5-13.b.i). A further 31pxls box filter was applied to the second set to smooth out strain concentrations arising from self-correlation (Figure 5-13.b.ii). An example of the correlated area is given below to show the effect of step size and filtering.

a. 1/3 step to subset size ratio – image for sanity check

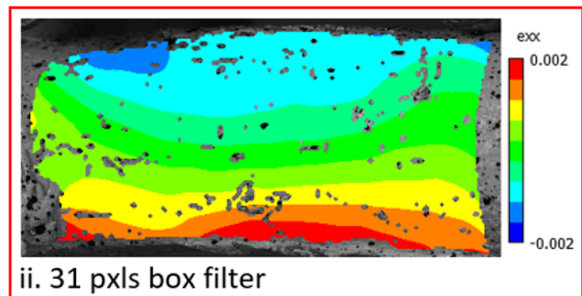


No box filter

b. 1/6 step to subset size ratio – result image



i. No box filter



ii. 31 pxls box filter

Figure 5-13: The image was correlated with a subset size of 61pxls and the strain was calculated with a default Gaussian filter of 15pxls; first using a step size of 20pxls (a), then using a step size of 10pxls (b.i) and a box smoothing factor of 31pxls (b.ii).

5.3 Results

The results section is split into two parts. The first part is an account of the main events that occurred during each test. These are shown on raw (i.e. uncorrelated) images and located on the raw force-displacement plots. The second part presents force-displacement plots corrected for pre-contact, as well as correlated images with surface strain maps on frames corresponding to the end of the linear regions on each plot.

5.3.1 Part one: critical experimental events

5.3.1.1 Bone O1001

The test on specimen O1001 did not progress as a typical four point bending test as the load was not applied simultaneously on the bone. The top left rod was the first to make contact with the bone at $t = 4s$, followed by the top right rod at $t = 8.4s$ (i.e. there was an estimated displacement of 0.22mm between the contact of the right and the top left rod). At $t = 27s$, the left rod started to indent into the bone. It reached a maximum load capacity of 3.30kN at $t = 87.7s$ followed by an “explosive” complete transverse fracture and a linear fracture along the long axis on the lateral side of the bone (Figure 5-14). The periosteum rupture was clean and followed the line of the bone fracture.



Figure 5-14: Fracture frame of bone O1001 showing a complete transverse fracture and a linear fracture across the shaft of the bone on the lateral side.

The raw force-displacement curve for bone O1001 showed a pre-contact phase (A), followed by a compliance phase (B). The force then increased linearly (C & E) with a saddle point at $t = 27\text{s}$ (D), and finally plateaued (F) before failure (Figure 5-15).

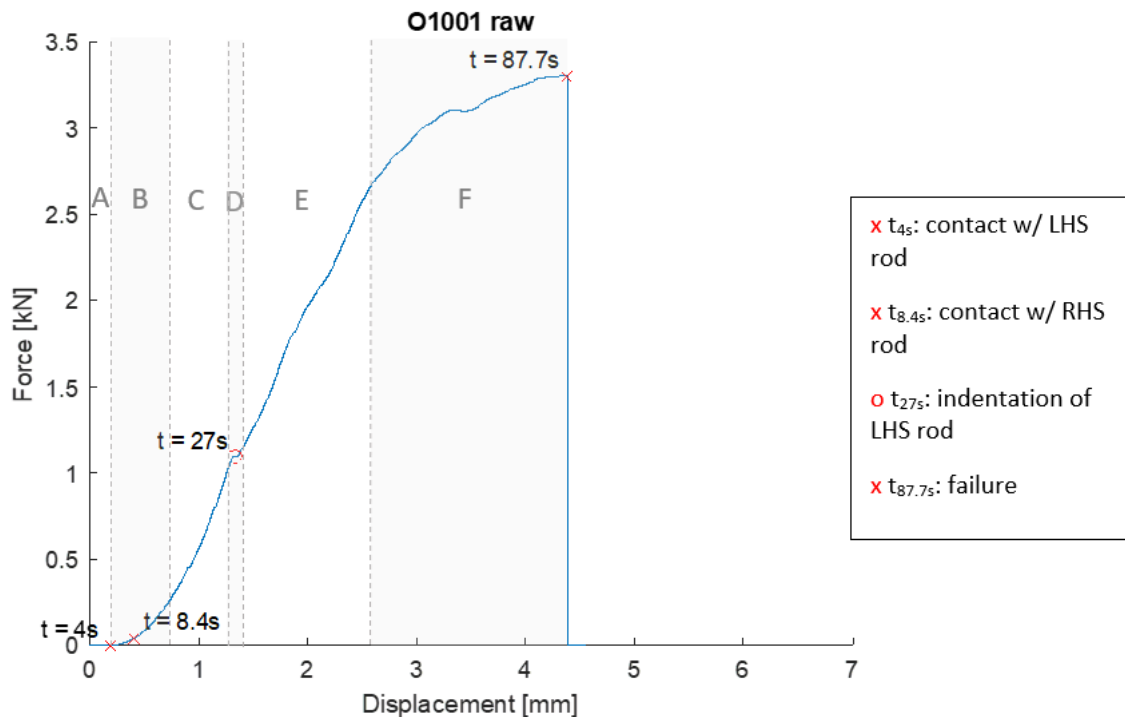


Figure 5-15: Raw force displacement graph of bone O1001 under four-point bending conditions. The crossed points represent critical events. The circled point represents the beginning of local failure under the top left rod. The graph is divided into six zones; A: pre-contact, B: compliance, C: linear phase, D: local failure, E: linear phase, F: failure.

5.3.1.2 Bone O1002

Similarly, during the bending test of bone O1002, the top right rod and top left rod made contact with the bone successively at $t = 5\text{s}$ and at $t = 9\text{s}$, respectively (i.e. there was an estimated displacement of 0.13mm between the contact of the right rod and the left rod). At $t = 33\text{s}$, the left rod started to indent into the bone. A comminute fracture initiated at $t = 126\text{s}$ and can be seen as an oblique fracture pattern under the left rod (Figure 5-16). The fracture propagated along the bone until complete failure at $t = 176\text{s}$. The periosteum did not rupture until $t = 156\text{s}$.

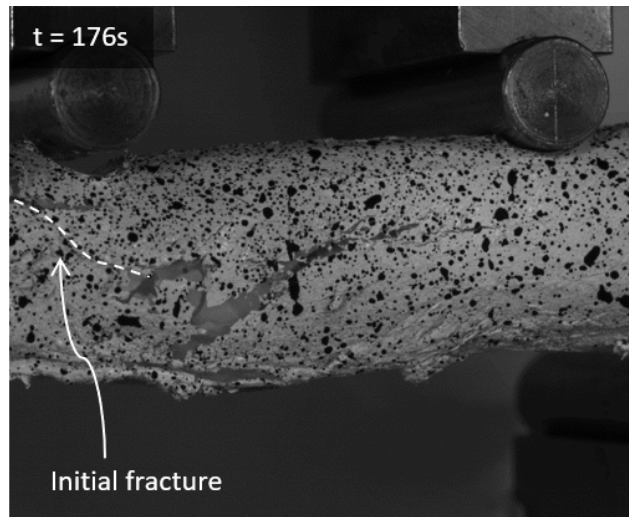


Figure 5-16: Complete failure frame of bone O1002 under four-point bending conditions. The frame was taken at time $t = 176s$.

Similar to bone O1001, the raw force-displacement for bone O1002 begins with a pre-contact phase (A) followed by a compliance phase (B). The force increased linearly (C & E) with a turning point at $t = 33s$ (D). In region F, the curve plateaued and dropped abruptly at 3mm displacement indicating a fracture before reaching a maximum load at $t = 126s$. Finally, the force gradually dropped until complete failure (Figure 5-17).

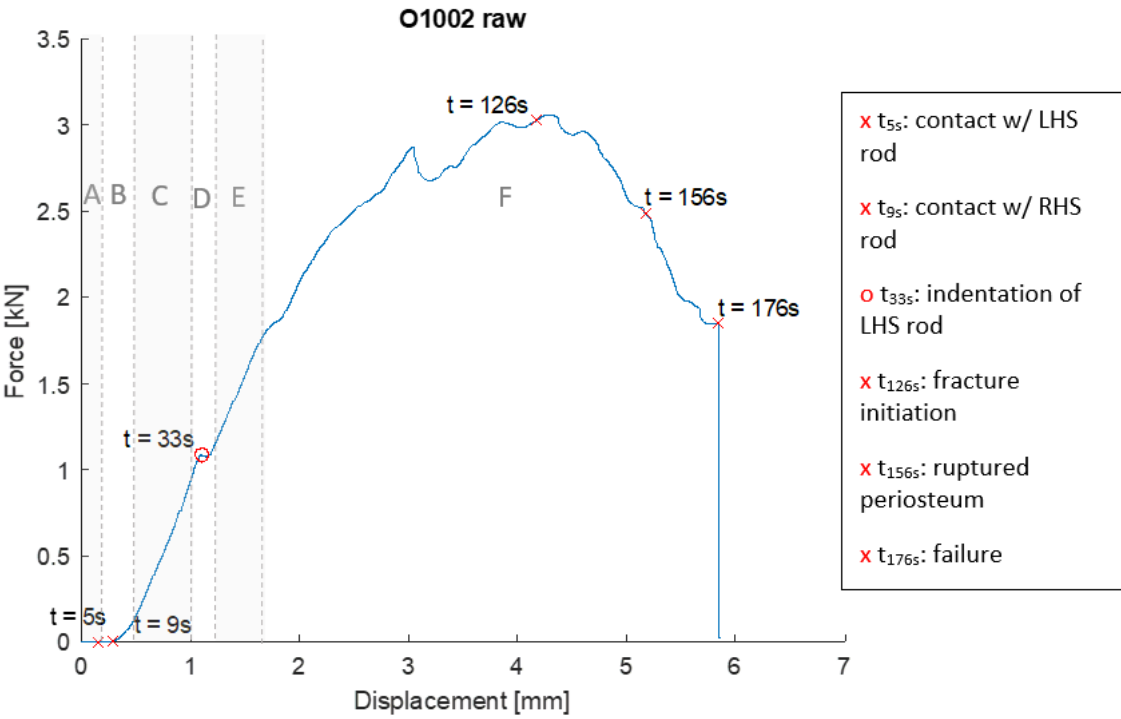


Figure 5-17: Raw force-displacement graph of bone O1002 under four-point bending conditions. The crossed points represent critical events. The circled point represents the beginning of local failure under the top left

rod. The graph is divided into six zones; A: pre-contact, B: compliance, C: linear phase, D: local failure, E: linear phase, F: failure.

5.3.1.3 Bone A1003

Similar to the other two bones, the top rods did not make contact with the bone simultaneously during the test for A1003. The load was first applied on the bone through the top left rod, which made contact with the bone at $t = 11.3s$. At $t = 41s$, the left rod started to indent into the bone. This initiated visible rigid body motion which carried on until the top right rod made contact with the bone at $t = 56.4s$, as shown in Figure 5-18. There was an estimated displacement of 2.25mm between the time of contact of the right rod and the left rod.

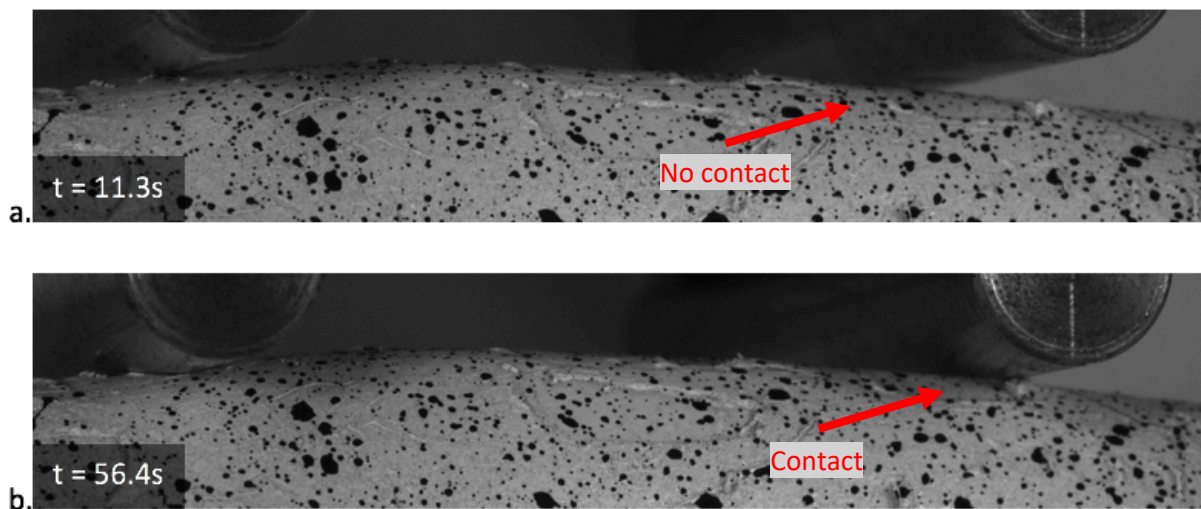


Figure 5-18: Frames showing top rods in contact with bone A1003. (a) Left rod at time $t = 11s$. (b) Right rod at time $t = 56s$.

The bone reached a maximum load capacity of 2.93kN at $t = 126s$. This was followed by the first visible fracture which appeared under the top left rod. The periosteum did not rupture at the first fracture; the fracture was only visible because of a change in exposure along the fracture site (Figure 5-19).

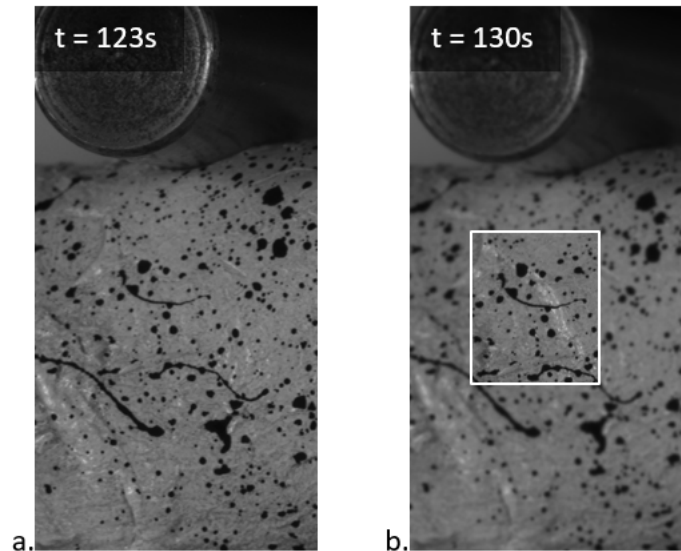


Figure 5-19: Frames showing fracture initiation of bone A1003 under the left rod. (a) Pre-fracture, (b) fracture line detected at time $t = 130s$.

The final fracture which led to the complete failure of bone A1003 occurred at $t = 137s$. The fracture presented as an open oblique fracture under the top right rod (Figure 5-20). The rupture of the periosteum did not coincide with the orientation of the final fracture.

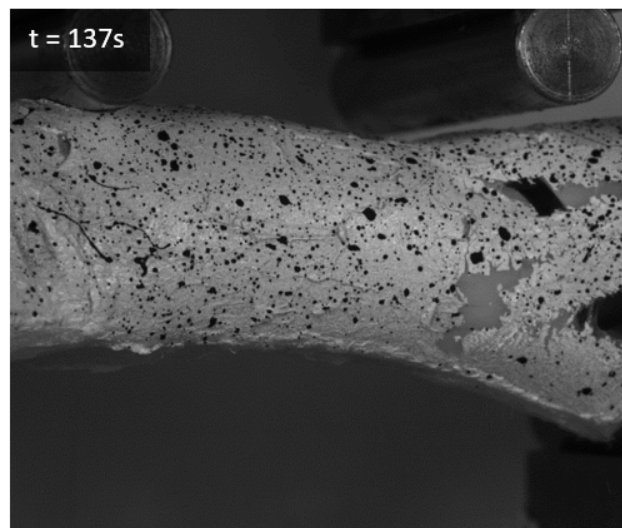


Figure 5-20: Complete failure frame of bone A1003 under four-point bending conditions. The frame was taken at time $t = 137s$.

The raw force-displacement plot in Figure 5-21 shows a pre-contact phase (A) followed by a compliance phase (B). Then, the force increased linearly (regions C & E) with two turning points (D), and gradually plateaued before failure (F) (Figure 5-21).

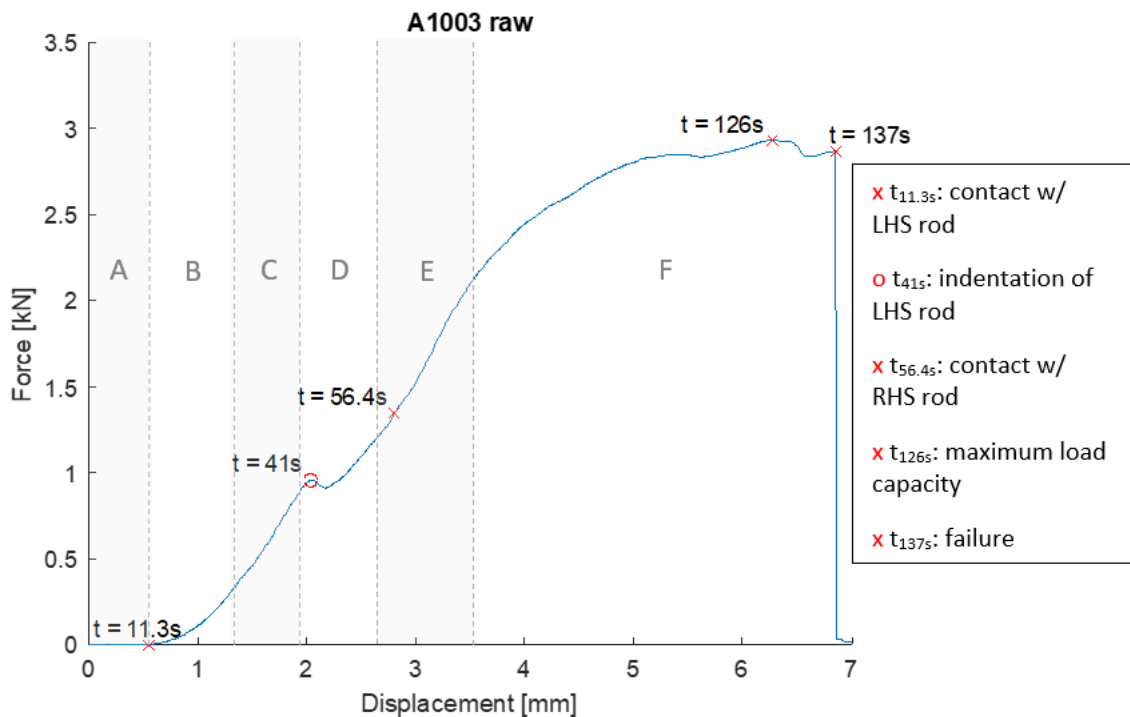


Figure 5-21: Raw force-displacement graph of bone A1003 under four-point bending conditions. The crossed points represent critical events. The circled point represents the beginning of local failure under the top left rod. The graph is divided into six zones; A: pre-contact, B: compliance, C: linear phase, D: local failure, E: linear phase, F: failure.

5.3.2 Part two: force-displacement plots and DIC surface strain contours

5.3.2.1 Projection error and floor noise

Image correlation was performed in static frames before each bone was tested. The table below gives the maximum noise for engineering strains, along with the stereo system projection error.

	Projection error [pixel]	exx strain		eyy strain		e1 strain		e2 strain	
O1001	14.138	-0.0004	0.0004	-0.0005	0.0005	-0.0001	0.0005	-0.0008	0.0002
O1002	14.127	-0.0002	0.0002	-0.0005	0.0005	-0.0001	0.0005	-0.0005	0.0001
A1003	0.061	-0.0004	0.0004	-0.0008	0.0005	0.00002	0.0009	-0.0008	0.0001

Table 5-8: DIC projection error with minimum and maximum values for engineering strains on static images, corresponding to the floor noise for each bone.

The projection error of bones O1001 and O1002 was high. This was not deemed important as the two bones' ROI did not appear to be displaced out-of-plane during testing, but should still

be taken into consideration. As the focus and the aperture were not disturbed, the projection error must have arisen from the set up being bumped, and/or the cameras being slightly moved. This could have had an impact on the measured displacements.

For all the bones, the floor noise was distributed along the edges. The noise frames of bone O1001 is given below to show an example of the noise distribution (Figure 5-22).

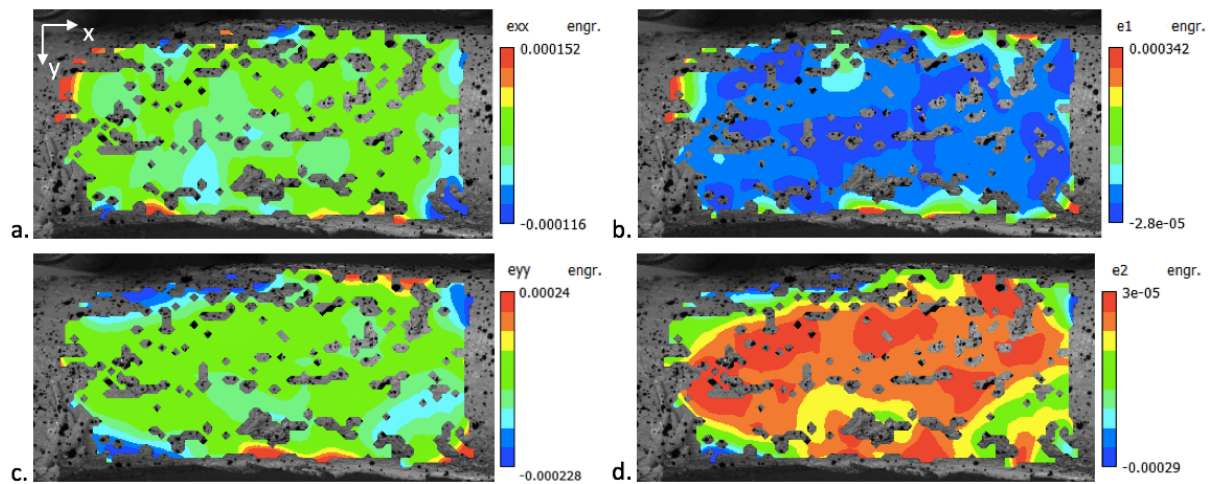


Figure 5-22: Floor noise captured on static frames of bone O1001. (a) Engineering plane strains in the x-direction. (b) First principal plane strain (tension). (c) Engineering plane strains in the y-direction. (d) Second principal plane strains (compression).

5.3.2.2 Force-displacement plots

Below are the four force-displacement plots corrected for pre-loading. Linear fits (LF) are plotted over the curves and the point at the end of each linear region is also highlighted on the curves (Figure 5-23).

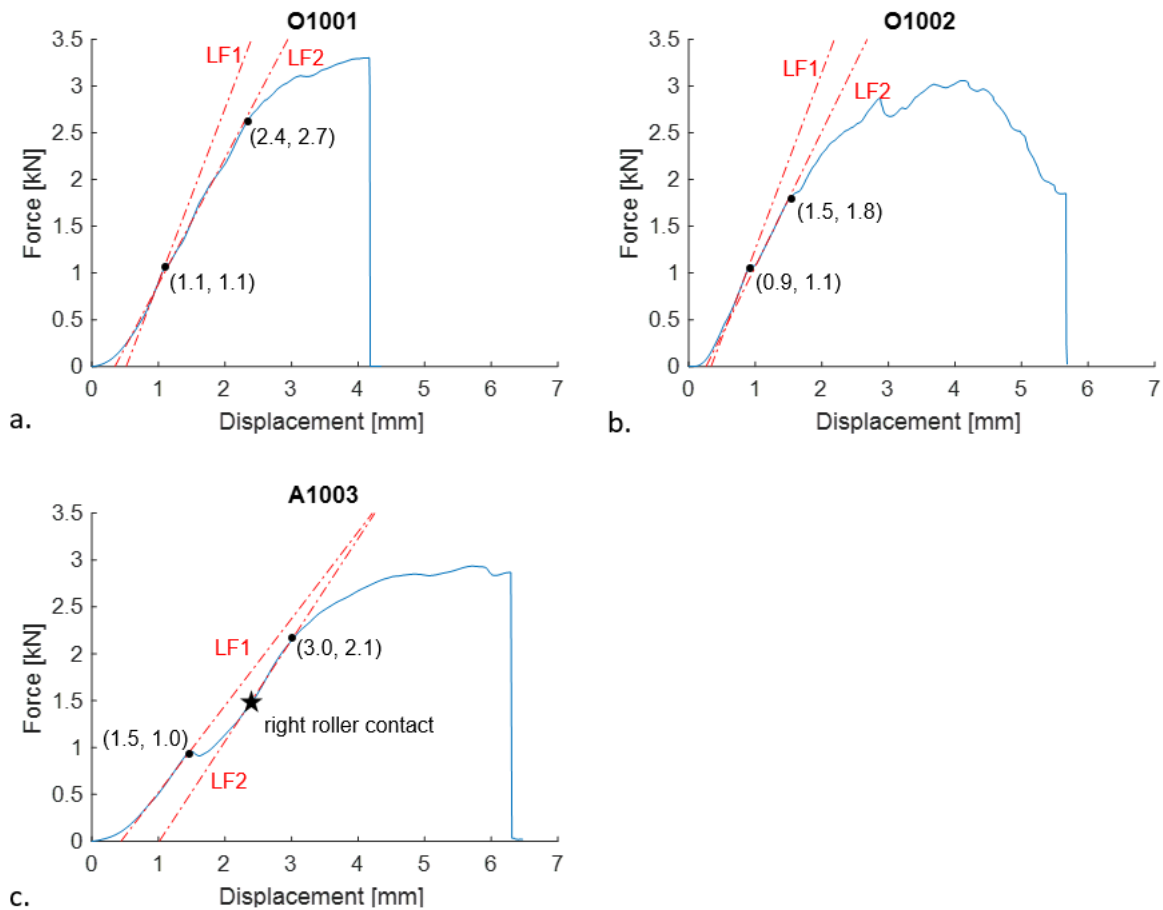


Figure 5-23: Force displacement plots corrected for pre-loading of bones under four-point bending. The dashed lines are linear fits (LF) of the linear regions of each bone. The two points given in each curve mark the end of each linear region.

The slopes and intercepts of the linear fit equations (in the form of Eq.5-1) is given in the table below.

$$Force = a \times Displacement + b \quad \text{Eq.5-1}$$

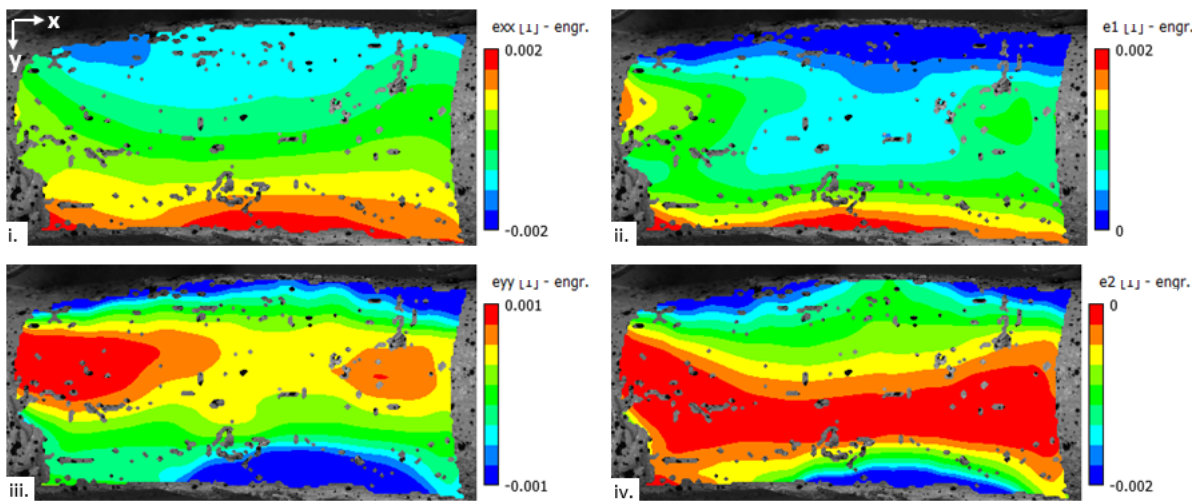
	Linear fit 1 (LF1)		Linear fit 2 (LF2)	
	Slope	Intercept	Slope	Intercept
	a [N/m]	b [kN]	a [N/m]	b [kN]
O1001	1.86	-0.96	1.35	-0.47
O1002	1.89	-0.63	1.45	-0.38
A1003	0.93	-0.41	1.08	-1.09

Table 5-9: Table of the slop and intercept of the linear fit for each bone.

5.3.2.3 Surface strain maps

This section presents the resulting surface strain contours obtained through DIC of each bone at the end of their respective linear regions as shown in the force displacement plots in the previous section (Figure 5-24 to Figure 5-26). Overall, the strain distributions for O1001, O1002, A1003 are similar at the end of each corresponding linear regions, with some differences in peak values. Due to the two top rods come into contact with the bone at different time points of the experiment, it can be seen that the strain distribution is sometimes asymmetrical (between left and right) and higher strain is experienced on one side of the ROI compared to the other.

a. O1001 – LF1 – (1.1mm, 1.1kN)



b. O1001 – LF2 – (2.4mm, 2.7kN)

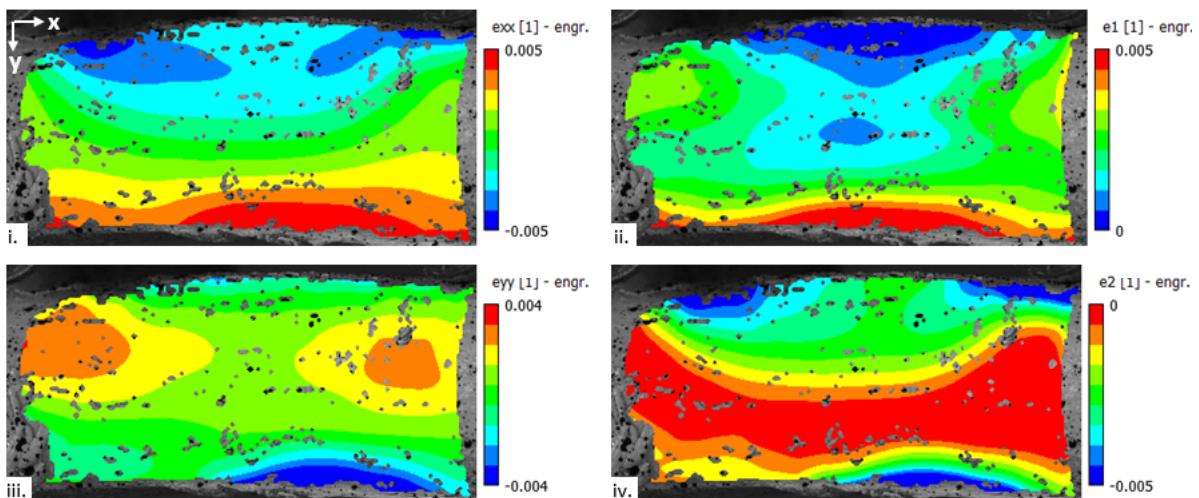
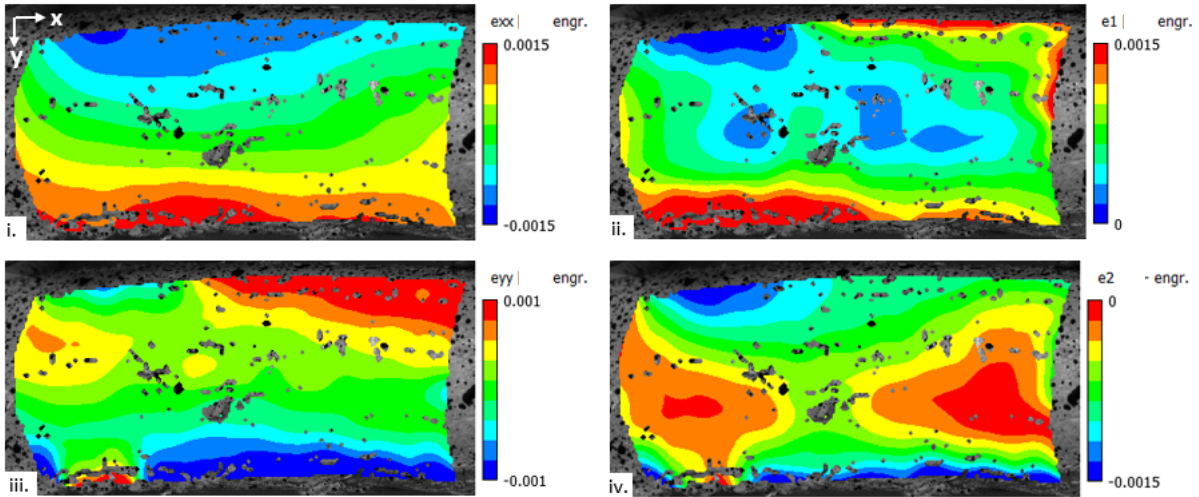


Figure 5-24: Surface strains of bone O1001 under four-point bending obtained through DIC at the end of the first linear region, LF1 (a), and second linear region, LF2 (b). (i) Engineering plane strains in the x-direction.

(ii) First principal plane strain (tension). (iii) Engineering plane strains in the y-direction. (iv) Second principal plane strains (compression).

a.O1002 – LF1 – (0.9mm, 1.1kN)



b.O1002 – LF2 – (1.5mm, 1.8kN)

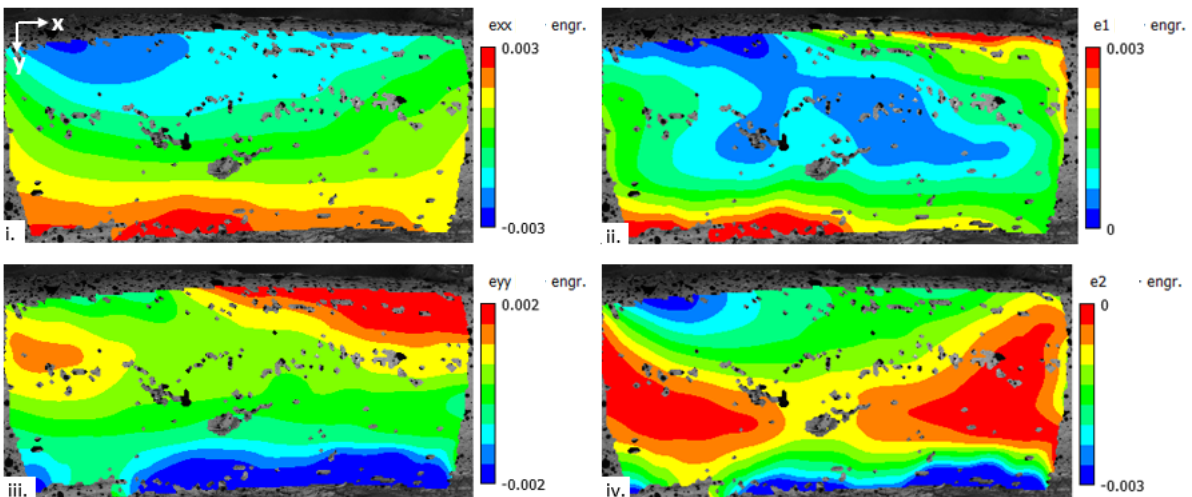
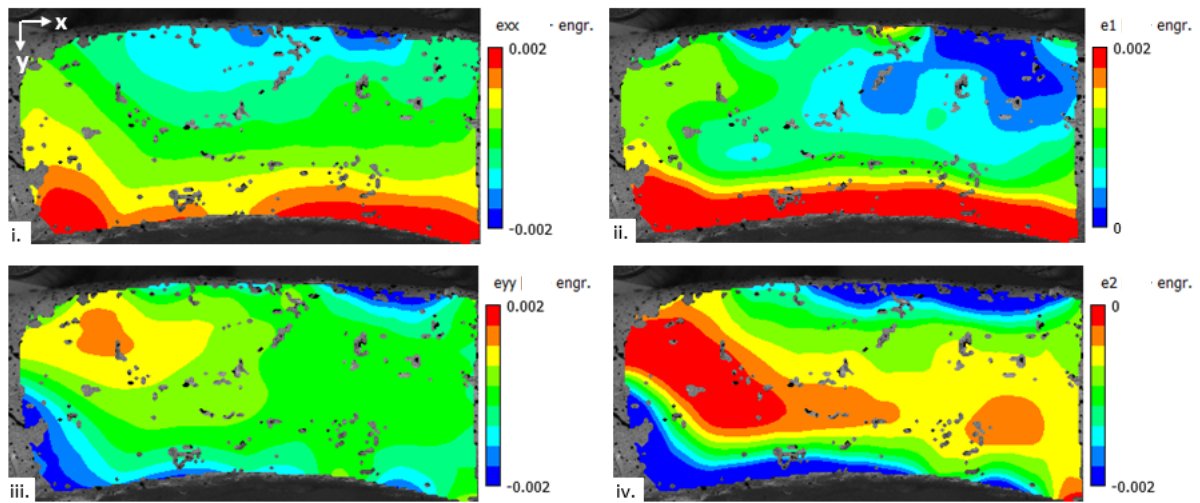


Figure 5-25: Surface strains of bone O1002 under four-point bending obtained through DIC at the end of the first linear region, LF1 (a), and second linear region, LF2 (b). (i) Engineering plane strains in the x-direction. (ii) First principal plane strain (tension). (iii) Engineering plane strains in the y-direction. (iv) Second principal plane strains (compression).

a.A1003 – LF1 – (1.5mm, 1.0kN)



b.A1003 – LF2 – (3.0mm, 2.1kN)

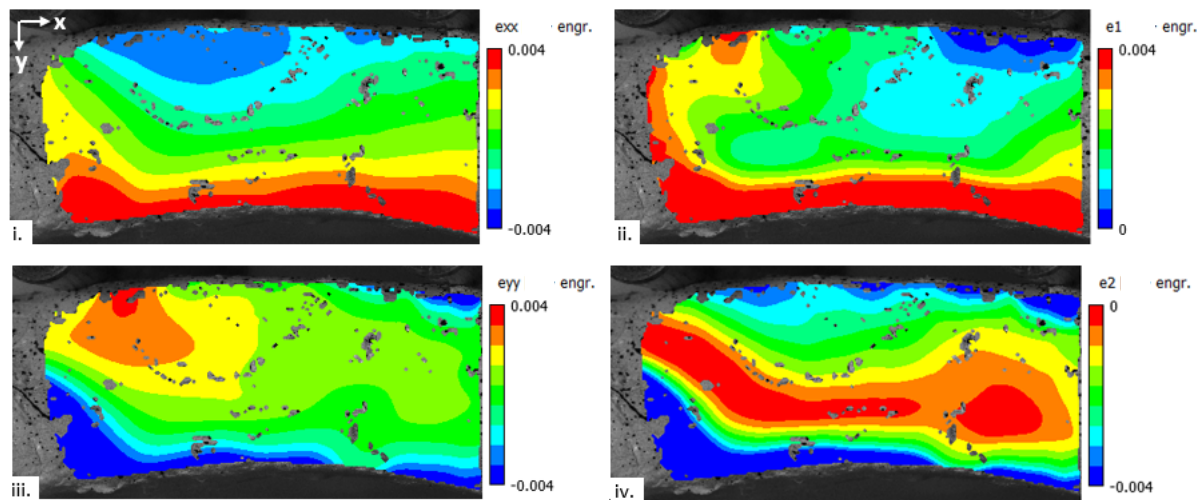


Figure 5-26: Surface strains of bone A1003 under four-point bending obtained through DIC at the end of the first linear region, LF1 (a), and second linear region, LF2 (b). (i) Engineering plane strains in the x-direction. (ii) First principal plane strain (tension). (iii) Engineering plane strains in the y-direction. (iv) Second principal plane strains (compression).

5.4 Discussion

This section analyses the force-displacement curves and the corresponding surface strain contours of the four bones. Additionally, it discusses the limitations of the experimental method as well as suggestions for potential improvements.

5.4.1 Force-displacement curves

The force-displacement curves for bones O1001, O1002, and A1003 followed a similar pattern. All three were left-limb femurs positioned in the same orientation on the rig, i.e. with the cranial side up and the distal end to the left. All three plots had two linear regions separated by a critical point around 1kN; which corresponded to local failure under the left rod, i.e. rod indentation caused by a point load. This suggests that the bones had similar strength without comparing detailed geometry and material property differences.

The first linear fit (LF1); which corresponds to the linear region before the rods began to indent into the bone, had very similar slopes for bones O1001 and O1002 (1.86Nm^{-1} and 1.89Nm^{-1} , respectively). However, the slope of LF1 for bone A1003 was much lower (0.93Nm^{-1}). The similarity in the LF1 slopes for bones O1001 and O1002 could be due to their similar average cortical thickness (2.68mm and 2.75mm, respectively) and sagittal curvature radius (232mm and 252mm, respectively). This would explain why the LF1 slope of bone A1003; which had a slightly thinner cortical thickness (2.42mm) and smaller curvature (165mm), was lower - approximately half of that of bone O1001 and O1002. However, with only three bones, it is not sufficient to establish a direct relationship between the geometry (cortical thickness and curvature) and the rigidity of immature femur under four-point bending.

The failure modes of bones O1001 and A1003 were also similar; the slope decreased after reaching a maximum load and subsequently failed with a complete transverse and oblique fracture, respectively. On the other hand, bone O1002 continued to carry a high load (>1.5kN) before reaching its maximum load, with a much wider plateau region. This was reflected in the fracture type which was heavily comminute. It is important to note that bone O1002 had a much thicker periosteum visually; which could have played a role in maintaining a high load beyond the first signs of fracture.

5.4.2 Surface strain contours

The x-axis strain contours of bone O1001 showed signs of typical four-point bending behaviour, i.e. compression at the top and tension at the bottom resulting from in-plane bending stresses. On the other hand, its y-axis strain contours (Figure 5-24.iii) showed two islands of tensile strain under the top rods on either side of the AOI, which were compatible with compression (Figure 5-27).

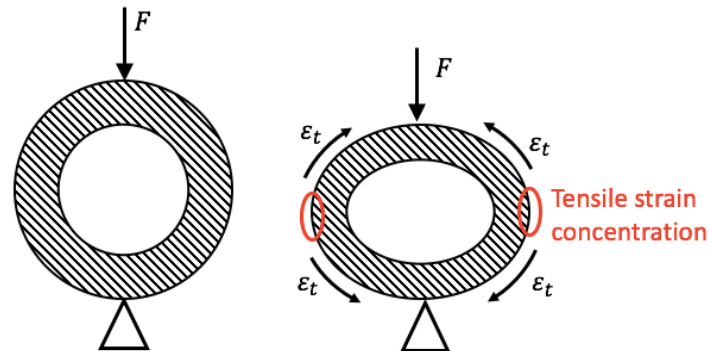


Figure 5-27: Diagram of the cross-section of a hollow cylinder under a point load.

Although the magnitude of the x-strains is higher, the effect of both x-strains and y-strains can be seen in the contours of the first and second principal plane strains.

The strain contours were slightly asymmetric at the end of the first linear region (Figure 5-24); e.g. the tensile strain on the left side of the y-strain map is higher in magnitude than on the right. This is likely caused by the rods not making contact with the bone simultaneously; the left rod made contact first followed by the right rod 0.22mm later, meaning that the load was not distributed symmetrically on both sides. Once the left rod indented into the bone, the load became more symmetrically distributed, hence the observation at the end of the second linear region when the strains became more symmetrical.

The x-axis strain contours of bones O1002 and A1003 also showed signs of typical four-point bending behaviour. The compression and tension caused by bending stress can also be seen in the first and second principal plane strain contours, respectively. However, some strain concentrations do not seem to follow a logical pattern. This could be due to limitations in the experimental method that is discussed in the next few sections.

5.4.3 Data for finite element model validation

there was a lot of displacement of the load cell between the time of contact of the left rod and the right rod during the test on bone A1003. This considerable asymmetry in load distribution would make it difficult to establish a suitable boundary condition in the FE model.

On the other hand, experimental data for bones O1001 and O1003 are more suitable to be used for FE validation. Particularly for bone O1001, which has a larger linear region that resulted in a relatively symmetrical strain contour. Therefore, O1001 is used to validate the FE model in the next chapter. The next section will focus the discussion on the limitations of the current experimental methods and suggest methods for improvements.

5.4.4 Limitations of the experimental method

5.4.4.1 Four-point bending method

Ovine femur bones are curved on all planes. This poses several difficulties when it comes to positioning the bone on the rig. First, the bones could not be accurately orientated as they naturally rotated to a minimum energy position when simply resting on the bottom rollers. Similarly, they slid transversally until reaching an equilibrium position, meaning that the mid-shaft could not be perfectly positioned at the centre of the rig.

As shown for bone A1003 (Figure 5-18), the rods did not come into contact with the bone simultaneously. This led to an un-equal and non-measurable load distribution through the top rods. Furthermore, since the bones were not constrained, they often rotated under loading and underwent rigid body motion. This implies that the boundary conditions, i.e the load position with respect to the bone, changed throughout the experiment, and thus was under a non-static loading condition.

All bones showed signs of local fractures or crushing beneath the top rods before reaching a state of complete structural failure (Figure 5-28). In the case of bone O1002, it seems that the small local cracks propagated to result in the final complete bone fracture. These small fractures also have the potential to disrupt the top periosteum layer, which could lead to unexpected strain patterns detected in the DIC.

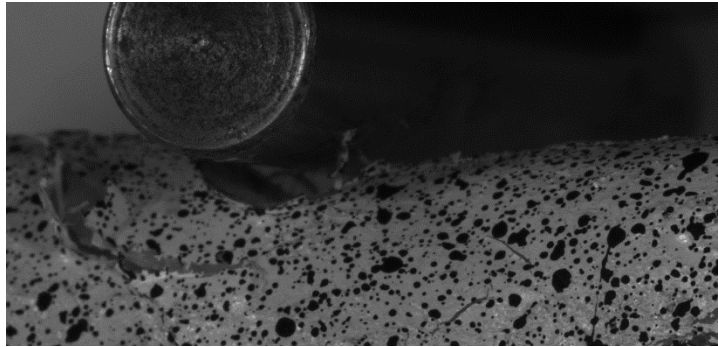


Figure 5-28: Frame of bone O1002 showing localised crushing of the bone under the top right rod.

5.4.4.2 DIC method

The DIC system was unable to correlate the very top and bottom of the AOI for all four bones. Additionally, the noise images showed that, in the area that was correlated, the noise was also distributed on the borders. When looking at the raw images, it is evident that the top and bottom of the AOI were not bright enough (Figure 5-29). The poor lighting was due to the curvature of the bone and to the positioning of the lamps in the experimental set-up. The acute angle of incidence of the camera onto the borders was particularly problematic for the measurements of strain in y-axis, which was tangent to the curvature.

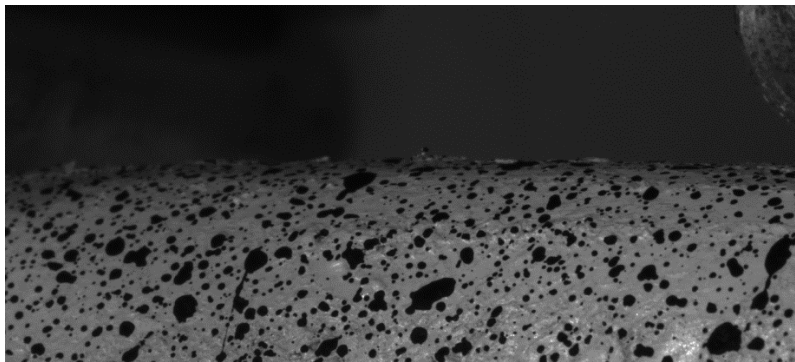


Figure 5-29: DIC image of the top surface of bone O1002 in the testing set up showing the poor contrast at the edges of the AOI.

On the other hand, there were also regions of over-exposure caused by reflection/shimmer. This could have been caused by the base paint; which was perhaps not matt enough, or even the periosteum; which is a very reflective material (Figure 5-2).

Although a lot of care was taken when cleaning the bones, the periosteum was sometimes damaged; which resulted in irregularities on the bone surface. With the white base coat on,

the damages of periosteum became more noticeable and appeared as wrinkled lines and bumps in the middle of the AOI (Figure 5-30). Consequently, the light reflected on the ridges leading to over exposure when capturing the images.

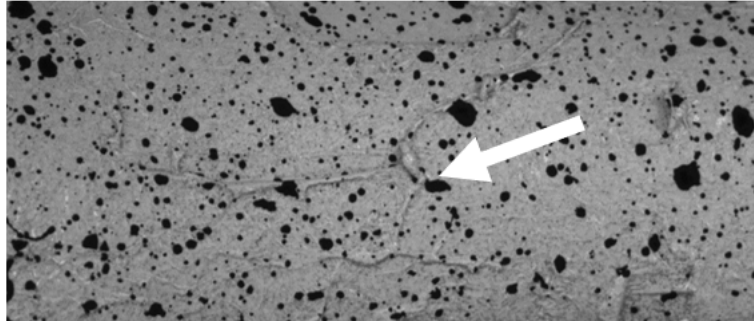


Figure 5-30: Ridges on the surface of bone A1003, caused by spray painting over the damaged periosteum.

These irregularities clearly distorted the correlation. Taking bone O1002 as an example, in images presented in the result section there is a large discontinuity in the strain contour of the second principal strain where a bump can be seen in Figure 5-25. This corresponds to the bump on the bone surface as shown in Figure 5-31 below.

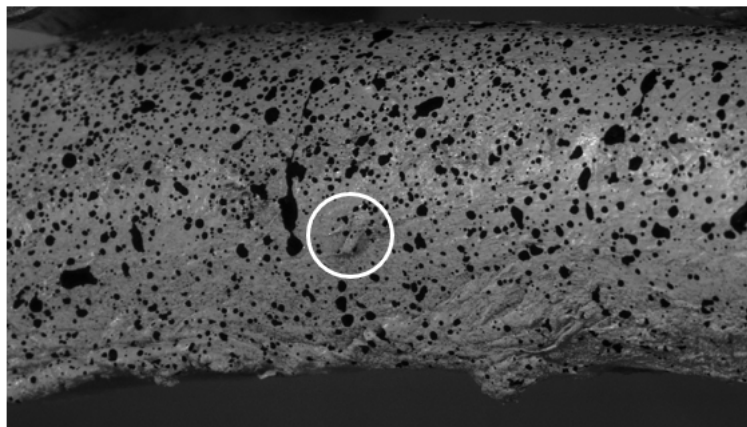


Figure 5-31: Bumps on the surface of bone O1002 cause by underlying tissue.

If this (bumpy) area is manually removed from the AOI, the resulting contour no longer has a discontinuity (Figure 5-32).

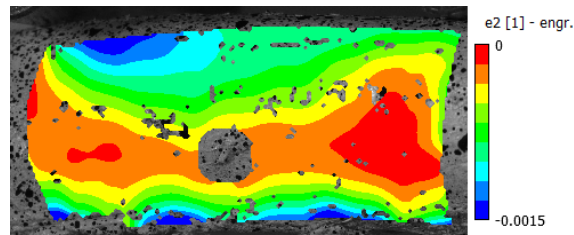


Figure 5-32: Second principal plane strain (compression) of bone O1002 under four-point bending obtained through DIC at the end of the first linear region as shown in Figure 5-25, but excluding the bumpy area.

It was also apparent that the paint was not adhering sufficiently to the periosteum surface and was detaching in patches upon contact. More importantly, post-fracture images showed that the periosteum sheath detaches from the bone and that the paint does not follow the bone surface strain but rather the periosteal membrane distortion (Figure 5-33).

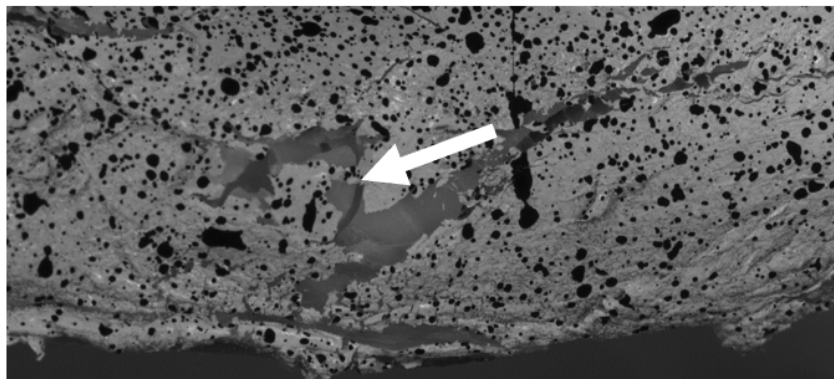


Figure 5-33: Post failure image of bone O1002. The periosteum is stretched causing the paint to crack. The underlying bone has fractured inside the periosteum.

The speckle pattern also played a big part in the quality and accuracy of the correlated strains. As can be seen in Figure 5-34, the speckle density and size were inconsistent with a high variance across the AOI.

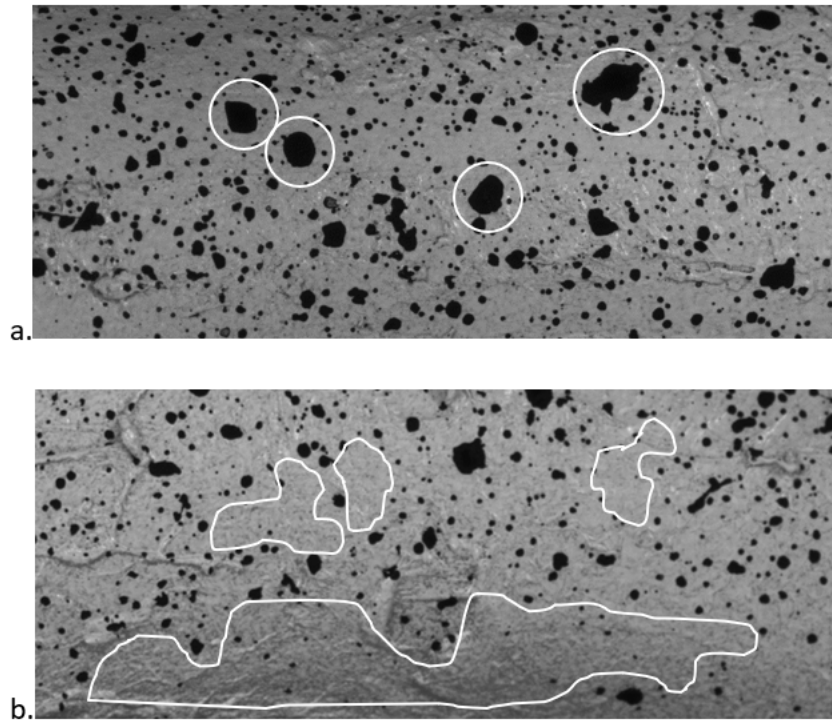


Figure 5-34: Image of poor speckle pattern; a. Large individual speckles on bone O1001; and b. Large empty areas on bone A1003.

The large speckles and empty areas would suggest that very large subset sizes (i.e. larger than the largest black or white area) would be needed for correlation. However, all bones also had uneven surfaces due to the periosteum. These created further smaller patterns; which enabled correlation with a smaller subset size. This phenomenon can be clearly illustrated by thresholding the image and converting it into a binary image (Figure 5-35).

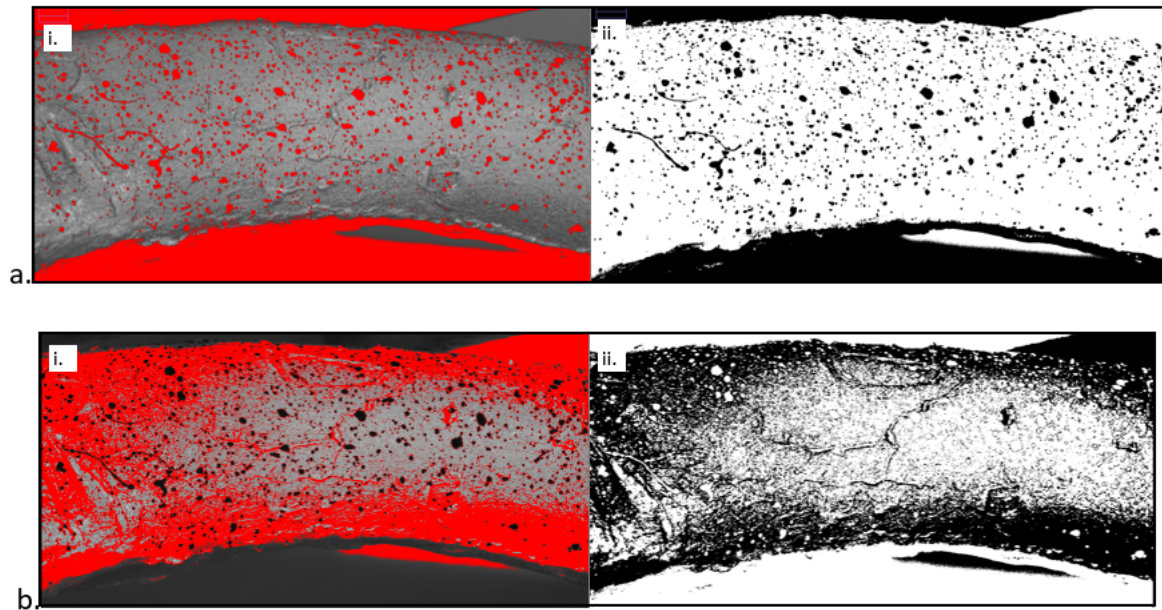


Figure 5-35: Processed image of bone A1003; a. Image processed to differentiate the speckles with i. speckles in red and ii. image converted in black and white; b. Image processed to exacerbate surface irregularities with i. irregularities in red, ii. image converted in black and white.

Consequently, full-field strain distribution in the AOI was obtained using subsets of 61 to 47 pixels in this chapter, which is still relatively high for the given AOI size.

5.4.5 Suggested improvements to the experimental method

5.4.5.1 Four-point bending method

One solution to reduce the amount of misalignment, rigid body motion, and uneven load distribution observed in the current set of experiments would be to embed both ends of the femur and apply the loads on the embedding (Figure 5-36). This practice is commonly used for the investigation of whole bone strength. It ensures that the bones can be consistently aligned when they are fixed in the embedding. The cubic shapes for the embedding at both ends will provide the flat surfaces needed to reduce movements during testing and achieve a more even distribution of load as both top rods can be brought in contact with the specimen simultaneously.

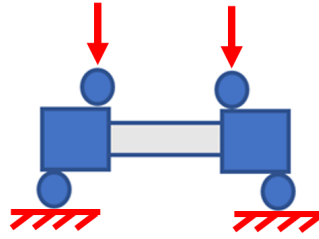


Figure 5-36: Diagram of alternative loading for four-point bending in order to achieve a more consistent experimental set up.

5.4.5.2 DIC method

The top and bottom of the ROI are particularly important when looking at the strains of a bone under four-point bending, as this is where the maximum compression and tension is expected. Therefore, it would be vital to improve the contrast at the very top and bottom sides of the bone. This could be done by rearranging the lights and by adding a black background behind the bone. In order to capture either the top or bottom side, the cameras would have to be angled accordingly.

Although the periosteum plays an important part in paediatric fracture mechanism, in this case it affects the direct evaluation of bone strain. The periosteum is mainly made of cartilage, a collagen-based tissue containing very large protein-polysaccharide molecules that form a gel in which the collagen fibres are entangled. The cartilage material cannot be readily captured in the CT scan, and therefore will not be included in the FE model. For an experimental validation study aimed at understanding immature bone tissue fracture, it would be more accurate for the measurements to be done with a pattern painted directly onto the bone surface. Once there is a better understanding of the mechanical behaviour of immature bones, the role of the periosteum tissue can then be further studied in future in order to evaluate its role during a fracture. However, this is beyond the scope of this thesis.

Finally, for a better overall precision in the correlated images, the speckle pattern would have to be made smaller, denser and more consistent. This could be achieved by using an airbrush. Although more labour-intensive and time consuming, the use of an airbrush or spray-can would allow for a denser and more evenly distributed speckle pattern across the ROI.

5.5 Conclusions

This chapter has presented preliminary results on a first set of four-point bending experimental testing with 3D-DIC image analysis for strain measurements. It discussed the viability of the data for the use in FE validation. It also discussed the various challenges encountered during the experiments so that suggestions could be made to improve the experimental set-up and image processing in order to achieve more accurate and reliable results. These improvements, carried out in the second set of experiment described in Chapter 7, are summarised below:

- Embed the bones at both epiphyseal ends using specialised PMMA in cubical moulds to improve accuracy of alignment during experimental testing.
- Apply the load on the embedded segments to minimise localised stress, non-equal load distribution, and rigid body motion.
- Capture the images with a black background to improve the resolution of the speckles for DIC image analysis.
- Angle the DIC cameras to capture the bottom (tensile) side of the ROI.
- Remove the periosteum over the ROI so that the paint for DIC can be directly applied onto the surface of the ovine bone.
- Paint the speckles with an airbrush to improve consistency in terms of size and distribution of speckles.

6 FOUR-POINT BENDING FEA ON WHOLE LAMB BONES

The mechanics of immature human bone are not well known. A few factors that make the study of paediatric bone challenging are: 1. the fact of life, young cadavers are naturally scarcer than adult cadavers, 2. the ethical implications when using paediatric cadavers for experimental research and 3. guardians seldom donate a deceased child's body. In the 60s and 70s, there was a series of experimental studies where children's bones were tested experimentally in order to study their mechanical properties, but the younger age range was not well-presented. Such studies have declined in the 90s, partly due to tightened ethics. In the past decade, with the development in advanced medical imaging and computational techniques, FEA has become a useful alternative tool that can be used to study the mechanics of immature bone without relying on the availability of paediatric cadavers. Needless to say, the validation of such FEMs remains a challenge.

CT-based FEM of the bone is an *in silico* technique that has been frequently used for femoral neck fracture prognosis. The CT2S pipeline, developed in Sheffield, is built on the idea that the human femur behaves linearly up to failure initiation (Juszczyk et al. 2011), with the cortical, trabecular and marrow modelled as heterogeneous materials, and the elastic modulus of each element derived from CT attenuation based on empirical correlation between stiffness and bone mineral density. This approach has been experimentally validated on adult cadaveric specimen (Grassi et al. 2012, Schileo et al. 2007, Schileo et al. 2008a, Schileo et al. 2008c, Zani et al. 2015) and recently applied to model paediatric bone to study flexural rigidity and strength (Li et al. 2015, Altai et al. 2018). However, the validity of applying this approach to immature bones has yet to be confirmed.

Validating a modelling approach specific to immature bone is essential as there are critical differences between an adult's and a child's femur, including size, structure and material properties. Focusing on the bending scenario as described in Chapter 5, the area investigated is mainly the shaft of the bone, where the change in mineralisation falls sharply from cortical bone to marrow. The free-meshing technique employed in the CT2S would therefore lead to greater partial volume effect in immature bone that is smaller in thickness and length. In addition, the boundary conditions for flexural strength also differ from the typical stance and fall conditions studied in adults.

The CT2S pipeline therefore needs to be adapted in order to model immature long bone. This chapter aims to validate the adapted CT2S pipeline against 3D-DIC data of lamb bone from Chapter 5. A few important adjustments in methods will be discussed including:

- the effect of a structured mesh around the marrow to avoid partial volume issues in the shaft.
- the need of heterogeneity when modelling the shaft.
- the different boundary conditions in order to find the most appropriate set up for simulating the experimental four-point bending reported in Chapter 5.

6.1 Method

This section will describe the steps taken to generate CT-based specimen-specific FEM of lamb femurs. The approach taken was based on the CT2S pipeline, with changes made to model ovine specimen (listed in Chapter 5) under four-point bending conditions as shown in the figure below.

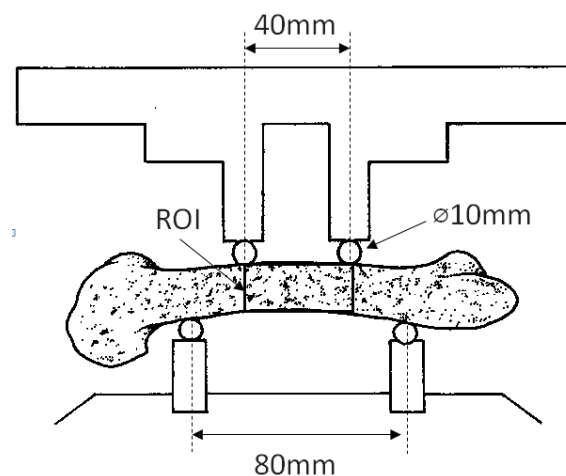


Figure 6-1: Front view of the four-point bending setup used in Chapter 5: A simply supported bone on 10mm diameter steel rods spanning 80mm, with loaded steel rods on the top, spanning 40mm. The region of interest (ROI) is defined as the frontal surface (squared) between the two top rods.

In order to determine the best approach to meshing, material property definition and boundary conditions, several modelling methods were investigated on bone O1001 at 2.7kN (towards the end of the linear response region) (Figure 6-2).

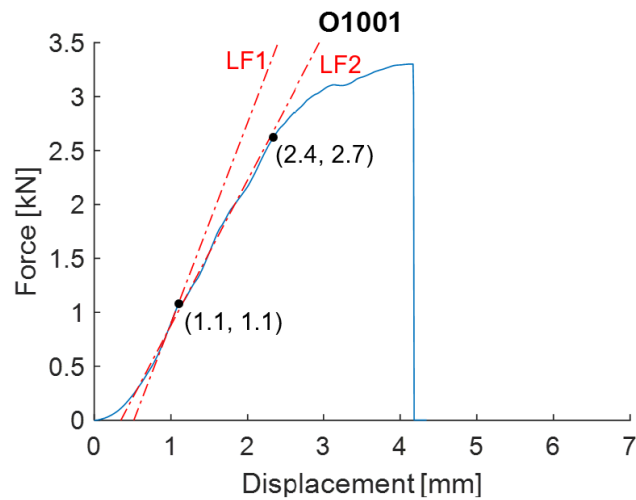
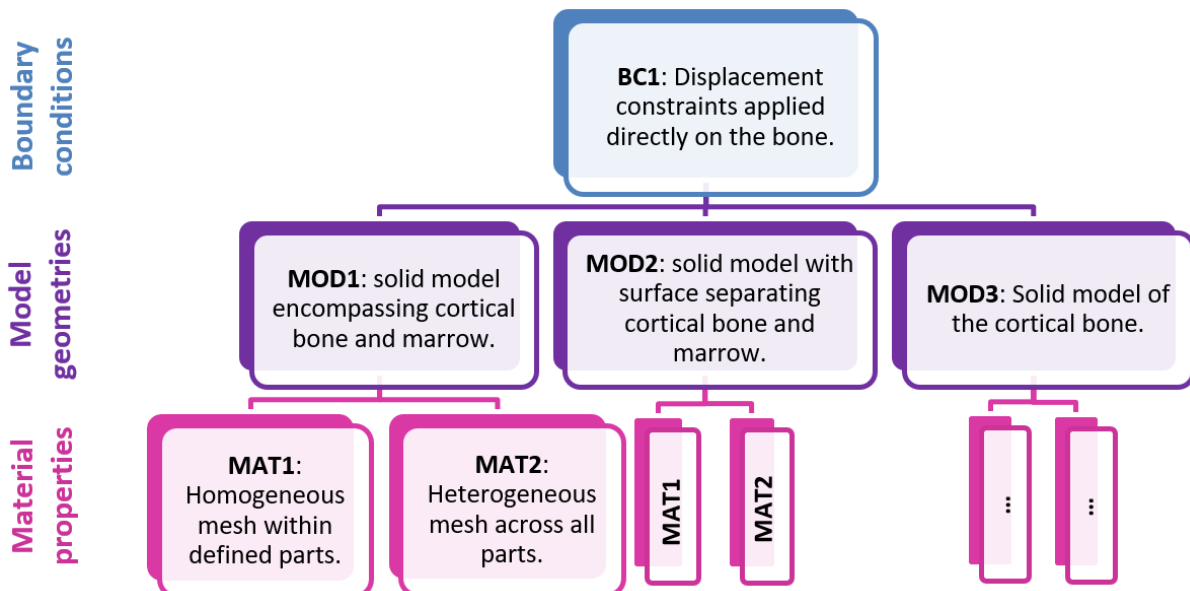


Figure 6-2: Force-displacement plot of bone O1001 under four-point bending corrected for pre-loading as seen in Chapter 5. The dashed lines are linear fits (LF) of the linear regions and the two points mark the end of each linear region.

A total of 24 simulations were carried out on bone O1001 by combining different boundary conditions (defined as BC1 and BC2), contact definitions (defined as CONT1, CONT2 and CONT3), model types (defined as MOD1, MOD2 and MOD3), and material definitions (defined as MAT1 and MAT2). A summary of the different simulations is given in the hierarchy below.



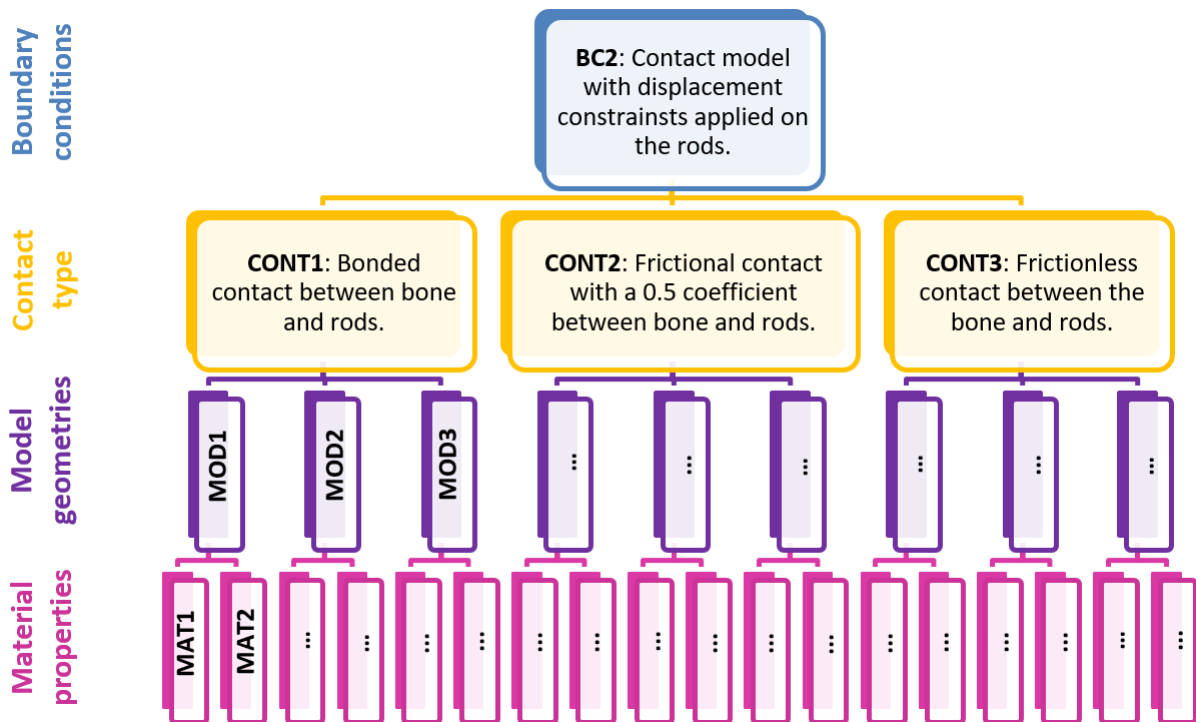


Figure 6-3: List of different FE models, combining boundary conditions (BC), contact definitions (CONT), model types (MOD) and material properties (MAT) used to simulate four-point bending on bone O1001.

Figure 6-4 gives an overview of the adapted CT2S pipeline. First, the lamb bone was CT-scanned. The geometry was then segmented and converted into solids (MOD1, MOD2 and MOD3). The solids were orientated and meshed. Material properties were derived from the CT-attenuation and assigned to the corresponding elements of the mesh (MAT1 and MAT2). Finally, boundary conditions were assigned to run the simulations (BC1 and BC2). Details of each step will be described in the following sections.

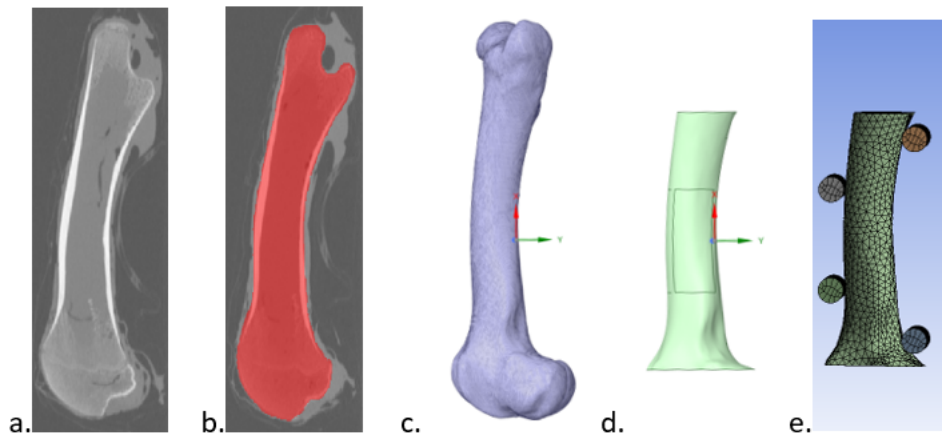


Figure 6-4: The adapted CT2S pipeline; a. QCT-scan of lamb femur (O1001); b. Segmentation of the scan using ITK-Snap; c. Faceted body of the segmentation; d. Reverse engineered solid model of the diaphysis using Space Claim Ansys R2 2021; e. Meshed assembly for contact simulation in Ansys R2 2021.

6.1.1 QCT scanning

Prior to the four-point bending tests (Chapter 5), the lamb bones were CT scanned at the Sheffield's Children Hospital with a GE Lightspeed VCT CT scanner. Each bone was individually scanned in a sealed bag along with a Mindways phantom. The scanner was set to the protocol named '9.1 Lower Extremity Bone'. The scanning parameters were: helical mode, slice spacing and thickness of 0.625mm, peak voltage of 100kVp and X-ray tube current of 50mA. The bones were scanned along their long axes. Two sets of DICOM images were produced for each bone, one with a 'Standard' convolution kernel and another with a 'Bone' convolution kernel (Figure 6-5).

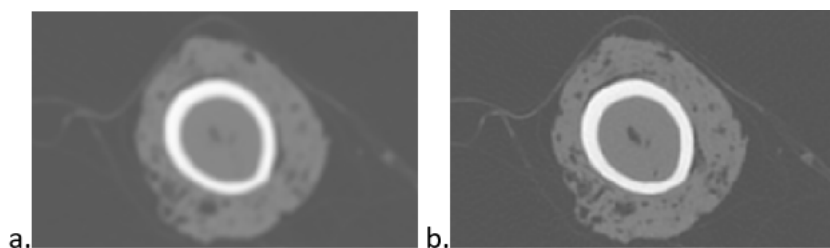


Figure 6-5: Cross-sectional CT scan of bone O1001 with 'Standard' kernel (a) and 'Bone' kernel (b).

6.1.2 Segmentation

The CT scan was segmented following a semi-automated segmentation procedure in ITK-Snap version 3.8.0 (Yushkevich et al. 2006). Bone O1001 was segmented on the 'Bone' kernelled DICOM files as these images provided a sharper edge over the cortical bone.

Two segmentations were performed. The first segmentation encompassed the whole bone (Figure 6-6), for which a threshold of $>200\text{HU}$ was used to mask the outer cortical contour of the whole bone.

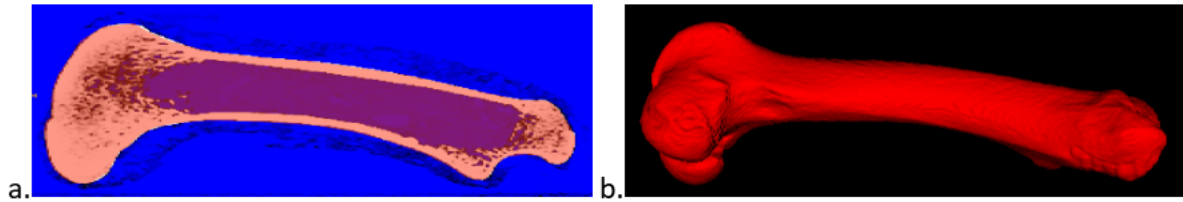


Figure 6-6: (a) Segmentation of the whole bone over the original CT image. (b) The resulting 3D volume of the whole bone.

The second segmentation resulted in a separate volume representing the marrow and the trabecular bone; which were segmented in two steps. First, the marrow was masked using a threshold of $<50\text{HU}$ (Figure 6-7.b). Then the segmentation was extended manually to a length of approximately 90mm over the trabecular bone towards both ends (Figure 6-7.d). Finally, the segmented volume (marrow plus some trabecular bone) was exported as STL file.

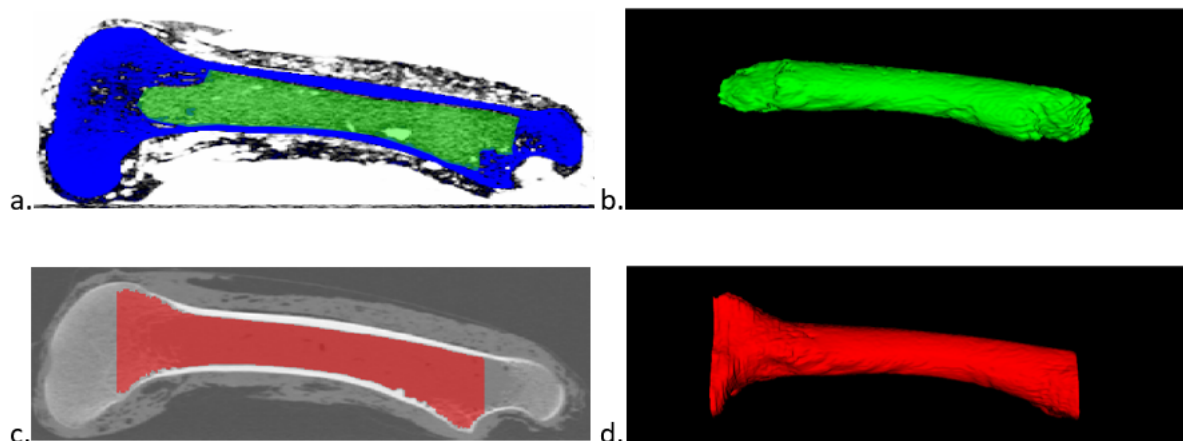


Figure 6-7: (a) Segmentation of the bone marrow (green) over the CT image. (b) 3D volume representing the marrow. (c) Segmentation of the marrow and trabecular bone over the CT image. (d) Resulting 3D volume of the marrow and trabecular bone.

6.1.3 Reconstruction

The segmented structures were reconstructed into solids before being meshed. This step allowed for better control over the mesh; and subsequently better repeatability in the alignment of each bone and the location of the boundary conditions.

In order to build a solid, the STL file of the whole bone was imported into Ansys SpaceClaim 2021R2. The ridges on the faceted body (which occur during segmentation) were smoothed out. A local coordinate system was created based on anatomical landmarks on the whole bone and a surface was formed over the faceted body to create a solid body. Only the diaphysis was modelled as it was assumed that the epiphyses did not carry any load under four-point bending conditions.

6.1.4 Alignment

The alignment system used in the FE modelling was re-defined from (Altai et al. 2018) in order to better suit immature ovine femurs so that the position of the bone during four-point bending can accurately be reflected. The new coordinate system allowed for a more repeatable alignment of different bones. The local coordinate system was defined based on a plane going through three anatomical landmarks and on the narrowest cross-section of the diaphysis over that plane.

The anatomical landmarks were determined by three points, which represented the shortest path along the bone in the longitudinal direction as shown in Figure 6-8.



Figure 6-8: Cranial view (a) and medial view (b) of a 3D printed model using geometry from bone O1001 with an elastic band showing the shortest path along the longitudinal direction.

As shown in Figure 6-9, point *a* was defined as the trough on the distal end of the trochlear groove, point *b* was defined as the trough of the cranial face of the trochlear groove, and point *c* was defined as the cranial trough of the femoral neck.

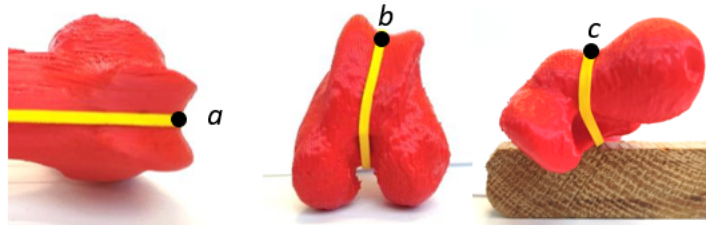


Figure 6-9: The three landmarks used for creating a local coordinate system of the ovine bone. (a) Trough on the distal end of the trochlear groove. (b) Trough on the cranial face of the trochlear groove. (c) Cranial trough of the femoral neck.

The same three points were selected manually on the faceted body in order to create a sagittal plane passing through them that cut across the long axis of the bone (Figure 6-10).

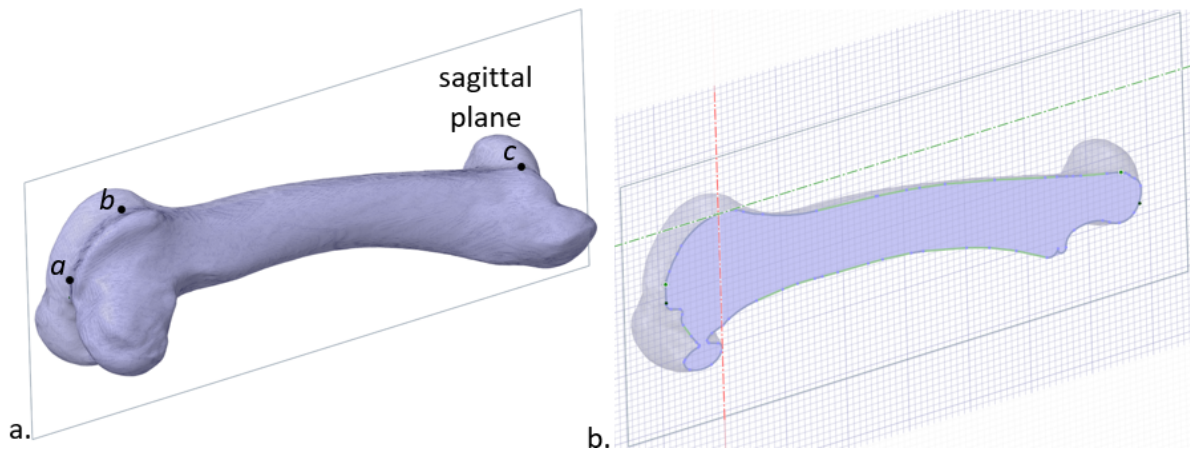


Figure 6-10: (a) Faceted body of bone O1001 obtained through CT segmentation with landmark points *a*, *b* and *c*, which defined the sagittal plane. (b) Sagittal cross-section of the faceted body.

The narrowest section of the diaphysis was located by fitting two circles onto the cranial and caudal edges of the sagittal cross-section. A line passing through the midpoint of each circle (and hence the narrowest section of the diaphysis) was used to define the transverse plane. A local coordinate system was then placed at the intersection between the caudal edge and the transverse axis as shown in Figure 6-11. The x-axis was defined as the tangent of the caudal circle, with the y-axis pointing towards the centres of the circles (perpendicular to the x-axis).

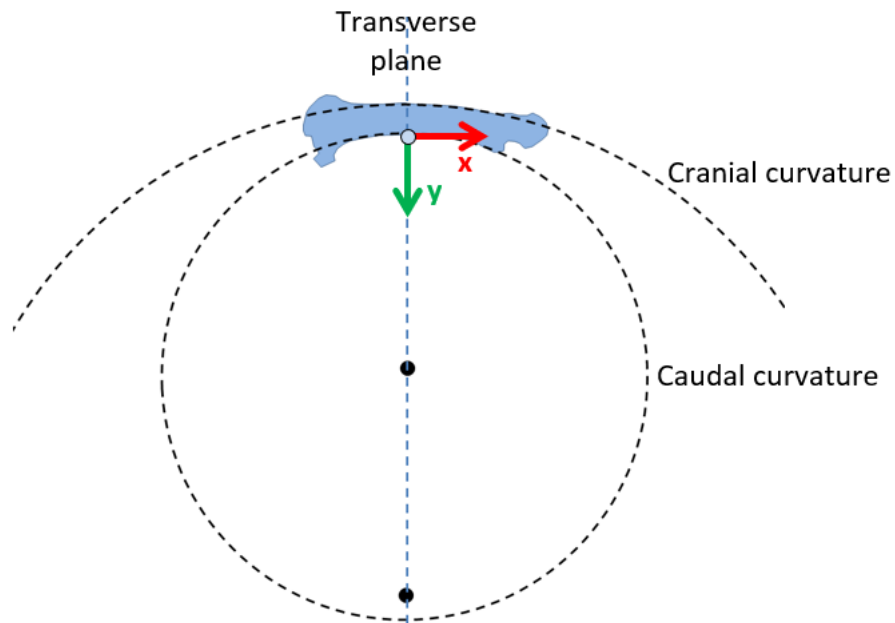


Figure 6-11: The cranial and caudal curvature with an axis passing through the midpoint of the curvature that was used to define the transverse plane.

Next, two planes were created on either side of the bone at 50mm offset from the transverse plane (Figure 6-12). Finally, the facets between the proximal and distal planes were converted into a geometrical surface to create a solid of the mid-shaft of the bone.

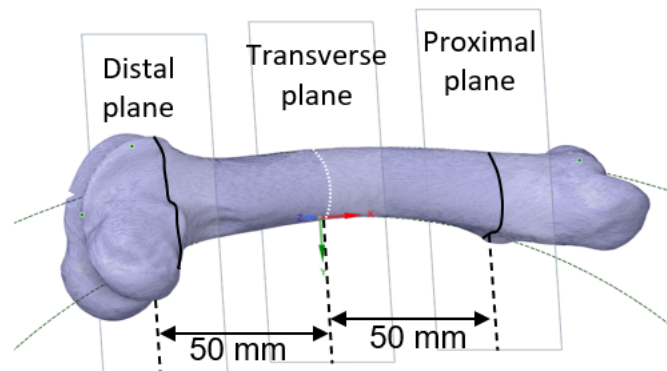


Figure 6-12: Faceted body of bone O1001 showing the distal and proximal planes between which the faceted body was converted into a solid body.

6.1.5 Outlining the cortical bone

As mentioned previously, three models were tested (Figure 6-13), one model encompassing both the bone and the marrow (MOD1), one model with a surface separating the marrow from the cortical bone (MOD2), and one model of the cortical bone only (MOD3). In order to delineate the cortical bone from the whole bone volume, the segmentation of the marrow

and trabecular bone was imported into the model, converted into a solid and then cut out of the bone. This operation is illustrated in Figure 6-13.

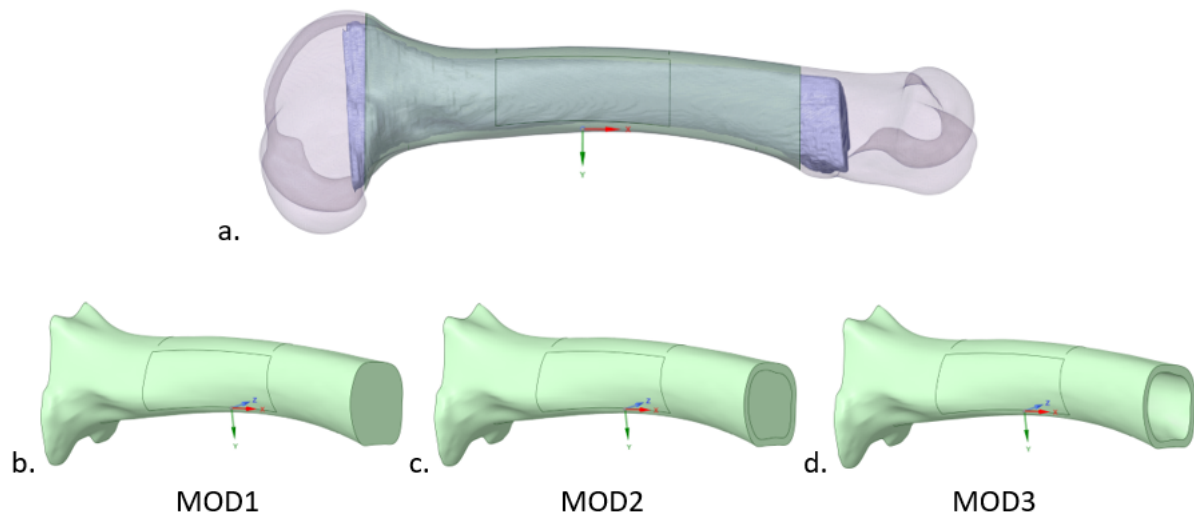


Figure 6-13: (a) Solid body of bone O1001 (transparent, whole bone volume; blue, marrow and trabecular bone segmentation). (b) Solid model of the whole shaft (MOD1). (c) Solid model of the whole shaft with a surface differentiating the cortical layer from the marrow (MOD2). (d) Solid model of the cortical layer only (MOD3).

The solid bodies were meshed in Ansys Workbench 2021R2 with quadratic order tetrahedral elements and assigned either heterogeneous or homogeneous material properties.

6.1.6 Material properties

The elastic modulus in this study was derived based on the empirical relationship established by (Grant et al. 2014). First, a densitometric calibration of the QCT images of bone O1001 was performed against the Mindways phantom which was scanned along with the lamb bone. The calibration was then corrected for dipotassium hydrogen phosphate (K_2HPO_4 , Mindways phantom) and hydroxyapatite (HA, European forearm phantom) in order to match the empirical relationship proposed by (Grant et al. 2014). This approach (described below) was taken due to the lack of data in direct densitometric calibration for ovine bones.

6.1.6.1 Elastic modulus and density relationship

A study by (Grant et al. 2014) found that the elastic modulus (E) of ovine cortical tibia is exponentially proportional to apparent density:

$$E[GP\alpha] = 12.35\rho_{app}^{1.32} \quad \text{Eq.6-1}$$

In their study the apparent density was measured via QCT. The HU in the QCT was calibrated against a European forearm Phantom (QRM-EFT, HA-based), and the regression between HU and HA density was used to derive the apparent density.

As explained in Chapter 2, although HA closely resembles bone mineral, the difference in attenuation and consequently the difference in HU is still significant. The difference between the phantom CT-density and bone density is usually accounted for by correcting the calibration. However, Grant did not apply a correction to convert HA density to apparent density in her study. After discussion with the author (email communication), it was concluded that the apparent density was in fact defined directly in terms of HA equivalent density, and consequently the elastic modulus was considered exponentially proportional to the HA equivalent density:

$$E[GP\alpha] = 12.35\rho_{HA}[g/cc]^{1.32} \quad \text{Eq.6-2}$$

6.1.6.2 Densitometric calibration

In the current study, the bones were scanned with a Mindways phantom, containing five rods of K_2HPO_4 . Thus, the QCT densitometry was calibrated for K_2HPO_4 as per the manufacturer's instructions. The composition of the materials in the Mindways phantom is given in Table 6-1.

Typical Composition of Various Solid Reference Materials		
Reference Rod	Eq. H ₂ O density (mg/cc)	Eq. K ₂ HPO ₄ density (mg/cc)
A	1012.2 +/- 2.3	-51.8 +/- 0.1
B	1057.0 +/- 1.9	-53.4 +/- 0.1
C	1103.6 +/- 1.7	58.9 +/- 0.1
D	1119.5 +/- 1.8	157.0 +/- 0.3
E	923.2 +/- 2.1	375.8 +/- 0.9

Table 6-1: Typical composition of the solid reference materials in a Mindways phantom.

All five cylinders in the Mindways phantom were segmented using ITK-Snap in order to derive the mean intensity of each rod (Figure 6-14).

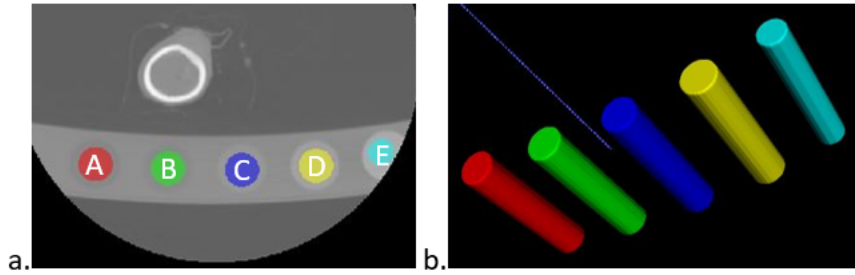


Figure 6-14: (a) A single CT image of a Mindways phantom scanned with bone O1001 with reference materials A-E segmented. (b) 3D segmentation of the five rods in the Mindways phantom.

The pixel value of each rod was calculated by adding 1000 to the mean intensity:

$$\text{pixel value} = \text{mean intensity} + 1000 \quad \text{Eq.6-3}$$

Then, the equivalent H₂O density (Table 6-2) was subtracted from the pixel value to give the K₂HPO₄ corresponding pixel value of each rod:

$$\text{pixel value corresponding to } K_2HPO_4 = \text{pixel value} - \text{eq. } H_2O \text{ density} \quad \text{Eq.6-4}$$

number	colour	intensity mean	pixel value	pixel value corresponding to K ₂ HPO ₄
A	red	-111	913	-99
B	green	-68	956	-101
C	blue	206	1230	127
D	yellow	407	1431	311
E	turquoise	612	1636	713

Table 6-2: The mean intensity of the reference materials in the Mindways phantom taken with bone O1001; and the resulting pixel value corresponding to K₂HPO₄.

Lastly, the K₂HPO₄ pixel value was plotted against the equivalent K₂HPO₄ density in order to find the linear correlation between K₂HPO₄ density and Hounsfield number (Figure 6-15):

$$\rho_{K_2HPO_4} [g/cc] = 0.0005 HU [HU] - 0.0027 \quad \text{Eq. 6-5}$$

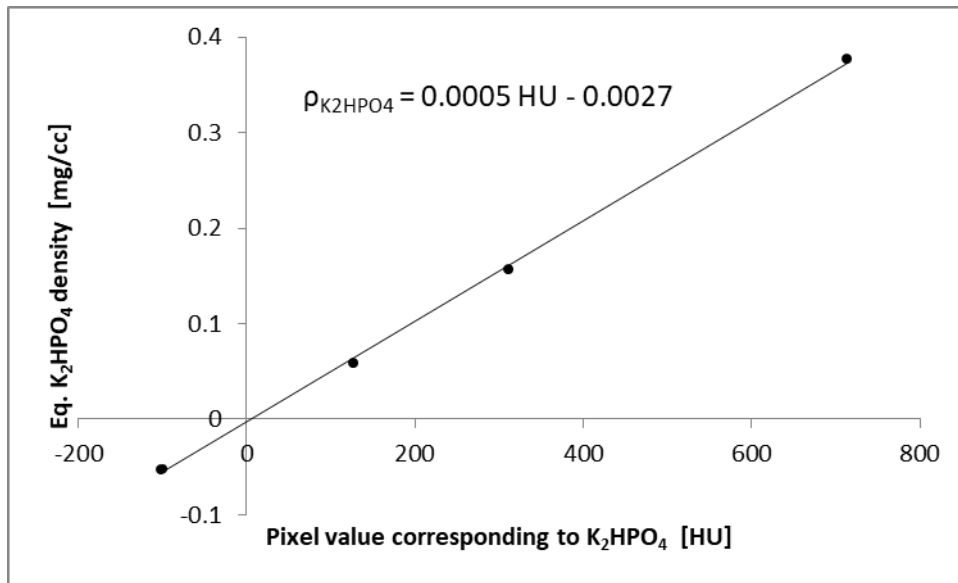


Figure 6-15: Plot of the given equivalent K_2HPO_4 density against the pixel value corresponding to K_2HPO_4 measured from the CT images taken of bone O1001 with the Mindways phantom (peak voltage 100kVp and X-ray tube current 50 mA).

6.1.6.3 Correction of the calibration to HA

The calibration equation reported in the previous section need to be corrected from K_2HPO_4 density to HA density in order to use the elastic modulus equation proposed by (Grant et al. 2014). The following two correction equations from K_2HPO_4 (Eq.6-6) and HA (Eq.6-7) to bone ash density were used.

The K_2HPO_4 correction equation to convert $\rho_{K_2HPO_4}$ to bone ash density, ρ_{ash} was taken from Knowles (Knowles et al. 2016):

$$\rho_{ash} = 1.22 \rho_{K_2HPO_4} - 0.0523 \quad \text{Eq.6-6}$$

The HA correction equation was taken from (Schileo et al. 2008b). This study used both human and bovine bones, which showed that the correction was applicable to both haversian and plexiform tissue; with ρ_{HA} to bone ash density, ρ_{ash} :

$$\rho_{ash} = 0.8772 \rho_{HA} + 0.07895 \quad \text{Eq.6-7}$$

An equation for HA equivalent density in terms of HU was hence derived:

$$\rho_{HA}[g/cc] = 0.0006954 HU[HU] - 0.1534 \quad \text{Eq.6-8}$$

6.1.6.4 Homogeneous mesh

Bone O1001 was modelled with both a homogeneous (MAT1) and a heterogeneous (MAT2) mesh. For the homogeneous mesh, the elastic modulus was derived from the mean Hounsfield number of the cortical bone at the midshaft using equations Eq.6-2 and Eq.6-8, as shown in Figure 6-16.a. The estimated Young's modulus for the homogeneous mesh was 15.91GPa and 14.32GPa for 'Bone' and 'Standard' kernel CT images, respectively.

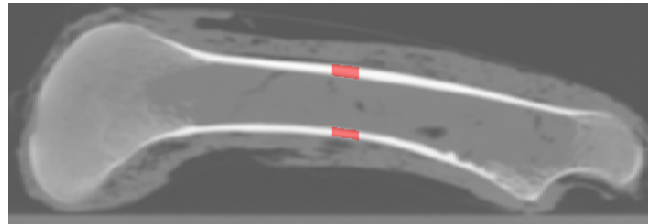


Figure 6-16: CT scan image of bone O1001 with midshaft section of the cortical bone segmented.

CT kernel	Mean intensity [HU]	Density [g/cc]			Elastic modulus [GPa]
		$\rho_{K_2HPO_4}$	ρ_{HA}	ρ_{ash}	
Bone	1963	0.98	1.14	1.21	15.91
Standard	1829	0.91	1.06	1.12	14.32

Table 6-3: Mean intensity and derived densities and elastic moduli of the segmented midshaft cortical section using 'Bone' and 'Standard' kernel images, respectively.

For verification purposes against literature values, the ash density and elastic modulus of three trabecular volume of interests (VOIs) were also derived; one at the centre of each condyle and one at the centre of the femoral head (Figure 6-17). These values were used later on in the Discussion section (towards the end of the chapter), but were not directly used in the modelling of the bone shaft.

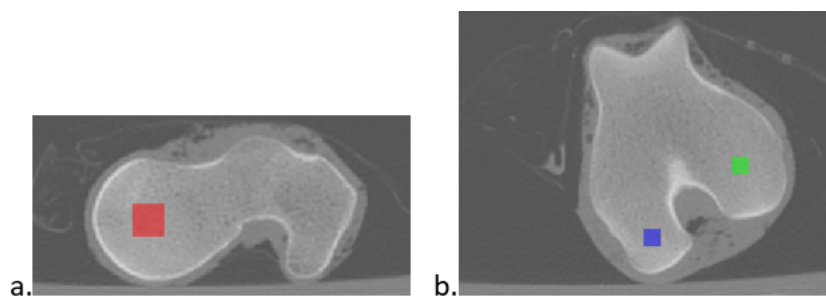


Figure 6-17: CT scan image of bone O1001 with segmented VOIs of trabecular bone in the femoral head (a) and the condyles (b).

a.

Bone kernel	Mean intensity [HU]	Density [g/cc]			Elastic modulus [GPa]
		$\rho_{K_2HPO_4}$	ρ_{HA}	ρ_{ash}	
Femoral head	790	0.39	0.40	0.43	3.64
Lateral condyle	544	0.27	0.22	0.28	1.72
Medial condyle	664	0.33	0.31	0.35	2.61

b.

Standard kernel	Mean intensity [HU]	Density [g/cc]			Elastic modulus [GPa]
		$\rho_{K_2HPO_4}$	ρ_{HA}	ρ_{ash}	
Femoral head	786	0.39	0.39	0.42	3.60
Lateral condyle	543	0.27	0.22	0.28	1.72
Medial condyle	667	0.33	0.31	0.35	2.64

Table 6-4: Mean intensity and derived densities and elastic moduli of three trabecular VOIs using ‘Bone’ kernel (a) and ‘Standard’ kernel (b) images.

In the structured mesh model with bone and marrow, MOD2 (Figure 6-13.c), the marrow was assigned an elastic modulus of 25kPa, which was found to be the upper limit in the literature (Jansen et al. 2015). Elements of both bone and marrow were assigned a Poisson’s ratio of 0.3.

6.1.6.5 Heterogeneous mesh

For the heterogeneous mesh, each element was assigned material properties using the software package Bonemat v3.2 in which equations Eq.6-2 and Eq.6-8 were inserted. This was performed both on the ‘Bone’ and ‘Standard’ kernel CT-images.

An elastic modulus convergence study was carried out in order to assess the CT-based elastic modulus mapping process on the ‘Bone’ convolution kernel images using bonemat. The convergence was performed on the three geometries of bone O1001 (MOD1, MOD2 and MOD3). For each model, the node number was plotted against the maximum and minimum elastic modulus. Five element sizes were tested, between and inclusive of 3mm and 1mm. The largest element size, 3mm, was chosen from the literature (Helgason et al. 2007b). The smallest element size, 1mm, was dictated by software limitations in Bonemat.

The elastic modulus convergence plots of MOD1, MOD2 and MOD3 mapped against ‘Bone’ kernel CT-images are shown in Figure 6-18. The convergence plots of the maximum elastic modulus showed a typical convergence curve. The percentage difference between the finest mesh (1mm) and the converged mesh (1.5mm) was 3% in the three model types.

Bone convolution kernel

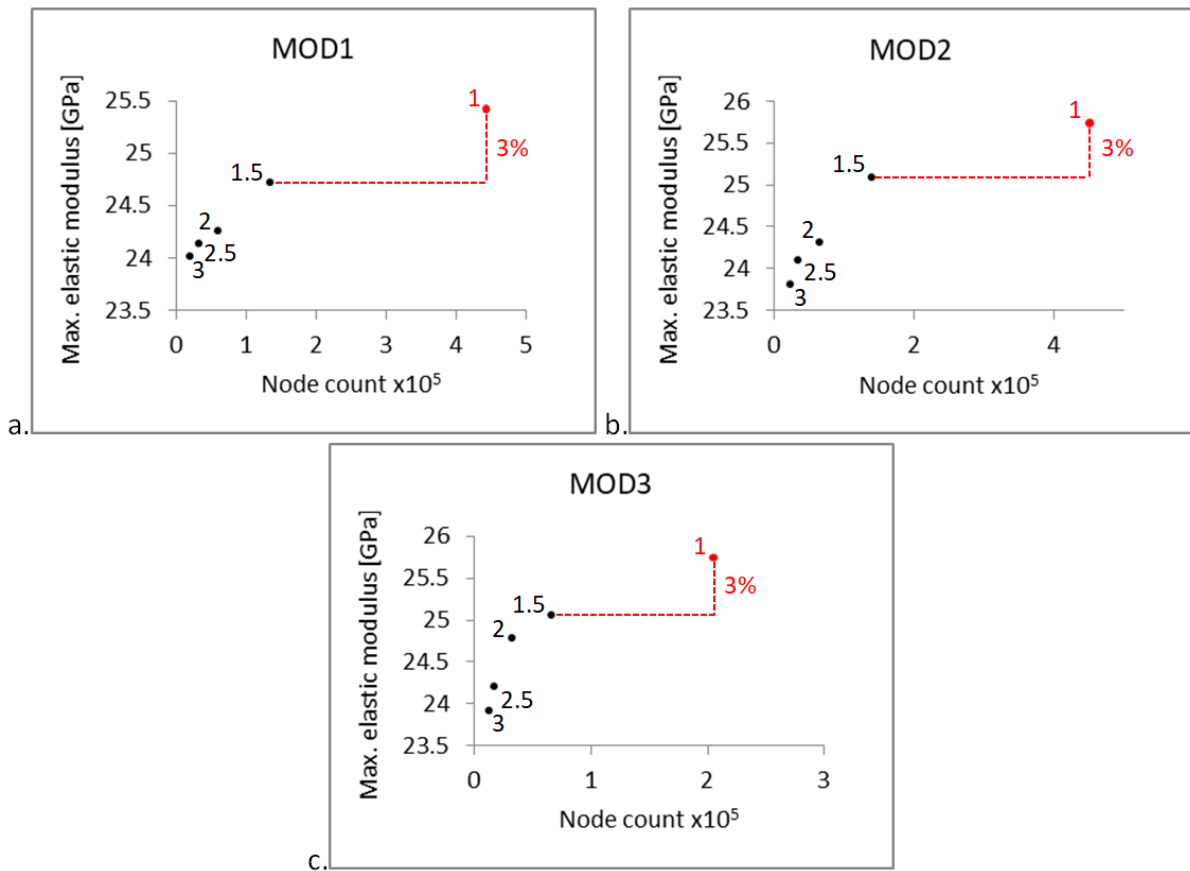


Figure 6-18: Elastic modulus convergence plots for element-specific CT-based material property mapping (MAT2) with element edge sizes 3mm, 2.5mm, 2mm, 1.5mm and 1mm. Convergence of the maximum elastic modulus are shown for geometries MOD1 (a), MOD2 (b) and MOD3 (c).

The resulting elastic modulus distribution derived from the ‘Bone’ kernel for each model type with a 1mm (finest) mesh is shown in Figure 6-19 for illustration purpose. The maximum elastic modulus was 25.4-25.7GPa. The elastic modulus derived from the ‘Standard’ kernel had a similar distribution to that of the ‘Bone’ kernel. For a 1mm mesh the percentage difference between the maximum elastic modulus found using the ‘Bone’ kernel and the ‘Standard’ kernel were small, being 4.3%, 5.8% and 5.5% for MOD1, MOD2 and MOD3, respectively. Therefore, results derived from the ‘Bone’ kernel images were shown here and used in subsequent sections.

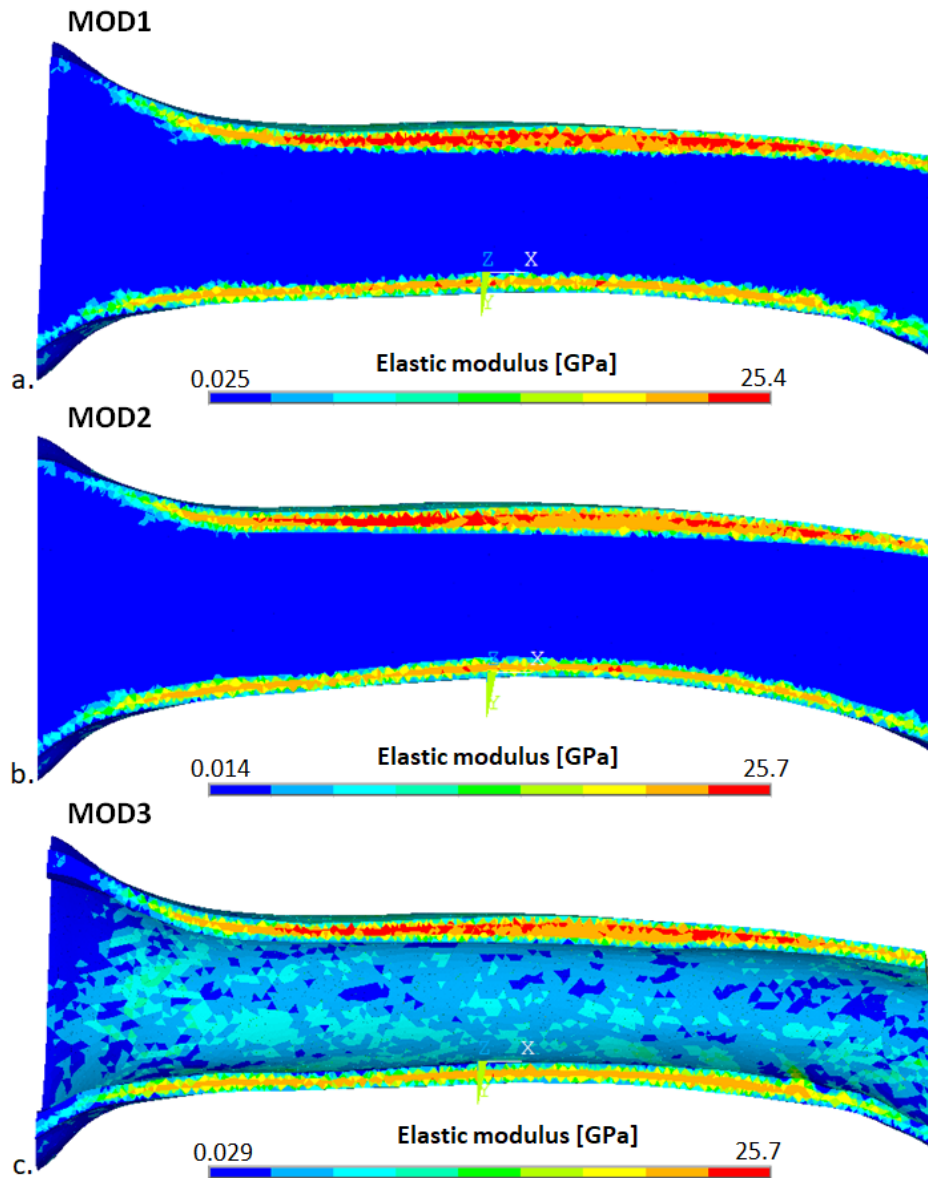


Figure 6-19: Cross-section of bone O1001 along the sagittal plane showing the elastic modulus derived from the 'Bone' kernel CT images on MOD1 (a), MOD2 (b) and MOD3 (c).

6.1.7 Boundary conditions

Two types of boundary conditions were investigated: a direct (BC1) simulation where the displacement was directly applied to the mesh of the bone, and a contact (BC2) simulation where the supporting rods of the testing rig were modelled, with displacement applied directly to the top rods. The structures used to define the boundary conditions were designed in Ansys SpaceClaim 2021 R2 and the boundary conditions were applied in Ansys Mechanical 2021 R2.

6.1.7.1 Linear model (direct, BC1)

Four oval surfaces were drawn on the shaft in order to represent the contact surfaces with the rods so that the locations of the direct boundary conditions were consistent (Figure 6-20). The oval surfaces were drawn by extruding four 10mm diameter cylinders (equivalent to the testing rods) along the z-axis and by imprinting the intersecting edges onto the bone. The top cylinders (A and B) were placed at 40mm apart and the bottom cylinders (C and D) were placed at 80mm apart, similarly to the experimental set-up. The centre-point of the cylinders was offset from the top and bottom edges of the sagittal cross-section by 4mm, i.e. creating an arbitrary 1mm penetration into the bone.

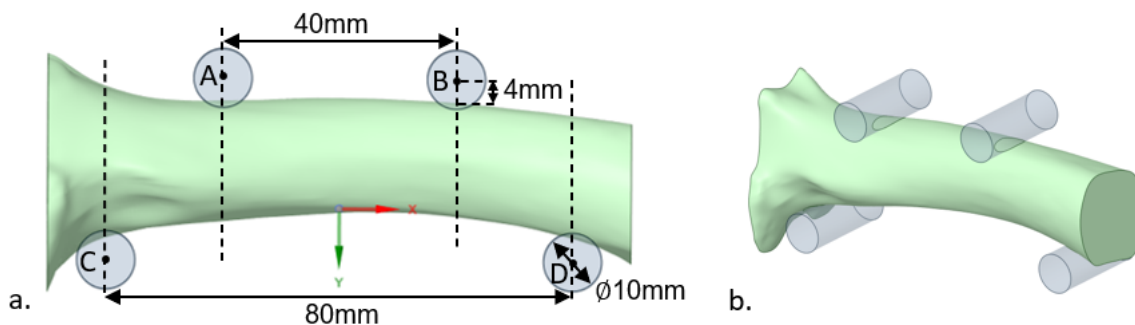


Figure 6-20: Lateral (a) and isometric (b) views of the shaft solid body of bone O1001 with cylindrical volumes representing the rods of the four-point bending experimental set up. The cylinders are modelled so that they penetrate the bone by 1mm and the intersecting surfaces were used to define the locations on which to apply the boundary conditions.

Transverse lines were then projected onto the bone within the intersecting area between the cylinders and the bone as shown in Figure 6-21. The model was opened and meshed in Ansys Mechanical, where direct boundary conditions were assigned to the nodes along the lines marked A, B, C and D.

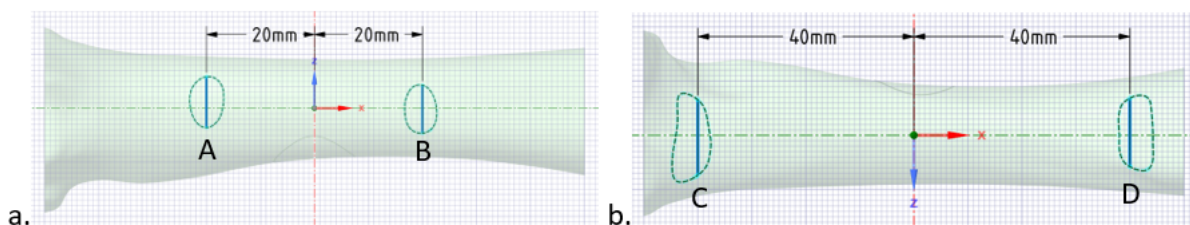


Figure 6-21: Cranial (a) and caudal (b) views of the bone shaft solid model showing the lines (A-D) along which the boundary conditions were applied.

In order to determine the linear displacement on the bone in the experiment, the force-displacement graph in Figure 6-22 was corrected for the linear region of the curve. The corrected displacement at the point of interest became 2.05mm (obtained by shifting the curve so that the linear fit passed through origin).

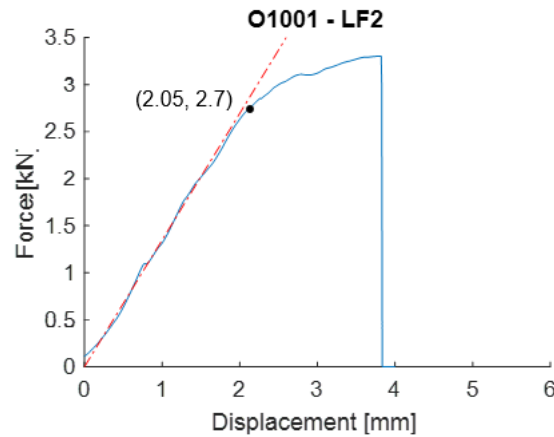


Figure 6-22: Force-displacement curve of bone O1001 under four-point bending with a linear fit (LF2) of the second linear region (Figure 6-2.a) showing the same point at 2.7kN with the corrected displacement.

A displacement d_y of 2.05mm was therefore applied to edges A and B in the y-axis. Edge C was fixed in all directions and edge D was constrained in the y-axis (Figure 6-23).

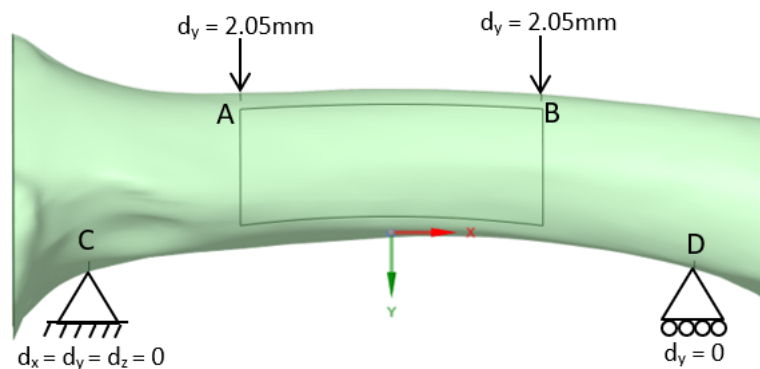


Figure 6-23: Diagram of the boundary conditions applied to bone O1001 to simulate four-point bending by applying displacement constraints directly onto the model (BC1).

A mesh convergence for each of the geometries (i.e. MOD1, MOD2 and MOD3) with homogeneous material properties (MAT1) was carried out using the direct boundary conditions (BC1). Figure 6-24 shows the principal strain convergence plots for MOD1, MOD2 and MOD3 with direct boundary conditions (BC1). The convergence plots showed a typical converging curve for both peak principal strains. The 1mm mesh (converged mesh size)

highlighted in red is shown to have a percentage difference of <6% compared to the most refined mesh (0.33mm).

Note that the convergence studies were performed by remeshing the models with a decreasing element size (i.e. equivalent to a first and second degree refinement). The 1mm element size is approximately equal to a third of the cranial and caudal cortical thickness of the bone, where maximum stress is expected.

Direct model (BC1)

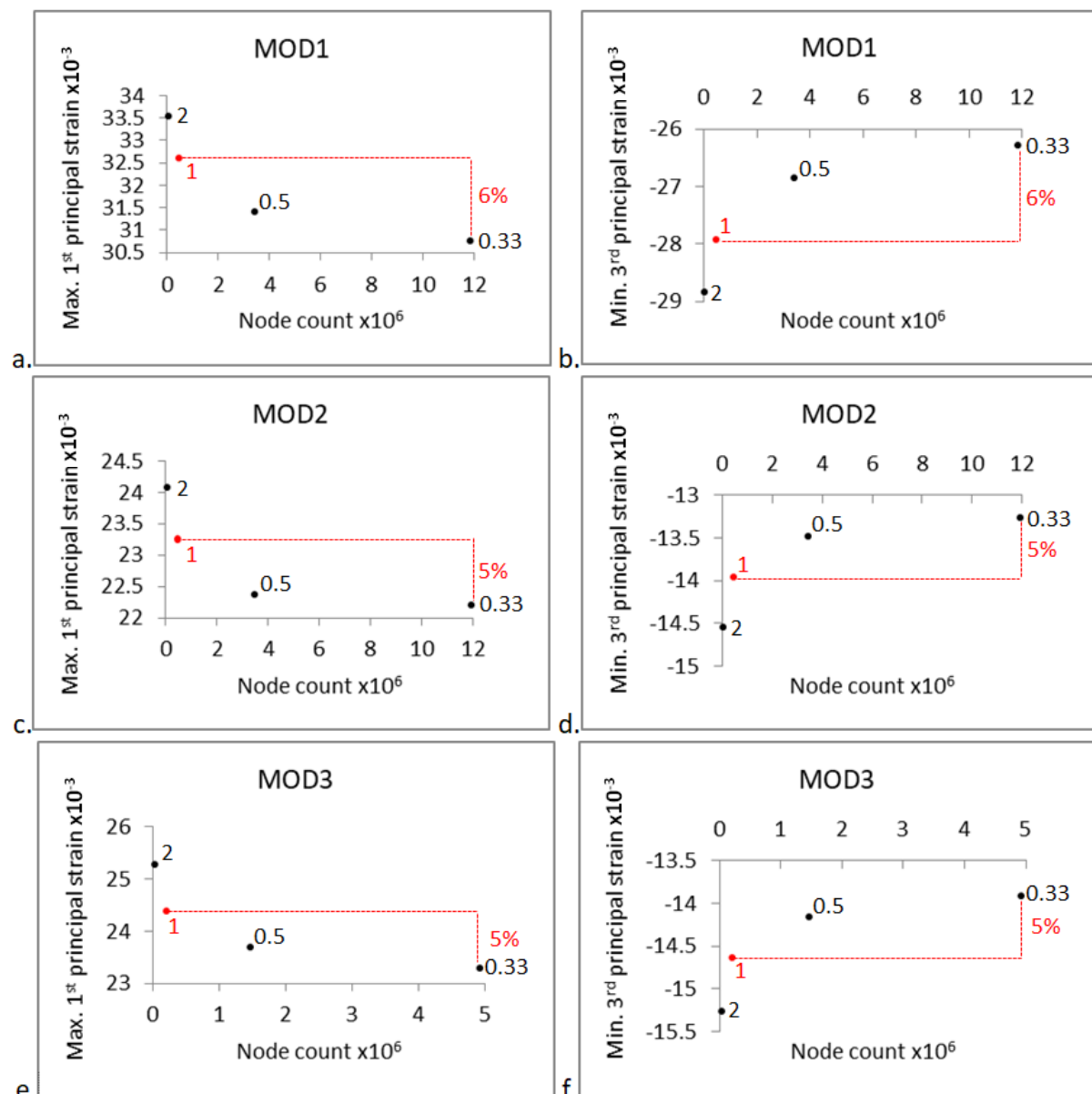


Figure 6-24: Principal strain convergence plots on direct boundary conditions model (BC1) with a homogeneous mesh at element edge sizes 2mm, 1mm, 0.5mm and 0.33mm. Convergence of the maximum first principal strain and the minimum third principal strain for geometries MOD1, MOD2 and MOD3.

6.1.7.2 Non-linear model (contact, BC2)

To create an assembly for the contact model, four 10mm diameter half cylinders were extruded along the z-axis at 40mm and 80mm as shown in Figure 6-25. The centre-points of the cylinders were offset by 5mm from the cranial and caudal fitted circles. The top and bottom rods were aligned and stayed parallel by definition. A small amount of penetration was present between the rods and the bone.

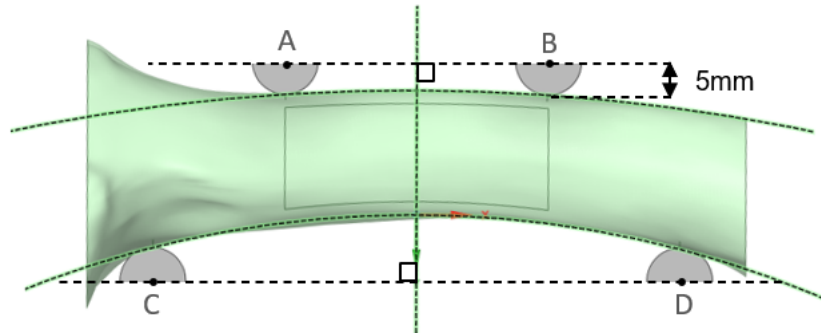


Figure 6-25: Assembly of the femoral shaft and the rods for the contact simulation of bone O1001 under four-point bending conditions (BC2).

The assembly was opened and meshed in Ansys Mechanical. A displacement of 2.4mm in the y-axis was assigned to rods A and B, while the other two directions were fixed (Figure 6-26). Note here the applied displacement was taken directly from the raw force-displacement plot (Figure 6-2) and not corrected, as the compliance phase was accounted for as part of the contact boundary constraint. The bottom rods were fixed in all directions. A contact pairing was created between the surface of each rod and the entire surface of the bone. The same contact condition was applied to all four contact pairings. The contact conditions studied were bonded (CONT1), frictional with coefficient of 0.5 (CONT2), and frictionless (CONT3).

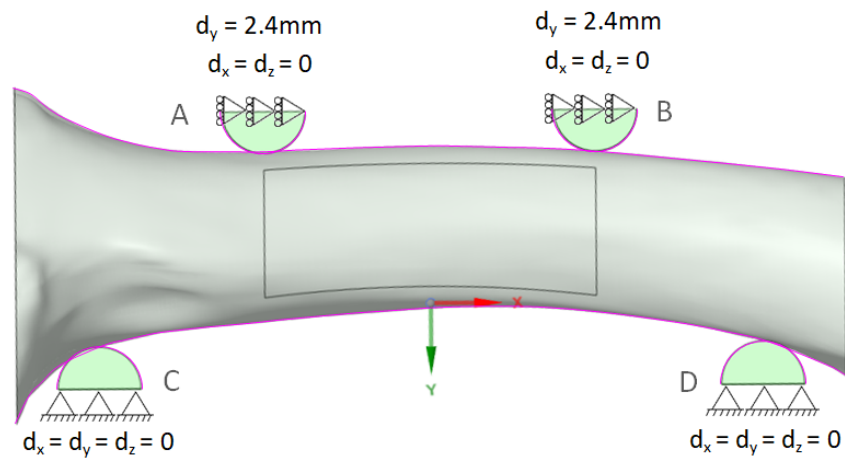


Figure 6-26: Diagram of the boundary conditions applied to the assembly of bone O1001 to simulate four-point bending by applying contact constraints between the rods and the bone (BC2).

A mesh convergence for each of the geometries (i.e. MOD1, MOD2 and MOD3) with homogeneous material properties (MAT1) was carried out for bonded (CONT1), frictional (coef. 0.5) (CONT2) and frictionless (CONT3) contact boundary conditions (BC2). Figure 6-27 shows the principal strain convergence plots for MOD1, MOD2 and MOD3 with bonded (CONT1) contact boundary conditions (BC2). The convergence plots showed a typical converging curve for both peak principal strains. The 0.5mm mesh (converged mesh size) highlighted in red is shown to have a percentage difference of <9% compared to the most refined mesh (0.33mm).

Contact model (BC2)

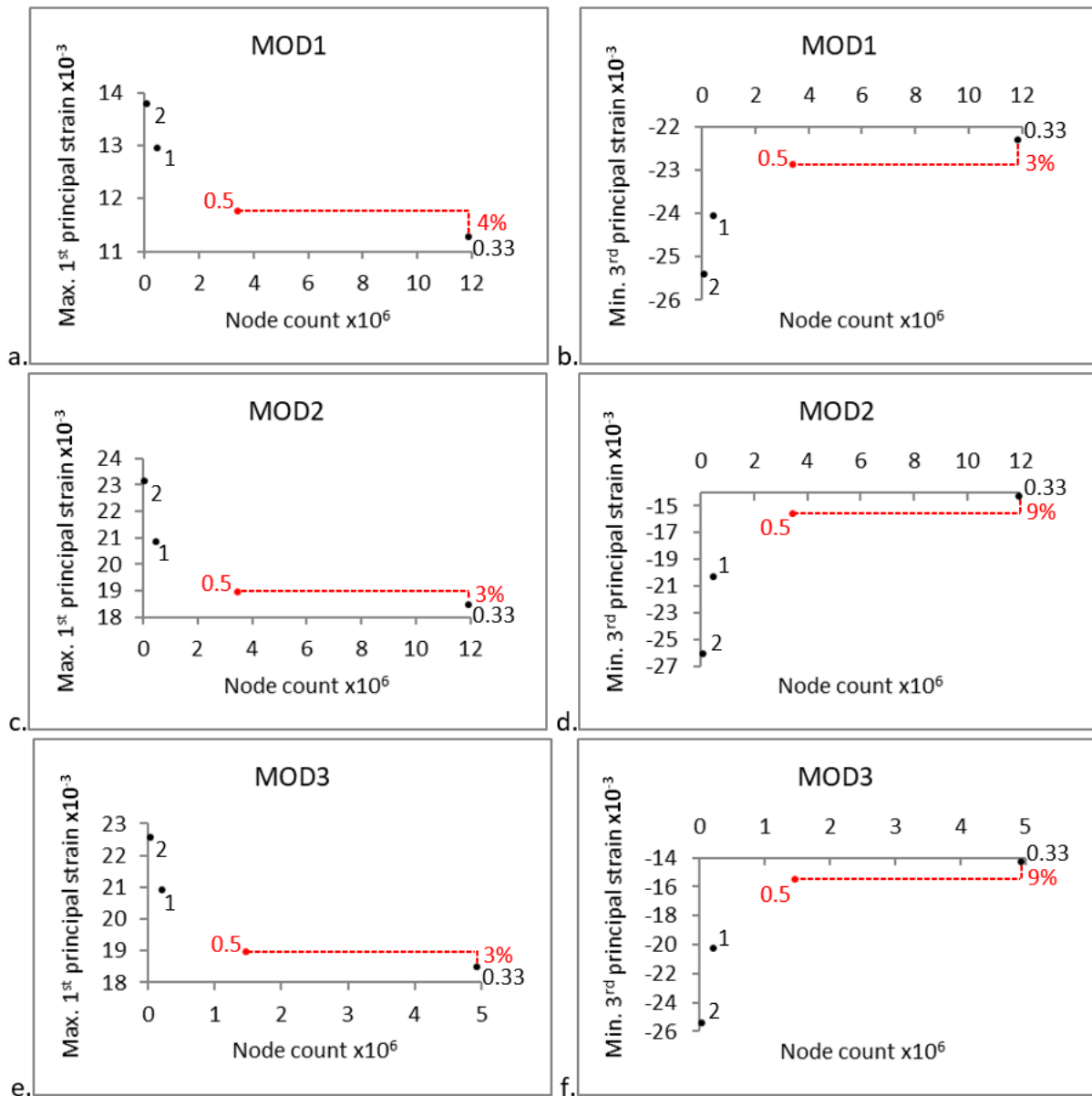


Figure 6-27: Principal strain convergence plots on bonded (CONT1) contact boundary conditions model (BC2) with a homogeneous mesh at element edge sizes 2mm, 1mm, 0.5mm and 0.33mm. Convergence of the maximum first principal strain and the minimum third principal strain for geometries MOD1, MOD2 and MOD3.

Neither the frictional nor the frictionless contact models were able to consistently achieve a stable and realistic solution at each mesh refinement. Some models did not converge at all, and some seem to experience excessive sliding and rigid body motion. An attempt to minimise the later was made by including initial penetration and increasing the frictional coefficient, however this was unsuccessful. It is possible that the multiple densities and material

properties (cortical bone and marrow) assigned to the bone had an impact on the solution and aggravated excessive sliding when the solution was unstable, given the model was not fully constrained.

6.1.8 Comparison against experimental results

The results from all finite element simulations using different combinations of boundary conditions (BC1 and BC2), contact definitions (CONT1, CONT2 and CONT3), model types (MOD1, MOD2 and MOD3) and material properties (MAT1 and MAT2) were compared qualitatively and quantitatively to the experimental data from Chapter 5 for bone O1001 at 2.7kN. The strain contours were first compared qualitatively against the DIC surface strain contours (shown in Figure 6-28) in order to narrow down the best modelling approach. The prediction from the best model was then compared quantitatively to the DIC by analysing the strain ranges as well as the force displacement curve measured on the load cell of the testing rig.

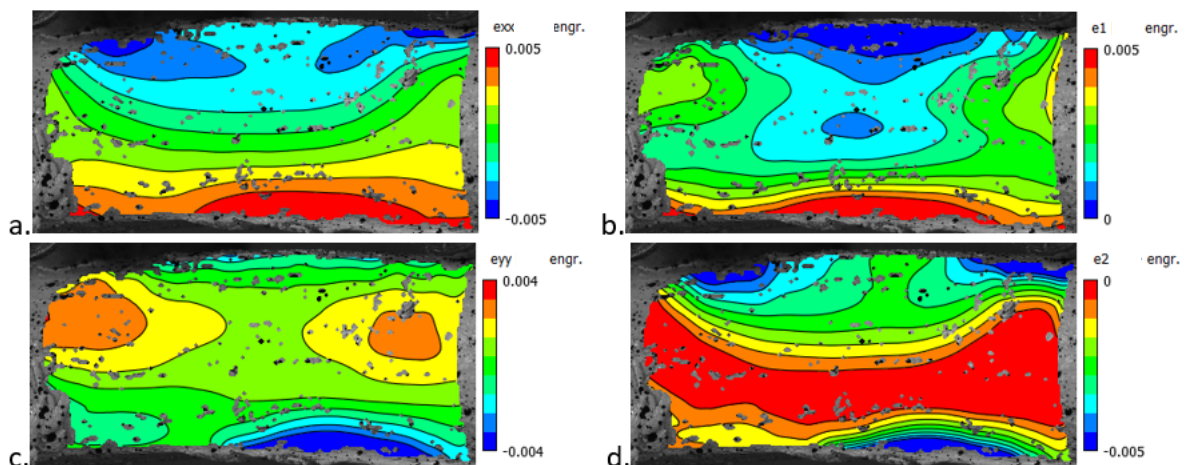


Figure 6-28: Surface strains of bone O1001 under four-point bending obtained through DIC at the end of the second linear region (LF2), at 2.7kN. (a) Engineering plane strains in the x-direction. (b) First principal plane strain (tension). (c) Engineering plane strains in the y-direction. (d) Second principal plane strains (compression).

The following list of features from the DIC images (above) was used as reference for qualitative comparison:

X-component of plain strain	Semi-circle of compressive strain at the top of the ROI.
	Compressive strain concentrations at the top right and left.
	Tensile strain band distributed longitudinally at the bottom of the ROI.
Y-component of plain strain	Flat ovals of tensile strain concentration on the left and right side at mid-height of the ROI; with the left oval slightly above and displaying higher strain.
	Low compressive strain band distributed longitudinally at the top and bottom of the ROI; with higher strain at the bottom right half and top right corner.
1 st principal plane strain	Peninsular tensile strain concentrations on right and left side at mid-height of the ROI; with the left side slightly above and more pronounced.
	High tensile strain band distributed longitudinally at the bottom of the ROI; connecting to the peninsulas at the corners.
2 nd principal plane strain	Semi-circle of compressive strain at the top of the ROI.
	Compressive strain concentration at the top corners and along the bottom border line on the right half of the ROI.

Table 6-5: Description of the strain contours for bone O1001 captured using DIC at 2.7kN.

6.2 Results

The results section is split into two parts. Part one exclusively presents solutions for bone O1001 at the end of the second linear region (2.7kN) of the experimental force-displacement plot with all the different FEM set ups. Part two shows the results of the best modelling approach applied to bones O1001 at end of both the first and the second linear regions for further qualitative and also quantitative comparison with the DIC.

6.2.1 Part one

From all FE models created using bone O1001, only **BC1/MOD1/MAT2** and **BC1/MOD2/MAT2** matched all the descriptions listed in Table 6-5. The FE-predicted strain maps generated with these two models are shown in Figure 6-29 and Figure 6-30. All contours were produced using the automatically generated strain range as this section is intended to focus on the strain distribution and not the magnitude (dealt with in Part two).

BC1/MOD1/MAT2

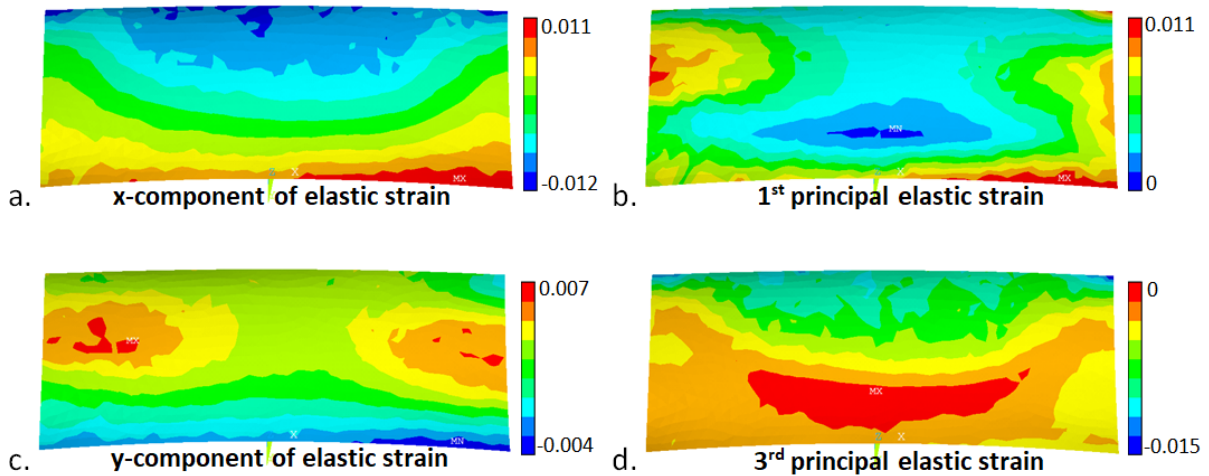


Figure 6-29: FE generated surface strains of bone O1001 using direct boundary conditions (BC1) on a whole shaft solid model (MOD1) with CT-based heterogeneous material properties (MAT2) at the end of the second linear region (LF2).

BC1/MOD2/MAT2

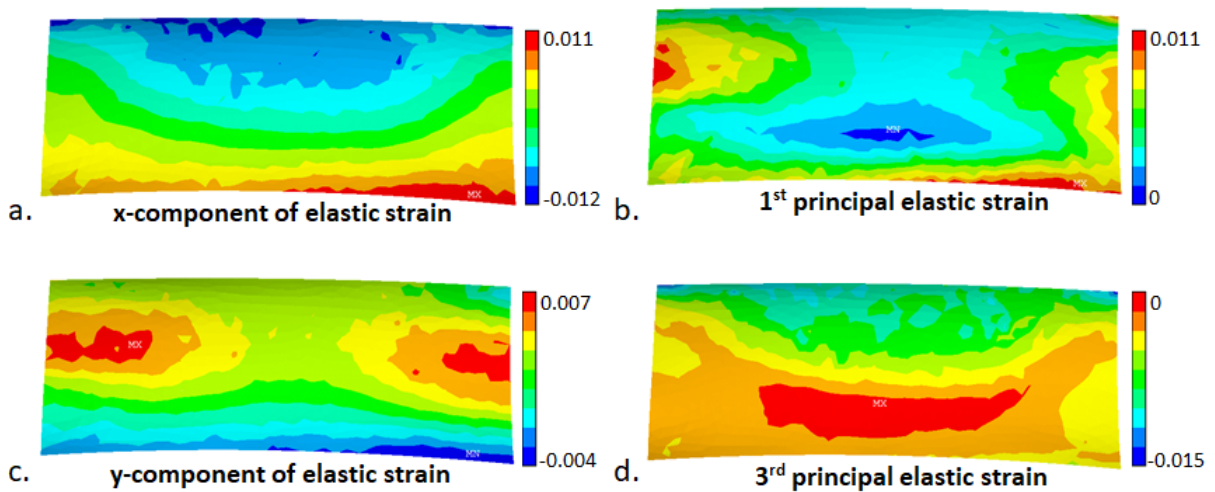


Figure 6-30: FE generated surface strains of bone O1001 using direct boundary conditions (BC1) on a whole shaft solid with a surface differentiating the cortical bone from the marrow model (MOD2) with CT-based heterogeneous material properties (MAT2) at the end of the second linear region (LF2).

Both simulations shown above resulted in very similar strain contours. MOD2 was ultimately chosen for further analysis (in part two below) as the model is geometrically more representative of the inner cortical surface (Figure 6-19). Note that the solutions obtained from the frictionless and frictional models were not presented here as they were deemed unstable during mesh convergence.

6.2.2 Part two

Part two presents the FE solutions (strains and reaction forces) using the model set up BC1/MOD2/MAT2 on bone O1001 at two points of interest, point 1 and point 2 (Figure 6-31); which represented the end of each linear region of the experimental force-displacement curves obtained in Chapter 5. At each point, the FE predicted strain was compared against the DIC results. Both the strain distribution and values were examined here.

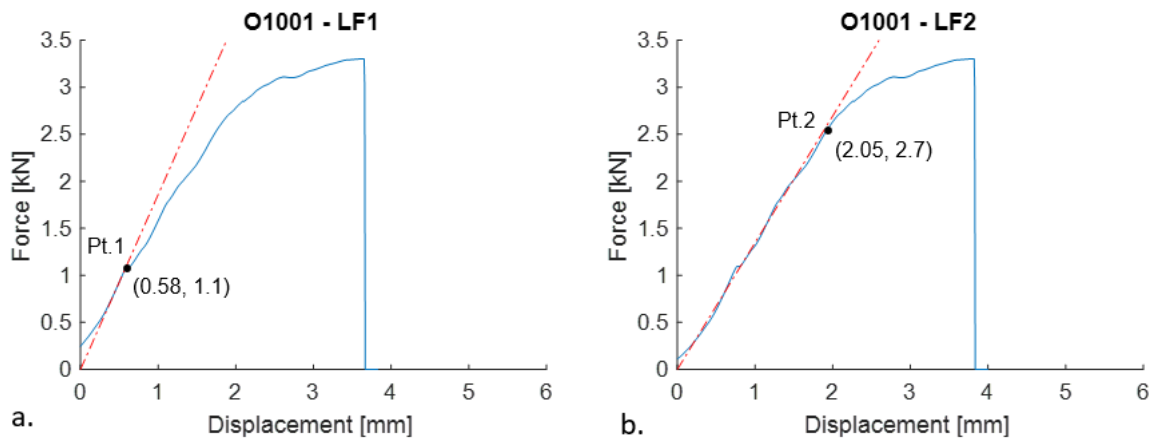


Figure 6-31: Linear corrections of force-displacement curves of bone O1001 obtained experimentally under four-point bending conditions in Chapter 5. The two linear fits are shown with the end points marked as point (Pt.) 1 and Pt.2, respectively, for each of the linear region.

The FE-predicted strain contours are shown below against the DIC surface strains in Figure 6-32 for point 1 and Figure 6-33 for point 2. The FE strains (right) are plotted in the same range as the DIC results (left). The FE predicted x and y components of elastic strains were compared against the DIC measured x and y components of plane strains. The FE predicted 1st and 3rd principal strains were compared against the DIC measured 1st and 2nd principal plane strains, respectively.

O1001 – Point 1

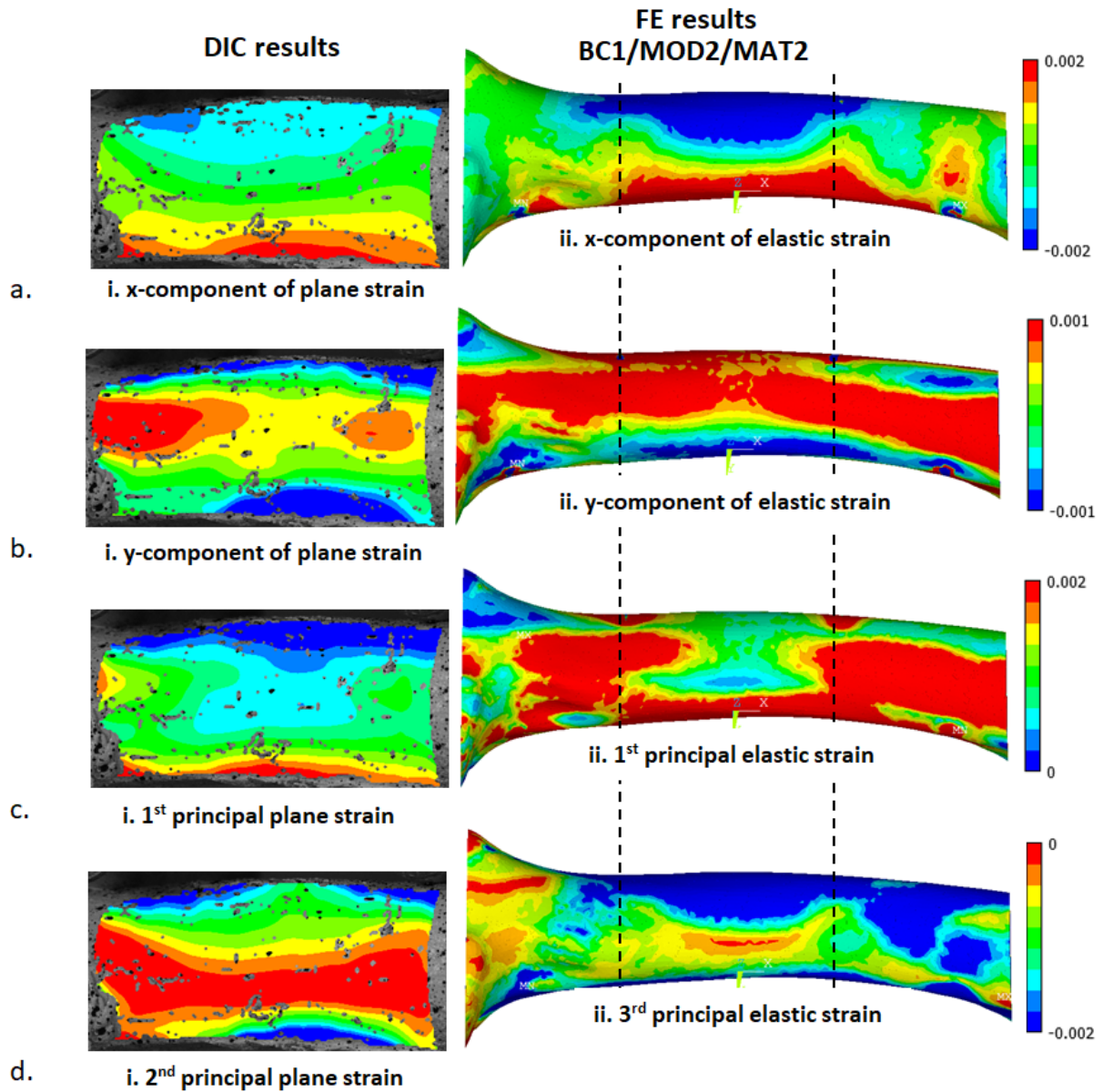


Figure 6-32: DIC measured (i) and FE predicted surface strains (ii) of bone O1001 using direct boundary conditions (BC1) on a whole shaft solid with a surface differentiating the cortical bone from the marrow model (MOD2) with 'Bone' kernel CT-based heterogeneous material properties (MAT2) at the end of the first linear region (LF1).

O1001 – Point 2

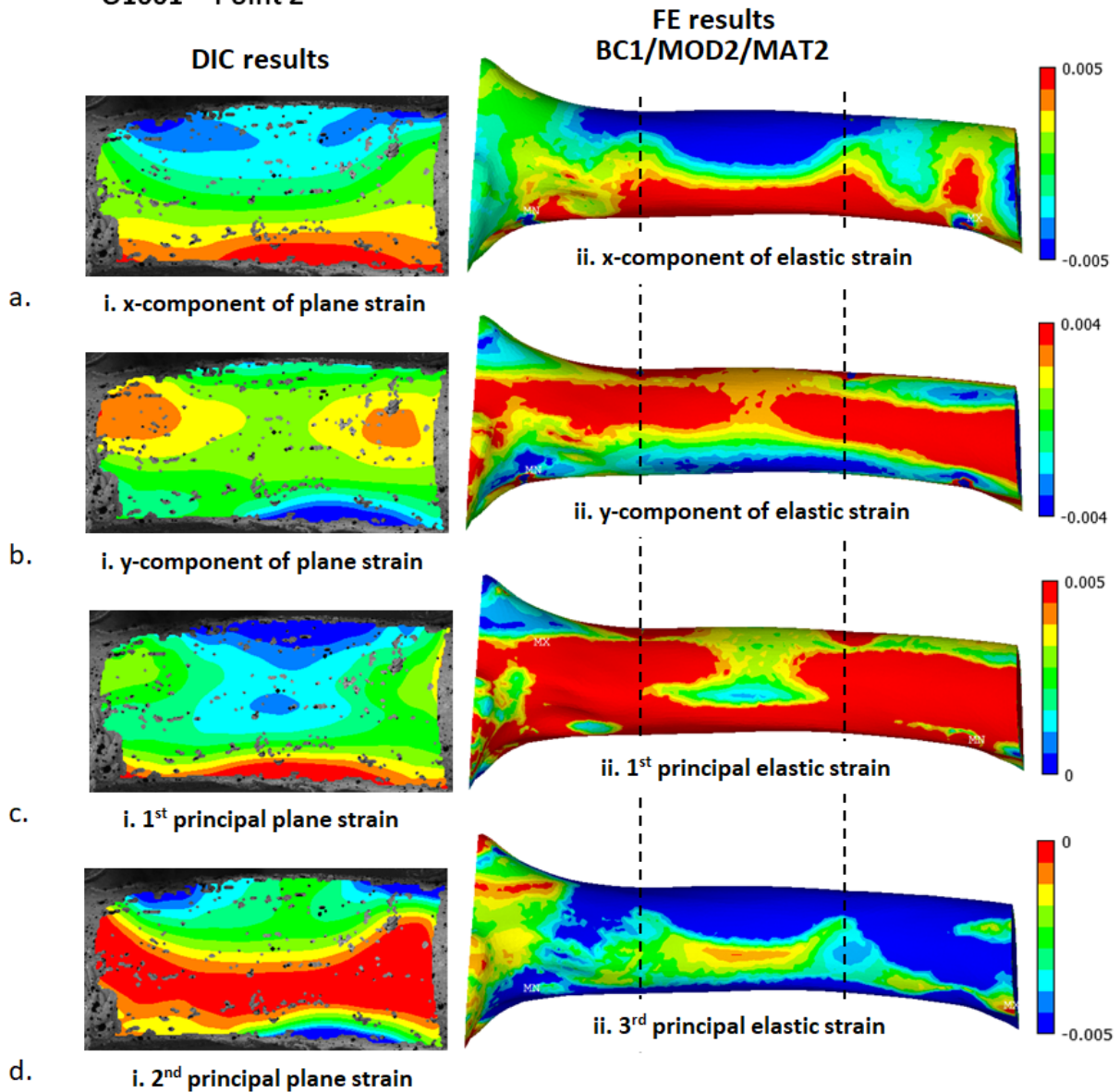


Figure 6-33: DIC measured (i) and FE predicted surface strains (ii) of bone O1001 using direct boundary conditions (BC1) on a whole shaft solid with a surface differentiating the cortical bone from the marrow model (MOD2) with 'Bone' kernel CT-based heterogeneous material properties (MAT2) at the end of the second linear region (LF2).

The overall magnitude of strains between DIC and FE results at points 1 and 2 were similar. Starting with the strain in the x-direction (Figure 6-32.a and Figure 6-33.a): the position of the neutral line (in green) and the magnitude of the tensile strain in the DIC image was accurately represented in the FE results. However, the FE produced a compressive strain (in blue) with a much higher magnitude. For the strain in the y-direction (Figure 6-32.b and Figure 6-33.b): the magnitude of the compressive strain in the DIC image was accurately represented in the

FE. However, the FE produced a tensile strain (in red) with a much higher magnitude. The magnitudes of both principal tensile and compressive strains were also over estimated by the FE (Figure 6-32.c&d and Figure 6-33.c&d).

The FE predicted y-component of the reaction force are listed in the table below (Table 6-6). At point 1, the reaction force obtained in the FEA was 3 times higher than the force measured in the experiment. At point 2, the reaction forces obtained in the FEA was 4.3 times higher than the force measured in the experiment.

	Reaction force FY [kN]	
	Point 1	Point 2
Experimental	1.1	2.7
FE	3.3	11.7

Table 6-6: FE predicted y-component of the reaction force measured on the nodes with applied displacement constraints for bone O1001.

6.3 Discussion

This section discusses the accuracy of the modelling techniques (boundary conditions, model geometries and material properties) and their limitations.

6.3.1 Boundary conditions

Two separate approaches were used to simulate bending on bone O1001: direct boundary conditions and contact boundary conditions. Direct boundary conditions were used to exclusively model the linear behaviour of the bone, whereas frictional and frictionless contact boundary conditions were used to model the overall behaviour including any non-linearity arising from full body motion (rotation). The solutions and limitations of the direct models and contact models are discussed below.

6.3.1.1 Direct (BC1)

The distribution of the strain contour obtained using direct boundary conditions compared well against the experimental plots. However, the magnitude of the FE predicted strains were much higher than those of the experimental strains. This discrepancy could be a potential effect of either material definition (discussed later on) or/and of an over estimation of the equivalent displacement of the rods within the linear region. It is possible that the

assumptions made in order to find the equivalent displacement of each linear region in the force-displacement plots (e.g. visual identification of the linear regions) could have led to an overestimation of the displacement, and subsequently of the strain magnitude.

6.3.1.2 Contact (BC2)

Frictionless (slide without resistance, CONT3) and frictional (slide with resistance, CONT2) contact models were used to replicate sliding and its non-linear effect. Both frictional and frictionless contact definitions were trialled on the three homogeneous model types (MOD1, MOD2, MOD3), however only the frictional model converged to a realistic solution; albeit being unstable and only reaching a solution for certain element sizes (Figure 6-34).

BC2/CONT2/MOD1/MAT2

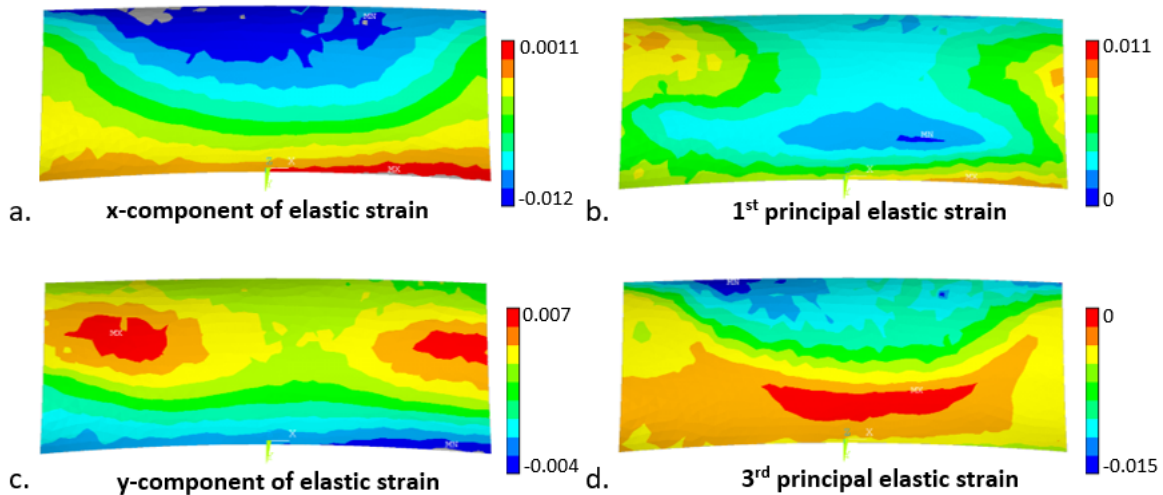


Figure 6-34: FE generated surface strains of bone O1001 using contact boundary conditions (BC2/CONT2, frictional with coefficient of 0.5) on a whole shaft solid with a surface differentiating the cortical bone from the marrow model (MOD2) with CT-based heterogeneous material properties (MAT2) at the end of the second linear region (LF2).

Unlike the frictional and frictionless models, the bonded contact models were able to quickly reach a solution. However, the resulting strain contours did not compare well against the experimental DIC strain contours; which highlighted the impact of over-restricting sliding and rotation.

6.3.2 Model types

The proximal femur is commonly modelled as a single body without any geometrical distinction between the cortical bone, trabecular bone and marrow (defined as MOD1). However, this has limitations in terms of material property distribution: it is not suitable when applying homogeneous material properties because of the inability to accurately capture the drastic material difference between the marrow and bone, particularly in immature bones that are smaller in size. Indeed, MOD1 did not compare well to the experimental results when assigned homogeneous material properties.

Not having any delineation between cortical bone and marrow also had limitations when assigning CT-based heterogeneous material properties, such as the partial volume effect which could misrepresent the inner cortical surface, and potentially the cross-sectional strain distribution. Nonetheless, the strain contours of MOD1 when assigned heterogeneous material properties (Figure 6-29) compared well qualitatively against the experimental DIC strain contours.

Partial volume effect was resolved by delineating the inner cortical surface (MOD2). When assigned heterogeneous (MAT2) material properties (Figure 6-30), the external surface strain contours compared well to the experimental DIC contours. When assigned with a CT-based homogeneous mesh (MAT1), MOD2 also nearly fit the comparison criteria (Figure 6-35) with the exception of the bottom left corner of the ROI in the principal strain contours shown below (Figure 6-35.b and Figure 6-35.d). The underestimation of strain seemed to be caused by an inaccurate modelling of a small region of trabecular bone (unexpectedly) found at the bottom left corner (Figure 6-36). A homogeneous mesh in this region (of cortical bone properties) would have led to an over-estimation of the actual mechanical properties.

BC1/MOD2/MAT1

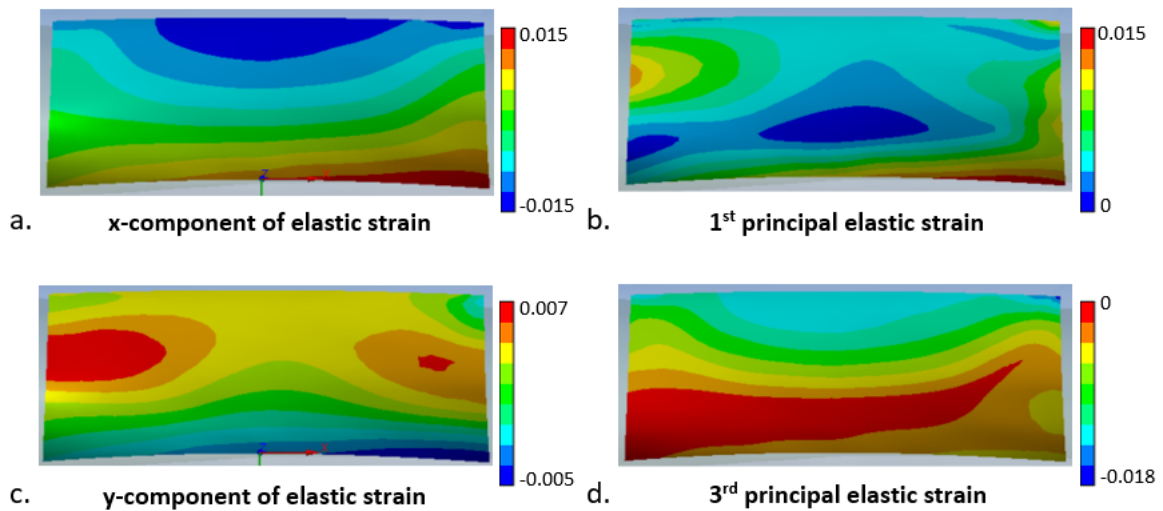


Figure 6-35: FE generated surface strains of bone O1001 using direct boundary conditions (BC1) on a whole shaft solid with a surface differentiating the cortical bone from the marrow model (MOD2) with CT-based homogeneous material properties (MAT1) at the end of the second linear region (LF2). Reaction force = 13.4kN.

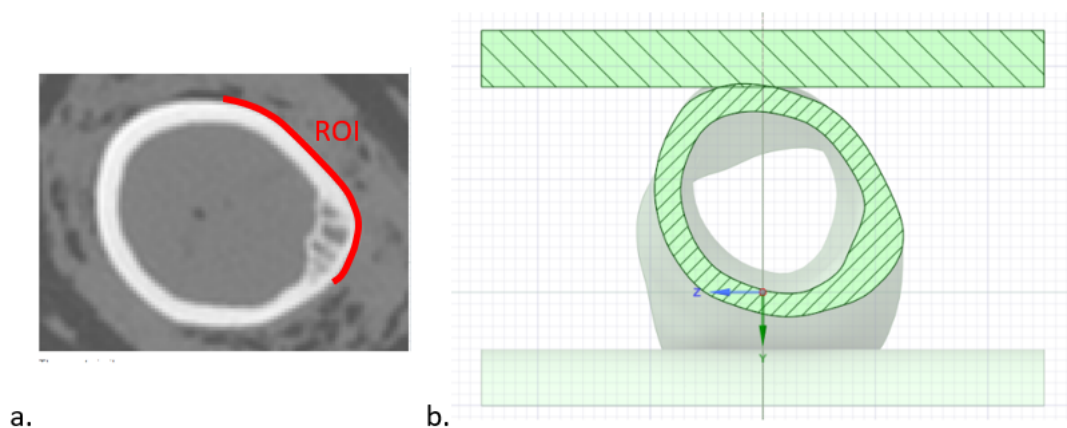


Figure 6-36: Cross-section of bone O1001 corresponding to the left border of the ROI seen on a CT-image (a) and FEM image (b). The small patch of trabecular bone can be seen at the bottom right corner of the cross-section on the CT image.

In order to reduce the computational time, the model was also simulated as a hollow shaft without the marrow (MOD3). However, the resulting strain contours of when assigned with heterogeneous material properties did not compare well against the experimental DIC contour strains.

6.3.3 Material properties

The accuracy of material property definition was assessed by looking at the derived ash density, the elastic modulus values, the FE predicted reaction force, and the maximum compressive and tensile strain values.

6.3.3.1 Ash density

The ash density values of bone O1001 derived from the CT-attenuation (mean intensity) compared well against ash density values reported in the literature, for both trabecular and cortical bones. The ash density derived at the centre of the femoral condyles (0.28-0.35g/cc) (Table 6-4) was close to the range of ash density measured at the tibial condyles of immature ovine bones in (Nafei et al. 2000). In the study, Nafei measured ash densities of 0.25g/cc, 0.29g/cc and 0.29g/cc, for lambs aged 3, 6 and 9 months, respectively.

The ash density derived at the midshaft (1.2g/cc) (Table 6-3) was also in range compared to values reported in the literature for children, adult and bovine cortical bones. (Dall'Ara et al. 2011) reported an ash density between 0.7-1.5g/cc for bovine and adult femoral cortical bones; (Öhman et al. 2011) reported measurements of 0.6-1.3g/cc in both children and adults; and (Tassani et al. 2010) reported values of 0.7-1.2g/cc in adult cortical bone.

6.3.3.2 Elastic modulus

In this chapter, two methods were used to assign material properties to the model. The first method assigned homogeneous material properties to the mesh with an elastic modulus calculated from the CT mean intensity over the cortical thickness (MAT1). The second method assigned element-based heterogeneous material properties by directly mapping elastic modulus from the CT images to the mesh (MAT2); i.e. using each voxel intensity value rather than using an average across the cortical thickness. For both MAT1 and MAT2, the modulus was obtained using Grant's suggested power equation for FE modelling (Eq.6-1) ((Grant et al. 2014). The resulting elastic modulus obtained with each method is discussed below.

The elastic modulus using MAT1 compared well against the literature for cortical bone, which was used in the models. The cortical elastic modulus used for the homogeneous model (16GPa using the 'Bone' kernel) was in range with Grant's own study. In comparison, Grant reported a longitudinal elastic modulus of 15-26GPa on the cortical bone of an adult ovine

tibia. MAT1 was also applied to trabecular VOIs for verification purposes (not used in modelling) (Table 6-4). The derived trabecular homogeneous modulus values did not compare well against the literature. The values obtained (1.72-2.61GPa) were at least twice the values published by (Nafei et al. 2000) for immature ovine tibia (0.6-0.76 GPa) and were also higher than the values reported for mature ovine tibia (0.87-1.51GPa). It is unsurprising that only the cortical elastic modulus compared well with Grant's findings as it was within the density range based on which the empirical equation was built. This suggests that Grant's empirical equation is limited to a short range across the cortical bone density only.

The estimated elastic modulus range of the cortical heterogeneous bone (MAT2) was unusually wide. The values obtained across the cortical thickness at the midshaft ranged from 3-25.7GPa. The minimum value was far smaller than what was expected for cortical bone and the maximum value was also above Grant's measured range (15-26GPa). The distribution of the elastic modulus across the midshaft cortical thickness also seemed inaccurate. In a non-pathological femur, the elastic modulus across a poreless cortical thickness should remain fairly constant over the majority of the thickness with a slight decrease at the periosteal and endosteal surfaces. However, in Figure 6-37 below, the estimated elastic modulus peaked over only a third of the thickness at midway. This unusual material distribution across the thickness could be caused by a combination of the cortical thickness, CT precision (slice spacing and thickness), filter backprojection (FBP), and Grant's power equation. The cortical thickness of the bone was thin with respect to the CT slice spacing and thickness, therefore, FBP blurred a large portion of the bone at the periosteal and endosteal surfaces. As a consequence, any changes in CT attenuation which were mostly caused by FBP were exacerbated by Grant's power equation. In addition, when using heterogeneous material (MAT2) over model types MOD1 and MOD2, the marrow resulted in an elastic modulus of 0.14-0.29GPa, compared to 0.25-24.7kPa found in the literature. This again suggests that Grant's power equation is only suitable for a short cortical density range and is very sensitive when used for material mapping on immature (small) bones based on QCT scans.

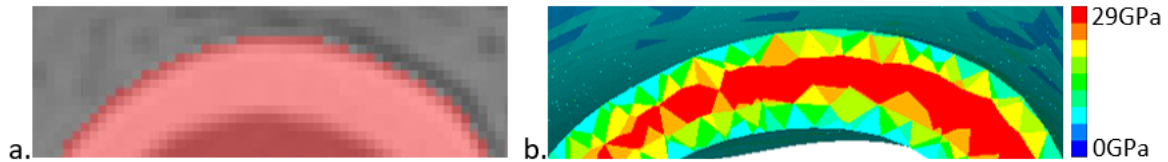


Figure 6-37: (a) Transverse segmentation over CT image of bone O1001 at the midshaft showing the cranial side. (b) Transverse cross-section of FE model at the midshaft showing the elastic modulus derived using heterogeneous material MAT2.

6.3.3.3 Reaction force

The FE predicted reaction forces of MAT1 and MAT2 models were higher than those measured experimentally in Chapter 5. The magnitude of the force was 13.4kN for the MAT1 models and 11.7kN for the MAT2 models compared to 2.7kN measured during the four-point bending test. The difference between FE and experimental reaction force was most likely a result of the elastic modulus derivation as discussed above.

6.3.3.4 Strain contours

The discussion focused on the FE results obtained through the modelling pipeline BC1/MOD2/MAT2, which was the best match against the DIC results. For bone O1001, the model returned a similar strain contour to that of the DIC measured strain for the x and y component and the principal strain maps. Therefore, the FE model can accurately predict strain distribution in the ovine bone.

6.3.3.5 Strain magnitudes

The FEM overestimated the magnitude of the compressive strain of the x-component strain map, and the tensile strain of the y-component strain map. Moreover, it also overestimated the magnitude of the principal tensile and compressive strains.

The heterogeneous model used here consisted of a mesh with isotropic elastic modulus. As stated in Chapter 2, haversian and in particular plexiform cortical bone in long bones, have a higher elastic modulus in compression than in tension when measured along the axis of the bone (defined as the x-axis). It is possible that the later also applies to immature lamb bone. Therefore, using an isotropic material may not be an accurate assumption and could have under-estimated the elastic modulus in compression in the long axis. This could have led to the overestimation of the compressive strain of the x-component strain map.

The tensile elastic modulus of harversian and plexiform bone is also stronger when measured along the axis of the bone as opposed to transversally (defined as the y-axis) (Chapter 2). As described in Chapter 5, the islands of tensile strains measured were caused by transversal stress. Therefore, the isotropic material assumption could have also caused the overestimation of the tensile strain in the y-component strain map.

The magnitude of the principal tensile and compressive strains were expected to be overestimated in the FEA. DIC only measures in-plane principal strain (e.g. 2D strain tensor), whereas the principal strains obtained in FEA also accounted for out of plane strains (e.g. 3D strain tensor). Due to the high thickness to effective length ratio, in theory the ovine bones should have both in and out of plane strains caused by the bending stress. This is another contributing factor to why the FEA principal strains were higher than those measured by DIC.

6.4 Conclusions

Applying direct boundary conditions onto the models achieved similar results as the (frictional) contact models. Furthermore, the direct models provided good solution stability compared to the (frictional) contact models. Therefore, direct models seem to be appropriate to simulate controlled four-point bending and elucidate femoral shaft bending behaviour while optimising computational efficiency.

Although both MOD1 and MOD2 compared well against the DIC strain results, MOD2 appeared to be a better modelling method. Delineating the cortical bone from the marrow produced a more accurate representation of the inner cortical surface. Moreover, by delineating the inner cortical surface, the model became more adaptable to the use of homogeneous material properties. Indeed, the results suggested that the diaphysis (where the bone is purely cortical) could be accurately modelled by a homogeneous model that differentiated the cortical bone from the marrow using two separate material definitions.

Grant's empirical equation was not suitable for neither the homogeneous nor the heterogenous bone models. The derived elastic modulus was too high, particularly for the marrow. This is likely why the FE over predicted the reaction force. Perhaps another ovine femur specific equation would better predict the elastic modulus of the cortical bone in future.

Finally, the differences between the FE and DIC strains suggested that isotropic material assumption may not be the most suitable for modelling of long bone harversian/plexiform cortical tissues. This should be investigated in future.

7 FOUR-POINT BENDING TEST ON EMBEDDED LAMB BONES

7.1 Introduction

The aim of this chapter was to collect full field surface strain data on immature ovine bone using DIC, by implementing some suggested improvements described in Chapter 5. It focuses on the flexural mechanical behaviour of the femoral diaphysis; more specifically strains on the lateral-cranial part of the mid-shaft.

The first improvement implemented based on Chapter 5 was to embed the bones at both epiphyses in cubes of resin (Figure 7-1). The embedding was used to stop the bones from undergoing free body motion during testing. It was also used to prevent local crushing under the rods as the bones were loaded indirectly and the load was distributed through the resins. Furthermore, the embedding allowed the experimental set up to be more consistent and the overall positioning of the bone to be more accurate compared to the first set of experiments reported in Chapter 5.

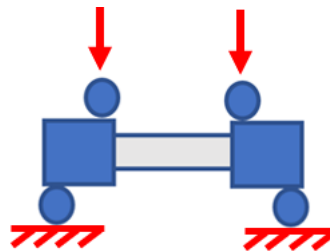


Figure 7-1: Diagram of improved experimental set-up for four-point bending in order to achieve a more consistent result.

Another change implemented was to remove the periosteum from the shaft of the bones and paint speckles over the bone directly. It was shown in Chapter 5 that the periosteum help hold the bone together after an initial fracture, and at high strains the periosteum detaches from the bone. In order to directly correlate speckle movement with the bone strain, the speckles should be painted on the bone rather than the periosteum surface.

Finally, the angle of the stereo system was also changed in order to capture the bottom region of the specimens where maximum tensile strain is expected in four-point bending.

The above improvements were made in order to produce the second set of experimental DIC data reported in this chapter, which will later be used for the validation of CT-based FE models in Chapter 8.

7.2 Methods

7.2.1 Materials (bones)

For this set of experiment, a total of nine food graded lamb femurs were collected. Ethical approval was waived on the basis that the bones were categorized as food produce.

Four lamb femurs, labelled D2001, D2002, O2001 and O2002 were purchased from a supermarket (Ozmen) in Sheffield, UK. These were pre-cut and left in a refrigerator. When collected, the bones showed signs of dryness and oxidation and the periosteum presented obvious damage. The origin of O2001 to O2002 was unknown.

Another five femurs, labelled A2001 to A2005, were collected from a local butcher (Beeches of Walkley) in Sheffield, UK. Femurs A2001 to A2005 were of a certified New Zealand origin. All five bones were butchered from the same frozen slaughter house leg batch (label attached in Appendix 3). The legs were defrosted and the femurs were removed by the butcher on demand and immediately stored frozen onsite.

Once collected, all bones were separated, double bagged individually, labelled and stored frozen at -20° degrees. Unlike the method used in Chapter 5, the bones were bagged without being wrapped in any saline solution. This decision was made because the saline solution needed to melt completely before cleaning and potting of each specimen, which would substantially increase the number of freezing cycles and overall storage time. The sample preparation details are explained in the following section.

The thickness and diameter of O2001, O2002 and A2001 to A2005 was measured in SpaceClaim Ansys 2021R2 and micro-CT as explained in Chapter 8. Bones D2001 and D2002 were used as dummies to practice the sample preparation method and four point bending test set-up. Therefore, no micro-CT measurements were presented here for these two bones. In addition, two unplasticized polyvinyl chloride (uPVC) pipe samples were used to test the stereo system set-up. Table 7-1 provides a summary of the nine ovine femurs used in this chapter.

Bone	Source	Origin	Batch	Limb
O2001	Ozmen	Unknown	n/a	Right
O2002	Ozmen	Unknown	n/a	Left
A2001	Beeches of Walkley	UK	LT2182970	Right
A2002	Beeches of Walkley	UK	LT2182971	Left
A2003	Beeches of Walkley	UK	LT2182972	Left
A2004	Beeches of Walkley	UK	LT2182973	Right
A2005	Beeches of Walkley	UK	LT2182974	Left
D2001	Ozmen	Unknown	n/a	--
D2002	Ozmen	Unknown	n/a	--

Table 7-1: List of lamb femur samples used for experimental testing. Samples D2001 and D2002 were under-lighted as they were used as dummies and no results were presented for either.

7.2.2 Sample preparation

The sample preparation was performed in three steps: the bones were cleaned and cut, they were then embedded in resin, and lastly rehydrated and painted. The cleaning, cutting and embedding processes were performed on frozen bone for practicality. The bones were also prepared one at a time in an attempt to keep them frozen and reduce the total amount of freezing cycles (and hence the decision not to wrap in saline solution); which has been shown to affect the material properties of bone (Zhang et al. 2018). Detailed procedures are described below.

7.2.3 Cleaning and cutting

Soft tissues were removed from around the diaphysis of each bone using surgical scalpels, blade no.10 and no.11 (Swan Morton). The periosteal sheath was peeled off the shaft using pliers. The bone was then slowly wiped with sanding paper grit 300 to remove any periosteal residuals.

Once cleaned, the bones were marked up for alignment. A line across the cranial face of the shaft was drawn by using an elastic band placed along the bone, similarly to the alignment method detailed in Chapter 6 (Figure 7-2).

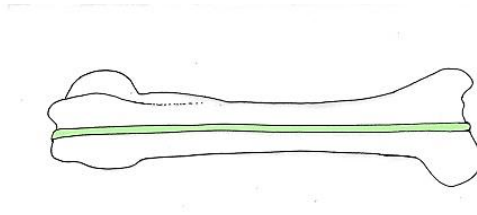


Figure 7-2: Cranial view of a lamb femur with an elastic band showing the shortest path along the longitudinal direction.

Immediately after, whilst the bones were still frozen, they were gripped using a Stanley rotary vice with rubber grips. The proximal and distal epiphyses were sawed off using a junior hack saw (Figure 7-3). Once cut, the shafts measured between 75mm and 85mm in length. The shafts were individually bagged and put back into the freezer (without saline).

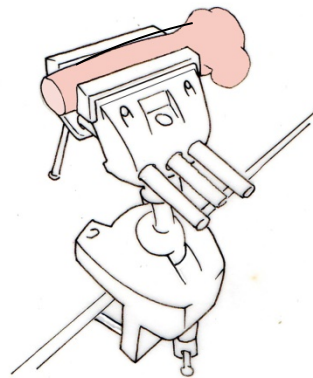


Figure 7-3: Illustration of lamb femur clamped in vice, sawed off at the proximal end.

7.2.4 Embedding

Technovit 4071, a two-part PMMA (Polymethyl methacrylate), was used to embed both ends (proximal and distal) of the cropped bone shafts. Technovit 4071 is often used as an embedding material for bones in CT-based studies. There are three advantages to Technovit: 1) it is a fast-curing two-part resin; thus, it is practical for the embedding of organic tissues which cannot be left at room temperature for long periods of time; 2) the reaction between the two components generates relatively low heat and is unlikely to alter the material properties of the bone, particularly if embedded frozen; 3) it has a lower X-ray attenuation than bone that contrasts well in CT-scans, making it ideal for segmentation (Chapter 8).

Both ends of each shaft were embedded in 35x35mm Technovit 4071 cubes using silicon moulds. The total length of the specimen (bone shaft and cubes) was determined according to the size of the cubes, the testing machine limitations and depth of embedding. In order to maximize bending moment, the span between the bottom and top rods had to be kept as wide as possible. A target 5mm distance (equivalent to the radius of the rods) between the edge of the embedding and the rods was chosen, leading to a span of 25mm between the bottom and top rods (CA and BD in Figure 7-4). The machine was limited to three pre-set spans for the top rollers, at either 50mm, 70mm or 90mm. Therefore, the three possible total length were 110mm, 130mm or 150mm (Figure 7-4).

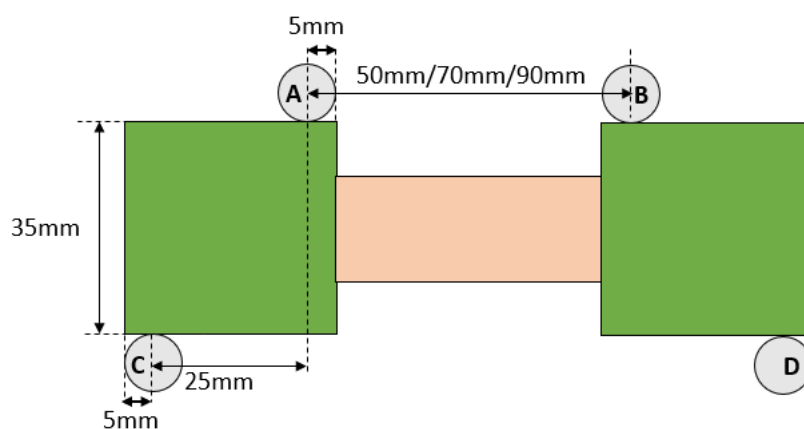


Figure 7-4: Dimensions for embedding (in green) of the proximal and distal ends of the lamb femoral shaft (in pink), where A/B, and C/D are the top and bottom rods of the testing rig respectively (in grey).

A trial was performed on specimens D2001 and D2002 in order to determine the depth of the embedding and the span of the four-point bending set up. For comparison, D2001 was shallowly embedded (150mm total length) and D2002 was deeply embedded (110mm total length) (Figure 7-5). During the preliminary tests, the embedding of bone D2001 broke very swiftly, causing the bone to slip out of the resin and the premature termination of the experiment. In contrast, bone D2002 achieved a fracture in the middle without obvious damage/slippage at either ends; showing that a deep embedding was preferable in order to see bending behaviour on the bone before failure of the embedding material itself. Therefore, all remaining specimens were deeply embedded to achieve an approximate total length of 110mm.

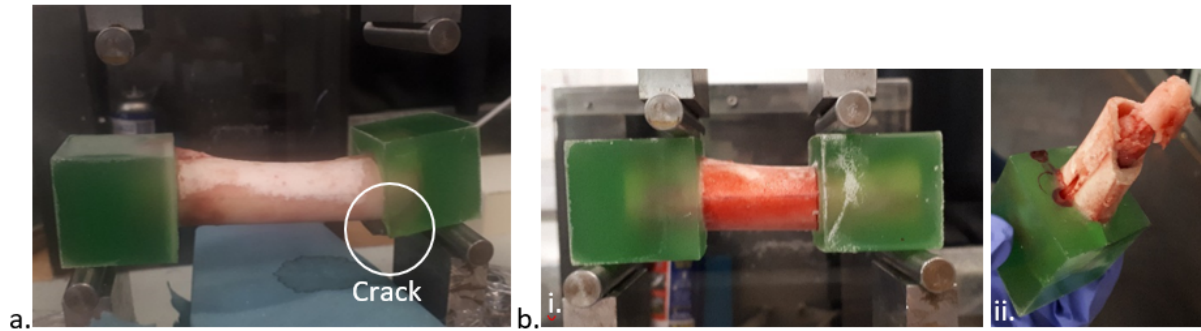


Figure 7-5: Images of the preliminary four point bending tests performed to find the most suitable depth of embedding and length. Specimen D2001 (a), which measured 150mm in length cracked promptly in the embedding material. Specimen D2002 (b), which measured 110m fractured at the midshaft (b-ii).

As mentioned previously, the embedding was poured on frozen bone. Performing this process on frozen bone prevented the blood from pouring out of the marrow, which would have created a blood pool within the embedding. Maintaining fluids within the marrow also ensured that the inner surfaces of the bones were kept hydrated for the mechanical tests later on. The embedding on each side was performed one at a time to allow for curing time. The bones were first embedded on the proximal end, put back in the freezer to fully freeze, and then taken back out to embed the distal end. The embedding process is detailed below.

To start with, the total length of the cropped femur was measured. The bone was then held up vertically by the chemistry stand with the cranial line facing forward and proximal end facing down (Figure 7-6). It was placed at an appropriate height to ensure it was centred, allowing for the same amount of embedding on both sides. A laser level was used to align the cranial line with the middle of the embedding mould (35x35mm silicone mould).

Once the bone was positioned, a Technovit 4071 mixture was prepared with a 1:2 liquid to powder ratio (as per product instructions). The quantity used for each cube was approximately 15g liquid and 30g powder, based on conversation with other researchers in the group. In order to minimize bubbles, the Technovit was mixed in different phases: 15g liquid was first poured in a mixing cup, 15g powder was then added and stirred until homogeneous, finally another 15g powder was added and stirred for another 20 seconds, as recommended by the manufacturer.

The mixture was poured into the mould and left to set for 20-30 mins under a fume cupboard. Once hardened, the bone was taken off the chemistry stand and put back in the freezer.

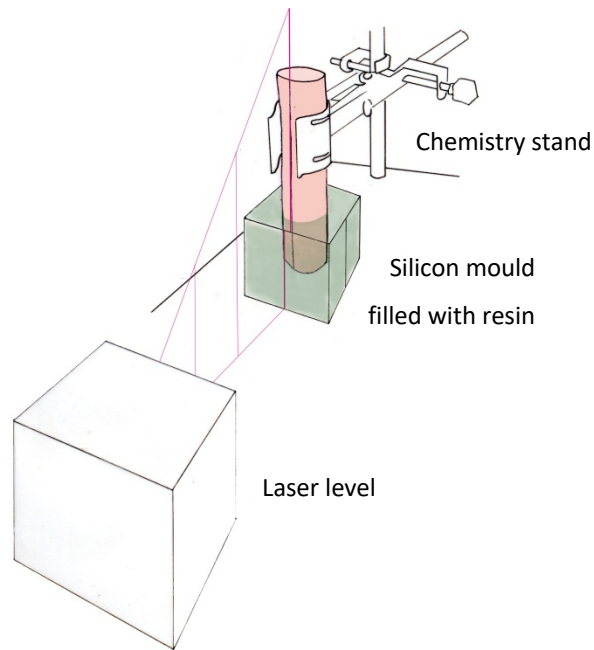
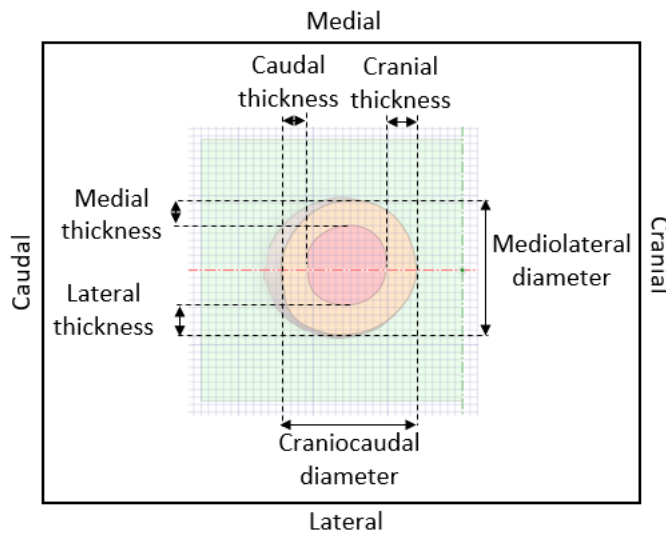
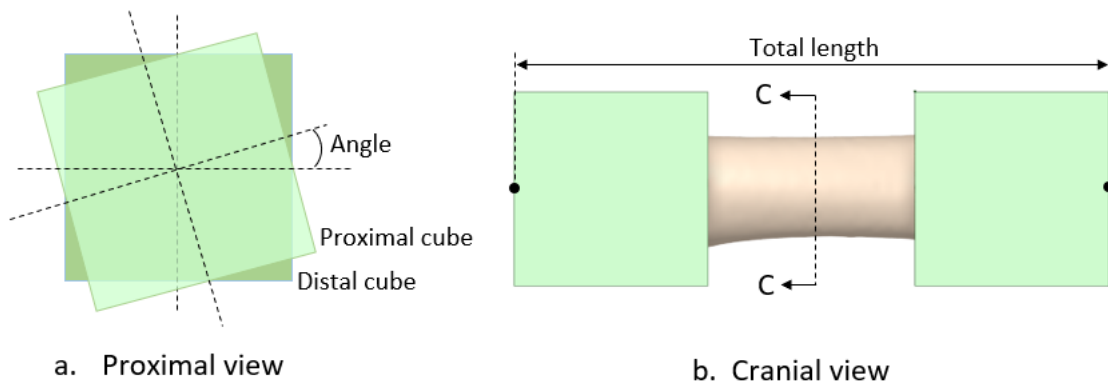


Figure 7-6: Set-up for aligning and embedding bone shafts into blocks of PMMA.

To embed the distal end, the bone was again held up vertically by a chemistry stand with the cranial line facing forward. A mini level was used to ensure that the proximal embedding was levelled. An angle ruler and a laser level were then used to align all sides of the distal mould with the proximal mould and the cranial line on the specimen. Another mixture of Technovit was prepared and poured in the silicon mould. The distal embedding was left to set for 20-30mins. Once hardened, the moulds were removed and the specimen was stored back in the freezer (without saline).

At the end of this process, all specimens were re-measured via CAE on micro-CT scans (as explained in Chapter 8) to check for alignment. Measurements of the angle between the two cubes (Figure 7-7.a), the total length of the specimen (Figure 7-7.b), and the diameter and thickness of the diaphysis at the mid-section (Figure 7-7.c) are illustrated and listed below (Table 7-2).



c. Section C-C

Figure 7-7: CT-based reverse engineered model of lamb femur bone O2001. (a) Proximal view showing the angle between two embedding blocks. (b) Cranial view showing the total length. (c) Transverse cross-section of the mid-shaft as defined in Chapter 8, showing the cranial-caudal, and medial-lateral diameter and cortical thickness in each direction.

Bone	Total length [mm]	Angle [deg]	Craniocaudal diameter [mm]	Thickness [mm]		Mediolateral diameter [mm]	Thickness [mm]	
				Cranial	Caudal		Medial	Lateral
O2001	107.4	1.4	18.07	3.98	3.56	18.03	3.96	3.36
O2002	114.1	0.2	19.77	3.91	3.15	19.79	3.58	3.36
A2001	110.0	4.5	22.63	3.43	2.44	22.71	2.50	3.34
A2002	107.9	1.7	23.31	4.43	2.78	21.70	3.77	2.81
A2003	111.9	1.6	21.25	2.87	2.55	22.18	3.41	2.43
A2004	110.5	0.4	24.06	4.51	2.59	21.03	3.13	2.90
A2005	110.2	3.3	20.09	3.99	2.98	18.67	3.08	3.31

Table 7-2: Dimensions of lamb femurs taken via CAD on micro-CT-based reverse engineered models.

In addition to the bones, two uPVC pipe samples, labelled PVC1 and PVC2, were made in order to test the set-up of the stereo system. A uPVC pipe with an external diameter of 20mm and a thickness of 1.7mm was sectioned into two tubes of length 95mm with a junior hacksaw. Each tube was embedded at either side with Technovit 4071, following the same procedure used to embed the lamb femur samples (Figure 7-8).

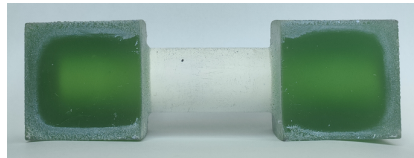


Figure 7-8: Embedded uPVC dummy, PVC1, used to test the set-up of the stereo system.

7.2.5 Rehydration and painting

Prior to testing, the samples were plunged in saline water and left to reach room temperature for 2-3hours. They were then left to drip for approximately 20mins and wrapped in cling film (Figure 7-9).

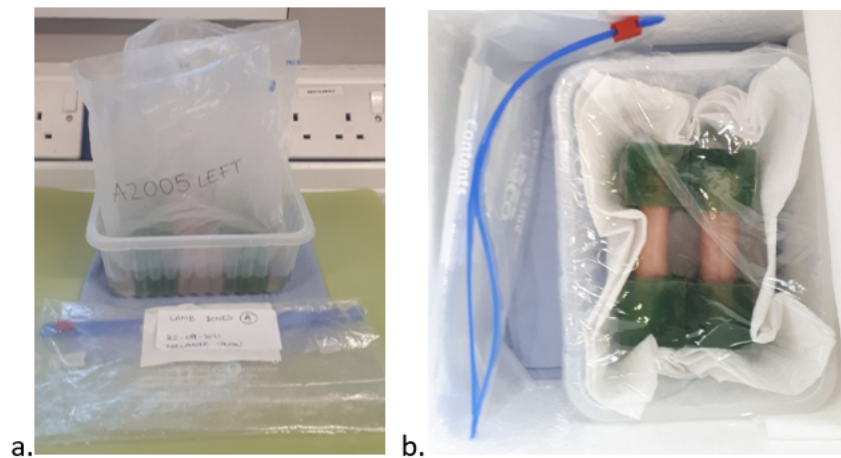


Figure 7-9: Rehydration process of bone A2004 and A2005 prior to speckle painting and four-point bending tests. (a) The bones were plunged in a physiological saline solution for 2-3hours to reach room temperature. (b) They were then left to drip in a tray layered with paper towel and covered with clingfilm for approximately 20mins.

The samples were painted with white background and black speckles for DIC acquisition. The painting was done one at a time before testing. The sample to be tested was thoroughly pat dried and placed in a spraying booth. Thin coats of multi-purpose matt white paint (Rust-Oleum) were sprayed onto the shaft on the medial, cranial and lateral quarters. This was done

until obtaining a uniform white layer. The paint was left to dry for a few minutes. Black speckles were then sprayed on using a matt black spray paint (RS-Pro).

Three different spraying techniques were used to obtain variational speckle sizes in order to investigate their effects. These are described and illustrated below with the resulting painted bone samples.

The first type of speckle pattern had finer uniform black speckles. In order to create this, the spray can was held directly towards the bone at a distance with the diffusing cap being pressed continuously. This technique was applied to bones O2001, O2002, A2001, which are shown in Figure 7-10 below.

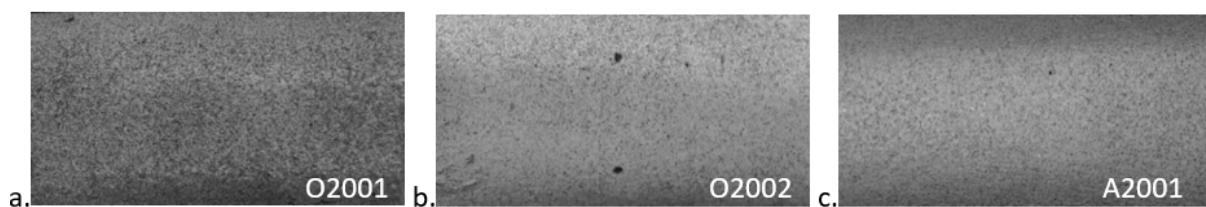


Figure 7-10: Fine and dense black speckle pattern spray painted over a matt white background used on bones O2001 (a), O2002 (b) and A2001 (c). For illustration purpose, two dots were manually added to bone O2002 to mark the midpoint on the cranial (top point) and lateral (bottom point) faces of the bone.

The second type of speckle pattern was a non-uniform fine to medium speckles. To achieve this, the spray can was held relatively close (approx. 30cm) and pointed directly towards the bone; the diffusing cap was pressed lightly in short bursts to control the paint density. This technique was applied to bone A2002, as illustrated in Figure 7-11 below.

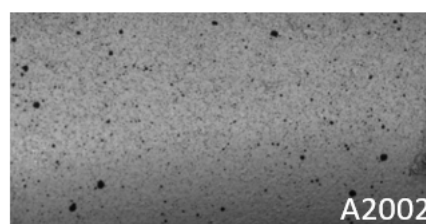


Figure 7-11: Non-uniform fine to medium black speckle pattern spray painted over a matt white background on bone A2002.

The last type of speckle pattern was dense with medium speckles. In order to achieve this, the paint was sprayed above the specimen and the diffusing cap was held continuously. This technique was applied to bones A2003, A2004, A2005 (Figure 7-12). After testing on O2001,

O2002, A2001 and A2002, it became apparent that the paint, albeit matt, was reflecting light in some areas. Therefore, specimens A2003, A2004 and A2005 were also given an additional coating of transparent mattifying paint (Kenro: Anti-Reflect) over the speckles to try and eliminate any over exposure caused by reflection. These three bones consequently produced the best DIC images.

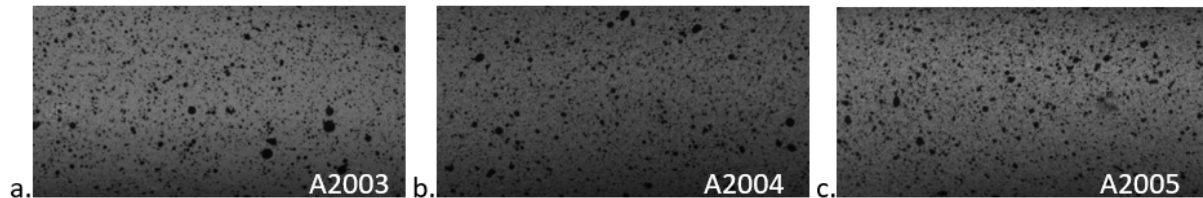


Figure 7-12: Dense pattern with medium size black speckles spray painted over a matt white background used on bones A2003 (a), A2004 (b) and A2005 (c). These bones were sprayed with an additional layer of transparent mattifying paint.

7.3 Experimental set-up

7.3.1 Four point bending set-up

The specimens were placed on two supporting steel rods (diameter 10mm), set at 100mm distance under a 25kN Tinius Olsen machine. Two loading steel pins (diameter 10mm), at a distance of 50mm were lowered onto the specimen at a constant rate of 1mm/min until failure (see Figure 7-13). All samples were placed with the cranial side towards the front and the medial side facing up (Figure 7-14). Load displacement data was recorded through the load cell.

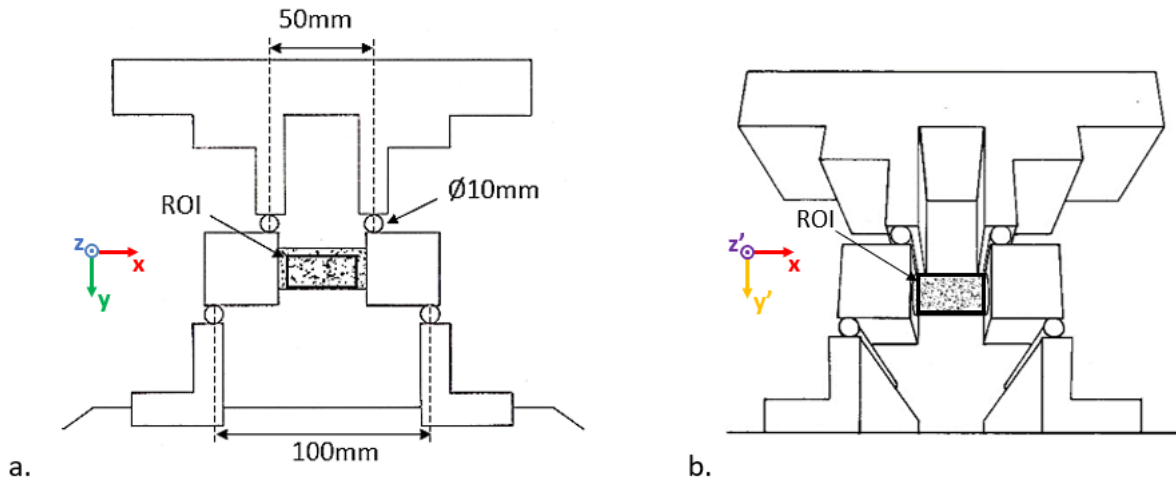


Figure 7-13: Simply supported embedded bone on 10mm diameter steel rods spanning 100mm, with loaded steel rods on the top, spanning 50mm. (a) Front view, defining plane xy , of the four-point bending setup. (b) Angled view, defining plane xy' , which is the xy plane rotated around the x -axis at an angle of -30° (i.e. view captured on DIC).

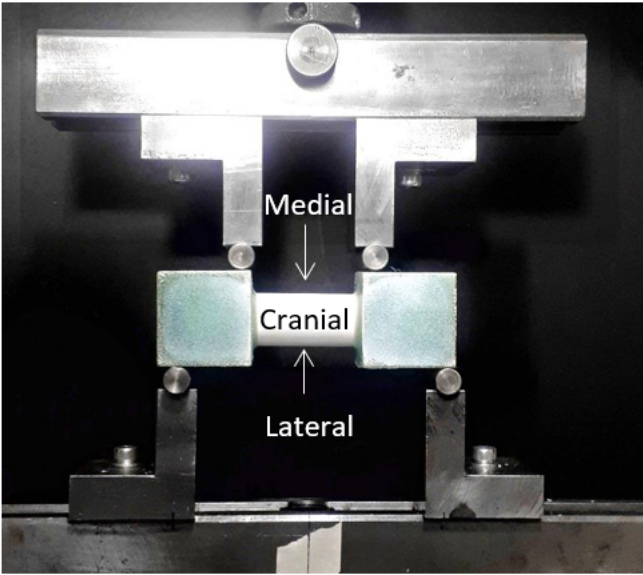


Figure 7-14: Front view image of a uPVC dummy placed in the four-point bending set-up. All specimens were placed with the lateral side facing down, the medial side facing up and the cranial side facing forwards.

7.3.2 Stereo system set up and calibration

The stereo system was initially adjusted using the uPVC samples. PVC1 was marked up with a large black dot at the centre of the front (corresponding to the cranial side) and bottom (corresponding to the lateral side) faces using a laser level (Figure 7-15).



Figure 7-15: Dummy uPVC sample, PVC1, painted with a fine speckle pattern and marked with large black dots indicating the centre of the front/cranial (a) and bottom/lateral (c) faces.

PVC1 was placed on the testing machine with the front faces of the cubes aligned with the front faces of the pins. Two cameras (Allied Vision: Pike F-505), were secured on a C-beam, which was in turn attached to a moving-head tripod. The beam was set parallel to the testing bench and the tripod head was tilted back by 30 degrees so that the cameras captured the lateral side (bottom edge) of the specimen; i.e. the region of expected maximum tensile strain (see Chapter 3 for bending theory). The stereo angle between the cameras was set to be 15 degrees. The resulting dimensions are detailed in Figure 7-16 below.

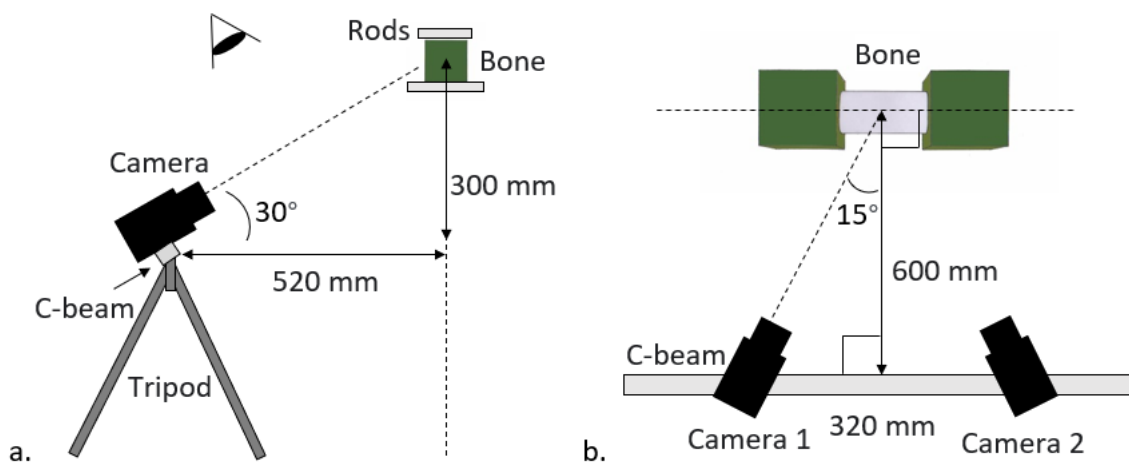


Figure 7-16: Diagram of the DIC stereo system set-up in relation to the sample and testing rig. (a) Side view showing the cameras placed at 300mm below and 520mm away from the specimen with a backward tilt of 30° from the horizontal plane. (b) 30° top view showing the cameras placed at 320mm away from each other (forming a 15° stereo angle) and at a 600mm incident distance from the specimen.

The position of the cameras was adjusted as explained in Chapter 3; the cameras were finely adjusted using the crosshead tool and focused with an open aperture (narrow depth of field) onto a distinguishable speckle in the middle of the ROI. For each camera position, the stereo system was calibrated using a 12x8x2.5mm calibration plate. All calibrations files had a minimum of 15 images and a standard deviation of <0.03pxls.

For bones O2001, O2002, A2001 and A2002, the position of the cameras was adjusted based on the uPVC specimen, PVC1 (Table 7-3).

O2001, O2002, A2001, A2002	Centre [pxls]		Focal length [pxls]		Magnitude [pxls/mm]		
	Camera	x	y	x	y	Average	Minimum
1	1202	1147	15919	15919	27	26	27
2	1254	1142	15862	15862	27	27	28

Table 7-3: Calibration data for the stereo system used to take DIC images of bones O2001, O2002, A2001 and A2002 (camera position adjusted using PVC1).

In order to improve the DIC accuracy on the three remaining specimens, the cameras were finely adjusted and re-calibrated for each individual bone. Note that fine adjustment and calibration took up to ten minutes to perform, adding minimal time between the painting and testing of the bone. The calibration data of bones A2003, A2004 and A2005 is listed in the table below:

a.

A2003	Centre [pxls]		Focal length [pxls]		Magnitude [pxls/mm]		
	Camera	x	y	x	y	Average	Minimum
1	1262	1044	15904	15904	27	27	28
2	1253	1019	15960	15960	27	26	28

b.

A2004	Centre [pxls]		Focal length [pxls]		Magnitude [pxls/mm]		
	Camera	x	y	x	y	Average	Minimum
1	1245	1035	15910	15910	27	26	28
2	1229	1011	15899	15899	27	26	28

c.

A2005	Centre [pxls]		Focal length [pxls]		Magnitude [pxls/mm]		
	Camera	x	y	x	y	Average	Minimum
1	1245	1053	15867	15867	27	26	28
2	1235	1018	15926	15926	27	26	28

Table 7-4: Calibration data for the stereo systems used to take DIC images of bones A2003(a), A2004 (b) and A2005 (c), respectively (camera position adjusted for each individual bone).

In order to assess projection error and floor noise, 50 images were taken of each bone specimen during the unloaded state prior to testing.

7.3.3 Lighting, aperture and shutter speed

Once the calibration procedure was complete, the specimens were placed back on the testing rig to set the light, aperture and shutter speed. The tests were performed in a dim room in order to minimize ambient light. A matt black background was also placed behind the testing rig to minimize any unwanted background illumination. Two studio lamps, with 28-watt 5000K-5500K bulbs, were placed over the cameras facing straight and down onto the bone. For specimens O2001 and O2002, a mirror was also placed under the shaft to illuminate the bottom (i.e. lateral) side (Figure 7-17). However, this did not seem to illuminate the middle of the ROI (cranio-lateral region) very well. Therefore, for the remainder of the bones, an additional LED light (200 lumens) was placed on the C-beam between the cameras instead of the mirror, which improved the lighting on the cranio-lateral region.

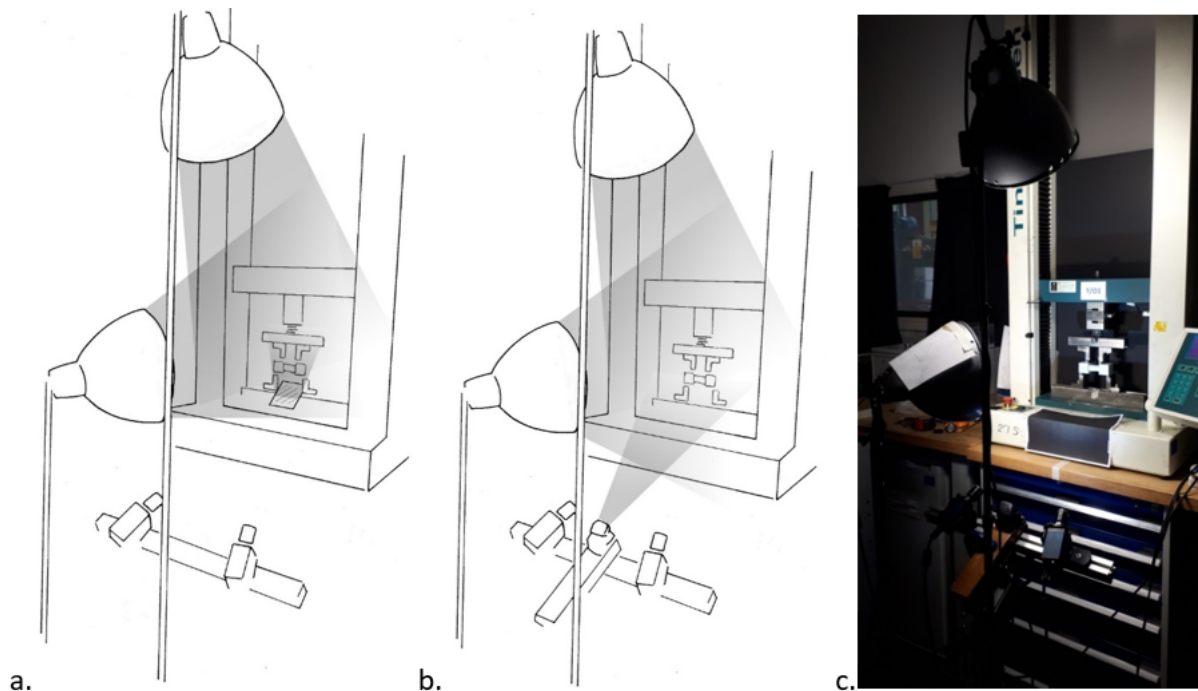


Figure 7-17: Lighting set-up used to capture DIC images of embedded bones during four-point bending test. Two studio lamps, with 28-watt 5000K-5500K bulbs, were placed over the cameras facing straight and down onto the sample. (a) For bones O2001 and O2002, a mirror was placed at an angle between the bottom rods to reflect light and illuminate the bottom (lateral) side of the bones. (b) For the other bones, the mirror was removed and a 200 lumens LED light was placed between (and aligned with) the two cameras.

The shutter speed and aperture were set to maximize the field of view over the ROI (Figure 7-18) without creating over exposure. The shutter speed was set to the maximum and the

aperture was slowly decreased on each camera until there was no over exposure and that the uncertainty interval calculated by the DIC software was lowest on the largest possible area of the ROI (Chapter 3).

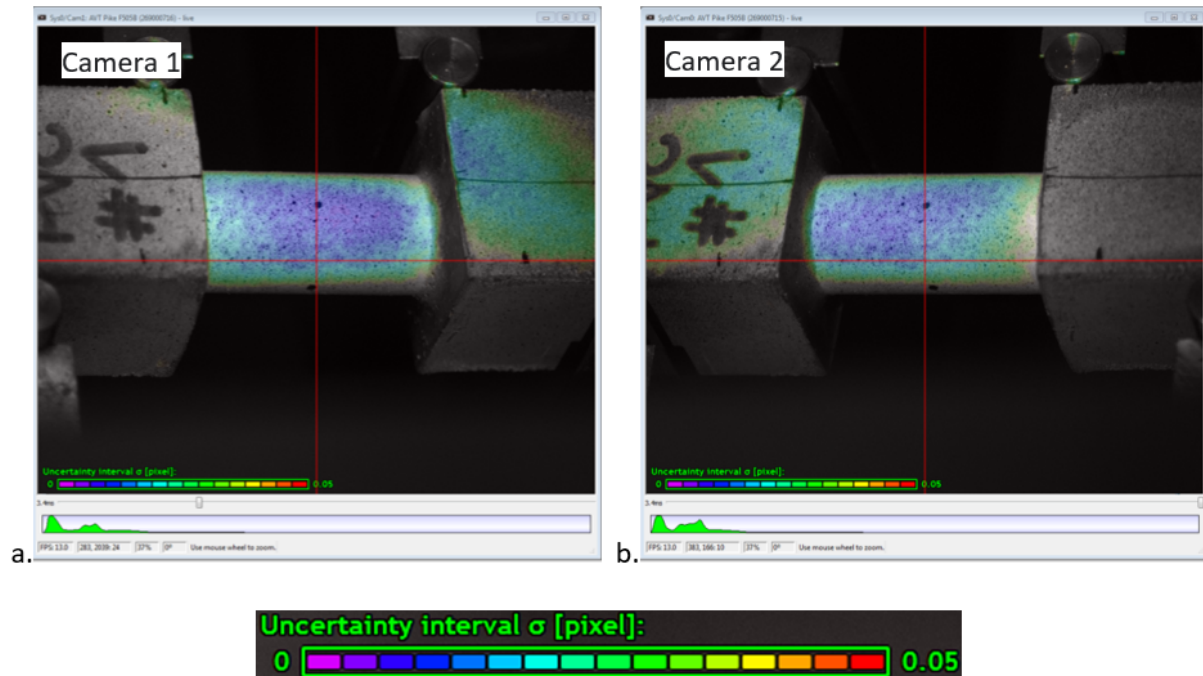


Figure 7-18: Image optimisation for correlation using VIC-Snap on PVC1. The colour map corresponds to the software calculated uncertainty interval over the captured image. (a) Image taken with camera 1 (left side of the stereo system). (b) Image taken with camera 2 (right side of the stereo system). The green histogram at the bottom of each frame shows the intensity distribution.

The above process was carried out for every bone specimen. The shutter speed and aperture used for each test is listed below.

	O2001	O2002	A2001	A2002	A2003	A2004	A2005
Aperture [f-number]	5.6	5.6	5.6	5.6	5.6	5.6	5.6
Shutter speed [ms]	12	12	10	5.1	9	7.5	8.4

Table 7-5: Lens aperture and shutter speed of DIC cameras used to capture images of each bone during the four-point bending test.

7.3.4 Force-displacement data processing

The testing machine and the cameras were set off manually. Images were taken at regular intervals of 500ms during the test until failure of the specimen. The DIC images and the force-displacement data were correlated in post-processing by matching the start time of the

tensile machine to the first DIC image in which the rods moved. Therefore, the maximum discrepancy between the DIC data and the Tinius data was assumed to be a single acquisition interval.

The force-displacement data of the load cell was recorded with time. The raw force was plotted against displacement. Once plotted, the pre-contact, compliance and linear phases were visually identified and analysed.

7.3.5 Digital image processing

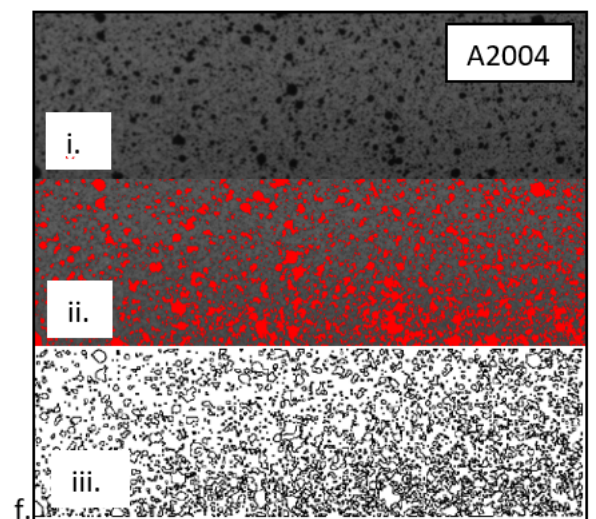
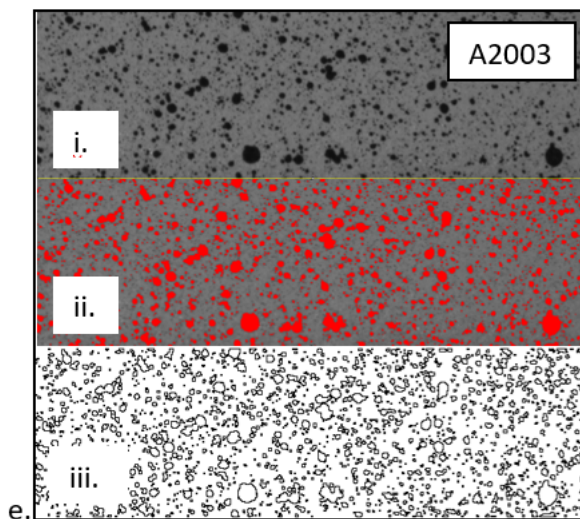
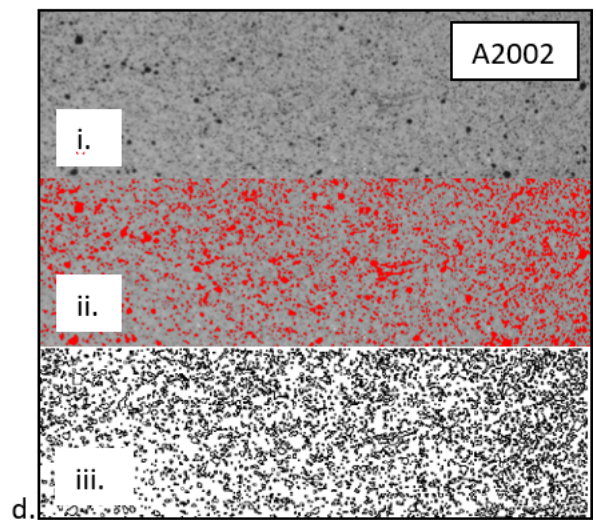
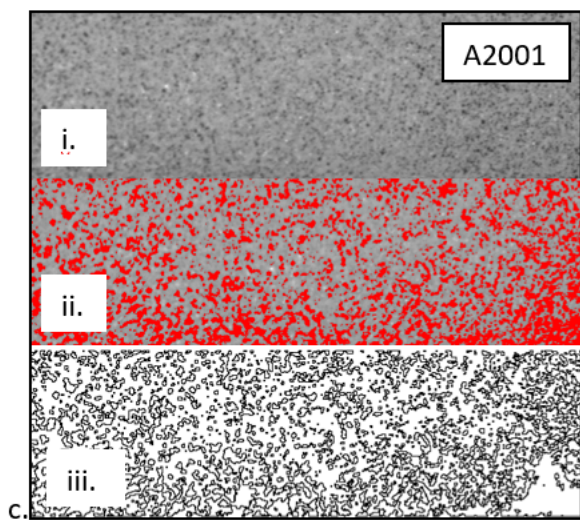
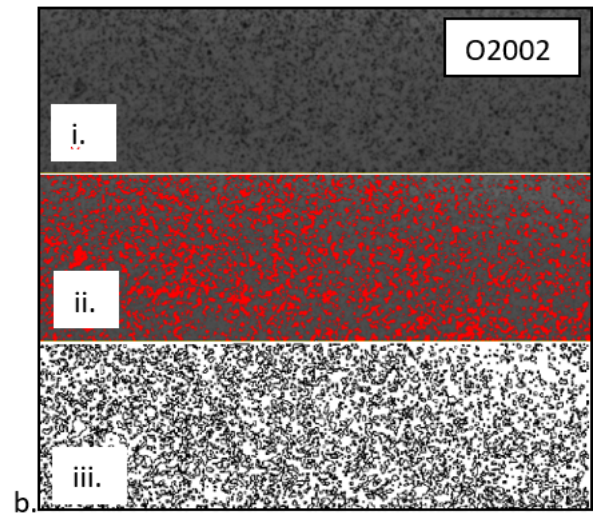
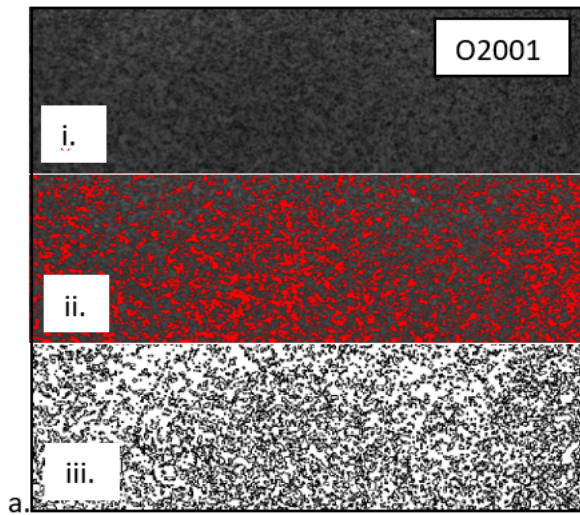
The raw force-displacement plots were corrected for pre-contact. Linear fits were calculated and plotted over each curve. For consistency, the strains were evaluated at two distinctive time points, one at 1mm displacement of the corrected force-displacement curves and one just before failure. DIC analysis was performed on the frames corresponding to each point with the software *VIC-3D Release 8* (Correlated Solutions Inc., Columbia, SC). The same points were later simulated using a μ CT-based FE modelling approach, and compared against the DIC results in Chapter 8. Engineering strain was chosen as an output as the deformation analysed was in the linear region, i.e. small strains. Both axial (in the x and y directions) and principal engineering strain maps were generated.

Two DIC parameters had to be selected in order to optimise the spatial resolution of the DIC, the subset size and the step size. The methodology used to select the subset and step size for the image correlation was similar to that used in Chapter 5, which is briefly described below.

7.3.5.1 Speckle analysis for subset and step size

An image analysis was carried out with the image processing program, ImageJ, to select the smallest suitable subset size for each bone. A systematic iterative method was used to determine the most appropriate subset size for each bone looking at both speckle pattern and surface irregularity.

Using ImageJ, the image was thresholded for the speckles (Figure 7-19). An area of interest between the two top rods was selected and the speckles were measured and outlined using the *Analyse Particles* tool. The dimension of each speckle was defined by its bounding rectangle (Table 7-6).



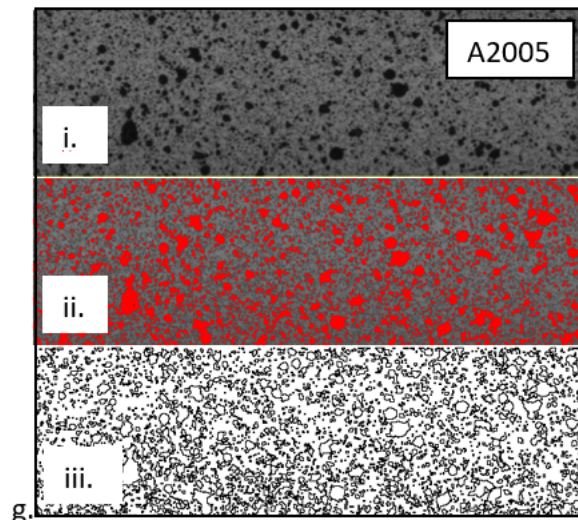


Figure 7-19: Bones O2001 (a), O2002 (b), A2001 (c), A2002 (d), A2003 (e), A2004 (f) and A2005 (g). (i) Raw image of the speckled AOI obtained through camera 2 (right side) of the stereo system. (ii) Thresholded image differentiating the speckles (red) from the background. (iii) Processed image with outline of the speckles identified through thresholding.

	Mean [pxls]		SD [pxls]		Min [pxls]		Max [pxls]	
	Width	Height	Width	Height	Width	Height	Width	Height
O2003	3.89	3.64	4.66	4.27	1	1	48	44
O2004	3.61	3.75	3.99	4.18	1	1	60	46
A2001	4.98 *	4.65	8.16	5.96	1	1	181	79
A2002	2.79	2.66	2.75	2.48	1	1	39	26
A2003	3.14	3.03	3.10	2.90	1	1	28	31
A2004	3.47	3.36	4.08	4.14	1	1	38	47
A2005	3.02	2.99	3.44	3.39	1	1	34	46

Table 7-6: Data from the speckle size analysis listing the mean, minimum and maximum speckle size (in terms of width and height) of each bone over the AOI with the higher value of mean width/height highlighted in blue. *Note that there is an area of poor contrast in the bottom right corner of bone A2001's AOI. The software was unable to pick up individual speckles and created a very large speckle instead, which in turn skewed the value of the mean speckle size.

For each bone, a convergence study was carried out by plotting subset size against the change in correlated area (Figure 7-20). This was performed to maximise the correlatable area at a constant step to subset size ratio. The step size was chosen to be approximately one third of the subset size (as recommended in the VIC-3D user manual) for each iteration. The starting subset size for convergence was set as three times the mean speckle size of each bone (the

higher width or height value highlighted in blue in Table 7-7). The image correlation was performed in the software VIC-3D, and the correlated area was measured using MATLAB.

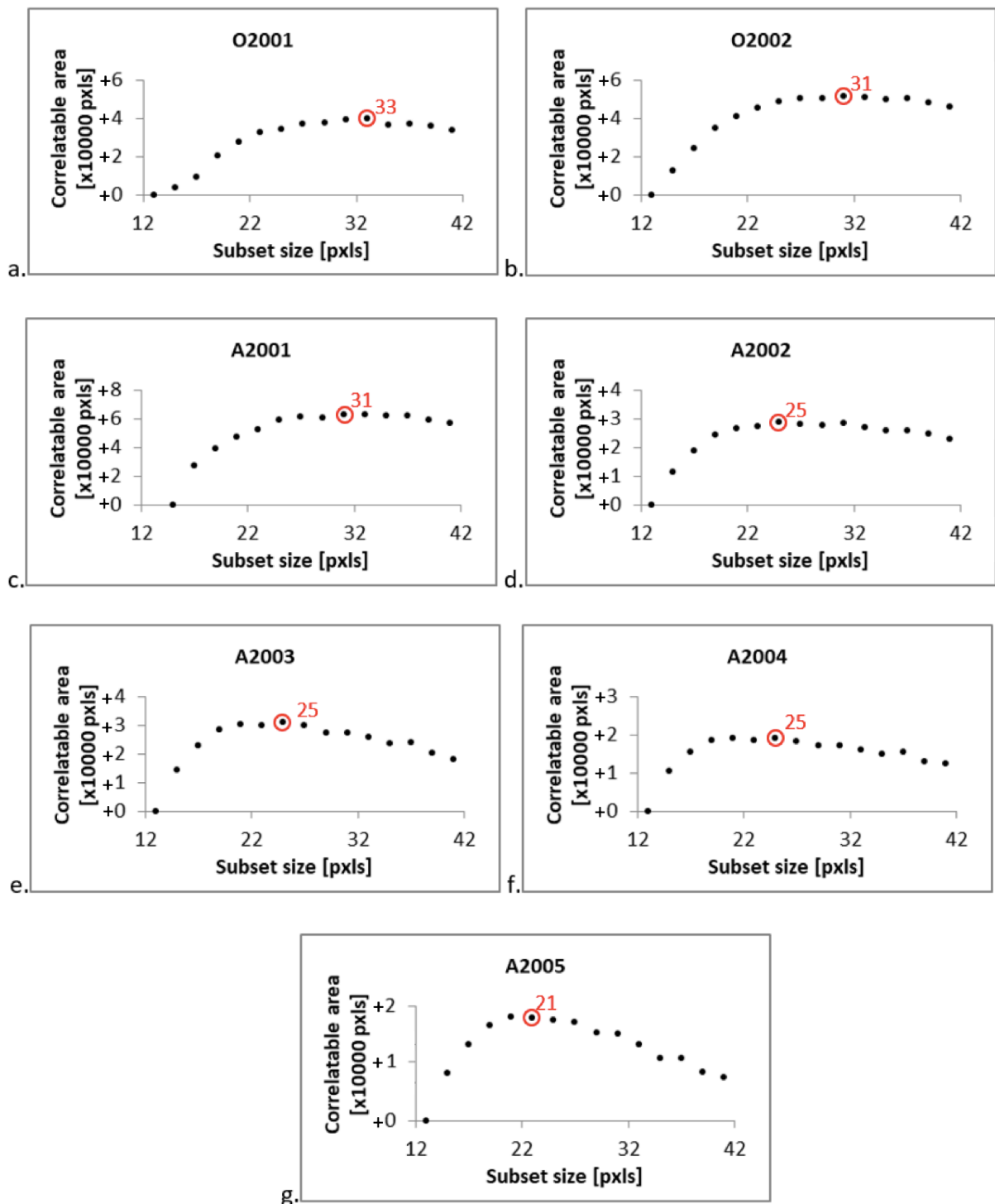


Figure 7-20: Plots of the increase in correlatable area over the AOI against the subset size used for correlation, in which the step size is approximately one-third of the subset size for each iteration.

The table below lists the subset sizes and step sizes that resulted in the maximum correlatable area for each bone. These sizes were used for the final DIC analysis. Note that the four bones (A2002-A2005) painted with medium speckle size achieved slightly lower subset and step sizes compared to those painted with fine speckle size (O2001, O2002, A2001).

	O2001	O2002	A2001	A2002	A2003	A2004	A2005
Subset size [pxls]	33	31	31	25	25	25	21
Step size [pxls]	11	10	10	8	8	8	7

Table 7-7: Optimal subset size for DIC determined for each bone. The subset size, which returned the largest correlatable area over the AOI of each bone, was selected.

7.4 Results

The results section is split into three parts. The first part analyses the resulting raw force-displacement curves and failure modes. The second part presents linearly corrected force-displacement plots. Finally, the third part shows DIC strain maps of the ROI at 1mm displacement of the aforesaid plots and at the point before failure.

7.4.1 Part one: Force-displacement and fracture type

Figure 7-21 to Figure 7-24 show raw force-displacement plots. All bones behaved similarly up to the point of maximum load. A pre-contact region (A) can be seen followed by a short linear region (B), an increase in slope (C) and another linear region (D). The maximum load was achieved towards the end of the linear region (D). The fracture results are categorized into two groups: (1) resin failure and (2) bone failure.

Bones O2001, O2002, A2002 and A2004 all failed at the resin (or embedding) material, while the bones were left without any visible damage. The raw force-displacement curves and images of resin damage for these bones are shown in Figure 7-21 below.

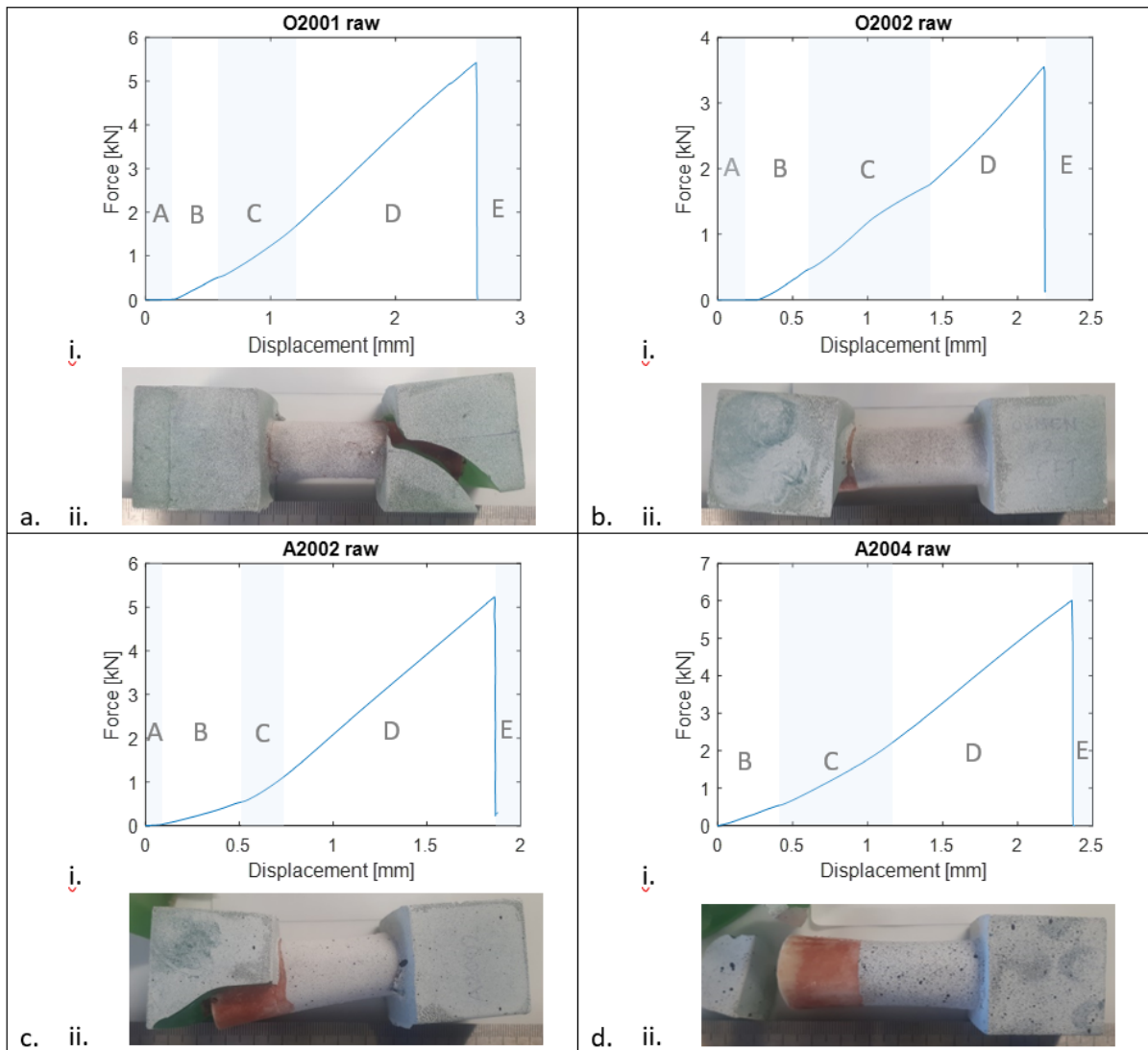


Figure 7-21: Embedded bones O2001 (a), O2002 (b), A2002 (c) and A2004 (d). (i) Raw force-displacement plots of specimens under four-point bending with a pre-contact region (A), short linear region (B), increase in slope (C), linear region (D), complete failure (E). (ii) Post-experiment images of the broken specimens.

The rest of the specimens had visible fractures in the bone. Sample A2001 presented with a comminute fracture with an axial fracture on the medial quarter and a transverse fracture at the junction with the embedding material on the proximal end (left side). A2001 reached a maximum load of 9.8kN (Figure 7-22).

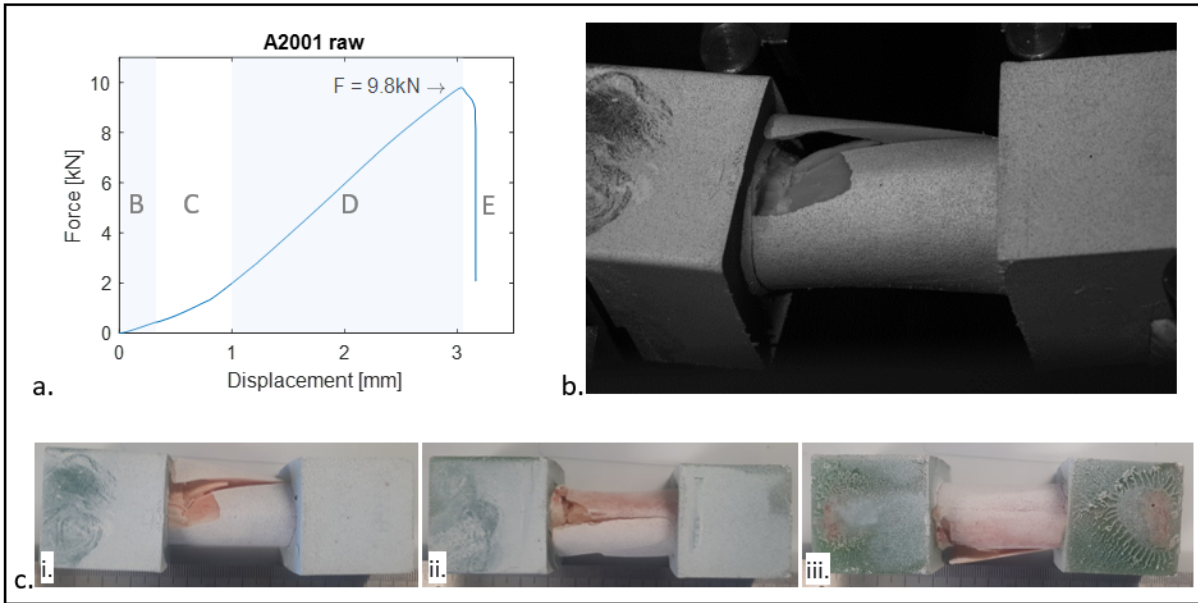


Figure 7-22: Embedded bone A2001. (a) Raw force-displacement plot of specimens under four-point bending with a short linear region (B), increase in slope (C), linear region (D), complete failure (E). (b) Frame of fractured bone in the testing rig. (c) Post-experiment images of the broken specimen: cranial view (i), medial view (ii) and caudal view (iii).

Sample A2003 presented with a single complete fracture on the distal (left) side of the bone. The fracture appeared as a continuous wave pattern (two cycles) around the shaft. Both the bone and the embedding material fractured at a maximum load of 4.3kN (Figure 7-23).

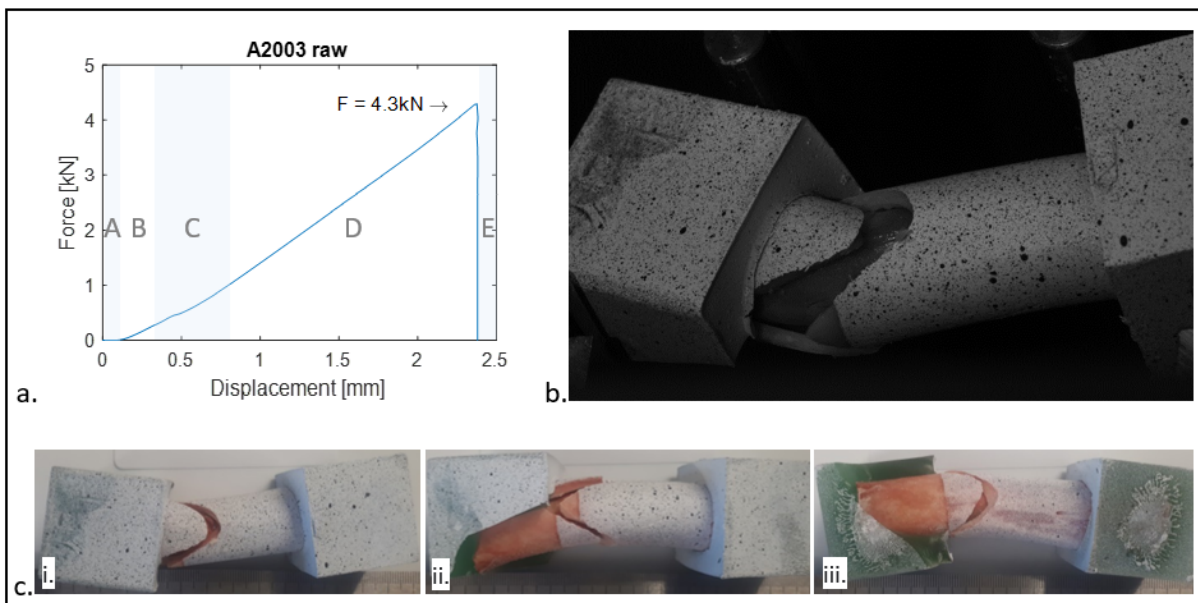


Figure 7-23: Embedded bone A2003. (a) Raw force-displacement plot of specimen under four-point bending with a pre-contact region (A), short linear region (B), increase in slope (C), linear region (D), complete failure (E).

(E). (b) Frame of fractured bone in the testing rig. (c) Post-experiment images of the broken specimen: cranial view (i), lateral view (ii) and caudal view (iii).

Sample A2005 showed a drop in force at two time points (red circles in Figure 7-24.a regions D and E). At $t = 117s$, a fracture can be seen at the top of the left-hand side embedding material. Shortly after that, at $t = 149s$, a second fracture initiated on the cranial side of the bone near the embedding of the proximal end (right) and propagated into a comminute fracture until complete failure. Bone A2005 reached a maximum load of 7.1kN.

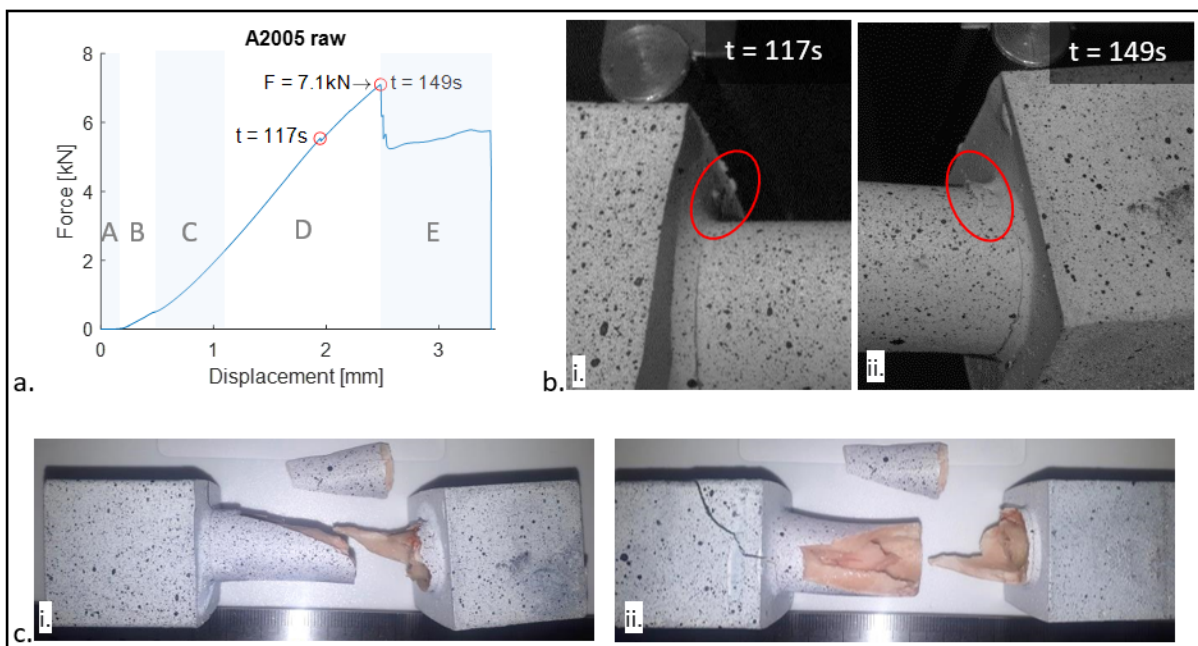
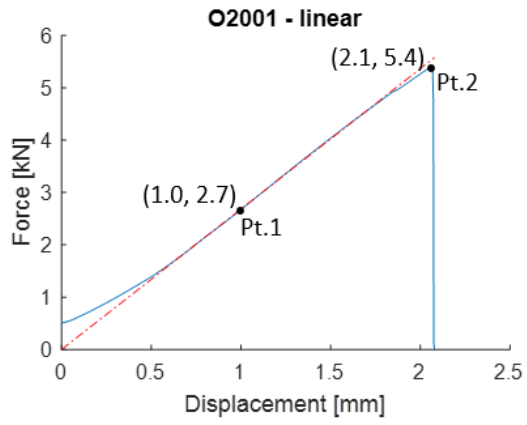


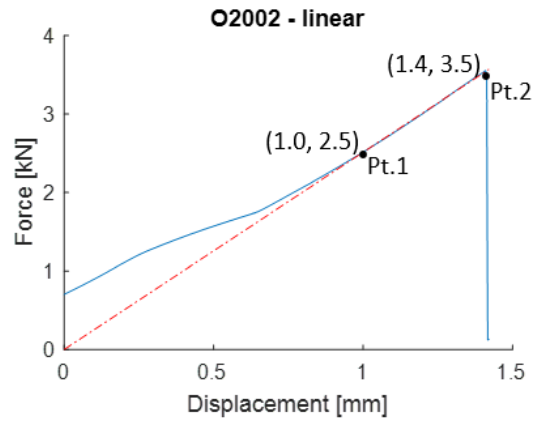
Figure 7-24: Embedded bone A2005. (a) Raw force-displacement plot of specimen under four-point bending with a pre-contact region (A), short linear region (B), increase in slope (C), linear region (D), complete failure (E). (b) Frame of fractured bone in the testing rig. (c) Post-experiment images of the broken specimen: cranial view (i), lateral view (ii) and caudal view (iii).

7.4.2 Part two: Linear correction of force-displacement plots

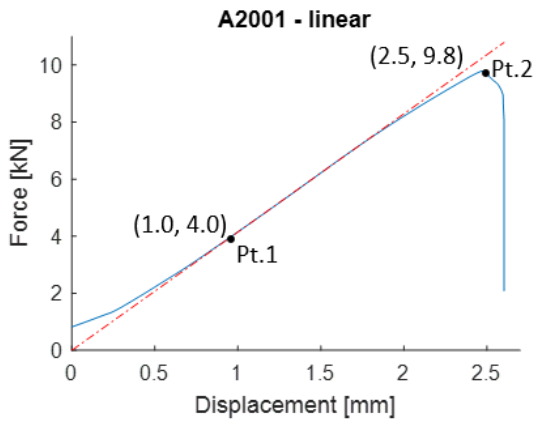
The raw force-displacement plots were linearly corrected for the second linear region (Figure 7-25). The correction was carried out by extending the linear fit line of the second linear region (D) so that it met with the origin. Two points were highlighted in each graph, one at 1mm displacement (Pt.1) and another just before failure (Pt.2). The force value for each point is presented in Table 7-8. DIC results were evaluated at each of the two time points. The slope of the linear regions (or stiffness) ranged from $2.1Nm^{-1}$ (A2003) to $4.0Nm^{-1}$ (A2001).



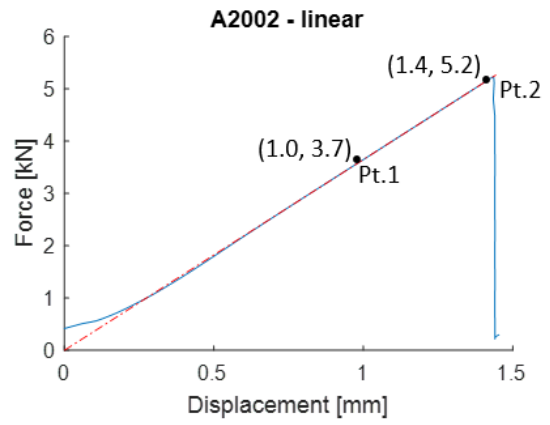
a.



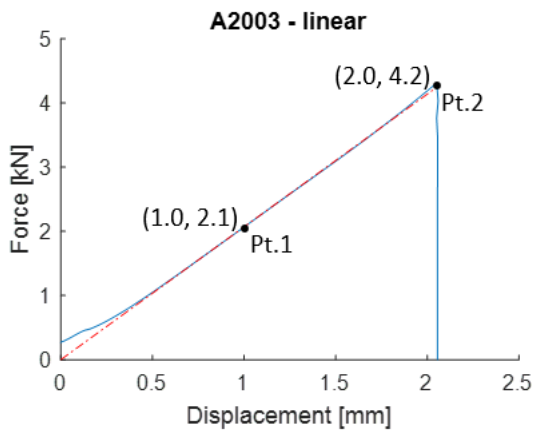
b.



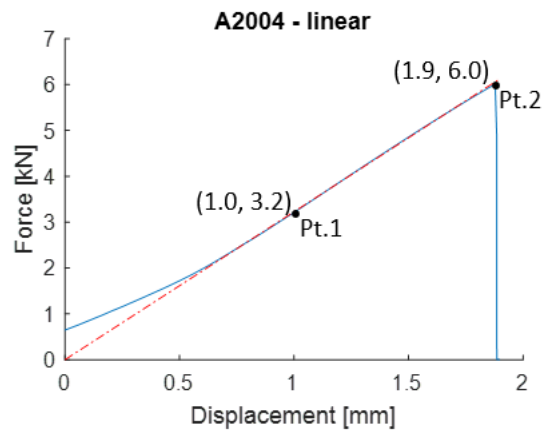
c.



d.



e.



f.

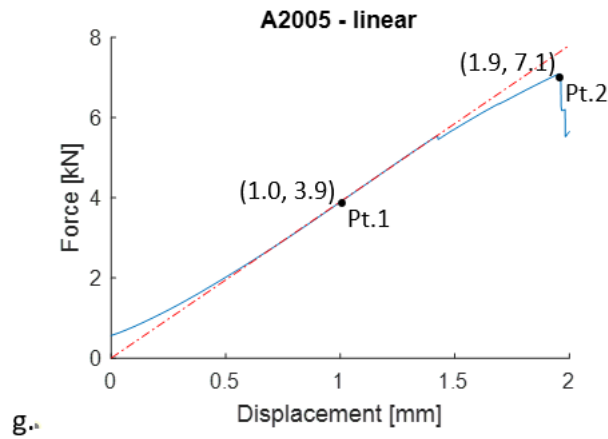


Figure 7-25: Four-point bending force-displacement plots linearly corrected for the second linear regions (region D in the raw plots) highlighting two points at which DIC was later performed; Pt.1 at 1mm displacement and Pt.2 at failure.

	Slope of linear fit [N/m]	Peak force [kN]	Displacement at peak force [mm]
O2001	2.68	5.42	7.07
O2002	2.51	3.55	1.41
A2001	3.95	9.79	2.54
A2002	3.65	5.23	1.44
A2003	2.07	4.29	2.05
A2004	3.23	6.01	1.88
A2005	3.90	7.10	1.96

Table 7-8: Slope, force and displacement data of the linearly corrected force-displacement plots.

7.4.3 Part three: DIC

DIC was carried out on the seven specimens to derive a strain contour on the cranial-lateral surface of the midshaft (i.e. at 30° from the cranial plane) during four-point bending test. The x-axis (along the long axis of the bone) and y'-axis (normal to the axis of the bone) of the correlated plane are defined in Figure 7-26. An image of the PVC dummy is given below to highlight the position of the cranial and lateral lines. All images presented were taken from the right-hand side camera (15° stereo angle).

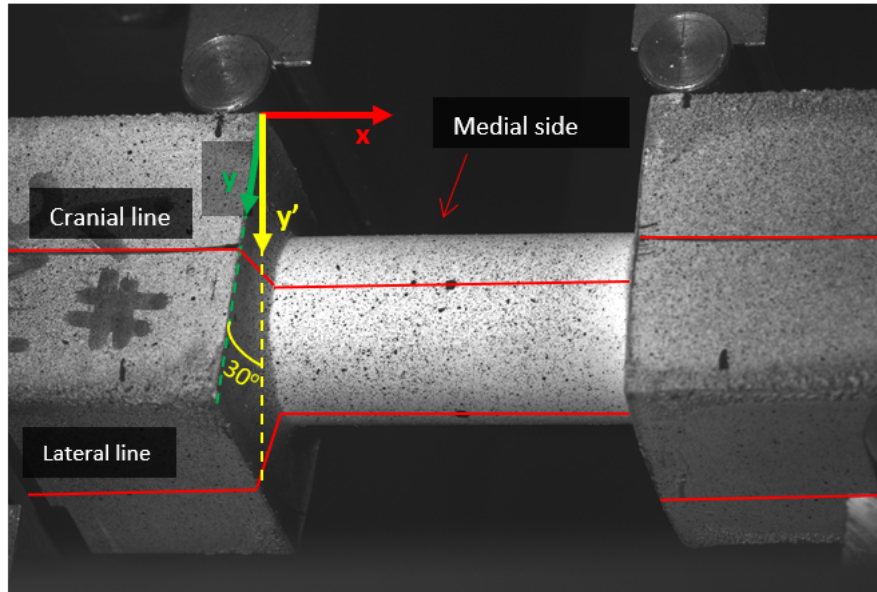


Figure 7-26: Frame of PVC1 placed on the testing rig taken through camera 2 (right side) of the DIC system. The stereo plane defines the x-axis (along the long axis of the bone) and the y'-axis (normal to the x-axis) of the correlated strains. Note that the y'-axis is at 30° from the lateral-medial axis (in yellow).

7.4.3.1 Projection error and floor noise

Image correlation was performed in static frames before the testing of each bone. The table below gives the maximum noise for engineering strains, along with the stereo system projection error.

	Projection error	exx strain		eyy strain		e1 strain		e2 strain	
		min	max	min	max	min	max	min	max
O2001	0.581	-0.0005	0.0008	-0.002	0.001	-0.0002	0.001	-0.002	0.0002
O2002	0.134	0.002	0.001	-0.004	0.007	-0.001	0.007	-0.007	0.0007
A2001	0.334	-0.002	0.001	-0.002	0.003	-0.0004	0.003	-0.002	0.0003
A2002	0.022	-0.002	0.002	-0.1	0.004	-0.0009	0.006	-0.01	0.0006
A2003	0.024	-0.005	0.002	-0.006	0.003	-0.001	0.004	-0.006	0.0008
A2004	0.019	-0.001	0.002	-0.003	0.005	-0.001	0.005	-0.004	0.0002
A2005	0.015	-0.006	0.003	-0.01	0.004	-0.0008	0.007	-0.008	0.002

Figure 7-27: DIC projection error with minimum and maximum values for engineering strains on static images, corresponding to the floor noise for each bone.

For all bones, the floor noise was distributed along the edges. The noise frames of bone O2002 are given below to show an example of the noise distribution (Figure 7-28).

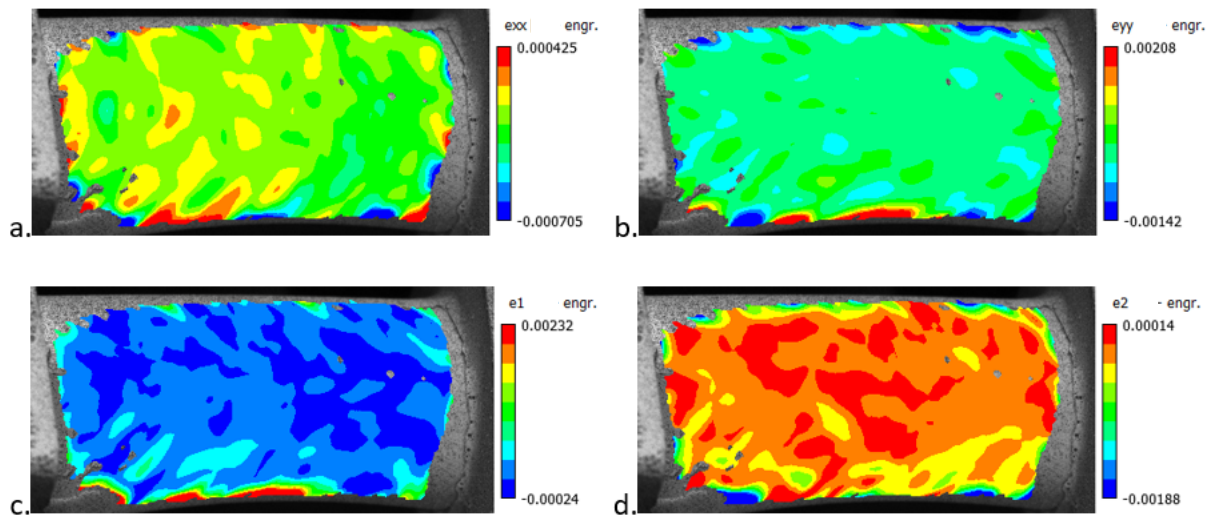


Figure 7-28: Floor noise captured on static frames of bone O2002. (a) Engineering plane strains in the x-direction. (b) Engineering plane strains in the y-direction. (c) First principal plane strain (tension). (d) Second principal plane strains (compression).

7.4.3.2 Surface strain maps

The correlation was performed at two time points for each bone; one at 1mm displacement (Pt.1) and one pre-failure (Pt.2). The results are shown below in Figure 7-29 to Figure 7-35. Each figure contains four plane strain maps: (a) strain in the x-direction, (b) strain in the y'-direction, (c) first (tensile) principal strain, and (d) second (compressive) principal strain.

All bones had a typical x-strain distribution (Figure 7-29-Figure 7-35) for a specimen under bending conditions (Chapter 3); with the maximum (tensile) strain at the bottom (lateral line) of the bone (red), a neutral (near zero) region extending along the midspan (cranial line) of the bone and the minimum (compressive) strain towards the top (medial side) region of the bone (blue). The colour maps showed that all the bones reached a higher tensile strain than compressive strain in the x-direction over the ROI.

In all cases, the magnitude and distribution of the first principal strain reflected the tensile strain in the x-direction; meaning that most of the tensile strain was in the x-direction.

In contrary to the x-strain, the strain in the y'-direction was at a maximum (tensile) towards the top (medial) region of the bone (red), and at a minimum (compressive) towards the bottom (lateral line) of the bone (blue). Again, a neutral (near zero) region extended along

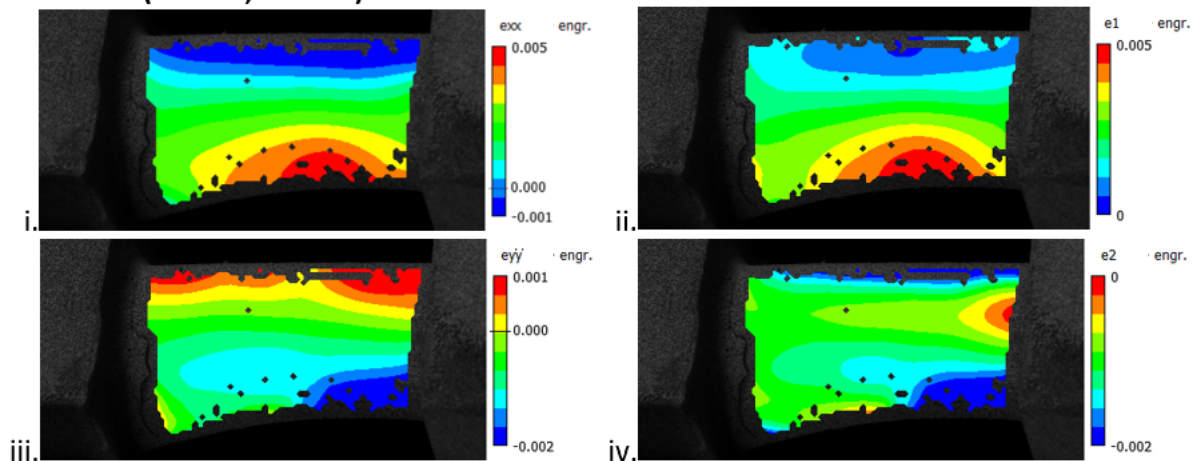
the midspan (cranial line) of the bone. The colour map shows that all bones reached a higher compressive strain than tensile strain in the y' -direction over the AOI.

In all cases, the magnitude and distribution of the second principal strain reflected the maximum compressive strain in the y' -direction; meaning that most of the compressive strain was in the y' -direction.

For all bones, the magnitude of strain in the x-direction was generally higher than in the y' -direction. Accordingly, the maximum first principal strain $e1$ was higher than the maximum absolute value of second (compressive) principal strain $e2$.

O2001

a. Point 1 (1.0mm, 2.69kN)



b. Point 2 – Pre-fracture (2.07mm, 5.42kN)

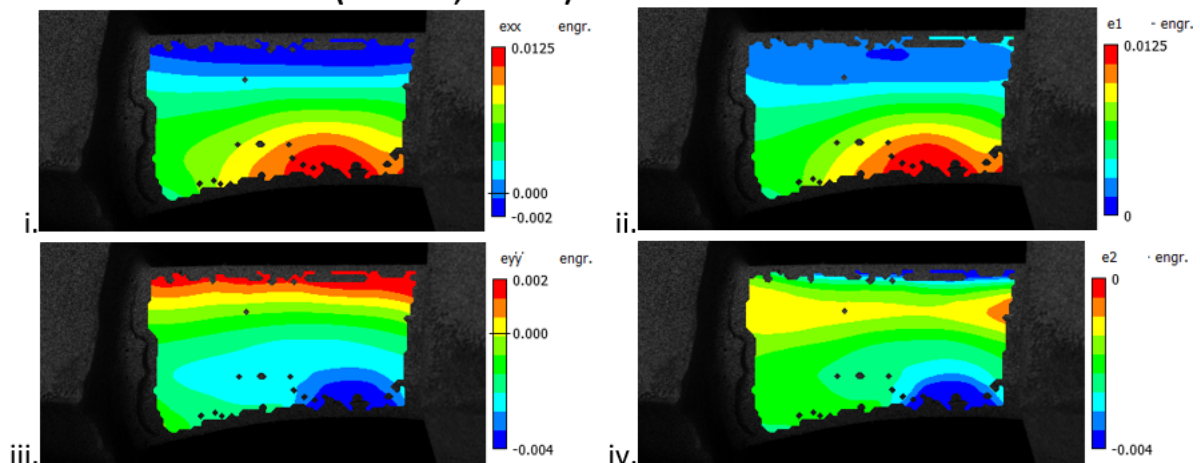
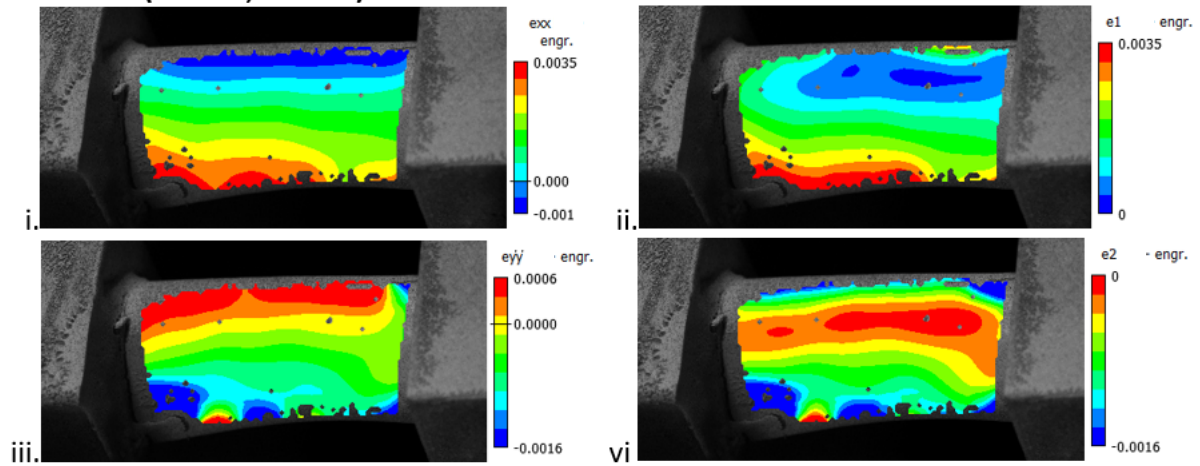


Figure 7-29: Surface strains of bone O2001 under four-point bending obtained through DIC at 1mm displacement (a) and before fracture (b). (i) Engineering plane strain in the x-direction. (ii) First principal

plane strain (tension). (iii) Engineering plane strain in the y' -direction. (iv) Second principal plane strain (compression).

O2002

a. Point 1 (1.0mm, 2.51kN)



b. Point 2 – Pre-fracture (1.41mm, 3.55kN)

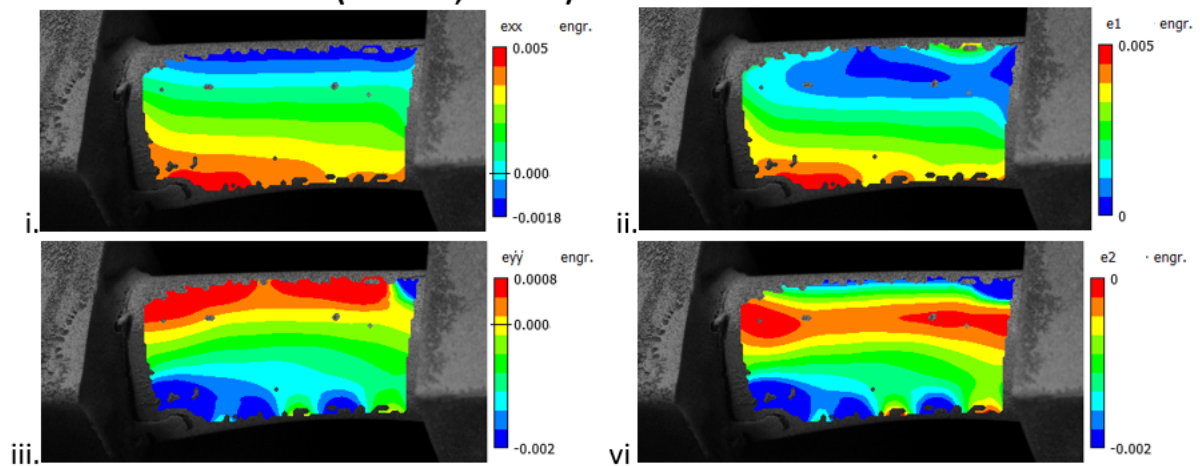
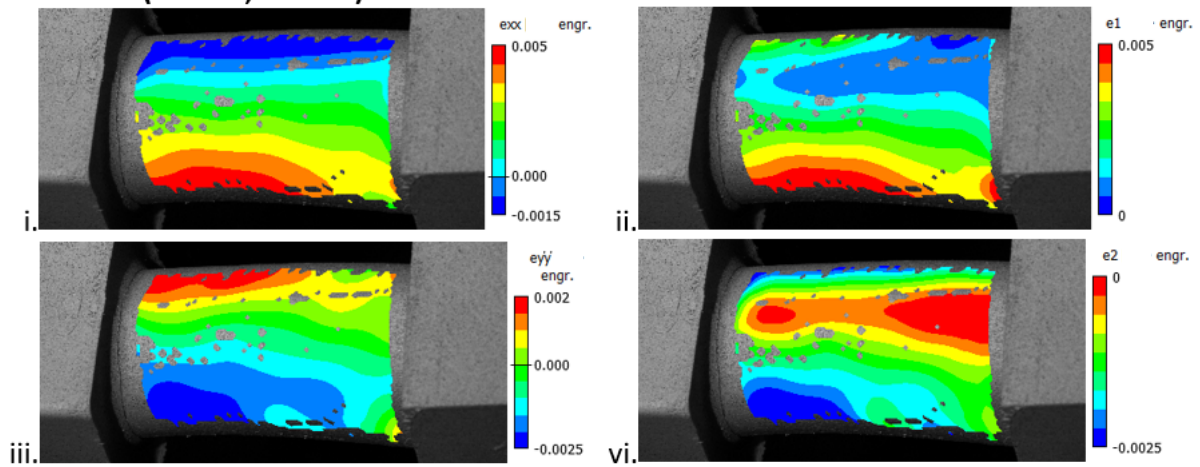


Figure 7-30: Surface strains of bone O2002 under four-point bending obtained through DIC at 1mm displacement (a) and before fracture (b). (i) Engineering plane strain in the x-direction. (ii) First principal plane strain (tension). (iii) Engineering plane strain in the y' -direction. (iv) Second principal plane strain (compression).

A2001

a. Point 1 (1.0mm, 3.89kN)



b. Point 2 – Pre-fracture (2.54mm, 9.79kN)

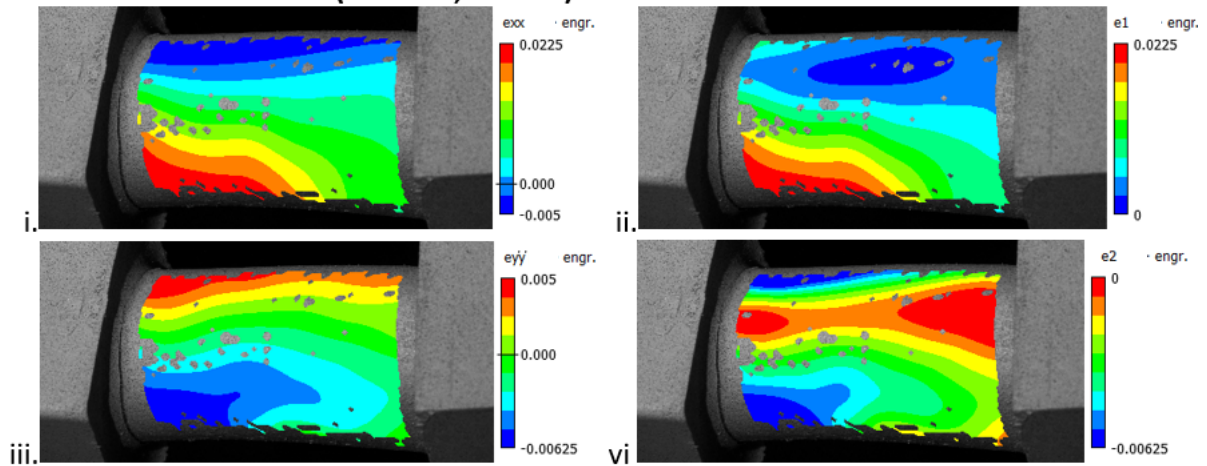
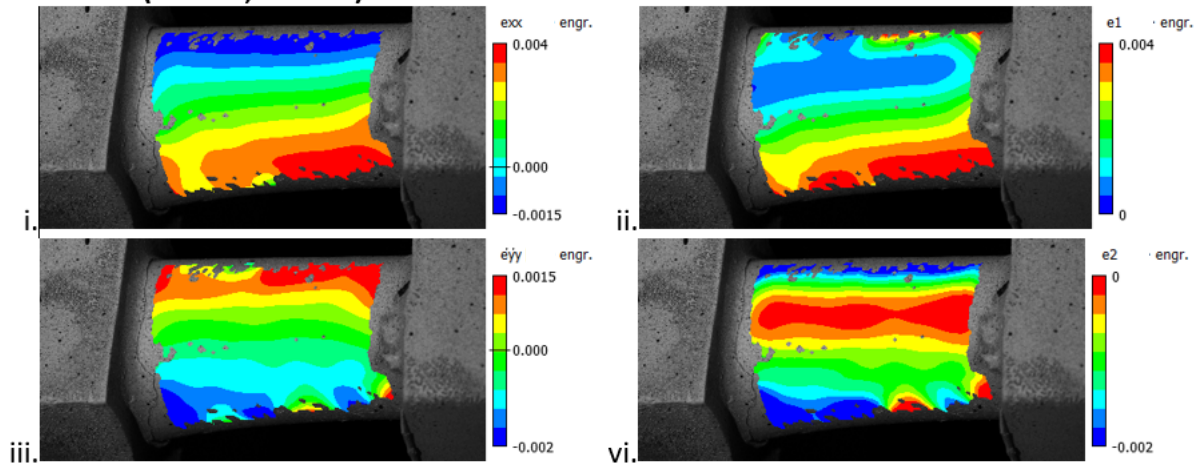


Figure 7-31: Surface strains of bone A2001 under four-point bending obtained through DIC at 1mm displacement (a) and before fracture (b). (i) Engineering plane strain in the x-direction. (ii) First principal plane strain (tension). (iii) Engineering plane strain in the y'-direction. (iv) Second principal plane strain (compression).

A2002

a. Point 1 (1.0mm, 3.66kN)



b. Point 2 – Pre-fracture (1.41mm, 5.23kN)

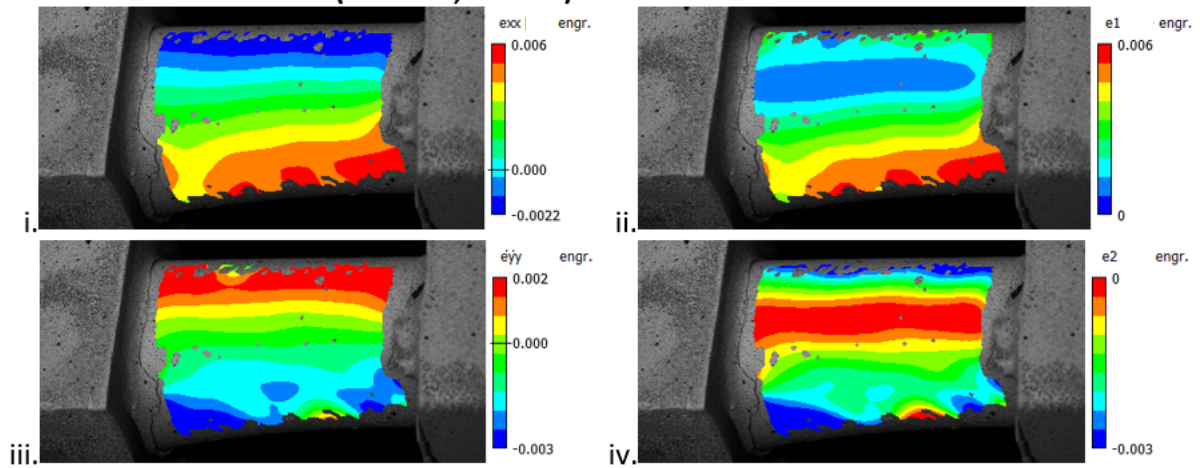
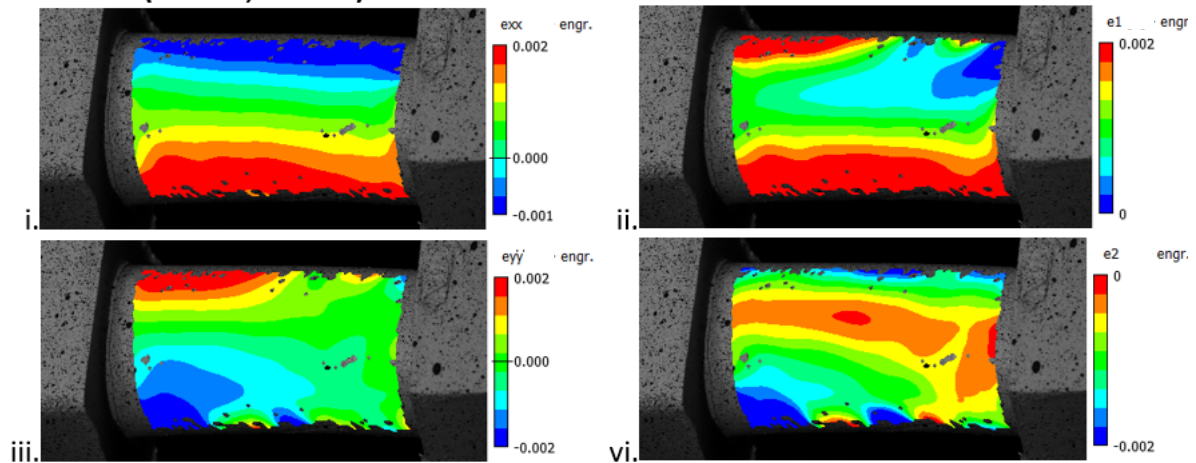


Figure 7-32: Surface strains of bone A2002 under four-point bending obtained through DIC at 1mm displacement (a) and before fracture (b). (i) Engineering plane strain in the x-direction. (ii) First principal plane strain (tension). (iii) Engineering plane strain in the y'-direction. (iv) Second principal plane strain (compression).

A2003

a. Point 1 (1.0mm, 2.05kN)



b. Point 2 – Pre-fracture (2.05mm, 4.29kN)

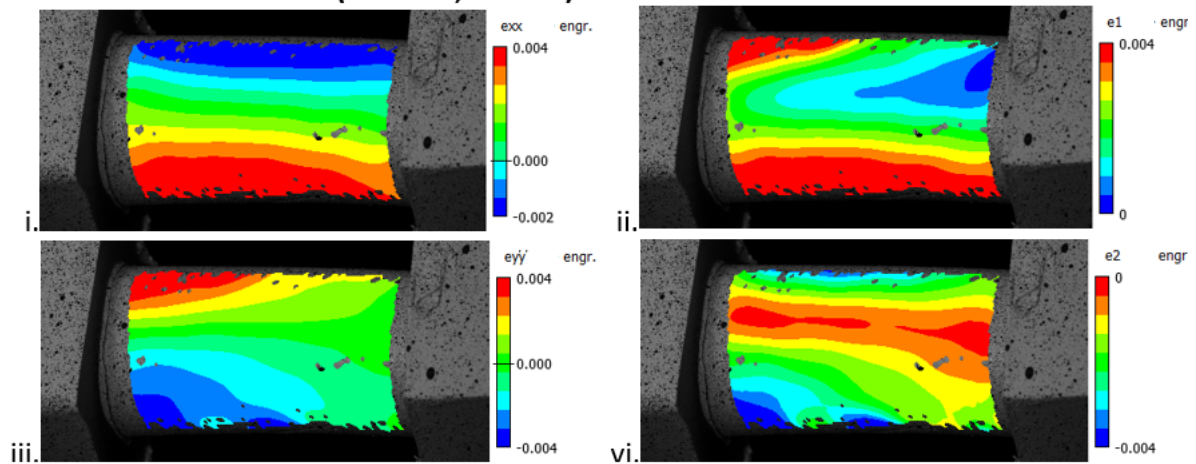
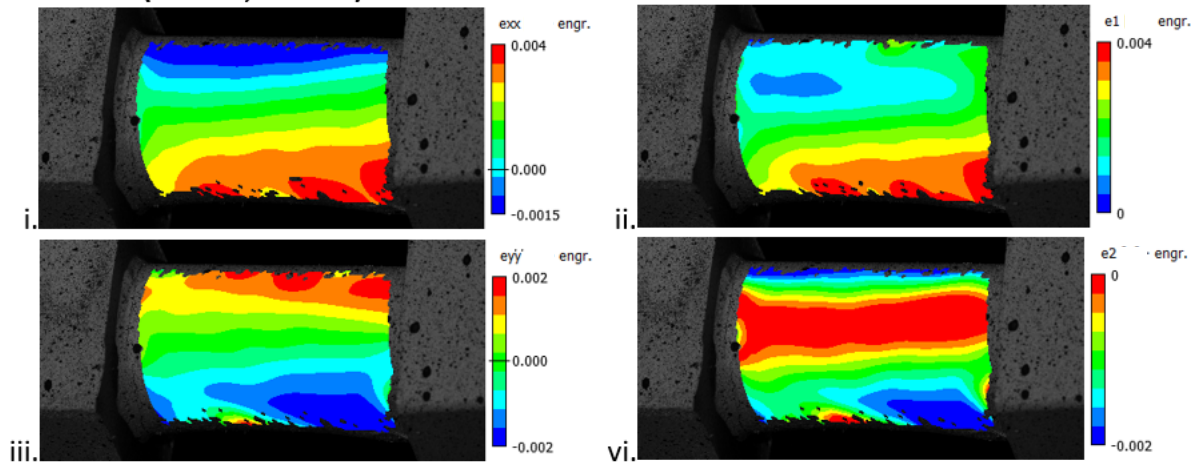


Figure 7-33: Surface strains of bone A2003 under four-point bending obtained through DIC at 1mm displacement (a) and before fracture (b). (i) Engineering plane strain in the x-direction. (ii) First principal plane strain (tension). (iii) Engineering plane strain in the y'-direction. (iv) Second principal plane strain (compression).

A2004

a. Point 1 (1.0mm, 3.25kN)



b. Point 2 – Pre-fracture (1.88mm, 6.01kN)

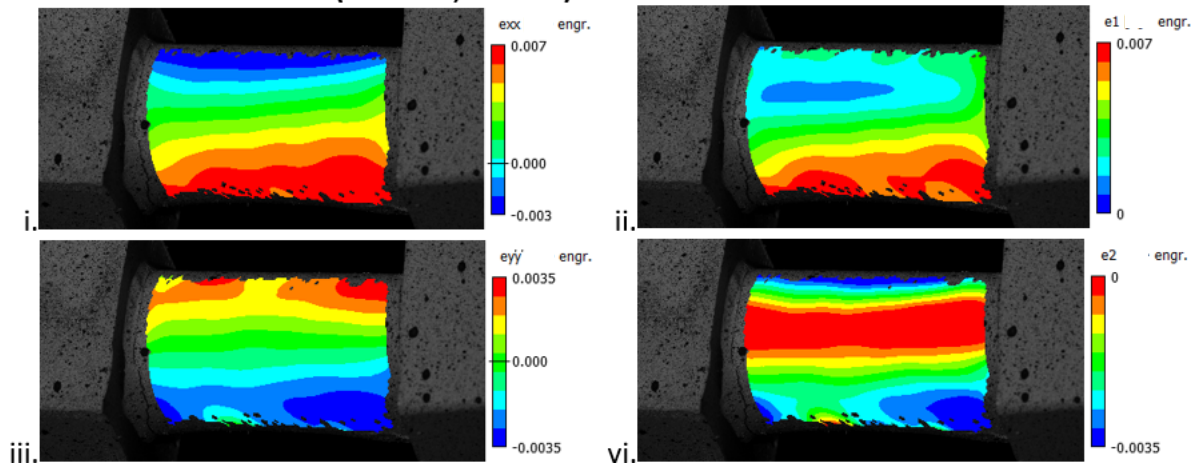
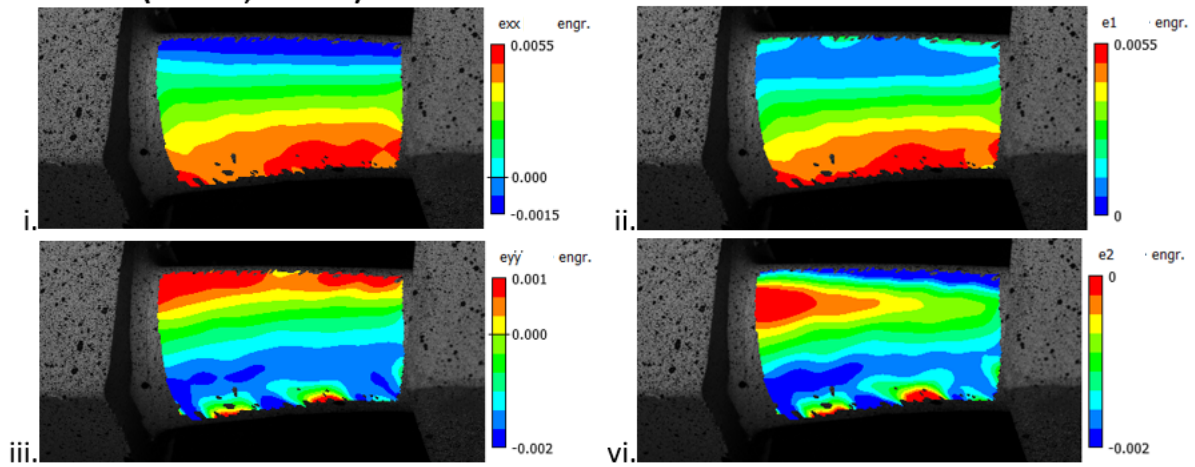


Figure 7-34: Surface strains of bone A2004 under four-point bending obtained through DIC at 1mm displacement (a) and before fracture (b). (i) Engineering plane strain in the x-direction. (ii) First principal plane strain (tension). (iii) Engineering plane strain in the y'-direction. (iv) Second principal plane strain (compression).

A2005

a. Point 1 (1.0mm, 3.94kN)



b. Point 2 – Pre-fracture (1.96mm, 7.10kN)

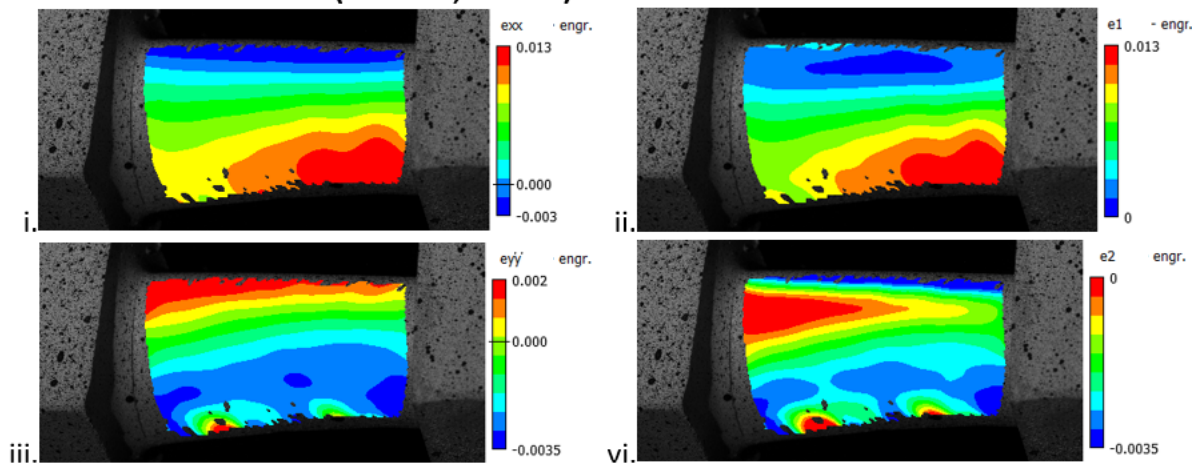


Figure 7-35: Surface strains of bone A2005 under four-point bending obtained through DIC at 1mm displacement (a) and before fracture (b). (i) Engineering plane strain in the x-direction. (ii) First principal plane strain (tension). (iii) Engineering plane strain in the y'-direction. (iv) Second principal plane strain (compression).

7.5 Discussion

This section analyses the force-displacement curves and the corresponding surface strain contours of the seven bones. Furthermore, it discusses the limitations of the experimental method as well as suggestions for future improvements.

7.5.1 Force-displacement curves

7.5.1.1 Experimental observations

During the initial phase of the four-point bending tests, it was visually observed that the angle difference between each cube (Table 7-2) delayed the bending motion. As the rods lowered onto the specimens, the cubes were first rotated until parallel; therefore, emulating torsion at the beginning of each test.

7.5.2 Slopes

The force-displacement curves followed a similar pattern for all bones. The plots were divided into six zones; A: pre-contact, B: short linear region corresponding to torsion, C: increase in slope corresponding to a change in loading type from torsion to bending, D: linear region corresponding to bending only, E: failure. Note that the length of pre-contact region (A) varied for each bone with some bones establishing contact straight away at the on-set (e.g. absence of region A).

The response of the specimens to bending was clearly linear, in other words the bending rigidity of each specimen was constant over region D. This suggests that had the elastic modulus between the bones been the same, the bending slope of the bones could be linearly proportional to their cross-sectional dimensions. A dimension equivalent to the term $r_1^4 - r_2^4$ of the second moment of area of a hollow cylinder was derived for each bone from CAD measurements (Table 7-9 and Figure 7-36). The bending slope was plotted against the latter, but no direct relationship could be found (Figure 7-37).

This could be due to several factors: (1) the differences in elastic modulus between each specimen, (2) the longitudinal asymmetry of each bone, (3) the difference in elastic modulus between the bones and the embedding material and (4) sample size. Indeed, Technovit has a lower Young's modulus with respect to the elastic modulus of cortical bone, therefore the force-displacement slope resulted from a combination of both the flexural rigidity of the bone and the shear rigidity of the embedding cubes. This was evident as the cubes also deformed and fractured during the tests. It should also be noted that only seven samples were analysed here, representing a relatively small population.

	Mediolateral diameter, d_{ml} [mm]	Mediolateral radius, r_{ml} [mm]	Thickness [mm]		Averaged thickness, t_{ml} [mm]
			Medial t_m	Lateral t_l	
O2001	18.03	9.01	3.96	3.36	3.66
O2002	19.79	9.89	3.58	3.36	3.47
A2001	22.71	11.35	2.50	3.34	2.92
A2002	21.70	10.85	3.77	2.81	3.29
A2003	22.18	11.09	3.41	2.43	2.92
A2004	21.03	10.51	3.13	2.90	3.01
A2005	18.67	9.34	3.08	3.31	3.20

Table 7-9: Cross-sectional mediolateral dimensions of the lamb femurs taken via CAD on CT-based reverse engineered models.

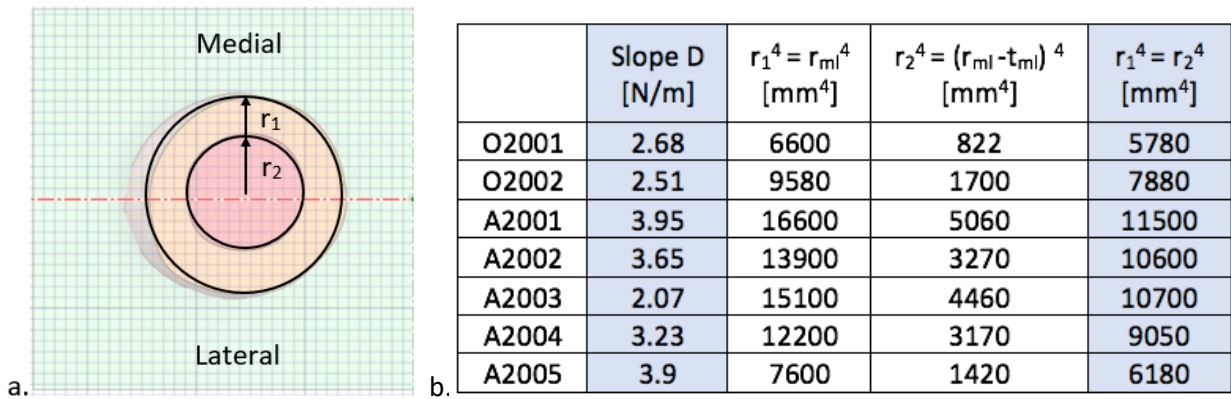


Figure 7-36: (a) Diagram of equivalent radius 1 and 2, r_1 and r_2 . (b) Table of the slope in region D attributed to bending and the derived term $r_1^4 - r_2^4$. M, medial; L, lateral; t, (cortical) thickness.

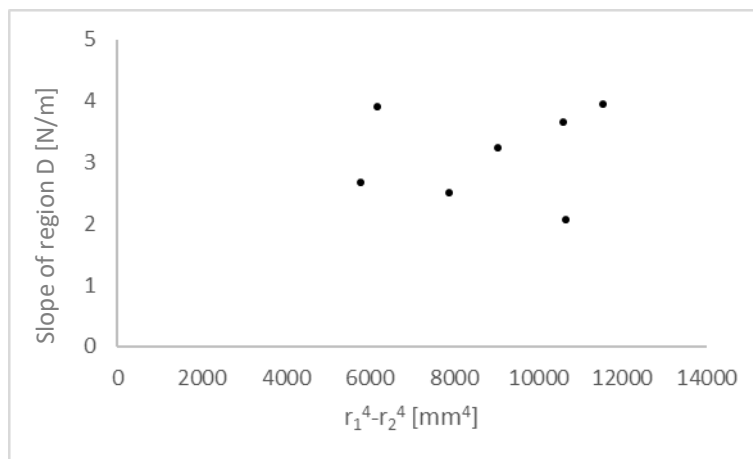


Figure 7-37: Plot of the slope of region D attributed to bending against the cross-sectional mediolateral dimension term $r_1^4 - r_2^4$.

7.5.2.1 Fracture behaviour

The force-displacement curves of specimens O2001, O2002, A2002 and A2004 were strictly linear until their embedding material cracked, bringing them to a complete failure between 3.5-6kN. Unfortunately, no conclusions can be made on the fracture behaviour of these bones since the failure occurred within the resin.

In contrast, specimens A2001, A2003 and A2005 all fractured at the bone. The failure mechanism of bones A2001 and A2005, namely the force-displacement curve, the fracture type and the fracture load appeared to be different from what was observed in bone A2003. A slight decrease in slope pre-fracture can be seen in the force-displacement curves of bones A2001 and A2005, suggesting that these two bones experienced yielding before fracturing at the shaft. This is congruent to the pre-fracture behaviour found in the literature for lamb tibia (Cheong et al. 2017). On the other hand, bone A2003 fractured abruptly with no sign of yielding.

Both bones A2001 and A2005 had multiple fractures including a comminute fracture, a transversal fracture (adjacent to the left embedding block for bone A2001 and to the right embedding block for bone A2005), and two longitudinal fractures. This was also apparent on the force-displacement curve as the bones failed in parts exposing bone fibres; which was also consistent with the results presented in (Cheong et al. 2017). On the other hand, bone A2003 was the only bone to sustain a single clean transverse fracture. Both bones A2001 and A2005 reached a peak force of 9.8kN and 7.1kN, respectively; whilst bone A2003 fractured at a much lower load of 4.3kN.

The differences in failure mechanism between the bones A2001 and A2005 compared to bone A2003, could be explained by the relatively larger angular misalignments between the embedding cubes of specimens A2001 and A2005; being 3.3° and 4.5° (as opposed to 1.6° for A2003) around the x-axis. As previously discussed, the angular misalignment would have introduced torsion and consequently shear stress in addition to the bending normal stresses. Therefore, causing both transverse and longitudinal fractures in the orientation of bone fibre. In comparison, a much smaller misalignment was measured on the embedding cubes of bone A2003 (at 1.6°). It can be seen on the force-displacement curve that there was no visible change in slope between region B (attributed to torsion) and region D (attributed to bending).

This would suggest that the torsional effect was negligible for this bone. Therefore, the failure mechanism of bone A2003 is more likely to be attributed to pure bending (normal) stresses.

7.5.3 Surface strain contours

Surface strain contours also provided information on the pre-fracture linear response of the bones. For each bone, the strain distribution pattern between point 1 (at 1mm displacement) and point 2 (pre-fracture) were nearly identical; which coincided with the linear behaviour of the bone in region D of the force-displacement curves. However, it is worth mentioning that there was a slight shift in the strains of bones A2001 and A2005 between the images of points 1 and 2. The tensile strains of bone A2001 shifted to the left, and the tensile strains of bone A2005 shifted to the right. Again, the latter was likely caused by the misalignment in the cubes.

The distributions of the x-axis strain (parallel to the bending axis) were typical of the four-point bending behaviour, with longitudinally distributed strain in compression at the top and tension at the bottom resulting from in-plane bending stresses. The strain distribution was as expected, with the maximum (tensile) strain at the bottom (lateral line) of the bone, the neutral (near zero) line extending along the midspan (cranial line) of the bone and the minimum (compressive) strain towards the top (medial side) of the bone.

The ROI encompassed the lateral line of the bone (predicted line of peak tensile strain), but did not encompass the medial line (predicted line of peak compressive strain). Therefore, it was also expected that, within the ROI, the magnitude of the maximum tensile strain would be higher than the magnitude of the minimum compressive strain.

Growing paint gaps were spotted on the DIC images during the bending tests. The gaps were located at the boundary between the bones and the cubes on the lateral side; meaning that the bones were not fully constrained in tension and had slipped slightly out of the cubes. Therefore, it can be assumed that the magnitude of the resulting DIC maximum tensile strain was lower than what would have been had the bones been fully constrained in tension by the resin.

The contour maps of the strains in the y' -axis were also congruent to the bending load. As explained in Chapter 3, due to the effect of Poisson's ratio, it was expected for the strains in

the y' and z' axes to be opposite in direction and lower in magnitude compared to the strains in the x -axis. This was effectively reflected in the y' -axis strain maps of all bones.

The principal strain contour maps were also consistent with the bending load. For a specimen under bending, one would expect to find the peak 1st principal plane strain at the bottom (which is under maximum tension in the x -axis) and the peak 2nd principal plane strain at the top (which is under maximum compression in the x -axis). This was true for the 1st principal strain. However, in the 2nd principal strain map, maximum compression was seen both at the top and bottom of the ROI, with the bottom concentration sometimes more obvious than the top. Again, this is because of the position of the ROI; the ROI encompassed the lateral line of the bone (where tensile strain is expected to peak around the specimen), but did not encompass the medial line (where the compressive strain is expected to peak). The compressive strain seen at the bottom of the 2nd principal plane strain map was in fact a reflection of the y' -strains, due to the Poisson's ratio and the incompressibility criterion.

7.5.3.1 Noise

Noise appearing as small islands of y' -strain concentrations can be seen at the bottom edge of the ROI of bones O2002, A2002 and A2005. As discussed in Chapter 5, since the bones are very curved around the x -axis, the angle of incidence of the camera onto the bone was by definition increasingly acute from the mid line to the top and bottom borders. This led to noise, which was particularly obvious on the y' -axis strain maps, which was tangent to the curvature.

7.6 Experimental set-up and techniques

7.6.1 DIC image quality

Particular attention had to be given to the speckle pattern and lighting because of the cylinder-like geometry of the bone. Both the speckle pattern and the lighting were tweaked and improved between the first test on specimen O2001 to the test on bone A2005. It was found that to obtain the best precision over the largest area, it was best to have a dense pattern with medium size black speckles (as seen on A2003, A2004 and A2005). In order to achieve this, the black spray paint was sprayed above the specimen and the diffusing cap was held continuously. An optimal lighting distribution over the ROI, particularly at the bottom,

was achieved by using three light sources, with one light source placed in between the cameras (i.e. parallel to the stereo plane).

7.6.2 Embedding material

Four specimens out of seven failed at the embedding material rather than the bones, i.e. the maximum load capacity was only determined for three bones. This suggests that it would be better to use a stronger embedding material such as dental cement in the future to avoid failure of the embedding material. Furthermore, if the embedding was made with a much stronger material, the force-displacement slope would be purely dependent on the bone. Therefore, allowing for direct conclusions to be drawn on the rigidity of the bone.

7.6.3 Embedding method

There were two main issues with the embedding method, the first being slipping of the bone out of the embedding blocks, and the second being misalignment between the cubes.

There are a few methods that have been used in the literature to secure bones within their embedding material, particularly for bending and torsion tests (Zdero et al. 2017). For instance, some studies placed a pin across the bone in the embedded ends (Figure 7-38.b). However, these studies suggested that perforating the bone could create weak points, which in turn may lead to crack initiation. Some other studies simply embedded the bones without removing the proximal and distal epiphyses (Figure 7-38.c). Logistically, this would be impractical for four-point bending tests on lamb femurs using DIC. The proximal and distal femur of lambs is very wide compared to the shaft length, therefore large blocks encasing the epiphyses would hinder the lighting and DIC view in the ROI.

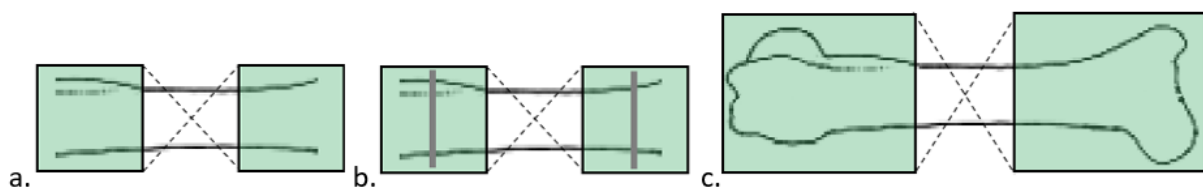


Figure 7-38: Embedding methods: (a) embedding of lamb femur shaft used in the current chapter, (b) embedding of lamb femur shaft with pins across each end, and (c) embedding of whole lamb femur without removing both ends.

7.6.4 Incident of the stereo system and ROI

Setting the stereo system at a 30° angle allowed for the lateral line (the expected area of maximum strain) to be visible within the AOI. The region of maximum tensile strain (ϵ_1) that appears in the DIC results is at the bottom of the AOI, as expected. However, the maximum strain was also located at the lower border for all bones. The border region of the bone was more prone to DIC errors as they could be out of focus due to the curvature. This suggested that the 30° angle may not be sufficient to confidently determine the maximum tensile strain on the bone. Ideally, the point of maximum first principal strain should be within the ROI at a distance away from the border. Placing the cameras at a lower angle, e.g. 45° would help capture the point of maximum strain. Similarly, in order to observe the maximum compressive principal strain (ϵ_2); which was expected at the medial line, a second set of cameras should be placed above the specimen at an incident angle of -45°. This would also allow a better understanding of the strain distribution over the cranial surface (from the medial to the lateral line).

In the current study, these higher angles could not be achieved due to limitations in the available experimental apparatus. A 30° angle was the maximum achievable angle with the current set up and is one of the limitations of our in-house DIC system. In the future, customized DIC set-ups could be developed in order to achieve a more flexible range of camera angles. Alternatively, commercial DIC system (such as ARAMIS 3D camera systems) could be used to obtain full-field measurements using high frame rates.

7.7 Conclusions

In this chapter, the changes proposed in the early experimental chapter (Chapter 5) have been implemented successfully. The resulting strain bands were in the majority longitudinal, indicating that the loading condition was consistent for each bone and consistent with in-plane bending. The contours appeared a lot more continuous than those seen in Chapter 5. The results obtained showed more consistency and were more suitable for FE comparison because:

1. Rigid body motion was minimized during the experiment;
2. Each bone specimen was aligned consistently with respect to the anatomical directions;

3. The ROI of DIC capture was set to capture peak tensile strains expected in bending;
4. Local crushing on the bone was minimized by loading on the embedding material;
5. The strains were captured directly from the bone rather than over the periosteum;
6. Speckles were made smaller and more consistent by using a spray can, and;
7. The lighting was better distributed over the ROI.

The results appeared to be suitable for the validation of a linear four-point bending model. However, there are four limitations that need to be considered during model creation and validation against DIC results: (a) the angular misalignment between the cubes, (b) the Young's modulus of Technovit (the embedding material), (c) the bones slipping out of the blocks, and (d) the noise at the lower portions of bones O2002, A2002 and A2005. These will be detailed in the next chapter.

8 FOUR-POINT BENDING FEA ON EMBEDDED LAMB BONES

8.1 Introduction

This chapter is built on the work of the first set of analyses described in Chapters 4 and 5; with the aim of finding a more accurate approach for the FE modelling of immature long bone under four-point bending conditions. The models presented here will be compared against experimental results reported in Chapter 7.

One specific aim of this chapter was to investigate the feasibility of using a homogenous isotropic mesh to model the cortical bone, which involved the segmentation of the inner cortical layer (e.g. MOD2/3 of Chapter 6). From the findings of Chapter 6, it was concluded that a model with a homogeneous mesh over purely cortical bone generated similar results to that of a model with a heterogeneous mesh. This provided evidence to further investigate the validity of using a homogeneous mesh to simulate four-point bending.

This is very useful in cases where CT scans were not available, but geometries can be obtained via alternative imaging modalities such as MRI or even ultrasound, which are more widely used in children due to their low radiation risk. This was also the case during the Covid pandemic, during which period the Sheffield Teaching Hospitals paused all research activities. Hence, the original plan of creating FE models based on CT scans (as presented in Chapter 6) could no longer be carried out due to the lack of access to QCT scanner. Therefore, an alternative plan had to be sought for obtaining 3D geometry of the lamb bones.

Two approaches were investigated: (1) Faro arm and (2) μ CT scanner. Both pieces of equipment were available at the University. The Faro arm was a very old model primarily used for non-biological samples. Upon testing the Faro arm approach, it was deemed unreliable due to the lack of maintenance (i.e. the machine only worked on some days and the technician could not troubleshoot it). The μ CT scanner was eventually selected as the final approach as it has been continuously used for bone applications in recent years. There was also an existing volume of knowledge within the research group on how to use the scanner. However, μ CT was an expensive equipment and I had to limit both the scanning resolution and volume in order to keep within the budget.

To sum up, in this chapter I attempted to validate a μ CT-based FEM pipeline using lamb femur, against 3D-DIC data from Chapter 7. A few adjustments need to be made to the original approach due to the switch from CT to μ CT. These include mainly segmentation of the geometry and the estimation of material properties. The advantage is that μ CT provides a higher resolution and should allow more accuracy in modelling the geometry. The disadvantage is the lack of a direct method to derive elastic modulus for ovine bones from the μ CT scans, due to the absence of relevant conversion parameters reported in the literature.

A structured mesh was chosen as the μ CT provides a clear surface separating the cortical bone from the marrow. The FE predictions were again compared against DIC results in order to check if a more consistent experimental approach (e.g. potting, removal of periosteum, etc.) improved the validation outcome.

8.2 Method

This section describes the steps taken to generate μ CT-based specimen-specific FE models of the lamb femurs tested in Chapter 7. The objectives were: to generate a whole bone model with embedding for each lamb femur, and to simulate the four-point bending behaviour (Figure 8-1).

First, the embedded femurs were μ CT-scanned. Then, the geometry was segmented from the μ CT images and converted into a three-part solid: two Technovit cubes and a bone shaft (cortical bone and marrow). The solid was orientated and meshed with homogeneous material properties. A set of boundary conditions were assigned to the model to run FE simulations. The simulations were performed at a displacement of 1mm applied to the top rods, which was shown to be within the linear region in the experimental results for all the tested bones (Chapter 7). Finally, the FE strain contours were compared against the DIC strain maps obtained in Chapter 7. These steps are detailed in the following sections.

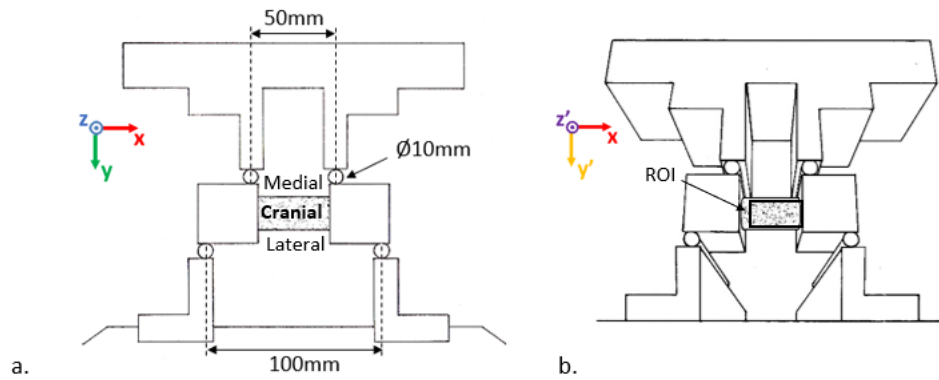


Figure 8-1: (a) The front (cranial) view shows the x-y plane of the four-point bending setup. A simply supported embedded bone was placed on two 10mm diameter steel rods spanning 100mm, with loaded steel rods on top, spanning 50mm. (b) The DIC stereo system view (cranial-lateral) defining the x-y' plane, which is the x-y plane rotated around the x-axis at an angle of -30° . The region of interest (ROI) is defined as the cranial-lateral surface between the embedding blocks.

8.2.1 μ CT scanning

Each bone was scanned individually using a SCANCO Medical μ CT scanner at the Animal Centre of the University of Sheffield. All scans were performed by a trained μ CT technician. The bones were kept frozen prior to each scan. They were mounted into a cylindrical jig and secured using a polystyrene cut out (Figure 8-2). A piece of aluminium foil was glued to the anterior face of the proximal cube to mark the orientation so that the bones could be mounted consistently with the proximal end positioned towards the front of the jig.

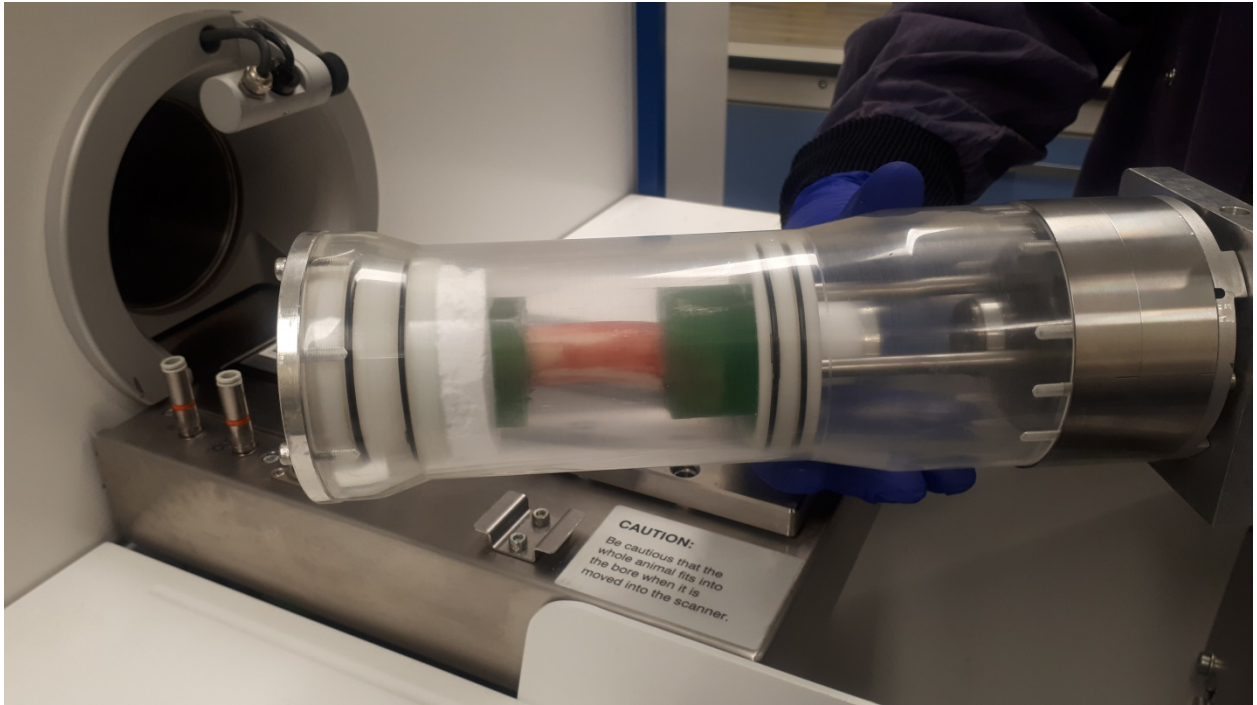


Figure 8-2: Jig for μ CT-scanning of embedded bone.

The scanning parameters were: slice spacing and thickness of 0.039mm, peak voltage of 70kVp and X-ray exposure of 34 μ As. The voxels were output as a single pixel and the pixels were 0.039mm. The bones were scanned along their long axes. A set amount of budget was given for the μ CT imaging and therefore the scanning time was limited to approximately two hours per bone. This was not sufficient to scan the whole specimen from one end of the embedding to the other. Therefore, a decision was made to scan only from the inner surface of the proximal embedding to the inner surface of the distal embedding (Figure 8-3). This was based on the assumption that the bone segments within the embedding was outside the ROI, and hence could be modelled as part of the resin material in the final FE model. Once scanning was completed, the bones were put back into the freezer. The μ CT images were then reconstructed using a third-party software provided by the manufacturer (Scanco Medical AG).

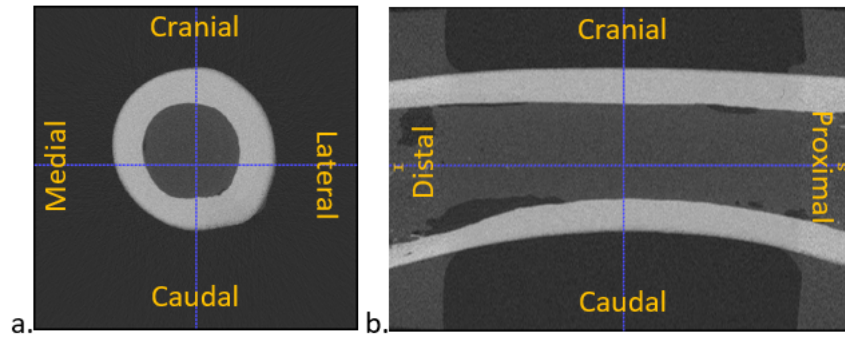


Figure 8-3: μ CT images of the transverse (a) and sagittal (b) sections of the embedded bone O2001, showing the total volume of specimen that has been scanned.

8.2.2 Segmentation

The DICOM files obtained from the μ CT scans of the bones were segmented with ITK-Snap version 3.8.0 (Yushkevich et al. 2006). Each bone was segmented into two faceted bodies, the cortical bone (red) and the marrow (green) (Figure 8-4). An intensity threshold of 150HU was used to mask the contour of the cortical bone. After the automatic segmentation, a layer of the embedding block was manually added forming a square at each end of the shaft. The corner of each square was later on used to orient the FE model.

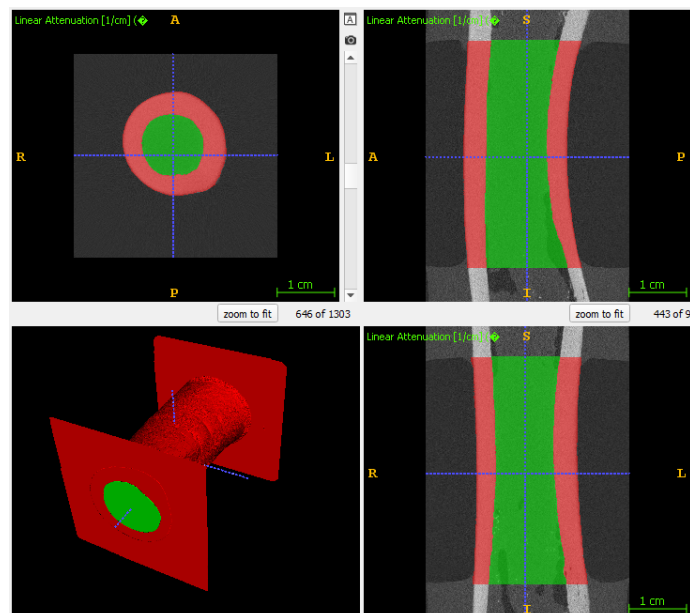


Figure 8-4: Segmentation of the cortical bone (red) and marrow (green) of embedded bone O2001 in the transverse (upper left), sagittal (upper right), and median (lower right) planes. Lower left view shows 3D representation of the segmented bone and inner surfaces of the embedding material.

8.2.3 Reconstruction

The STL files of the segmentation were imported into Ansys SpaceClaim 2021R2 for reverse engineering reconstruction. Each specimen was reconstructed as an assembly of two components: the embedding blocks and the bone shaft (cortical bone and marrow). Note that the orientation of the segmentation within the CAD global coordinate system XYZ was imported from the DICOM files and was dependent on the position of the bone in the μ CT-scanner. This was why the bones needed to be secured in the jig during the scans so that when imported into SpaceClaim, the proximal and distal surfaces of the embedding blocks were parallel to the XY-plane. These surfaces were used to define the proximal and distal planes, with the proximal side in the negative Z-direction and the distal side in the positive Z-direction (Figure 8-5).

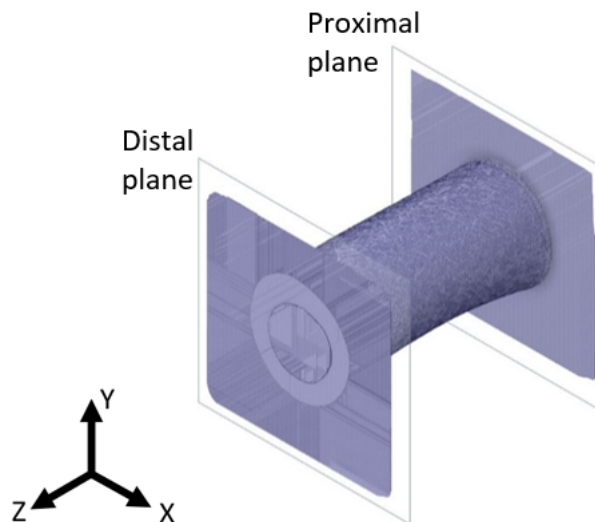


Figure 8-5: Faceted body of the segmentation of bone O2001 within the global coordinate system of the CAD space in ANSYS SpaceClaim 2021 R2.

8.2.3.1 Embedding blocks

The embedding blocks were built over the faceted squares as 35x35x35mm cubes. The four corners of the segmented squares were used as landmarks to locate the cubes within the proximal and distal planes. Small misalignments (XY translation of $<2\text{mm}$ and Z rotation of $<4.5^\circ$) were measured between paired squares. However, for simplification, the position of both squares was averaged for each bone and the embedding blocks were reconstructed

perfectly aligned with one another. The calculations to derive the final position of each pair of cubes is detailed below.

First, the location of each corner on the proximal and distal segmented squares was recorded (Figure 8-6). Then the centre of each square, O_{proximal} and O_{distal} , was derived by calculating the midpoint between all four corners. Finally, the centre points of both proximal and distal squares were averaged to define the new centre location, O . Similarly, the angular position (from the vertical plane) of each square, θ_{proximal} and θ_{distal} , was derived from the locations of the four corner points by finding the angle between each point and then averaged to define the new angle, θ .

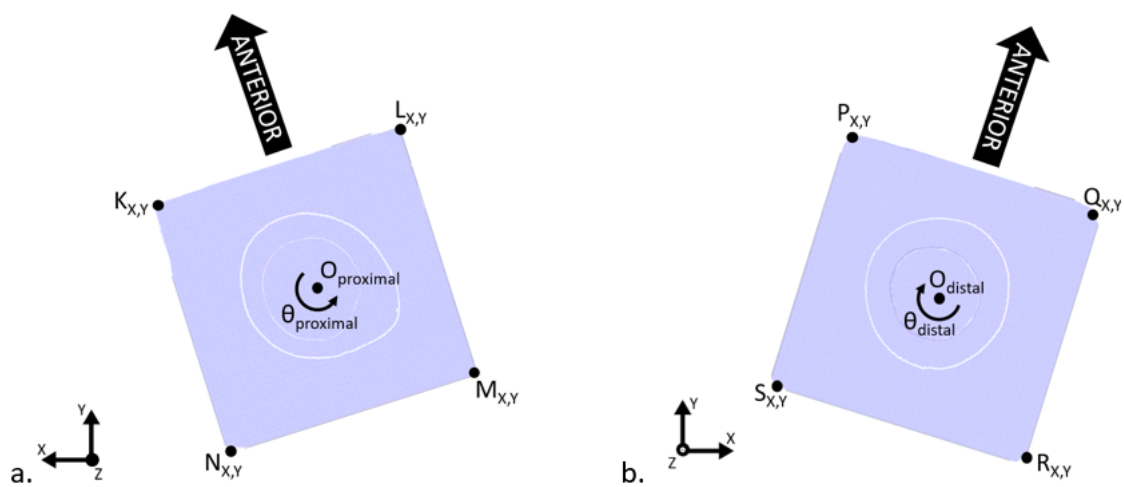


Figure 8-6: Proximal (a) and distal (b) views of the segmentation of embedded bone O2001, where $O_{\text{proximal/distal}}$ is the centre and $\theta_{\text{proximal/distal}}$ is the angle of rotation of each corresponding embedding square within the global coordinate system, XYZ. Note that rotations were substantially exaggerated for illustration purposes.

Finally for each bone model, cubes of 35x35x35mm centred at O and rotated by θ from the vertical plane, were extruded over the segmentation (Figure 8-7).

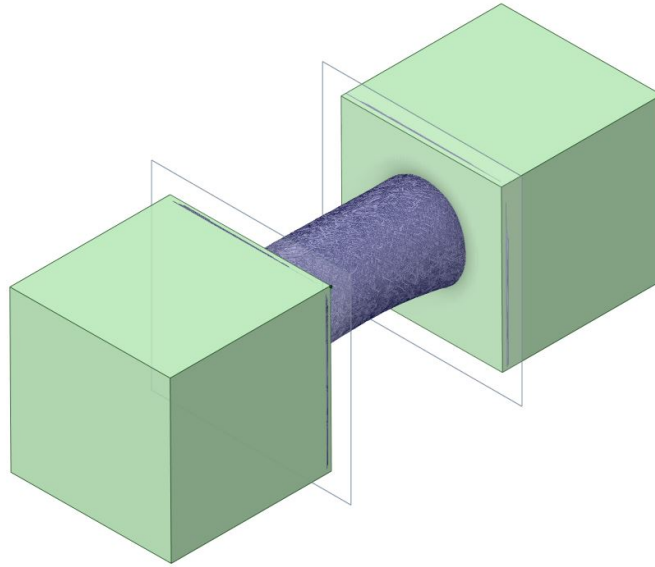


Figure 8-7: Solid bodies of the embedding cubes (green) extruded over the faceted body of bone O2001.

8.2.4 Cortical bone and marrow

Surfaces were extrapolated from the cortical bone and marrow segmentations between the proximal and distal planes. Similar to MOD2 in Chapter 6, the whole shaft was converted into a solid with a surface differentiating the cortical layer from the marrow (Figure 8-8). Both cortical bone and marrow were set to share topology in order to later create a structured but continuous mesh over both entities.

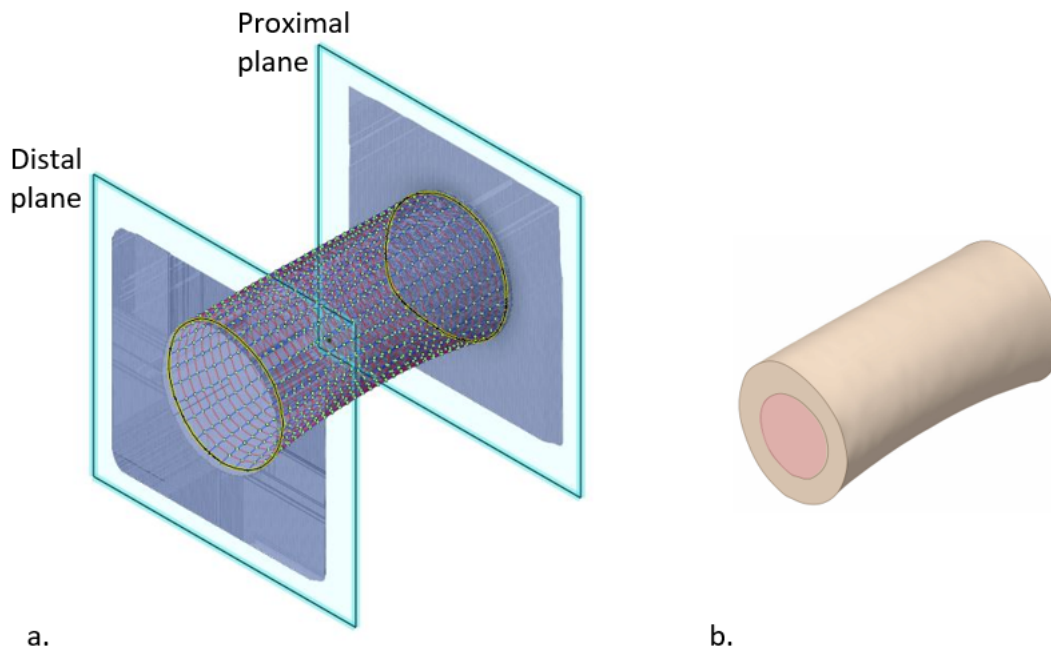


Figure 8-8: Extraction of surface points over the faceted body of bone O2001 between the distal and proximal planes (a) to convert the shaft into a two-part solid body consisting of the cortical bone and the marrow (b).

8.2.4.1 Local coordinate system

Two local coordinate systems were created using the edges of the embedding cubes. These were set to match the experimental four-point bending plane (Figure 8-1.a) and DIC plane (Figure 8-1.b) established in Chapter 7. The first system, xyz , was placed so that the x -axis was aligned with the long axis of the bone; in the distal-proximal direction for left femurs (O2002, A2002, A2003 and A2005), and in the proximal-distal direction for right femurs (O2001, A2001 and A2004). The y -axis was aligned in the medial-lateral direction, and the z -axis was aligned in the cranial-caudal direction (Figure 8-9.a). The second coordinate system, $xy'z'$, was defined so that axes y' and z' were at 30° from the original y and z axes, respectively, representing the DIC plane (Figure 8-9.b).

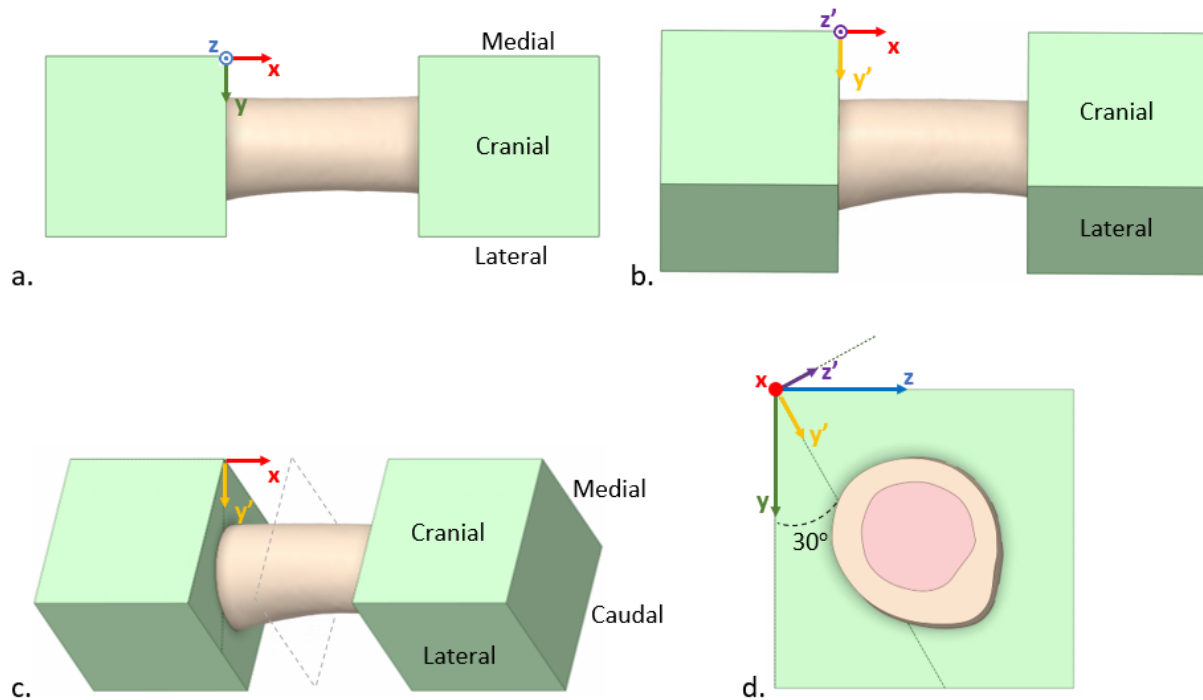


Figure 8-9: FE model assembly of specimen O2001. (a) Cranial view showing the x-y plane, which corresponds to the experimental bending plane where y is the loading axis and x is the bending axis. (b) Cranial-lateral view showing the x-y' plane, which is the x-y plane rotated around the x-axis at an angle of 30° and corresponds to the experimental DIC stereo system plane. (c) View corresponding to Camera 2 (left side) of the stereo system, which is rotated around the y'-axis at an angle of 15° (stereo angle). (d) Cross-sectional view of the right cube taken at the midplane between the proximal and distal planes showing both coordinate systems xyz and xy'z'.

8.2.5 Boundary conditions

Lines were drawn onto the medial and lateral faces of each cube in order to create guiding edges where displacement constraints can be applied. These lines were set to match the positions of the rods in the experiment (Figure 8-10). The two lines on the medial (A and B) and lateral (C and D) faces of the cubes spanned 50mm, and 100mm, respectively.

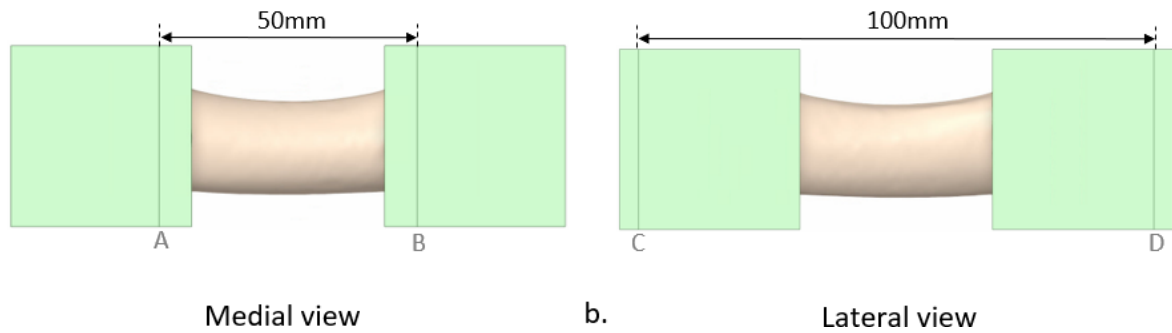


Figure 8-10: Medial (a) and lateral (b) views of the bone O2001 assembly showing the lines corresponding to the positions of the top (A, B) and bottom (C, D) rods during the experiment.

Each assembly was imported into Ansys Mechanical 2021R2 to apply boundary conditions and assign contact pairings. To replicate the experiment at 1mm displacement of the top rods, a displacement d_y of 1mm was applied to lines A and B in the y-axis. Line C was fixed in all directions and line D was constrained in the y-axis (Figure 8-11). Bonded contact pairings were created between the shaft's proximal and distal surfaces and each cube's inner surface. Note that no contact pairing was needed between the cortical bone and the marrow because they were set to share topology and were meshed as a single body.

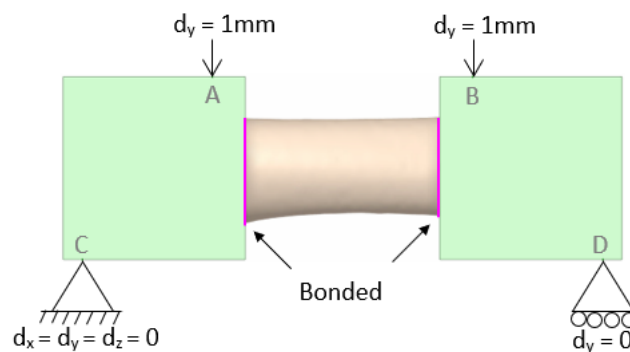


Figure 8-11: Diagram of the boundary conditions applied to lines A, B, C and D, and contact pairings (bonded) applied to the interface of bone O2001 and resin cubes to simulate the four-point bending experiment in Chapter 7.

8.2.6 Material properties

8.2.6.1 Embedding cubes and marrow

For all models, the marrow was assigned a constant elastic modulus of 25kPa (Jansen et al. 2015), and the embedding cubes (Technovit 4071) were assigned a constant elastic modulus of 2.5GPa (Grassi et al. 2016).

8.2.6.2 Cortical bone

Unlike in Chapter 6, the derivation method for CT-based bone mineral density (BMD) differed from that based on μ CT (Dall’Ara et al. 2011). Moreover, to the authors knowledge, an empirical relationship between ovine bone elastic modulus and μ CT density has not been established yet. Thus, there was not enough information to confidently derive specimen-specific elastic modulus values from the μ CT intensity attenuation. Nevertheless, the mean intensity of each bone was still recorded for discussion purposes. The μ CT-scan’s mean intensity of the cortical bone for each specimen was measured in ITK-Snap as shown in Table 8-1. Note that the Scanco μ CT-scanner has been calibrated weekly using a scanner specific densitometric phantom with five insertions (800, 400, 200, 100 and 0mg HA/cc) in order to monitor the stability of the calibration parameters.

	O2001	O2002	A2001	A2002	A2003	A2004	A2005
Intensity mean [HU]	5004	5147	5307	5290	5271	5248	5524

Table 8-1: Scanco μ CT-scan mean intensity of the cortical bone.

For the purpose of this study, the bones were assigned an estimate of the highest possible elastic modulus based on the literature. The highest elastic modulus value was associated to a bone with no pores; i.e. a bone with a bone volume to total volume ratio of 1 (BV/TV = 1). Studies on cortical bone found ash density to be linearly proportional to BV/TV. This was reported in adult tibia, adult femur and spine, and bovine femur (Dall’Ara et al. 2011, Tassani et al. 2010). Based on these linear relationships, cortical bone without pores (BV/TV = 1) could be estimated to have an ash density ranging from 1.2-1.4g/cc. Hence, the highest elastic modulus value was derived from the upper bound of this range (1.4g/cc).

First, the ash density was converted to an equivalent HA density (Eq.6-7) using a CT calibration correction equation for HA (used previously in Chapter 6):

$$\rho_{HA} = 1.14 \rho_{ash} - 0.09 \quad \text{Eq.8-1}$$

Plugging in the ash density upper bound value (1.4g/cc),

$$\rho_{HA} = 1.14 (1.4[g/cc]) - 0.09 \quad \text{Eq.8-2}$$

$$\therefore \rho_{HA} = 1.5 [g/cc] \quad \text{Eq.8-3}$$

Then, the HA equivalent density was converted to elastic modulus by applying Grant's ovine-specific empirical equation (used previously in Chapter 6 Eq.6-1),

$$E = 12.35\rho_{HA}^{1.32} \quad \text{Eq.8-4}$$

$$\therefore E \leq 20 \text{ [GPa]} \quad \text{Eq.8-5}$$

8.2.6.3 Visual assessment and sensitivity analysis

Note that 20GPa was estimated to be the elastic modulus for cortical bone with a BV/TV = 1 (non-porous mature cortical bone). However, immature cortical tissue in long bone is typically porous (Ambrose et al. 2018), and thus 20GPa is likely to be an over-estimation (see section 2.1.5 and 2.2.1). In order to determine the porosity in the ovine samples, a visual assessment was made where transverse μ CT images of the bones were taken at five different locations (Figure 8-12): at the most proximal end (A), between the proximal end and the midshaft (B), at the midshaft (C), between the midshaft and the distal end (D), and at the most distal end (E).

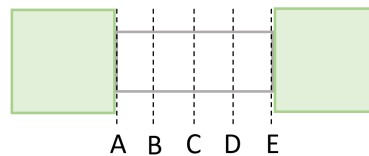
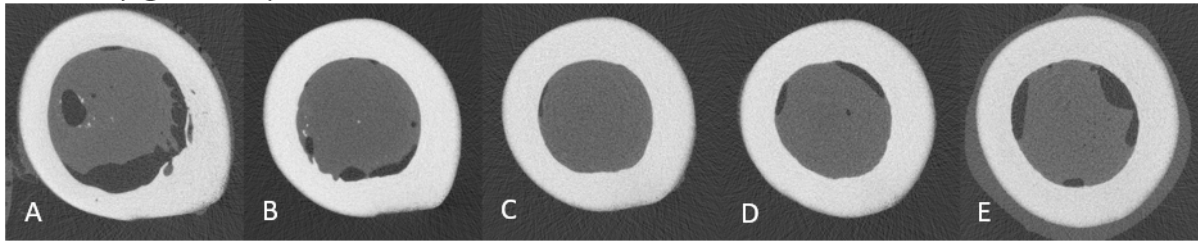


Figure 8-12: Diagram of the five cross-sections used for image analysis on porosity.

Pores were present in most of the bones; some bones had no identifiable pores and others presented with pores on the caudal side of the bone, particularly towards the proximal (A) and distal (E) ends of the bone. Below are images of bone O2001 (Figure 8-13.a), which had no visible porosity, and of bone A2005 (Figure 8-13.b), which had the highest level of porosity amongst the samples.

a.O2001 (right femur)



b.A2005 (left femur)

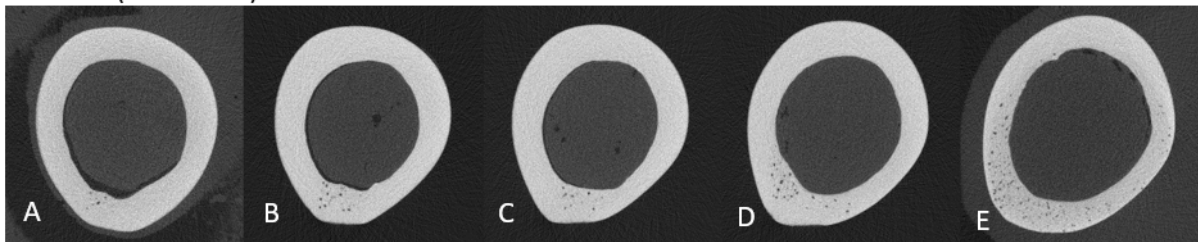


Figure 8-13: Transverse μ CT images of bone O2001 (a) and A2005 (b) of the five planes at the most proximal end (A), between the proximal end and the midshaft (B), at the midshaft (C), between the midshaft and the distal end (D), and at the most distal end (E).

Following this visual assessment, it was decided that a sensitivity analysis should be performed for each bone to study the effect of different elastic moduli. As 20GPa was the theoretical highest value that could be expected, the elastic modulus values were systematically decreased (20GPa, 15GPa, 10GPa and 5GPa) in order to examine their effects on the predicted reaction force and strains.

8.2.7 Mesh

The solid bodies were meshed in Ansys Workbench 2021R2 with quadratic order elements. For each bone, the shaft was meshed with tetrahedral elements and the cubes were meshed with hexahedral elements (Figure 8-14).

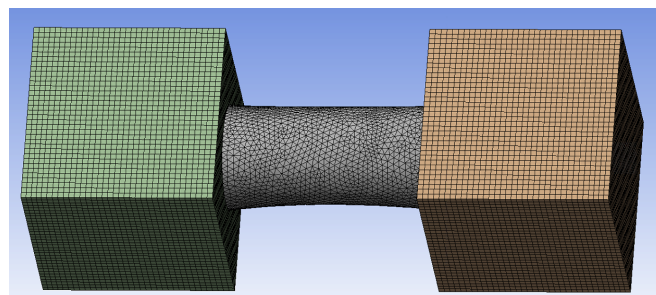


Figure 8-14: Meshed FE assembly of specimen O2001 with 1mm hexahedral (cubes) and tetrahedral (shaft) elements.

A mesh convergence study was performed on specimen O2001. Similar to the method adopted in Chapter 6, the convergence was performed by remeshing the model with a decreasing element size, equivalent to a first and second degree refinement. The element sizes used for the convergence studies were: 2mm, 1mm, 0.5mm and 0.33mm based on the cortical thickness (i.e. the thickness through which maximum stress is expected). Both the peak values of the first and third principal strains were plotted against the total number of nodes (Figure 8-15). The convergence plots showed a typical converging curve for both peak values of the principal strains. The 1mm mesh highlighted in red was shown to have a percentage difference of <3% compared to the most refined mesh (0.33mm). Therefore, 1mm was used for final analysis.

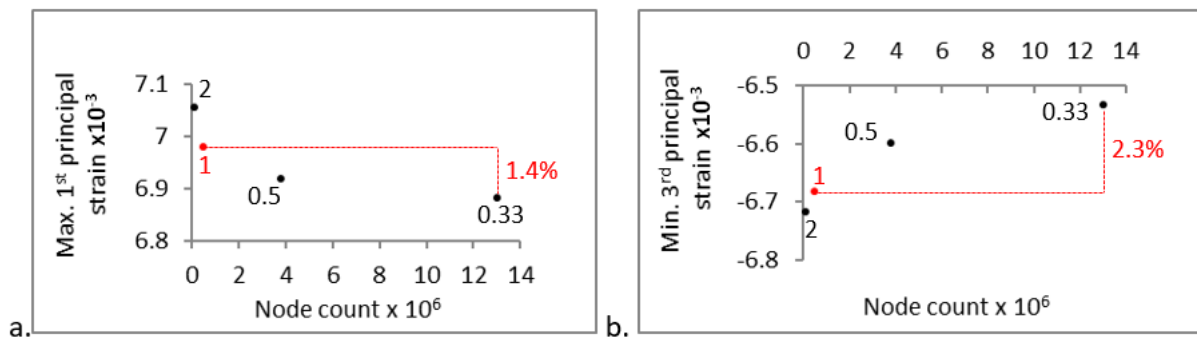


Figure 8-15: Principal strain convergence plots with element edge sizes 2mm, 1mm, 0.5mm and 0.33mm, showing convergence of the maximum first principal strain (a) and the minimum third principal strain (b). The red dashed line indicates the percentage difference in predicted strain between the converged mesh and the most refined mesh.

8.3 Results

FE results were obtained at an equivalent 1mm displacement of the top rods (displacement obtained through linear correction of force-displacement plots in Chapter 7). The cranial-lateral surface strains and reaction forces obtained through the FEA were compared against the experimental results in Chapter 6.

Normal strains were calculated in the axes corresponding to the DIC plane, i.e. the x and y' axes. The FE-predicted 1st (tensile) and 3rd (compressive) principal strains were also plotted and compared against the DIC 1st (tensile) and 2nd (compressive) plane strains. For consistency, all DIC strain maps were plotted onto the frames taken through Camera 2, which was on the right side of the stereo system. Accordingly, all FE strain contours were presented

from the same angle (30° below the horizontal and 15° from the vertical). Note the positions of the cranial and lateral lines shown in Figure 8-16.

The sum of reaction forces on lines A and B (Figure 8-16) were evaluated in the y-axis (loading axis) and compared to the experimental reaction force.

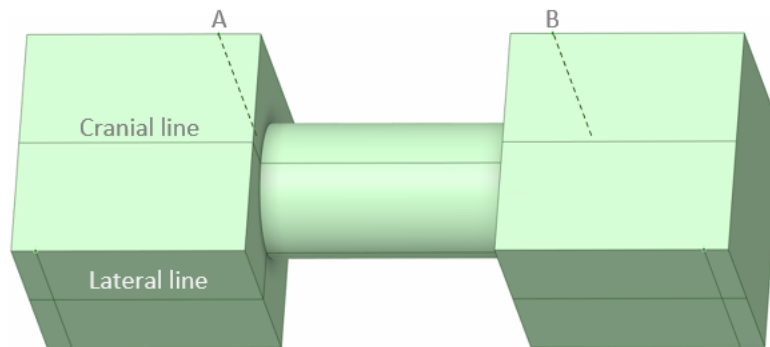


Figure 8-16: Diagram showing the positions of the cranial and lateral lines, and lines A and B where the reaction force was evaluated in the FE model.

8.3.1 Strain contours (with cortical bone elastic modulus of 20GPa)

The results presented below are for models which were assigned 20GPa for the cortical bone elastic modulus.

Across all bones, the FE-predicted strains showed consistent and repeatable patterns expected with a typical four-point bending profile. In terms of general strain patterns, the FE-predicted contours compared well with the DIC contours. The position of the neutral line (where strain was close to 0) appeared at a consistent location across all bones comparing FE versus DIC. All strain values compared well above the cranial line, with the FE over predicting the strains below the cranial line for both compression and tension.

The FE-predicted reaction forces were consistently higher (ranged from 1.4 to 3.5 times) than the measured values. The comparison between FE and DIC results (strains and reaction forces) are illustrated in a series of figures and tables below for all seven bones.

O2001

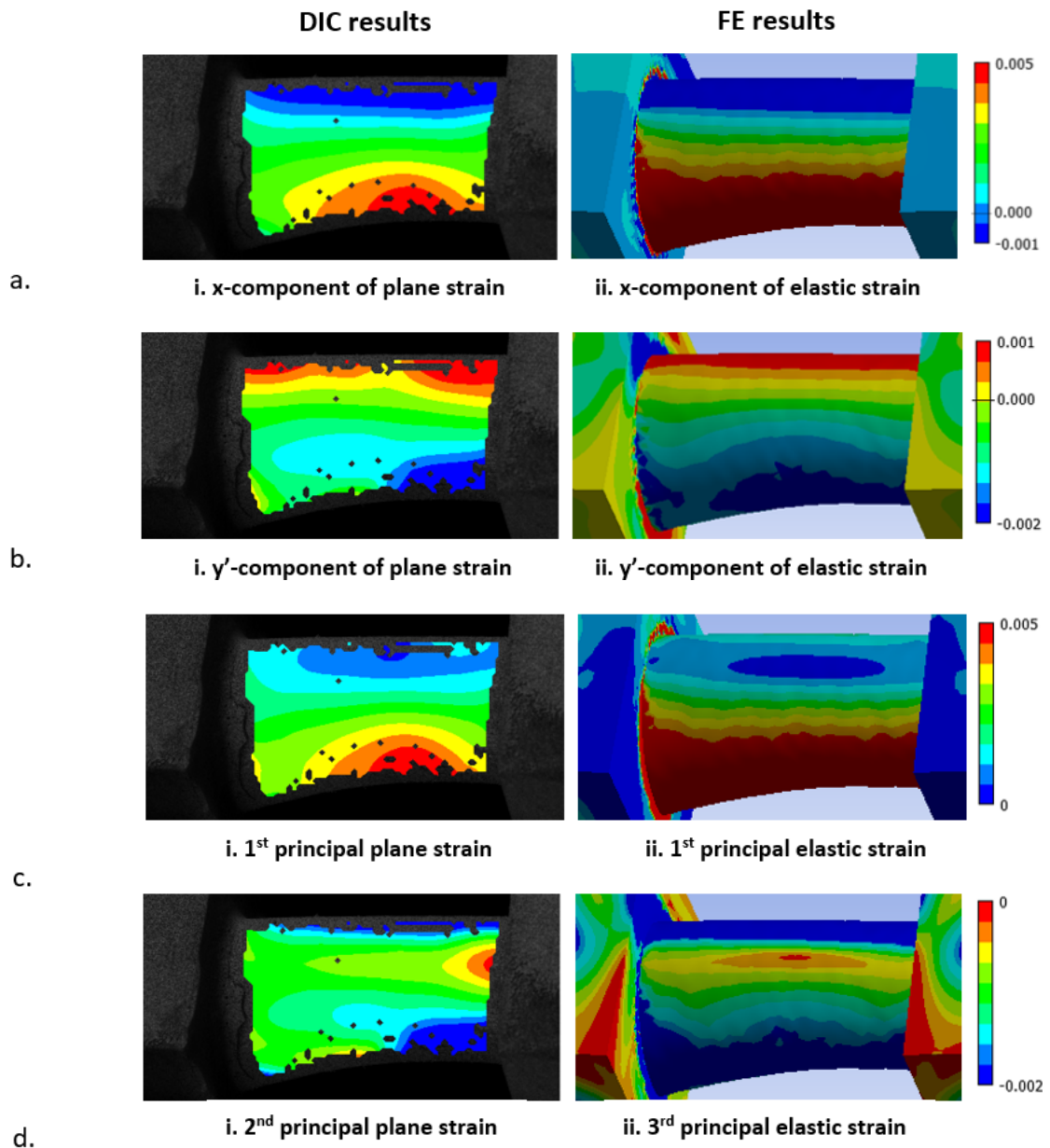


Figure 8-17: DIC measured (i) and FE predicted surface strains (ii) of bone O2001. (a) Strains in the x-direction. (b) Strains in the y' -direction. (c) Principal tensile strain. (d) Principal compressive strain.

O2001	Experimental	FE
Reaction force [kN]	2.69	5.19

Table 8-2: FE predicted y -component of the reaction force measured on the nodes with applied displacement constraints for bone O2001.

O2002

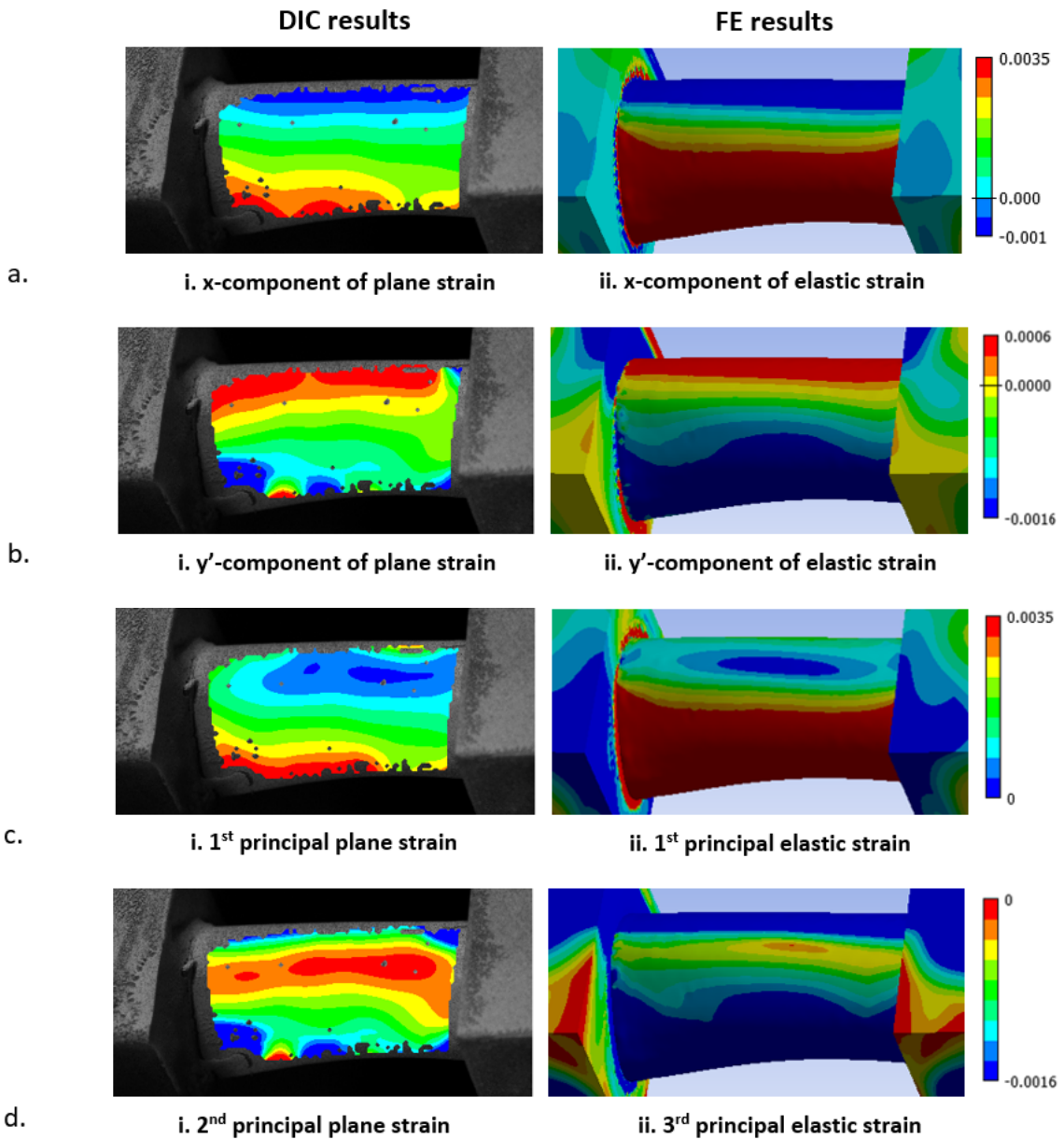


Figure 8-18: DIC measured (i) and FE predicted surface strains (ii) of bone O2002. (a) Strains in the x-direction. (b) Strains in the y' -direction. (c) Principal tensile strain. (d) Principal compressive strain.

O2002	Experimental	FE
Reaction force [kN]	2.51	6.13

Table 8-3: FE predicted y -component of the reaction force measured on the nodes with applied displacement constraints for bone O2002.

A2001

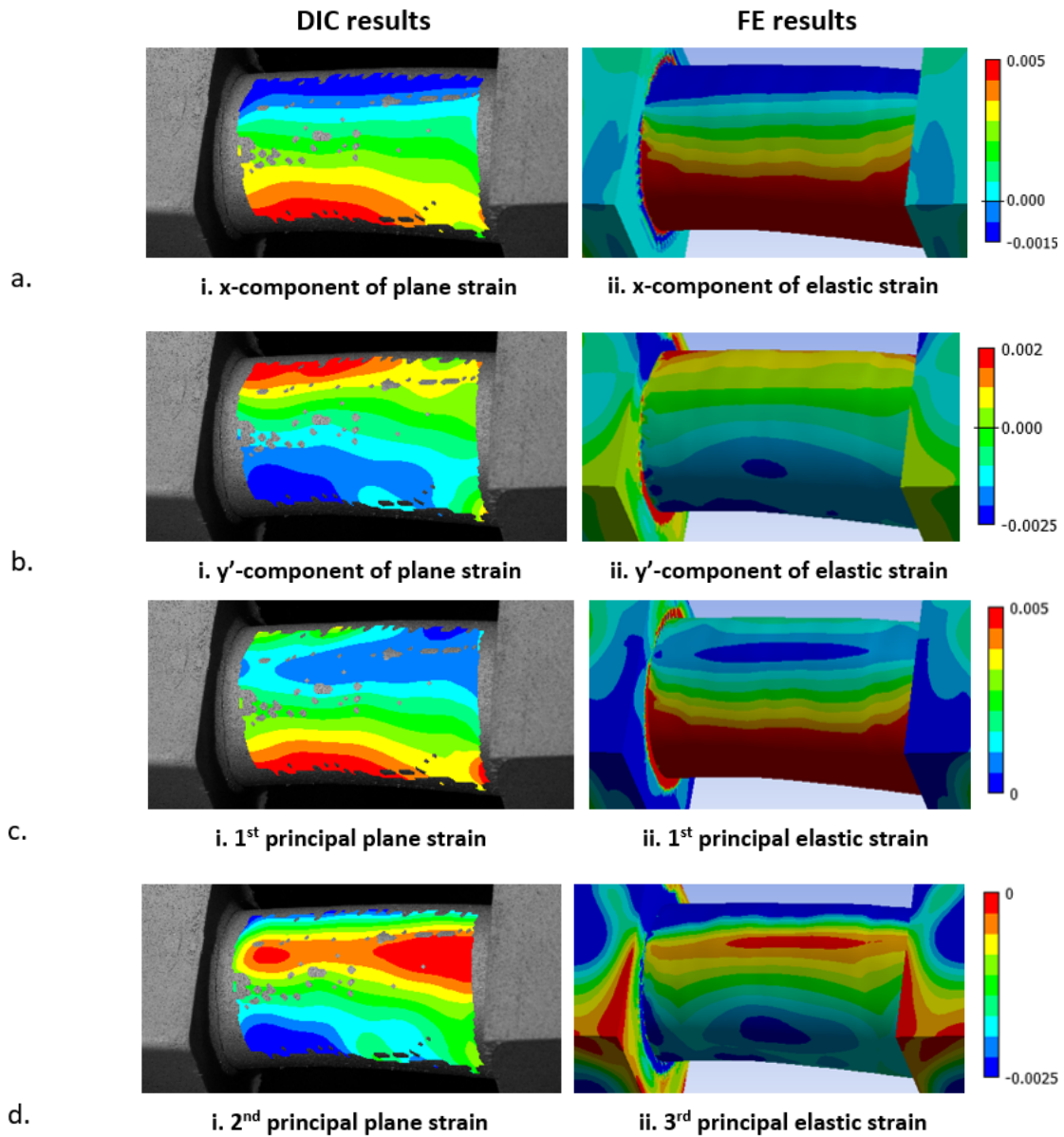


Figure 8-19: DIC measured (i) and FE predicted surface strains (ii) of bone A2001. (a) Strains in the x-direction. (b) Strains in the y' -direction. (c) Principal tensile strain. (d) Principal compressive strain.

A2001	Experimental	FE
Reaction force [kN]	3.89	7.40

Table 8-4: FE predicted y -component of the reaction force measured on the nodes with applied displacement constraints for bone A2001.

A2002

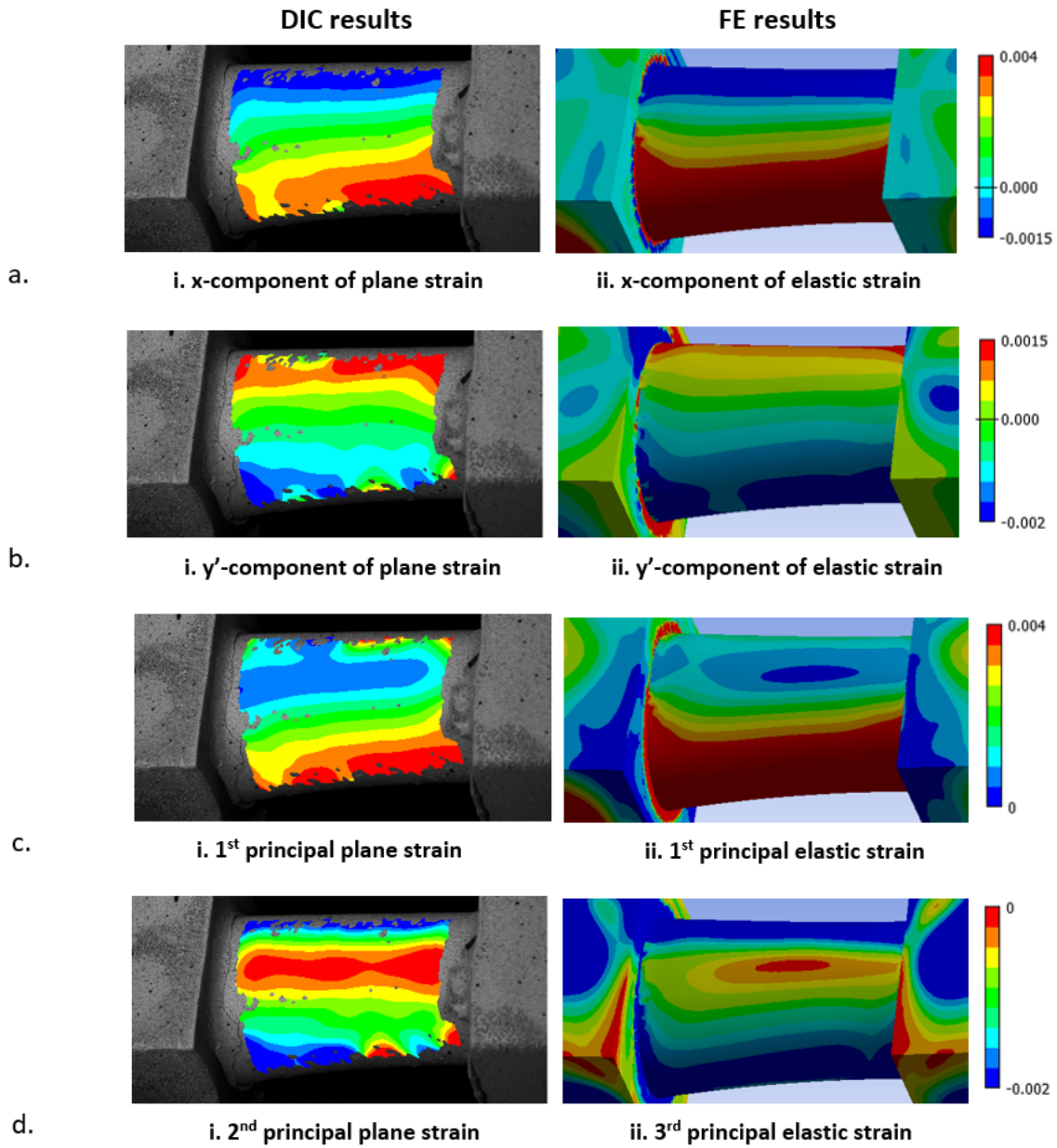


Figure 8-20: DIC measured (i) and FE predicted surface strains (ii) of bone A2002. (a) Strains in the x-direction. (b) Strains in the y' -direction. (c) Principal tensile strain. (d) Principal compressive strain.

A2002	Experimental	FE
Reaction force [kN]	3.66	7.80

Table 8-5: FE predicted y-component of the reaction force measured on the nodes with applied displacement constraints for bone A2002.

A2003

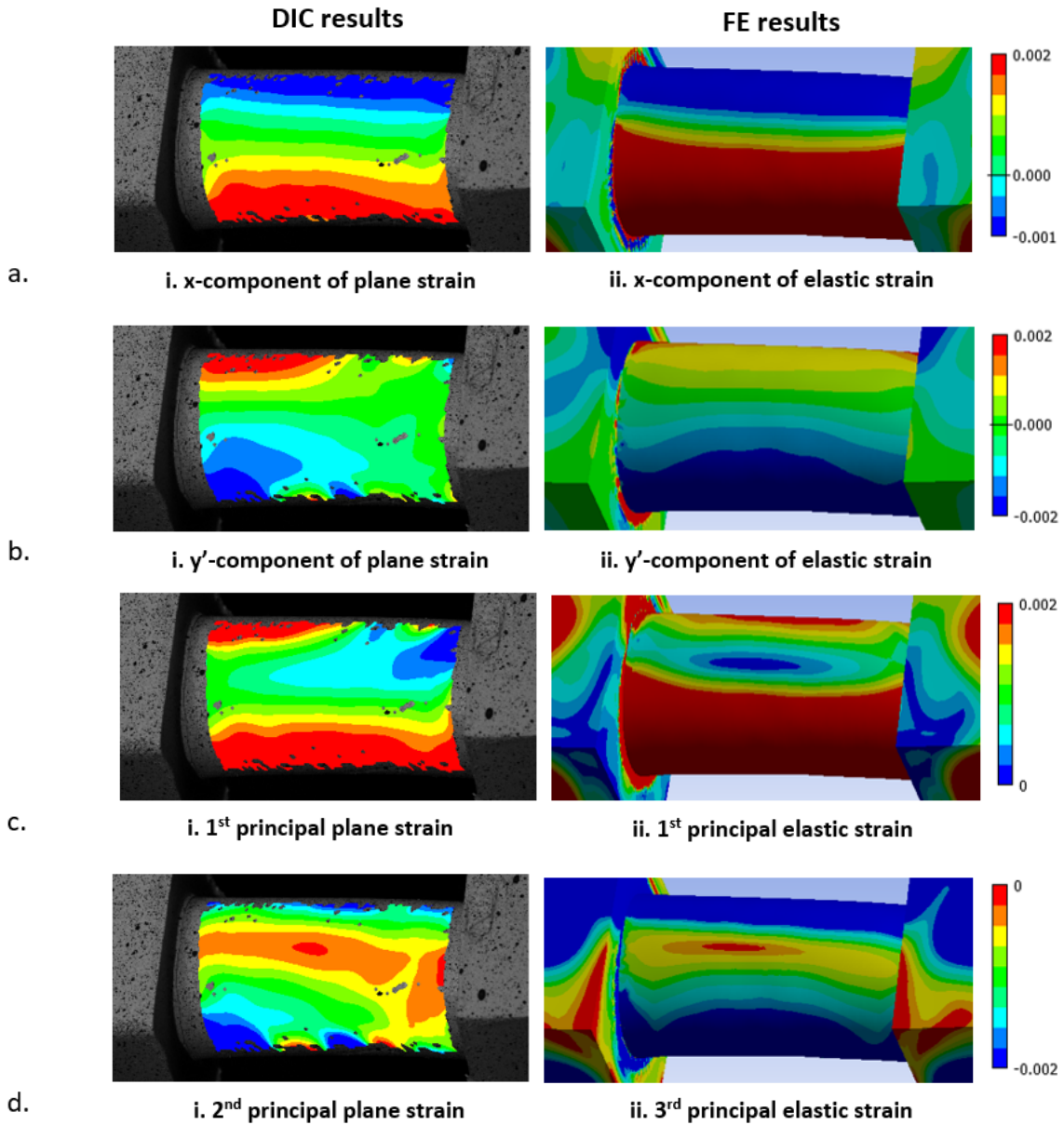


Figure 8-21: DIC measured (i) and FE predicted surface strains (ii) of bone A2003. (a) Strains in the x-direction. (b) Strains in the y' -direction. (c) Principal tensile strain. (d) Principal compressive strain.

A2003	Experimental	FE
Reaction force [kN]	2.05	7.29

Table 8-6: FE predicted y -component of the reaction force measured on the nodes with applied displacement constraints for bone A2003.

A2004

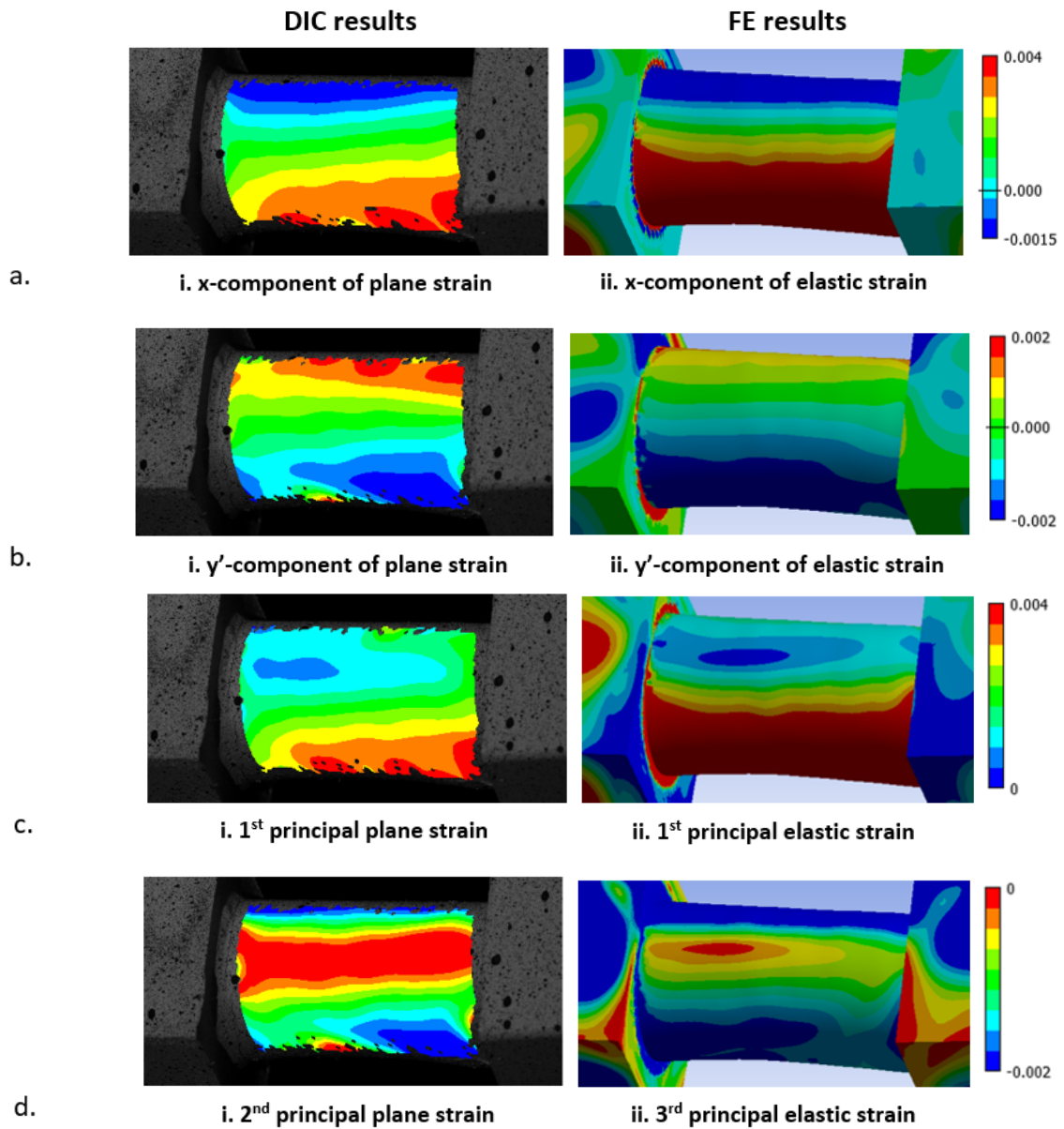


Figure 8-22: DIC measured (i) and FE predicted surface strains (ii) of bone A2004. (a) Strains in the x-direction. (b) Strains in the y' -direction. (c) Principal tensile strain. (d) Principal compressive strain.

A2004	Experimental	FE
Reaction force [kN]	3.25	7.31

Table 8-7: FE predicted y -component of the reaction force measured on the nodes with applied displacement constraints for bone A2004.

A2005

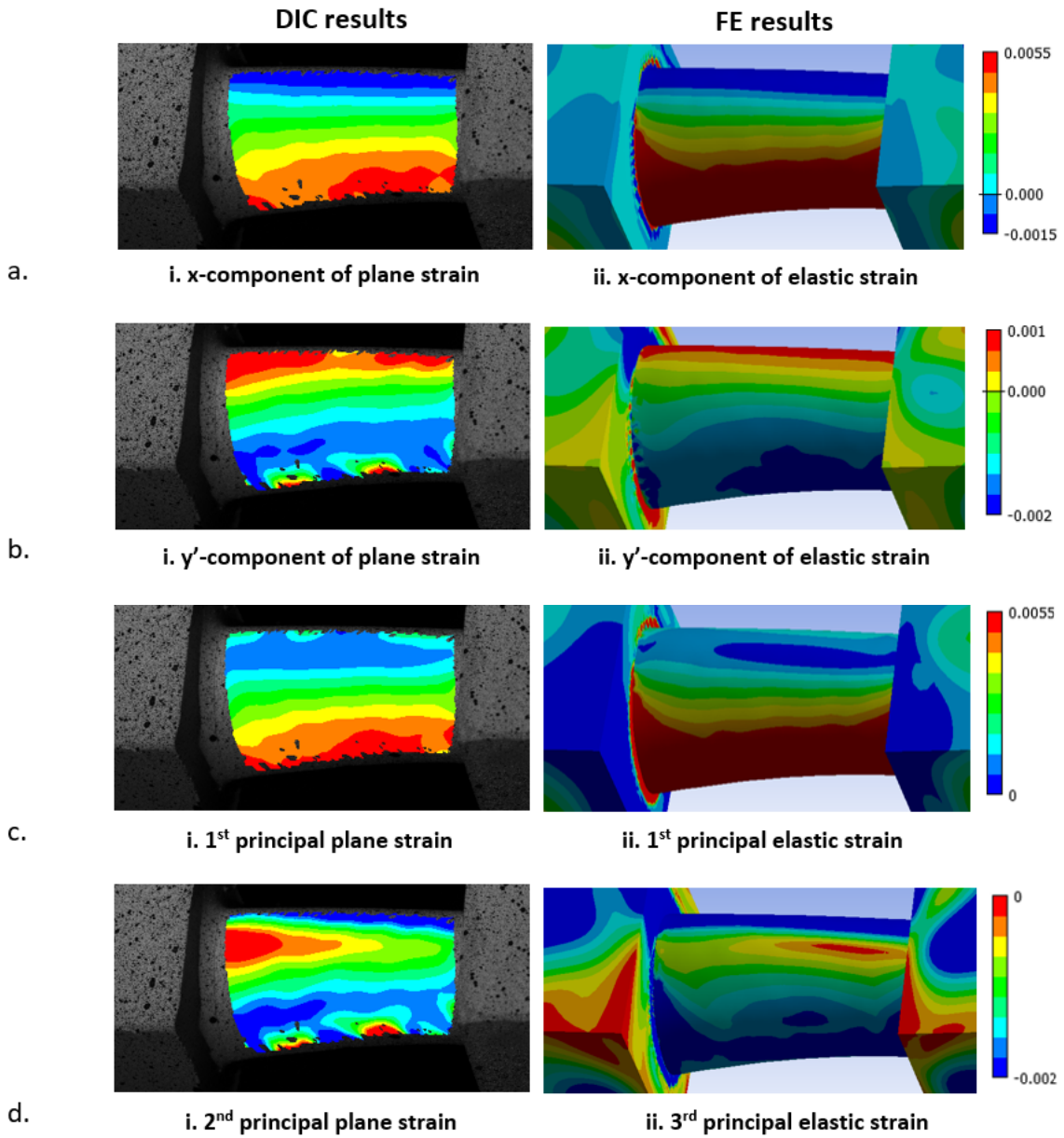


Figure 8-23: DIC measured (i) and FE predicted surface strains (ii) of bone A2005. (a) Strains in the x-direction. (b) Strains in the y' -direction. (c) Principal tensile strain. (d) Principal compressive strain.

A2005	Experimental	FE
Reaction force [kN]	3.94	5.48

Table 8-8: FE predicted y -component of the reaction force measured on the nodes with applied displacement constraints for bone A2005.

8.3.2 Sensitivity analysis of the cortical bone elastic modulus

Decreasing the elastic modulus of the cortical bone in the FE models resulted in a nonlinear decrease in the reaction force and a nonlinear increase (Figure 8-24) in the principal strains' magnitudes, however the strain distribution over the ROI remained unchanged (Figure 8-25). This was true for all specimens. The results of the sensitivity analysis for bone O2001 are presented below for illustration purpose.

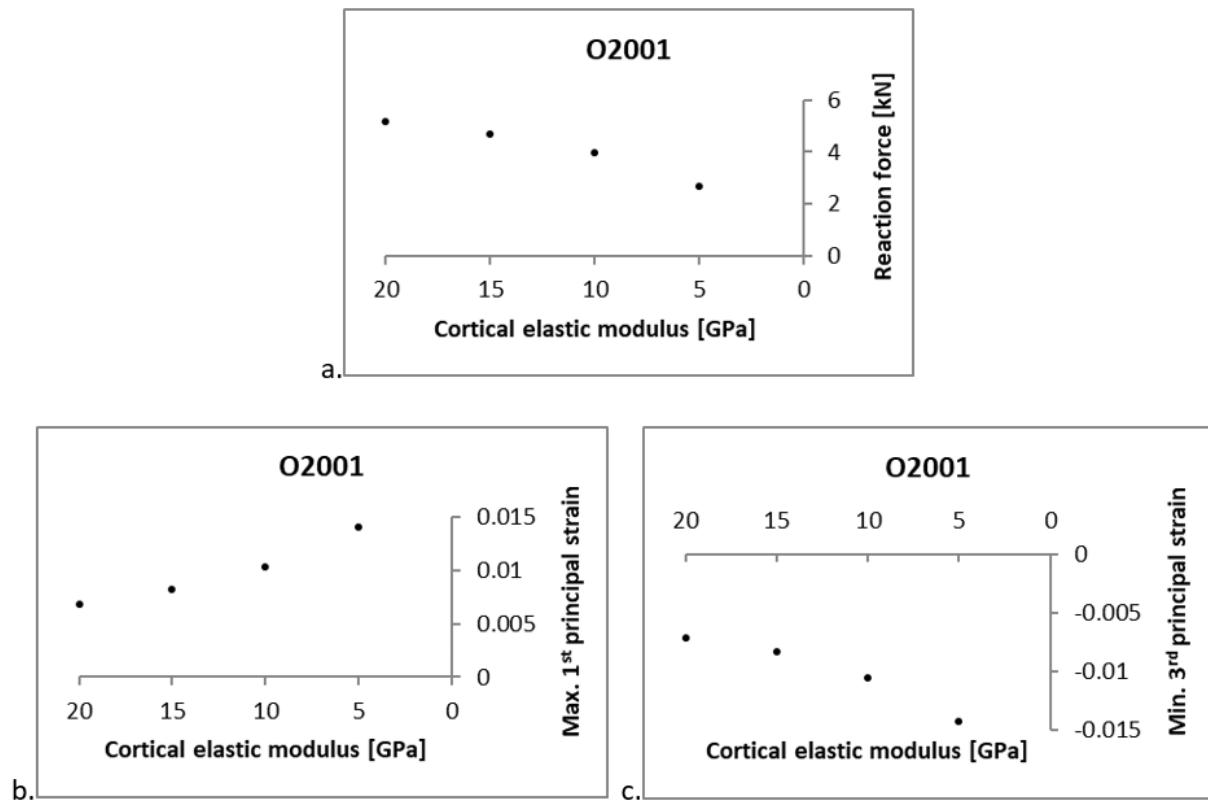


Figure 8-24: FE predicted reaction force (a), maximum 1st principal strain (b) and minimum 3rd principal strain (c) of the ROI plotted against the cortical elastic modulus for bone O2001.

Figure 8-25 illustrates the two extreme values of elastic modulus (20GPa and 5GPa) tested in this study on bone O2001. Although the absolute value of the strain increased, the strain distribution in the bone remained the same. In contrast, the strain distribution in the resin blocks and the bonded region (between bone and resin) changed slightly when the elastic modulus decreased.

O2001

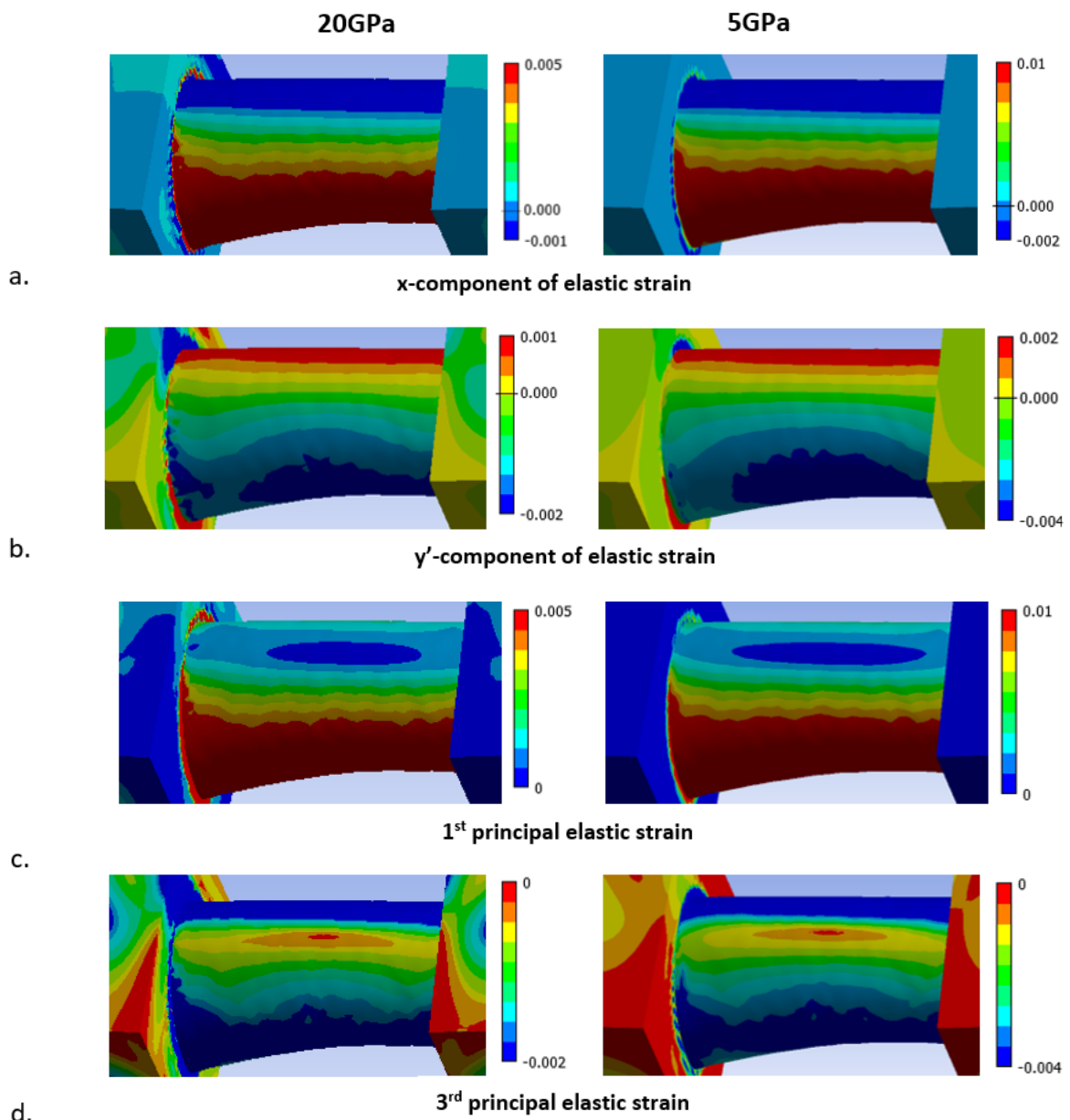


Figure 8-25: FE predicted surface strains of bone O2001 with a cortical elastic modulus of 20GPa (left column) and 5GPa (right column). (a) Strains in the x-direction. (b) Strains in the y'-direction. (c) Principal tensile strain. (d) Principal compressive strain.

8.4 Discussion

This section discusses the accuracy of the modelling techniques (boundary conditions, model geometries and material properties) used in this chapter and their limitations.

8.4.1 Reaction forces

When assigned a cortical elastic modulus of 20GPa, the FE predicted reaction forces were up to three times higher than the experimental reaction forces. The discrepancy between the FE and experimental results could be attributed to a potential overestimation of the elastic modulus. As illustrated early in the chapter, porosity was observed in most of the bones, and therefore 20GPa (estimated for a non-porous cortical bone) represented the upper bound of the stiffness value. Indeed, when the elastic modulus of the bone was reduced, the predicted reaction force also decreased. However, it is difficult to inversely estimate the correct elastic modulus value for cortical bone from the experimental reaction force, due to the uncertainty around the Technovit material property and the boundary condition at the bone-resin interface, which will be discussed below.

The contact type assigned between the shaft and cubes in the FE models could have also caused an overprediction of the force. As discussed in Chapter 7, the bones were seen to slip out of the embedding blocks during the experiments. Consequently, towards the end of the experiment, the bones were not properly constrained on the tension (lateral) side along the x-axis. On the other hand, in the FE models, the shafts were bonded to the cubes, and thus were equally well constrained on both the lateral (primarily tension) and medial (primarily compression) sides throughout the simulation, leading to a higher reaction force compared to the experiment.

8.4.2 Strain contours

When assigned a cortical elastic modulus of 20GPa, the FE x and y strain contours compared well qualitatively and quantitatively from the cranial line upwards. Note that the y-strains in the DIC images of bones A2002 and A2005 had strain concentration attributed to noise at the upper and lower borders of the ROI. These strain islands should be ignored when comparing against the FE strains. The position of the neutral line (0 strain) was accurately predicted in the FE. However, the strains compared less well below the cranial line. On the lateral side, tension was over-predicted for all bones, except for bone A2001. This could again be attributed to the slipping of the bone from the embedding material in the experiment.

Both principal strains were overpredicted in the FEA. As explained in Chapter 6, the magnitudes of the principal strains were expected to be higher in the FEA because DIC only measures in-plane principal strain (e.g. 2D strain tensor), whereas the principal strains obtained in FEA also accounted for out of plane strains (e.g. 3D strain tensor). Note that the discrepancy was greater in the lateral side than in the medial side; this could again be attributed to the slipping of the bones in the experiment.

The sensitivity analysis showed that lowering the cortical bone elastic modulus increased the magnitude of the strains but did not affect the strain distribution over the ROI. This suggests that the load transfer across the bone and the resin (via the bonded contact) is sensitive to the material property of the bone, and in fact the property of the resin too if a similar sensitivity analysis was conducted on the elastic modulus of the resin. This makes the bonded contact condition one major limitation in the current modelling approach.

8.4.3 Assumptions and limitations

Due to financial constraints, it was only feasible to scan the shaft with the innermost sides of each resin cubes. Ideally however, it would be nice to scan the whole specimen so that the entire structure can be created from μ CT images in order to include the whole bone (with both embedded ends) and two resin cubes as one continuous volume. As a consequence, two aspects of the embedding part of the specimens were modified. First, the bone structure within the embedding material was ignored, and the embedding parts were modelled as perfect cubes consisting only of Technovit. This has limited the study to the cortical section of the diaphysis, neither the epiphyses nor the trabecular tissue was modelled. Second, the bone was constrained to the embedding cubes using bonded contact. This means that the effective shaft length was shorter and that the load transfer between the bone and the embedding material was different from the reality (also some slippage occurred in the experiment). In the FEA, the bonded contact would have over-constrained the bone-resin interface, overpredicting the strains and reaction forces compared to the experiment.

Another limitation was the estimation and derivation of the material properties. The material properties assigned to Technovit were taken from the literature, in which the Young's modulus of Technovit was mentioned without appropriate citation (Grassi et al. 2016). Therefore, its accuracy requires further investigation. Moreover, the derivation of the elastic

modulus of the cortical bone was based on assumptions of the ovine bones' porosity and on one equation reported by (Grant et al. 2014), the validity of which needs to be confirmed by other groups.

Lastly, this study was limited to the linear region of the bending experiment, and did not model the torsional behaviour observed in the first instance of the experiment. In Chapter 6, the bending response of the bones was visually differentiated from the torsional response in the force-displacement curves. Then, the curves were linearly corrected for the bending linear region in order to obtain the equivalent displacement. This manual process could have introduced uncertainties. Furthermore, although the bending behaviour was differentiated from the torsional behaviour in the force-displacement curve, the torsional and bending strains were not differentiated in the strain maps. Strains caused by torsion at the start of the experiment were not evaluated. Therefore, the DIC strain maps shown in this chapter were a result of both torsion and bending, whereas the FE strain maps resulted mainly from bending. However, the torsional angles were small in most samples and any torsional strains would in theory have presented as shear strains, and would not have appeared on the normal strain maps. Therefore, the effect of torsion is likely to be negligible (with the exception of bones A2001 and A2005 that had a larger angle difference).

8.5 Conclusions

The experimental approach taken in Chapter 6 allowed for a more consistent FE modelling approach in this chapter; mainly with respect to the orientation of the bone and the successful reduction in rigid body motion. Consequently, the validation process was greatly improved. Each specimen was accurately aligned in the CAD space by simply using the embedding cubes as landmarks. The FE results showed higher consistency and compared well with the experimental images, particularly above the cranial line. The dissimilarities below the cranial line were attributed to: (1) the bonded contact assumption defined between the bones and the embedding material, as a result of the limited scanning range with the μ CT, and (2) uncertainties around the elastic moduli of both ovine cortical bone and Technovit. It would appear that the use of homogeneous isotropic elements in the modelling of the diaphysis of immature long bone is a valid approach, provided that the material properties of the bone

can be accurately estimated. In case of ovine bones, this could be carried out in future using conventional tensile/compression tests on bone samples.

9 CONCLUSIONS, LIMITATIONS AND FUTURE WORK

This thesis has been successful in broadening the knowledge on immature bone fracture mechanism. The in-house CT-based patient-specific FEM pipeline (CT2S) was experimentally validated for the mineralized cortical part of the lamb femur. This was undertaken in three steps. First, methods to carry out a four-point bending tests on lamb femurs were investigated using DIC to capture surface strains. Second, the four-point bending experiments were replicated using in-house FE pipeline incorporating further necessary adaptations for immature lamb bones. Finally, critical steps and assumptions in the FE model were assessed and discussed to achieve the best representation of immature bone.

Two experimental and modelling methodologies were investigated: one performing four-point bending on whole femur bones (including the periosteum), and another performing four-point bending on embedded shafts (no periosteum). When performing the bending tests, a few important aspects which had substantial impact on the results became apparent. This chapter will highlight these important findings associated with both the experiment and modelling approaches, before providing an outlook to the future and the implications on modelling children's bones based on the lamb bone findings.

9.1 Conclusions

This section provides a list of recommendations for setting up experimental and computational pipelines based on the findings of this thesis, detailing how each setting improves the reliability of experimental measurements or model prediction compared to other alternatives.

9.1.1 Experimental recommendations

- **An alignment system for lamb femurs based on the shortest path around the long axis of the bone can be used for quick and repeatable alignment.** The Standardization and Terminology Committee (STC) of the International Society of Biomechanics (ISB) defines the principal axis of the human femur as a line passing through the centre of the femoral head, which is coplanar to an axis passing through the centre of both condyles (Wu et al. 2002). However, defining the centre of the femoral head and condyles in an experimental setting is time consuming, which is less advisable when

working with biological samples. Finding the centre of the femoral head and condyles is also very difficult due to the natural asymmetries of the bone, as well as the lack of a prominent femoral head in lambs, which can lead to inaccuracies. Hence an alternative alignment system specific to lamb femurs was developed in this thesis, whereby anatomical landmarks were determined by three points, which coincide with the shortest path along the bone in the longitudinal direction. This path is found using an elastic band, which is a fast process and ensures accurate repeatability.

- **For accurate DIC measurement of immature whole bone shafts, the periosteum should be removed.** The periosteum itself hinders the use of the DIC method for measurements of surface strain. Periosteum membrane has a strong sheen. The sheen on the periosteum easily came through the layers of paint, creating areas of overexposure in the captured images, thus turning into errors in DIC measurements. This is particularly problematic for smaller bones with narrow curvatures, where the light hits the specimen at different angles, exacerbating overexposure. Furthermore, when reaching a certain strain, the periosteum detaches from the bone and surface measurements over the periosteum are no longer representative of bone tissue strain, i.e. the strain measurement associated to fracture criterion (Bayraktar et al. 2004).
- **To achieve a more controlled loading during bending tests of lamb femurs, the femurs should be embedded at the extremities and the load should be applied on the embedding material.** In this thesis, different loading methods were investigated for each set of experimental tests. For the first set, the load was applied directly onto the bones (Chapter 5), whereas for the second set the bones were embedded and the load was applied onto the embedding material (Chapter 7). In the first set, applying the load directly on the bone led to full body motion, i.e. poor repeatability between tests. This was reflected in the results. On the other hand, the embedding material used in the second set allowed for much more precise positioning of the bone, and increased repeatability.

In the first set of experiment, due to their curved geometries, the bones experienced out of plane deformation and crushing under the loading pins. This introduced errors/uncertainties in the strain distribution within the ROI, as well as the force-displacement readings. On the other hand, in the second set, the strain results did not show evidence of out of plane bending. In fact, the resulting strain contours had a typical pure bending distribution. This indicates that using an embedding material to indirectly induce bending moment appeared to be a promising method for more accurate and repeatable results.

9.1.2 Computational recommendations

- **Clinical and μ CT-scans can be used to accurately extract the geometry of the mineralised shaft of an immature long bone.** The work in this thesis demonstrated that the geometry of immature bone can be accurately extracted using both clinical and μ CT-scans. This has shown promise that paediatric bone geometry can be extracted from both aforementioned imaging modalities provided that the resolution is adequate. The μ CT-scans can provide more details with the structure at the tissue level, but are more computationally expensive to process due to the larger file sizes.
- **The alignment of the lamb femur can be replicated computationally by determining the trough on the distal end of the trochlear groove, the trough of the cranial face of the trochlear groove, and the cranial trough of the femoral neck.** The work in this thesis showed the orientation of the bones in the FEMs can be accurately replicated using anatomical landmarks specific to lamb femur.
- **The segmentation should be converted into a solid to define geometrical features on which to apply boundary conditions prior to meshing.** In previous studies modelling bending of paediatric femurs, the CT-based models were generated by directly meshing the segmentation, meaning that nodes onto which boundary conditions were applied were not well controlled. Based on the work of this thesis, it is recommended that the segmentation is first converted into a CAD model in order

to create geometrical definitions onto it, which can then be used to generate a more controlled mesh.

- **In CT-based models of immature femurs, the cortical bone should be delineated from the marrow and assigned homogeneous material properties.** One of the common approaches of CT-based patient specific FEM of the adult femur is that it is best modelled with a heterogeneous mesh using material properties derived from CT scans, bypassing the need to delineate the cortical bone. Not having any delineation between cortical bone and marrow poses a big challenge when modelling children's bones, because as the size of the specimen decreases (cortical thickness reaching the limit of voxel resolution in standard clinical CT), heterogeneous material mapping becomes more prone to errors due to increased inaccuracy in local material estimation. For smaller specimen, the change in material property in the cortical region drops drastically towards the periosteal and endosteal surfaces. Therefore, the voxel size, the effect of FBP blurring, and the element size of the model, can lead to partial volume of a relatively large portion of the cortical thickness; which translates into a misrepresentation of the mineral density of the outer layer, and hence the elastic modulus. This is particularly problematic when validating the model against surface strain measurements (i.e. using DIC or even SG). The results in Chapter 5 revealed that a homogeneous mesh was equally able to predict strains when only the shaft of lamb femur was considered. Therefore, based on the findings of this thesis, it is recommended to assign homogeneous material properties over cortical bone in immature femurs.
- **Isotropic material properties can be assumed to model mineralized bone (or shaft region) in infants and toddlers with adequate accuracy.** The results of Chapter 7 and 8 confirmed that isotropic material properties can be assumed to model lamb femurs. In Chapter 6, the idea to include the orientation and anisotropy when modelling the cortical part of a long bone for better accuracy was considered. This would only apply if the microstructure of the bone purely consisted of lamellar bone, i.e. children aged three years and above, as woven bone (primarily found in very young children 0-2

years) is not stress orientated. Furthermore, for the correct application of anisotropic material properties, the orientation of the model would need to be defined based on tissue microstructure orientation, greatly increasing the complexity of the modelling pipeline. Therefore, it is concluded that isotropic material is appropriate for modelling immature cortical bone.

9.2 Limitations

This section clarifies how the recommended experimental and computational choices differ from reality (the clinical context) with a discussion on the implications of these gaps.

9.2.1 Experimental limitations

9.2.1.1 Effect of the periosteum

It is evident that the periosteum plays an important part in the mechanical behavior of immature bone. This was highlighted in the differences seen in the fracture propagation between the first and second set of experiments. Under load, the periosteum was capable of holding a fractured bone together, allowing the whole structure to carry further load until complete failure (i.e. when the periosteum ruptures). As a result, the bones in the first experimental set appeared to have much more comminuted fractures than those in the second set. This was particularly true for bone O1002, which had a visually thicker periosteum. This finding highlights the importance of including the periosteal sheath in FE models for a better representation of *in vivo* fracture behavior of the whole immature bone.

9.2.1.2 Experimental loading method and embedding

Controlled loading during bending tests of lamb femurs can be achieved by embedding at the extremities and applying the load onto the embedding material. However, it is important to note that in the second set of experimental tests, some bones slipped out of the embedding material. Therefore, the bones were not appropriately constrained. This could explain when the femur specimens were embedded in Technovit in a previous study, large differences were found in tensile strains between DIC results and FE predictions (Grassi et al. 2013).

9.2.2 Computational limitations

9.2.2.1 Replicating the alignment in CAD

The alignment approach defined in this thesis is only applicable for femurs with proximal and distal epiphysis that are sufficiently mineralised, so that the trough on the distal end of the trochlear groove, the trough of the cranial face of the trochlear groove, and the cranial trough of the femoral neck are distinguishable. For younger femurs, a different approach will need to be defined.

9.2.2.2 Material properties for mineralised bone

Deriving elastic modulus of bone tissue from CT images relies on the derivation of ash density from the CT attenuation, and empirical relationships between the elastic modulus and the ash or apparent density of the bone. The derivation of ash density from CT-attenuation is straight forward and follows the same principles as the adult femur. However, the relationship between elastic modulus and mineral density is more complex for immature bone and needs further investigating. Empirical relationships relating elastic modulus to bone density (Öhman et al. 2011), are limited to children over the age of four years old. This relationship cannot be readily assumed for younger children, because the microstructure of bone changes from woven to lamellar around the age of three to four.

9.2.2.3 Material properties for mineralising bone

It is important to highlight that, unlike adults, a large portion of immature bone is not fully mineralized. Although not mineralized, this portion of the bone still plays a part in the fracture mechanism of the said bone. In this thesis, both models (whole bone and embedded) were focused on understanding the mechanical response of the shaft only. The parts of the femur which have yet to mineralize during development, such as the epiphyses, that are primarily (if not completely) composed of cartilage cannot be imaged with CT scans, limiting the CT-based pipeline to the modelling of mineralized bone.

9.3 Future work

In the application to create more accurate FE models in order to study long bone mechanical properties in children, the findings from this thesis suggest that CT-based personal specific

modelling of immature bone is a promising technique to explore, and that further efforts should be placed on the accurate quantification of immature bone properties across a variety of age range. In particular:

- **The experimental set-up.** Further investigation into different types of embedding materials (those stronger than the bone tissues) and methods could help improve the end constraints and prevent resins from failing prior to the bone.
- **The effect of the periosteum.** Given the current available technology, it became evident that the periosteum and the bone are best regarded as two separate entities during testing. The periosteum should be removed from the bone tissue so that one can first understand the mechanical behavior of immature bone only. Separate mechanical tests can then be carried out on periosteum samples at a tissue level in order to characterize its properties independently, such as tensile tests. Such information can then be brought together in a FE model to characterize the whole bone property including the periosteum.
- **The relationship between elastic modulus and bone density.** Further studies are required in order to accurately characterize the empirical relationship between elastic modulus and mineral density. This can then be used to quantify cortical bone properties based on available CT scans of children at various ages. Whenever available, further mechanical tests need to be carried out on bone samples (both normal and diseased) of children at all ages in order to directly quantify their material properties.
- **The properties of mineralizing bone.** The material properties of mineralizing bones should be characterized in order to be added to the FE model to present a more complete representation of the bone *in vivo*.

Once validated, a future modelling pipeline could influence medical-legal decision-making framework in medical child abuse cases. CT-based FEM could be used to better understand immature bone fracture mechanism and could also in turn generate quantitative estimates of fracture loads, patterns and locations for any given bone structure. This information could be used to provide a table of bone injury tolerances; which would serve as an assisting tool

for the diagnosis and prognosis of paediatric fracture, as well as a quantitative tool to differentiate accidental from non-accidental injuries.

REFERENCES

- Aerssens, J., S. Boonen, G. Lowet & J. Dequeker (1998) Interspecies Differences in Bone Composition, Density, and Quality: Potential Implications for in Vivo Bone Research1. *Endocrinology*, 139, 663-670.
- Agna, J. W., H. C. Knowles & G. Alverson (1958) The mineral content of normal human bone. *The Journal of clinical investigation*, 37, 1357-1361.
- Altai, Z., M. Qasim, X. Li & M. Viceconti (2019) The effect of boundary and loading conditions on patient classification using finite element predicted risk of fracture. *Clinical Biomechanics*, 68, 137-143.
- Altai, Z., M. Viceconti, A. Offiah & X. Li (2018) Investigating the mechanical response of paediatric bone under bending and torsion using finite element analysis. *Biomechanics and Modeling in Mechanobiology*, 17, 1001-1009.
- Ambrose, C. G., M. Soto Martinez, X. Bi, J. Deaver, C. Kuzawa, L. Schwartz, B. Dawson, A. Bachim, U. Polak, B. Lee & C. Crowder (2018) Mechanical properties of infant bone. *Bone*, 113, 151-160.
- Bayraktar, H. H., E. F. Morgan, G. L. Niebur, G. E. Morris, E. K. Wong & T. M. Keaveny (2004) Comparison of the elastic and yield properties of human femoral trabecular and cortical bone tissue. *J Biomech*, 37, 27-35.
- Bilo, R. A. C., S. G. F. Robben & R. R. VanRijn (2010) Forensic Aspects of Paediatric Fractures: Differentiating Accidental Trauma From Child Abuse. *Forensic Aspects of Paediatric Fractures: Differentiating Accidental Trauma from Child Abuse*, 1-209.
- Butchart, A. 2006. *Preventing Child Maltreatment: A Guide to Taking Action and Generating Evidence*. World Health Organization.
- Carter, D. R. & W. C. Hayes (1977) The compressive behavior of bone as a two-phase porous structure. *J Bone Joint Surg Am*, 59, 954-962.
- Carter, D. R., W. C. Hayes & D. J. Schurman (1976) Fatigue life of compact bone—II. Effects of microstructure and density. *J Biomech*, 9, 211,IN1,215-214,IN3,218.
- Castro, A. P. G., Z. Altai, A. C. Offiah, S. C. Shelmerdine, O. J. Arthurs, X. Li & D. Lacroix (2019) Finite element modelling of the developing infant femur using paired CT and MRI scans.
- Cech, D. 2011. *Functional movement development across the life span*. Philadelphia, Pa. ; London: Philadelphia, Pa. ; London : Saunders, 2011.
- Cheong, V. & A. Bull (2015) A novel specimen-specific methodology to optimise the alignment of long bones for experimental testing. *Journal of Biomechanics*, 48, 4317-4321.
- Cheong, V. S., A. Karunaratne, A. A. Amis & A. M. J. Bull (2017) Strain rate dependency of fractures of immature bone. *Journal of the Mechanical Behavior of Biomedical Materials*, 66, 68-76.
- Cowin, S. C. 2001. *Bone mechanics handbook*. Boca Raton, Fla. ; London: Boca Raton, Fla. ; London : CRC, 2001.

- Cristofolini, L. & M. Viceconti (1999) Towards the standardization of in vitro load transfer investigations of hip prostheses. *Journal of Strain Analysis for Engineering Design (UK)*, 34, 1-15.
- Currey, J. D. (1988) The effect of porosity and mineral content on the Young's modulus of elasticity of compact bone. *J Biomech*, 21, 131-139.
- Currey, J. D. & G. Butler (1975) The mechanical properties of bone tissue in children. *J Bone Joint Surg Am*, 57, 810-814.
- Dall'Ara, E., P. Varga, D. Pahr & P. Zysset (2011) A calibration methodology of QCT BMD for human vertebral body with registered micro-CT images. *Med Phys*, 38, 2602-2608.
- Deckard, C., A. Walker & B. Hill (2017) Using three- point bending to evaluate tibia bone strength in ovariectomized young mice. *Journal of Biological Physics*, 43, 139-148.
- Le Page, W., 2019. DIC fundamentals. <https://digitalimagecorrelation.org/>.
- Dickinson, A. S., A. C. Taylor, H. Ozturk & M. Browne (2011) Experimental validation of a finite element model of the proximal femur using digital image correlation and a composite bone model. *Journal of biomechanical engineering*, 133, 014504.
- Forman, J. L., E. D. P. De Dios, I. Symeonidis, J. Duarte, J. R. Kerrigan, R. S. Salzar, S. Balasubramanian, M. Segui-gomez & R. W. Kent. 2012. Fracture tolerance related to skeletal development and aging throughout life: 3-point bending of human femurs. In *2012 IRCOBI Conference Proceedings - International Research Council on the Biomechanics of Injury*, 524-539.
- Goldman, L. W. (2007) Principles of CT and CT Technology. *J Nucl Med Technol*, 35, 115-128.
- Grant, C. A., L. J. Wilson, C. Langton & D. Epari (2014) Comparison of mechanical and ultrasound elastic modulus of ovine tibial cortical bone. *Medical Engineering and Physics*, 36.
- Grassi, L. & H. Isaksson (2015) Extracting accurate strain measurements in bone mechanics: A critical review of current methods. *Journal of the Mechanical Behavior of Biomedical Materials*, 50, 43-54.
- Grassi, L., E. Schileo, F. Taddei, L. Zani, M. Juszczak, L. Cristofolini & M. Viceconti (2012) Accuracy of finite element predictions in sideways load configurations for the proximal human femur. *Journal of Biomechanics*, 45, 394-399.
- Grassi, L., S. P. Väänänen, S. Amin Yavari, H. Weinans, J. S. Jurvelin, A. A. Zadpoor & H. Isaksson (2013) Experimental validation of finite element model for proximal composite femur using optical measurements. *J Mech Behav Biomed Mater*, 21, 86-94.
- Grassi, L., S. P. Väänänen, M. Ristinmaa, J. S. Jurvelin & H. Isaksson (2016) How accurately can subject-specific finite element models predict strains and strength of human femora? Investigation using full-field measurements. *J Biomech*, 49, 802-806.
- Grassi, L., S. P. Väänänen, S. A. Yavari, J. S. Jurvelin, H. Weinans, M. Ristinmaa, A. A. Zadpoor & H. Isaksson (2014) Full- field strain measurement during mechanical testing of the human femur at physiologically relevant strain rates. *Journal of Biomechanical Engineering*, 136.

- Halat, G., M. Sasso, S. Naili & M. Matsukawa (2008) Ultrasonic velocity dispersion in bovine cortical bone : An experimental study. *J Acoust Soc Am*, 124, 1811-1821.
- Helgason, B., E. Perilli, E. Schileo, F. Taddei, S. Brynjólfsson & M. Viceconti (2007a) Mathematical relationships between bone density and mechanical properties: A literature review. *Clin Biomech (Bristol, Avon)*, 23, 135-146.
- Helgason, B., O. S. Gilchrist, J. D. Ariza, G. Chak, R. P. Zheng, S. J. Widmer, P. Ferguson, P. A. Guy & P. A. Cipton (2014) Development of a balanced experimental– computational approach to understanding the mechanics of proximal femur fractures. *Medical Engineering and Physics*, 36.
- Helgason, B., F. Taddei, H. Pálsson, E. Schileo, L. Cristofolini, M. Viceconti & S. Brynjólfsson (2007b) A modified method for assigning material properties to FE models of bones. *Med Eng Phys*, 30, 444-453.
- Hirsch, C. & F. G. Evans (1965) Studies On Some Physical Properties of Infant Compact Bone. *Acta Orthopaedica Scandinavica*, 35, 300-313.
- International Digital Image Correlation Society, 2008. A Good Practices Guide for Digital Image Correlation.
- Jansen, L. E., N. P. Birch, J. D. Schiffman, A. J. Crosby & S. R. Peyton (2015) Mechanics of intact bone marrow. *J Mech Behav Biomed Mater*, 50, 299-307.
- Juszczyk, M. M., L. Cristofolini & M. Viceconti (2011) The human proximal femur behaves linearly elastic up to failure under physiological loading conditions. *Journal of Biomechanics*, 44, 2259-2266.
- Kaffman, A. (2009) The Silent Epidemic of Neurodevelopmental Injuries. *Biological Psychiatry*, 66, 624-626.
- Kalender, W. A., D. Felsenberg, H. K. Genant, M. Fischer, J. Dequeker & J. Reeve (1995) The European Spine Phantom — a tool for standardization and quality control in spinal bone mineral measurements by DXA and QCT. *European Journal of Radiology*, 20, 83-92.
- Kemp, A. M., F. Dunstan, S. Harrison, S. Morris, M. Mann, K. Rolfe, S. Datta, D. P. Thomas, J. R. Sibert & S. Maguire (2008) Patterns of skeletal fractures in child abuse: systematic review. *British Medical Journal*, 337, 8.
- Key Non Parliamentary Papers Office For National, S. 2018. Homicide in England and Wales: Year ending March 2017.
- Key Non Parliamentary Papers Office for National, S. 2020. Child abuse extent and nature, England and Wales: year ending March 2019.
- Keyak, J. H. & Y. Falkinstein (2003) Comparison of in situ and in vitro CT scan-based finite element model predictions of proximal femoral fracture load. *Med Eng Phys*, 25, 781-787.
- Knowles, N. K., J. M. Reeves & L. M. Ferreira (2016) Quantitative Computed Tomography (QCT) derived Bone Mineral Density (BMD) in finite element studies: a review of the literature. *J Exp Orthop*, 3, 1-16.

- Li, X., M. Viceconti, M. C. Cohen, G. C. Reilly, M. J. Carré & A. C. Offiah (2015) Developing CT based computational models of pediatric femurs. *Journal of Biomechanics*, 48, 2034-2040.
- Linde, F. & H. C. F. Sørensen (1993) The effect of different storage methods on the mechanical properties of trabecular bone. *J Biomech*, 26, 1249-1252.
- Lipson, S. F. & J. L. Katz (1984) The relationship between elastic properties and microstructure of bovine cortical bone. *J Biomech*, 17, 231,237-235,240.
- Lu, P. W., C. T. Cowell, S. A. Lloyd-Jones, J. N. Briody & R. Howman-Giles (1996) Volumetric bone mineral density in normal subjects, aged 5- 27 years. *The Journal of clinical endocrinology and metabolism*, 81, 1586-1590.
- Martini, L., M. Fini, G. Giavaresi & R. Giardino (2001) Sheep model in orthopedic research: a literature review. *Comparative medicine*, 51, 292-299.
- Morgan, E. F., H. H. Bayraktar & T. M. Keaveny (2003) Trabecular bone modulus– density relationships depend on anatomic site. *Journal of Biomechanics*, 36, 897-904.
- Morgan, E. F., G. U. Unnikrisnan & A. I. Hussein (2018) Bone Mechanical Properties in Healthy and Diseased States. *Annu Rev Biomed Eng*, 20, 119-143.
- Nafei, A., C. C. Danielsen, F. Linde & I. Hvid (2000) Properties of growing trabecular ovine bone. Part I: mechanical and physical properties. *The Journal of bone and joint surgery. British volume*, 82, 910-920.
- Norman, R. E., M. Byambaa, R. De, A. Butchart, J. Scott & T. Vos (2012) The long- term health consequences of child physical abuse, emotional abuse, and neglect: a systematic review and meta- analysis. *PLoS medicine*, 9, e1001349-e1001349.
- Öhman, C., M. Baleani, C. Pani, F. Taddei, M. Alberghini, M. Viceconti & M. Manfrini (2011) Compressive behaviour of child and adult cortical bone. *Bone*, 49, 769-776.
- Osterhoff, G., E. Morgan, S. J. Shefelbine, L. Karim, L. McNamara & P. Augat (2016) Bone mechanical properties and changes with osteoporosis. *Injury-Int. J. Care Inj.*, 47, S11-S20.
- Palanca, M., G. Tozzi & L. Cristofolini (2016) The use of digital image correlation in the biomechanical area: a review. *International biomechanics*, 3, 1-21.
- Pan, B. (2018) Digital image correlation for surface deformation measurement: historical developments, recent advances and future goals. *Measurement Science and Technology*, 29.
- Pearce, A. I., R. G. Richards, S. Milz, E. Schneider & S. G. Pearce (2007) Animal models for implant biomaterial research in bone: A review. *European Cells and Materials*, 13, 1-10.
- Qasim, M., G. Farinella, J. Zhang, X. Li, L. Yang, R. Eastell & M. Viceconti (2016) Patient- specific finite element estimated femur strength as a predictor of the risk of hip fracture: the effect of methodological determinants. *With other metabolic bone diseases*, 27, 2815-2822.

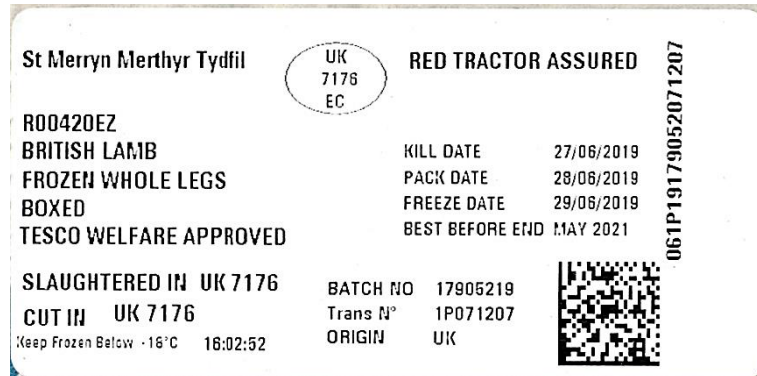
- Robyn, K. F. a. W. R. T. a. S. J. W. 2019. 2 - Bone biology. In *Bone Repair Biomaterials (Second Edition)*, ed. M. P. a. J. A. P. Kendell, 15-52. Woodhead Publishing.
- Schaffler, M. B. & D. B. Burr (1988) Stiffness of compact bone: Effects of porosity and density. *J Biomech*, 21, 13-16.
- Scheuer, L. 2000. *Developmental juvenile osteology*. San Diego, Calif. ; London: San Diego, Calif. ; London : Academic, c2000.
- Schileo, E., L. Balistreri, L. Grassi, L. Cristofolini & F. Taddei (2014) To what extent can linear finite element models of human femora predict failure under stance and fall loading configurations? *J Biomech*, 47, 3531-3538.
- Schileo, E., E. Dall'Ara, F. Taddei, A. Malandrino, T. Schotkamp, M. Baleani & M. Viceconti (2008a) An accurate estimation of bone density improves the accuracy of subject-specific finite element models. *Journal of Biomechanics*, 41, 2483-2491.
- Schileo, E., F. Taddei, L. Cristofolini & M. Viceconti (2008b) Subject-specific finite element models implementing a maximum principal strain criterion are able to estimate failure risk and fracture location on human femurs tested in vitro. *Journal of Biomechanics*, 41, 356-367.
- Schileo, E., F. Taddei, A. Malandrino, L. Cristofolini & M. Viceconti (2007) Subject-specific finite element models can accurately predict strain levels in long bones. *Journal of Biomechanics*, 40, 2982-2989.
- Shea, G. (2003) Textbook of Veterinary Anatomy. *Australian Veterinary Journal*, 81, 270-270.
- Standring, S. 2005. *Gray's anatomy [electronic resource]*. Elsevier / Churchill Livingstone, c2005.
- Sutton, M. A. 2009. *Image correlation for shape, motion and deformation measurements : basic concepts, theory and applications*. New York, N.Y.: New York, N.Y. : Springer, c2009.
- Taddei, F., L. Cristofolini, S. Martelli, H. S. Gill & M. Viceconti (2006) Subject-specific finite element models of long bones: An in vitro evaluation of the overall accuracy. *Journal of Biomechanics*, 39, 2457-2467.
- Taddei, F., I. Palmadori, W. R. Taylor, M. O. Heller, B. Bordini, A. Toni & E. Schileo (2014) European Society of Biomechanics S.M. Perren Award 2014: Safety factor of the proximal femur during gait: A population-based finite element study. *Journal of Biomechanics*, 47, 3433-3440.
- Taddei, F., E. Schileo, B. Helgason, L. Cristofolini & M. Viceconti (2007) The material mapping strategy influences the accuracy of CT-based finite element models of bones: An evaluation against experimental measurements. *Medical Engineering and Physics*, 29, 973-979.
- Tassani, S., C. Öhman, F. Baruffaldi, M. Baleani & M. Viceconti (2010) Volume to density relation in adult human bone tissue. *J Biomech*, 44, 103-108.
- Theobald, P. S., A. Qureshi & M. D. Jones (2012) Biomechanical investigation into the torsional failure of immature long bone. *Journal of Clinical Orthopaedics and Trauma*, 3, 24-27.

- Tommasini, S. M., P. Nasser, M. B. Schaffler & K. J. Jepsen (2005) Relationship Between Bone Morphology and Bone Quality in Male Tibias: Implications for Stress Fracture Risk. *J Bone Miner Res*, 20, 1372-1380.
- Torzilli, P. A., K. Takebe, A. H. Burstein & K. G. Heiple (1981) Structural properties of immature canine bone. *Journal of biomechanical engineering*, 103, 232-238.
- Townsley, W. (1948) The influence of mechanical factors on the development and structure of bone. *Am J Phys Anthropol*, 6, 25-46.
- Van Buskirk, W. C., S. C. Cowin & R. N. Ward (1981) Ultrasonic Measurement of Orthotropic Elastic Constants of Bovine Femoral Bone. *J Biomech Eng*, 103, 67-72.
- Viceconti, M. (2014) Biomechanics-based in silico medicine: The manifesto of a new science.
- Viceconti, M., F. Taddei, L. Cristofolini, S. Martelli, C. Falcinelli & E. Schileo (2012) Are spontaneous fractures possible? An example of clinical application for personalised, multiscale neuro-musculo-skeletal modelling. *Journal of Biomechanics*, 45, 421-426.
- Weaver, K. J. (1966) The Microscopic Hardness of Bone. *The Journal of Bone & Joint Surgery*, 48, 273-288.
- Winsor, C., X. Li, M. Qasim, C. R. Henak, P. J. Pickhardt, H. Ploeg & M. Viceconti (2021) Evaluation of patient tissue selection methods for deriving equivalent density calibration for femoral bone quantitative CT analyses. *Bone*, 143, 115759-115759.
- Wu, G., S. Siegler, P. Allard, C. Kirtley, A. Leardini, D. Rosenbaum, M. Whittle, D. D. D'lima, L. Cristofolini, H. Witte, O. Schmid & I. Stokes (2002) ISB recommendation on definitions of joint coordinate system of various joints for the reporting of human joint motion—part I: ankle, hip, and spine. *Journal of Biomechanics*, 35, 543-548.
- Yushkevich, P. A., J. Piven, H. C. Hazlett, R. G. Smith, S. Ho, J. C. Gee & G. Gerig (2006) User-guided 3D active contour segmentation of anatomical structures: Significantly improved efficiency and reliability. *Neuroimage*, 31, 1116-1128.
- Zani, L., P. Erani, L. Grassi, F. Taddei & L. Cristofolini (2015) Strain distribution in the proximal Human femur during in vitro simulated sideways fall. *Journal of Biomechanics*, 48, 2130-2143.
- Zannoni, C., A. Cappello & M. Viceconti (1998) Optimal CT scanning plan for long- bone 3-D reconstruction. *IEEE Transactions on Medical Imaging*, 17, 663-666.
- Zdero, R., M. S. R. Aziz & B. Nicayenzi. 2017. *Experimental Methods in Orthopaedic Biomechanics*. Academic Press.
- Zhang, G., X. Deng, F. Guan, Z. Bai, L. Cao & H. Mao (2018) The effect of storage time in saline solution on the material properties of cortical bone tissue. *Clinical Biomechanics*, 57, 56-66.
- Zimmermann, E. A., C. Riedel, F. N. Schmidt, K. E. Stockhausen, Y. Chushkin, E. Schaible, B. Gludovatz, E. Vettorazzi, F. Zontone, K. Püschel, M. Amling, R. O. Ritchie & B. Busse. 2019. Mechanical Competence and Bone Quality Develop During Skeletal Growth. 1461-1472. *Journal of Bone and Mineral Research*.

Zioupos, P. & J. D. Currey (1998) Changes in the Stiffness, Strength, and Toughness of Human Cortical Bone With Age. *Bone*, 22, 57-66.

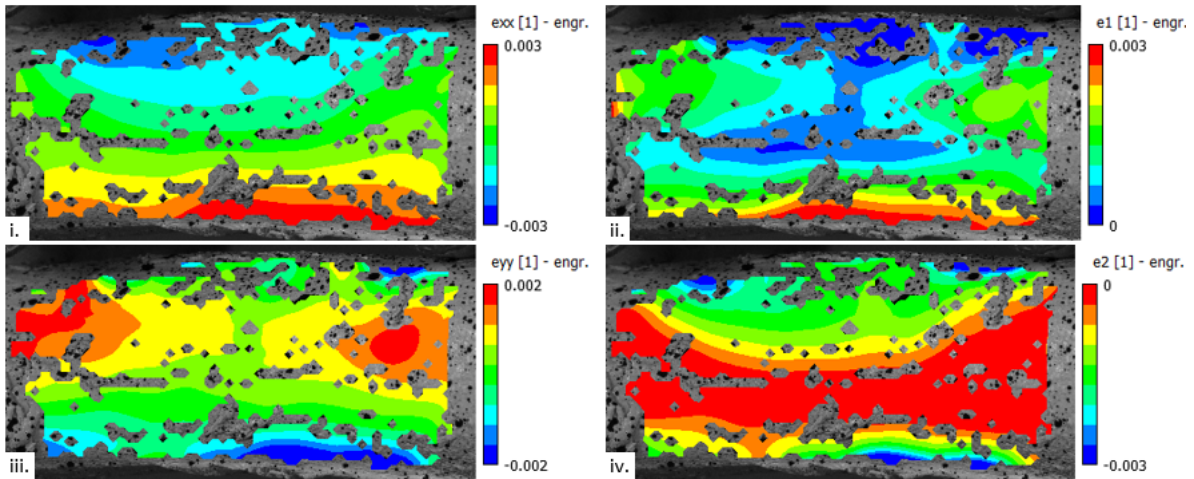
APPENDIX

Chapter 5 appendix

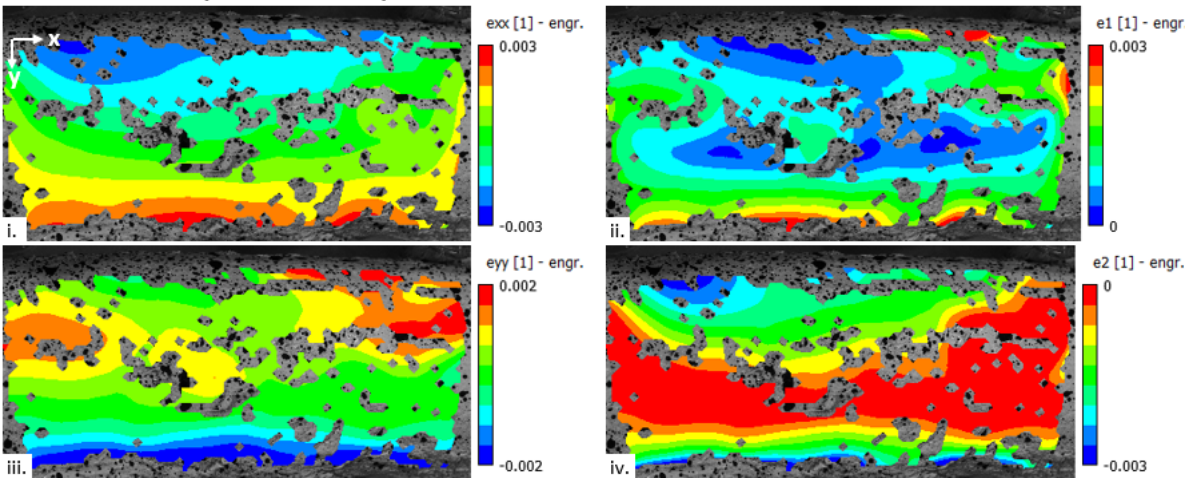


Appendix 1: Slaughter batch tracking label for lamb bones A1003, A1004, D1005 and D1006.

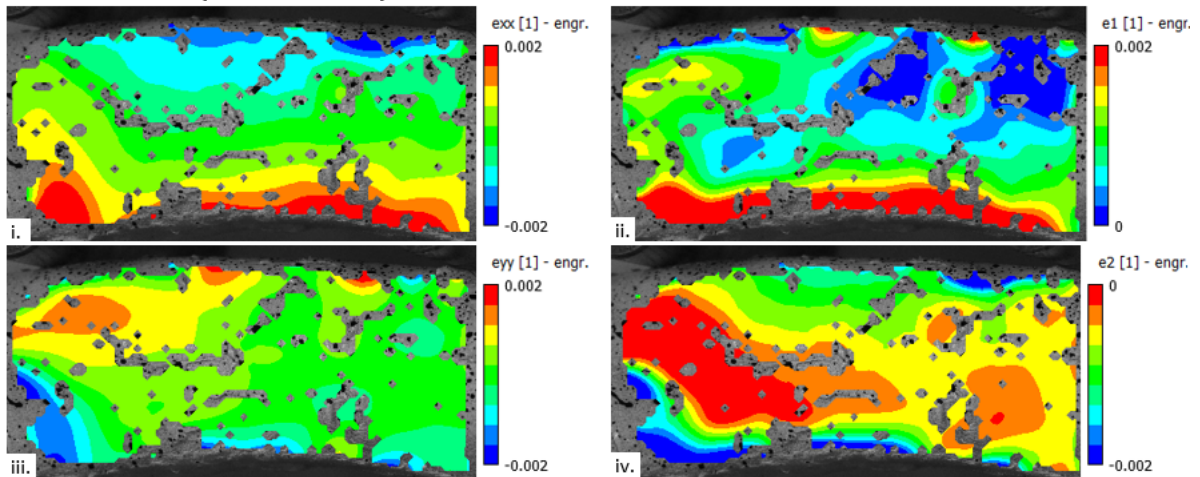
a. O1001 – LF1 – (1.1mm, 1.1kN)



b. O1002 – LF1 – (0.9mm, 1.1kN)



c.A1003 – LF1 – (1.5mm, 1.0kN)



Appendix 2: Surface strains of bone O1001 (a), O1002 (b), and A1003 (c) under four-point bending at the end of the first linear region, LF1, obtained through DIC a using a step to subset size ratio of 1/3. (i) Engineering plane strains in the x-direction. (ii) First principal plane strain (tension). (iii) Engineering plane strains in the y-direction. (iv) Second principal plane strains (compression).

Chapter 7 appendix



Appendix 3: Slaughter batch tracking label for lamb bones A2001 - A2005 and D2001 - D2002.